Continuum based modelling and simulation of rate-dependent effects in inelastic solids: Applications for biological growth and damage mechanics

Von der Fakultät für Bauingenieurwesen
der Rheinisch-Westfälischen Technischen Hochschule Aachen
zur Erlangung des akademischen Grades eines Doktors der Ingenieurwissenschaften
genehmigte Dissertation

vorgelegt von

Lukas Adrian Lamm, M. Sc.

Berichter*innen: Prof. Dr.-Ing. habil. Stefanie Reese
Prof. Dr.-Ing. habil. Udo Nackenhorst

Tag der mündlichen Prüfung: 19. Juli 2024

Program terminated signalling SIG segfault

FEAP

Acknowledgements

This dissertation is the results of my work as a research associate at the *Institute of Applied Mechanics (IFAM)* at *RWTH Aachen University*. During my time at the institute, I had the great privilege to get to know and work with many wonderful people. I would therefore like to express my gratitude to all these people who assisted me and have contributed (in one way or another) to the success of this thesis. All English-speaking readers may forgive me for writing the following personal acknowledgements in my native tongue, which is German.

Was für ein Ritt! Es ist wahrlich nicht leicht eine Doktorarbeit zu schreiben und ohne die Unterstützung so vieler wundervoller Menschen, die mich auf meiner Reise begleitet haben wäre dies auch sicherlich nicht möglich gewesen.

Mein erster Dank gilt meiner Betreuerin Frau Prof. Dr.-Ing. habil. Stefanie Resse, die mir die Möglichkeit gab in ihrem Team und unter ihrer Leitung jene Forschung zu betreiben, welche letztlich zu dieser Arbeit geführt hat. Ihre kontinuierliche Unterstützung und Loyalität mir und allen anderen Angestellten gegenüber rechne ich ihr hoch an. Ich möchte mich dabei vor allem für die vielfältigen interessanten und anregenden Diskussionen bedanken, sowie für das hervorragende und bereichernde wissenschaftliche Umfeld, welches sie mit ihrem Team geschaffen hat.

Desweiteren möchte ich Herrn Prof. Dr.-Ing. habil. Udo Nackenhorst aufrichtig danken. Mit seinen Grundlagenvorlesungen zur Mechanik und Simulation war er es, der während meines Studiums an der Leibniz Universität Hannover mein Interesse für diesen Fachbereich entfacht hat. Meine Mitarbeit als studentische Hilfskraft an seinem Institut brachte mir nicht nur die vielen Facetten der numerische Mechanik nahe, sondern ließ auch die Entscheidung in mir Reifen in diesem Bereich promovieren zu wollen. Und obwohl ich ein Angebot zur Promotion an seinem Lehrstuhl aus persönlichen Gründen ausschlug, unterstützte er mich bei der Suche nach einer geeigneten Stelle. Er war es, der mich somit erst nach Aachen und an das IFAM gebracht hat. Für all diese Unterstützungen sowohl während als auch nach dem Studium möchte ich mich an dieser Stelle herzlichst bedanken.

Ferner möchte ich mich herzlichst bei Herrn Prof. Dr.-Ing. Markus Feldmann dafür bedanken, dass er den Vorsitz der Promitionskommission übernommen hat.

Den Kolleginnen und Kollegen am Institut möchte ich für eine wirklich tolle Zeit und die außergewöhlich gute und offene Athmosphäre danken. Für die vielen fachlichen und privaten Diskussionen, den freundschaftlichen Umgang und die stete Hilfsbereitschaft. Obwohl ich euch alle sehr ins Herz geschlossen haben, so möchte ich mich doch bei einigen von euch noch besonders bedanken. Hierzu zählen meine beiden Büropartnern, Elisabeth Toups und Kiran

Manjunatha. Bei euch möchte ich mich vor allem für die wundervollen und freundschaftliche Athmosphäre in unserem gemeinsamen Büro bedanken. Desweiteren möchte ich Dr.-Ing. Tim Brepols für seine stetige Unterstützung und die vielen guten Gespräche, sowohl fachlicher als auch privater Natur, bedanken. Ohne die Unterstützung durch Dr.-Ing. Hagen Holthusen, wäre ich sicherlich nicht in der Lage gewesen, diese Arbeit in der vorlegenden Form abzuliefern. Hierfür und für unser freundschaftliches Verhältnis bin ich sehr dankbar.

Diese Arbeit wäre sicherlich nicht möglich gewesen ohne die Unterstützung meiner HiWis und Abschlussarbeiter*innen. Ich möchte ihnen daher an dieser Stelle aufrichtig danken. Von ihnen sind vor allem meine beiden langjährigen HiWis, Jan Pfeifer und Ahmad Awad, besonders zu würdigen. Ihr beiden habt durch eure tatkräftige Hilfe und das Stellen der richtigen Fragen zum richtigen Zeitpunkt einen großen Teil zum Gelingen dieser Arbeit beigetragen. Denn nicht nur ihr habt von mir gelernt, sondern ich auch von euch.

Neben all den Menschen, die mich im Rahmen meiner Studien- und Doktorandenzeit als Vorgesetzte, Kolleg*innen und Freunde begleitet haben, möchte ich an dieser Stelle auch meiner Familie danken. Ohne euch wäre ich nicht und ohne euch hätte ich niemals so weit kommen können. Meinen Eltern und meinem Bruder für all die Unterstützung und Liebe, die mich auch in schweren Zeiten getragen hat. Meinen Kindern für all die Aufgaben vor die ihr mich stellt und an denen ich tagtäglich wachsen darf. Ihr steckt mich mit eurer wundervollen Neugier an und lasst das innere Kind in mir erwachen. Zu guter letzt will ich meiner Frau Judith danken. Für alle Höhen und Tiefen die wir gemeinsam erlebt und durchlebt haben. Für deine Liebe und Fürsorge zu mir und unseren Kindern. Es mag nicht immer leicht im Leben sein, aber mit dir an meiner Seite bin ich gewiss, dass ich eines Tages auf ein gutes und erfülltes Leben zurückblicken werde.

Summary

Nowadays, model-based simulation methods play a major role in the research and development of new technologies. This is not least due to the time and cost savings associated with their use. Ideally, however, physically motivated simulation models also provide a deeper insight into the processes depicted, which is otherwise difficult to achieve in many places. In the context of engineering sciences, the prediction of the behaviour of a wide variety of materials under mechanical loading plays a particularly important role. Since almost all materials tend to non-linear material behaviour under certain circumstances, the modelling can be very challenging depending on the effect under consideration. Especially in the area of rate- and time-dependent modelling of a wide variety of material properties, many open research questions remain yet to be answered. These include, for example, the description of time-dependent growth processes in biological materials or the modelling of rate-dependent damage phenomena.

The present cumulative dissertation presents a compilation of the author's (and his co-authors') work that has been published on topics of continuum mechanical modelling of rate-dependent material behaviour. After the introduction, the overview of the current state of research and the clarification of the research-relevant questions, four published research papers are presented.

The dissertation starts with a paper on the topic of modelling growth processes in artificially grown tissue. Based on experimental observations, a so-called homeostatic state is postulated in this work. Such a state describes a state of tension preferred by the tissue, which the material always tries to adopt through active contraction or expansion. This consideration forms the basis for modelling the corresponding growth-induced change in shape and volume. Following classical models for the description of plastic material behaviour, it is shown that by introducing a homeostatic potential, the development of the growth-related, inelastic strains can be elegantly described. For the description of the temporal component in the evolution of the inelastic strains, a classical Perzyna approach is used. In addition to the theoretical derivation, the numerical realization as well as the implementation in finite element (FE) software will be discussed in the following. Using numerical examples, it is shown that the new formulation is able to predict the growth behaviour more precisely than other well established models. This is especially illustrated by considering the influence of complex boundary conditions. Finally, a first investigation of the prediction quality of the model based on experimental data shows that the developed model is able to reasonably approximate the growth-induced homeostatic stress in the tissue.

Besides growth process effects, many other inelastic effects can occur in complex materials.

Polymers show a strong dependence in their deformation behaviour with respect to both loading rate and temperature. Furthermore, rate-dependent damage effects play a important role in these materials. In the further course of this dissertation, two articles and one conference proceeding are presented, dealing with the thermodynamically consistent modelling of rate-dependent damage behaviour in polymers. In the first two publications on this topic, the purely mechanical continuum model is presented. Based on the multiplicative decomposition of the deformation gradient, the viscoelastic material behaviour is described via a viscous potential. A Perzyna approach is used to model the rate-dependent evolution of the scalar damage variable. The thermodynamically consistent derivation is discussed in the following as well as the numerical treatment of the equations and their implementation in FE software. Finally, it is shown that the developed model is able to adequately represent creep damage and polymers. This is a great advantage compared to classical, rate-independent models, as these are not able to represent this effect in a meaningful way. Building on the previous publications, the last article in this work deals with the thermodynamically consistent extension of the proposed damage model to take thermal effects into account. For this purpose, a fully thermomechanically coupled formulation is presented on the basis of a further decomposition of the deformation gradient. Using appropriate parameter studies and numerical examples, the influence of temperature on the development of damage is investigated. Finally, the results of various structural calculations demonstrate the applicability of this mutliphysical simulation model for various applications.

In the last chapter, this dissertation concludes the research questions investigated herein and gives an outlook for further potential research based on the findings of this work.

Zusammenfassung

Modellbasierte Simulationsmethoden spielen heutzutage eine große Rolle im Bereich der Forschung und Entwicklung neuer Technologien. Dies ist nicht zuletzt auf die mit ihrem Einsatz verbundene Zeit- und Kostenersparnis zurückzuführen. Im Idealfall liefern physikalisch motivierte Simulationsmodelle jedoch auch einen tieferen Einblick in die abgebildeten Prozesse, welche sonst an vielen Stellen nur schwer möglich sind. Im Rahmen der Ingenieurwissenschaften spielt hierbei vor allem die Vorhersage des Verhaltens verschiedenster Materialien unter mechanischer Belastung eine große Rolle. Da fast alle Materialien unter entsprechenden Umständen zu nichtlinearem Materialverhalten neigen, kann die Modellierung je nach betrachtetem Effekt sehr herausfordernd sein. Insbesondere im Bereich der raten- und zeitabhängigen Modellierung von verschiedensten Materialeigenschaften sind noch viele offene Forschungsfragen zu klären. Hierzu gehören beispielsweise die Beschreibung von zeitabhängigen Wachstumsprozessen in biologischen Materialien oder die Modellierung von ratenabhängiger Schädigung.

In der vorliegenden kumulativen Dissertation wird in diesem Kontext eine Zusammenstellung der bereits veröffentlichten Arbeiten des Autors (und seiner Koautor*innen) zu Themen der kontinuumsmechanischen Modellierung von ratenabhängigem Materialverhalten präsentiert. Nach der Einleitung, dem Überblick über den aktuellen Stand der Forschung und der Klärung der forschungsrelevanten Fragen werden vier veröffentlichte Fachartikel vorgestellt.

Die Dissertation startet hierbei mit einer Arbeit zum Thema der Modellierung von Wachstumsprozessen in künstlich gezüchtetem biologischen Gewebe. Basierend auf experimentellen Beobachtungen wird in dieser Arbeit eine sogenannter homeostatischer Zustand postuliert. Ein solcher Zustand beschreibt einen vom Gewebe präferierten Spannungszustand, welchen das Material durch aktive Kontraktion oder Expansion stets versucht einzunehmen. Diese Überlegung bildet darauf aufbauend die Grundlage für die Modellierung der entsprechenden wachstumsinduzierten Form- und Volumenänderung. In Anlehnung an klassische Modelle zur Beschreibung von plastischem Materialverhalten wird gezeigt, dass durch die Einführung eines homeostatischen Potentials die Entwicklung der wachstumsbezogenen, inelastischen Dehnungen elegant beschrieben werden kann. Zur Beschreibung der zeitlichen Komponente in der Evolution der inelastischen Dehnungen wird dabei auf einen klassischen Perzyna Ansatz zurückgegriffen. Neben der theoretischen Herleitung wird im Folgenden auch auf die numerische Umsetzung, sowie die Implementierung in Finite Elemente (FE) Software eingegangen. Anhand numerischer Beispiele wird anschließend gezeigt, dass diese neue Formulierung in der Lage ist das Wachstumsverhalten präziser vorherzusagen als bis dahin gängige Modelle. Dies

wird vor allem unter Berücksichtigung des Einflusses komplexer Randbedingungen verdeutlicht. Abschließend zeigt eine erste Untersuchung der Vorhersagequalität des Modells anhand experimenteller Daten, dass das entwickelte Modell in der Lage ist die durch Wachstum induzierte homeostatische Spannung im Gewebe sinnvoll zu approximieren.

Neben Wachstumsprozesses können noch viele weitere inelastische Effekte in komplexen Materialien auftreten. Polymere weisen zum Beispiel eine stark ausgeprägte Abhängigkeit in ihrem Deformationsverhalten sowohl in Bezug auf die Belastungsrate als auch die Temperatur auf. Ferner spielen in diesen Materialien ratenabhängige Schädigungseffekte eine entsprechende Rolle. Im weiteren Verlauf dieser Dissertation werden daher zwei Artikel und ein Konferenz Proceeding vorgestellt, welche sich mit der thermodynamisch konsistenten Modellierung von ratenabhängigen Schädigunsverhalten in Polymeren beschäftigen. In den ersten beiden Veröffentlichungen zu diesem Thema wird das rein mechanische Kontinuumsmodell vorgestellt. Basierend auf der multiplikativen Zerlegung des Deformationsgradienten wird das viskoelastische Materialverhalten über ein viskoses Potential beschrieben. Zur Modellierung der ratenabhängige Entwicklung der skalaren Schädigungsvariable wird auf einen Perzyna Ansatz zurückgegriffen. Die thermodynamisch konsistente Herleitung wird im Folgenden genauso thematisiert wie die numerische Behandlung der Gleichungen und deren Implementierung in FE Software. Abschließend wird gezeigt, dass das entwickelte Modell in der Lage ist Kriechschädigung und Polymeren adäquat abzubilden. Dies ist ein großer Vorteil im Vergleich zu klassischen, ratenunabhängigen Modellen, da diese nicht ohne Weiteres in der Lage sind diesen Effekt sinnvoll abzubilden. Der letzte Artikel in dieser Dissertation beschäftigt sich aufbauend auf den vorherigen Publikationen mit der thermodynamisch konsistenten Erweiterung des vorgeschlagenen Schädigungsmodells zur Berücksichtigung von thermischen Effekten. Hierzu wird auf Grundlage einer weiteren Zerlegung des Deformationsgradienten eine thermomechanisch voll gekoppelte Formulierung vorgestellt. Anhand entsprechender Parameterstudien und numerischer Beispiele wird der Einfluss der Temperatur auf die Entwicklung der Schädigung im Polymer untersucht. Die Ergebnisse verschiedener Strukturrechnungen demonstrieren abschließend die Anwendbarkeit dieses mutliphysikalischen Simulationsmodells für verschiedene Anwendungsfälle.

Die vorliegende Dissertation schließt im letzten Kapitel mit einem Fazit zu den untersuchten Forschungsfragen und gibt einen Ausblick für weitere potentielle Forschungsziele, welche sich auf Grundlage der vorgelegten Ergebnisse sinnvoll ergeben.

Contents

1 Introduction

> We may regard the present state of the universe as the effect of its past and the cause of its future. An intellect which at a certain moment would know all forces that set nature in motion, and all positions of all items of which nature is composed, if this intellect were also vast enough to submit these data to analysis, it would embrace in a single formula the movements of the greatest bodies of the universe and those of the tiniest atom; for such an intellect nothing would be uncertain and the future just like the past could be present before its eyes.
>
> *Pierre Simon Marquis de Laplace*
> in Laplace [1902]

1.1 Motivation and research relevant questions

Even though current research in the field of artificial intelligence is constantly working on evoking *Laplace's demon*, an omniscient intelligence seems to be more an idea of science fiction literature than reality at this point in time. We are therefore left with the possibility of approaching the complexity of our world with the help of cleverly chosen modelling approaches. From a mechanical point of view, this is particularly the case in the area of predicting the behaviour of various types of materials. These cover a very large domain, ranging from classical engineering materials such as rubber to more exotic materials such as artificially grown tissue. Despite all their differences, most materials are similar in one simple point:

their mechanical behaviour is far from simple. It is therefore one of the great challenges in material modelling to find formulations that are simple enough to allow a meaningful interpretation and at the same time include all relevant effects of the problem at hand. If this balancing act is successful, such modelling approaches are valuable tools for predicting the behaviour of complex materials. When used properly, model-based simulation methods can accelerate the development of new technologies drastically. This is especially the case if experimental investigations are very time-consuming or cost-intensive. In this case, the number of experiments needed during the development process can be reduced to a minimum on the basis of a meaningful model.

A prominent example for the need of computational modelling is the development of so-called biohybrid implants. Here, to put it simply, the patient's own tissue is artificially cultivated in a bioreactor for use as an implant. In order to ensure the mechanical stability of the tissue, it is supplemented with non-biological components. These can be simple polymer fibres, among others. The aim of this addition can be, for example, to counteract excessive deformation of the implant under mechanical stress. Experimentally determining the ideal fibre position for this purpose is, without exaggeration, a hopeless endeavour. It is therefore of great advantage to use a mathematically based model that can reasonably predict the growth process together with the deformation behaviour of the implant. While the material behaviour of fibre-reinforced biological materials has already been researched extensively, there are still many open questions in the field of growth modelling of such systems. A very prominent effect in the cultivation of artificially grown tissue is tensional homeostasis. It describes a deformation process induced by the tissue itself, which leads to a build-up of tensile stresses in the material. A common hypothesis is that the smooth muscle cells actively contract the surrounding tissue because they need a certain tension in the material in order to exist. From a mechanical point of view, this effect is very interesting due to the self-induced tensions and should therefore not be neglected when modelling artificially cultured tissue. As will be described in more detail in the following paragraph, some models which are based upon the multiplicative decomposition of the deformation gradient into elastic and growth related parts already exist. Unfortunately, most of these approaches to model the self-induced growth process are not able to represent the material behaviour under arbitrary boundary conditions in a meaningful way. It is therefore of great interest to find new modelling formulations that are also able to represent the desired effect of homeostasis well also under complex structural conditions.

Another example of the need for meaningful simulation models in the field of material theory is that of general damage processes in arbitrary materials. While the final failure of a material

is comparatively easy to observe experimentally, the same cannot be said for the development of damage before the ultimate failure. Especially in the case of mechanical loading of complex structures, an experimental investigation of early damage arising within the material is often not feasible in a meaningful way. Here, damage models can make a useful contribution to understanding the effects that lead to the failure of a corresponding structure. In this respect, the modelling of the damage behaviour of polymers is particularly interesting. This type of material is characterised not only by its strong temperature dependence but also by a strongly rate-dependent material behaviour. While the area of classical viscoelasticity has already been researched and modelled many times over the last decades, the same cannot be said for rate-dependent damage processes. A prominent example of such a rate-dependent damage process is that of creep damage in polymers. In this case, the material fails under creep load only with a time delay after a certain creep strain has already set in. However, a combination of viscoelastic models with classical damage formulations is usually not able to reproduce this behaviour properly. With regard to the use of polymers, e.g. as adhesives in the construction industry, a meaningful modelling of creep failure is of great interest and should therefore be the subject of current research. Due to the pronounced temperature dependence of polymer materials already mentioned above, a thermodynamically consistent multi-physical modelling is indispensable. Such a modelling approach must include both, the thermal influence on the material as well as heat generated due to dissipative processes in the material itself.

This dissertation presents approaches to clarify the research questions described above on inelastic, rate-dependent material behaviour in biological tissue and as well as polymers. A brief outline of the current state of research on this topic is presented in the following section.

1.2 State of the art

All models presented in this dissertation are based on the basic idea that the deformation gradient can be multiplicatively decomposed into different components, for which the underlying assumption is that any inelastic deformation can be described by means of a stress-free intermediate material configuration. Whilst this basic idea dates back to the works of Eckart [1948] and Kröner [1959], the overall concept has been adapted multiple times to model various inelastic effects under finite deformations (see e.g. Lubarda [2004]; Sadik and Yavari [2015]). In the field of non-linear thermoelasticity Stojanovic et al. [1964] were the first to formally introduce the split into elastic and thermal parts. Soon after, Lee and Liu [1967] and Lee [1969] used the similar concept to model finite plasticity. Some decades later, Rodriguez et al. [1994] introduced a multiplicative split to describe the growth related deformation of living systems.

Also in the field of rate-dependent material modelling, the multiplicative decomposition was introduced, e.g. for finite viscoelasticity as shown in Reese and Govindjee [1998] or Bergström [1998]. Within all these approaches mentioned above, the concept of hyperelasticity is used as a ground model to describe the elastic contribution of the material response. Here, the existence of a specific and differentiable strain energy is postulated, which acts as a potential for the stresses (see e.g. Coleman and Noll [1963]). When modelling inelastic effects, information on the current state of inelastic deformations must be tracked throughout the mechanical process. To achieve this, the pioneering works of Coleman and Gurtin [1967]; Rice [1971] and Germain et al. [1983] introduced the concept of internal state variables in a mathematically sound and thermodynamically consistent manner. This concept has subsequently been used in countless modelling approaches and is also included in the models developed within this dissertation.

1.2.1 Biological growth

As described earlier, one of the important aspects of modelling the mechanics of growth processes within soft tissue is the description of active geometry changes due to contraction or expansion of the material. Throughout this dissertation, this effect will be referred to as *volumetric growth* and must not be confused with the change in density or internal structure of the material, which is also often reffered to as growth in the common literature. It is clear, that a detailed modelling approach of such growth processes must also take the multiphysical nature of the problem into account. This would not only include the influence of mechanical stimuli but also of other physiological factors such as e.g. nutrients, hormones, among many others. Examples for such complex modelling approaches are the recent works of e.g. Escuer et al. [2019] or Manjunatha et al. [2022]; Gierig et al. [2023]. However, it is generally assumed that the mechanical stimulation plays one of the dominant roles in this process, since it triggers e.g. the production of growth factors. Therefore, the complex problem of volumetric growth is often reduced and studied merely from the mechanical perspective.

While early works of Skalak [1981] and Skalak et al. [1982] already dealt with the changes in size and chapes of growing soft tissue, it was the work of Rodriguez et al. [1994] and the introduction of the multiplicative split which laid the foundation for most of the models in this field to come. Since then many publications have been made to describe volumetric growth using this basic framework. For a comprehensive overview the interested reader is referred to the works of Goriely [2018] or Ambrosi et al. [2019]. In general, models based on the multiplicative decomposition of the deformation gradient can be divided into two categories; Isotropic and anisotropic growth models.

Isotropic models assume that the growth related part of the deformation gradient is proportional to the identity tensor, which leads to a uniform change of volume and shape in all spatial dimensions. Due to its simplicity, isotropic growth models are applied widely throughout the literature. Among others, Lubarda and Hoger [2002]; Himpel et al. [2005] as well as Hajikhani et al. [2021]; Lee et al. [2021] are some examples for models based on this assumption. Unfortunately, such models are often strongly limited when it comes to the prediction of structures with complex boundary conditions. This is due to the fact that the assumption of an uniform change in volume is way to restrictive form a kinematical point of view. As it has been shown e.g. in Braeu et al. [2017, 2019], an isotropic growth response is rather the exception than the norm when it comes to real biological systems.

Rejecting the assumption of isotropic expansion naturally leads to an anisotropic growth formulation. Anisotropy in this case means that the growth related expansion does not need to be uniform in all spatial dimensions but can rather differ for individual spatial components. The most simple way of discribing an anisotropic growth relation is by assuming that growth always takes place along a certain preferred direction. Such approaches have been made by Göktepe et al. [2010]; Firouzi and Rabczuk [2022] or Groh [2022]; Rahman et al. [2023]; Sempértegui and Avril [2023], among others. These approaches have proven to work reasonably well when it comes to systems where the direction of growth can be determined a-priori, e.g. in the case of growing fibres. For more general case in which the direction of growth can not be predetermined, other models are needed, which describe growth in a more general sense. Such models have been developed by Menzel [2005]; Soleimani et al. [2020] or Lamm et al. [2021, 2022]; Holthusen et al. [2023], to name but a few.

In addition to the phenomenological models listed here, a completely different approach to describing anisotropic growth has become established on the basis of the work of Humphrey and Rajagopal [2002]. These are the so-called constrained mixture models. Their approach differs in such a way that it is assumed that a continuous increase and decrease in mass leads to the desired change in volume and shape. Since this modelling approach needs to track the overall change in mass throughout the whole duration of the growth process, the computational costs can be very high. To overcome this problem, a temporally homogenised version of this approach was developed by Cyron et al. [2016] and Cyron and Humphrey [2017]. More recent publications in this field, such as Braeu et al. [2017, 2019], build on this work and extend it to a more general formulation that has similar properties to the general anisotropic formulations mentioned above. For a detailed overview on various models and applications of constrained mixture theory, the interested reader is kindly referred to the comprehensive overview given in Humphrey [2021].

Within this dissertation, the focus lies on the phenomenological modelling approach of anisotropic volumetric growth which has been successfully introduced and further established in Lamm et al. [2021, 2022] and Holthusen et al. [2023]. This approach uses the mutliplicative decomposition to describe the growth related part of the deformation. To define its evolution, a potential for the homeostatic stress state is postulated and used as the basis for the derivation of appropriate evolution equations. Here, many ideas from the field of classic plasticity theory are reused in a modified manner to capture growth towards a preferred homeostatic stress state.

1.2.2 Viscoelasticity

When it comes to the description of rate-dependent material behaviour in solids, viscoelasticity is the classic effect that has been studied extensively in the computational mechanics community over the last decades. The result of this is a large number of various different modelling approaches describing viscoelastic material response under small and finite deformation. Although this dissertation focuses only on the modelling of large deformations, the literature on this topic is so extensive that an all-inclusive literature review cannot be provided here. Therefore, only the most important and influential modelling approaches in the author's opinion will be mentioned in the following.

Leaving aside the classical rheological modelling approaches, viscoelastic material models for large deformations can be roughly divided into two classes. Models that assume a linear relationship between stress and strain rate include, for example, the works of Lubliner [1985]; Simo [1987]; Holzapfel and Simo [1996]; Kaliske and Rothert [1997]; Simo and Hughes [1998]; Bonet [2001]. Such models have been applied successfully for various applications within the literature (see e.g. Xiang et al. [2020] for reference). Due to their linear nature, these models are only valid for small pertubations from the thermodynamic equilibrium, rendering them infeasible for many thermo-mechanical processes of interest. In contrast to that, more general models that also include a non-linear relation between stresses and strain rate, are also applicable for large pertubations from the thermodynamic equlibrium. The most commonly cited and used models of this kind are, for example, the ones of Reese and Govindjee [1998]; Bergström [1998] or Haupt et al. [2000]. One of the interesting features of such non-linear approaches is their ability to be easily reducable to the linear theory, which gives them more flexibility then classical linear models can provide. More recently, modelling approaches made by Fancello et al. [2006]; Kumar and Lopez-Pamies [2016]; Wang and Chester [2018]; Rambausek et al. [2022], among others, have followed this path of non-linear modelling and sucessfully applied the ideas established in the literature listed above.

Within this dissertation, the viscoelastic nature of the materials under consideration is

modelled using an adapted version of the general finite viscoelastic model developed by Reese and Govindjee [1998], which is again based on the multiplicative decomposition of the deformation gradient into elastic and viscous parts. To describe the evolution of the inelastic kinematic quantities, this approach postulates the existence of a viscous potential from wich the appropriate evolution equations are derived.

1.2.3 Thermo-mechanical coupling

If we consider inelastic processes, the mechanical energy lost through this process must also be considered. Since this energy is usually lost to the mechanical process in the form of heat, a multi-physical consideration taking temperature into account is appropriate for modelling such processes. For this, in addition to the mechanical balance equations, the balance of heat must also be solved in a coupled form. Furthermore, the kinematical constraints due to heat expansion of the material has to be considered.

Classical thermo-mechanically coupled models start from the fundamental relation between the materials heat capacity and the Helmholtz free energy (see Chadwick [1974]), which is subsequently integrated twice to determine the general form of the overall free energy. Based on this general idea, the model of Reese and Govindjee [1997] introduces a temperature and deformation dependent heat capacity yielding a non-linear relation between stresses and temperature. The description of heat expansion within this framework is then directly described via the Helmholtz free energy. Following this approach, more recent models of Xiao and Nguyen [2015]; Behnke et al. [2016]; Mehnert et al. [2017, 2018] or Dai et al. [2020], among others, adapted the same methodology successfully. Although such approaches are elegant and simple, they tend to pose a problem as soon as the modelling of damage processes come into the picture. Felder et al. [2022] showed that the damage growth criterion (see Wulfinghoff et al. [2017]) is not easily fulfilled a-priori by this kind of modelling attempt.

In contrast to the classical thermo-mechanical models listed above, the approach first introduced by Stojanovic et al. [1964] as well as Lu and Pister [1975] is based on a multiplicative split of the deformation gradient to describe the thermal expansion of the material by means of an individual part of the deformation gradient. The Helmholtz free energy is consequently additively split into mechanical and thermal contributions. The dependence of the stresses on the temperature is furthermore determined by introduction of temperature dependent material parameters (see e.g. Holzapfel and Simo [1996] and Lion [1996, 1997], among others). Considering the fundamental connection between the heat capacity and the free energy, this approach leads to a non-linear function of the heat capacity in terms of all internal variables considered. Therefore, the thermal part of the free energy must be chosen appropriately to en-

sure that unwanted dependencies do not arise from the model. Since this is usually not trivial, many approaches based on the split methodology assume that the heat capacity is constant and that the thermal energy takes whatever form needed to assure this assumption being true (see e.g. Canadija and Mosler [2011]; Aldakheel and Miehe [2017]; Dittmann et al. [2020]; Felder et al. [2022]). Only few approaches can be found in literature, which take the effort to actually determine a specific form of the thermal energy for a given material. Among them are, for example, the works of Lion [1996, 1997] or Lion et al. [2017].

Within the thermomechanical modelling approaches described in this dissertation, the multiplicative modelling approach is used to ensure that the damage growth criterion is a-priori fulfilled for arbitrary damage processes. Furthermore, a constant heat capacity is assumed.

1.2.4 Damage modelling

Although most materials differ greatly in their elastic and inelastic properties, one fact is certain: a continuous increase in load will, at a certain point, lead to damage of the material and ultimately to its failure. Especially when analysing complex structures and their maximum load capacity, a proper description of the damaging behaviour of different materials is of great importance and can give valuable insights for the optimal design of a mechanically loaded system. In times of raw material scarcity and global warming, this can contribute to a reduction in the consumption of valuable resources and the emission of climate-damaging substances.

When considering the micromechanical perspective, damage arising in deformable bodies is usually associated with the physical processes of the formation and development of microscopic cracks or cavities within the material itself. Depending on the type of material, a detailled modelling approach for these effects on the micro level is often not trivial and for many applications not even neccessary. This is especially true, if the overall macroscopic material response under damage and failure is rather simple. It is therefore often assumed, that damage can be described by means of a continuous reduction of the materials stiffness. Based on the pioneering works of Kachanov [1958] and Rabotnov [1969] many models in the field of the so-called *Continuum Damage Mechanics (CDM)* approach have been developed over the years. The assumption that the stiffness of a given material is degraded due to damage such that all spatial dimensions are effected equally leads to the classical isotropic damage models. The modelling approaches use a scalar valued internal damage variable to describe the amount of damage accumulated within the material. Many approaches choose this variable to be defined on the finite intevall $[0, 1]$ (e.g. Chaboche [1978]; Lemaitre [1984, 1985*a*,*b*]), whereas the works of Dimitrijevic and Hackl [2008]; Junker et al. [2019], among others, use

the open intervall $[0, \infty)$ for the definition of the damage variable. In both cases a value of zero referres to the virgin, undamaged state of the material. Whilst a value of one within the former approach corresponds to the fully damaged material, the latter modelling assumption only asymptotically approaches the fully damaged state while the damage variable approaches ∞. The evolution of the internal variable is usually derived from thermodynamic principles and the the hypothesis of strain (see Lemaitre [1971]; Lemaitre and Chaboche [1978]) or energy equivalence (Cordebois and Sidoroff [1982]). Over the years, extensions for various applications have been made to these original modelling approaches, e.g., aging effects in Marquis and Lemaitre [1988], crack-closure in Pires et al. [2003], introduction of Lode‘s angle in Lian et al. [2014], extension to finite strains in de Souza Neto et al. [2008], or material dissolution in van der Velden et al. [2021, 2023], to name but a few. For a comprehensive overview on various types of phenomenological CDM models, the interested reader is kindly refferd to the work of Skrzypek [1999].

The assumption of an isotropic damage response can be a strong one, since materials show a dependency of the damage evolution on the loading direction. To account for this, models considering the anisotropic evolution of the damage response have been developed over the years. Such models often make use of a higher order damage tensor instead of an scalar damage variable. A first order apporach has been made, for example, by Davison and Stevens [1973]; Krajcinovic and Fonseka [1981]; Dorn and Wulfinghoff [2021], while the works of Murakami and Ohno [1981]; Cordebois and Sidoroff [1982]; Fassin et al. [2019]; Reese et al. [2021] and Holthusen, Brepols, Reese and Simon [2022], among others, make use of second order damage tensor. There exist also approaches in literature using tensors of fourth or eighth order (see e.g. Chaboche et al. [1995] or Pituba and Fernandes [2011]).

Independent of the choice of the type of damage variable, all classical, local continuum damage models suffer from the same inherent problem when it comes to the simulation of structures. They show severe pathological mesh dependencies and non-uniqueness of the solution of the damage field. Since the initial reports made by Bažant et al. [1984] and de Borst et al. [1993], those issues have been studied extensively in the literature and various approaches have been developed in order to cure this problem. In the field of continuum damage modelling, two main research directions have been established among others. The *non-local integral type models* as developed and applied, for example, by Pijaudier-Cabot and Bažant [1987]; Ganghoffer et al. [1999]; Borino et al. [2003]) use a non-local integration of the damage variable to overcome the issue of damage localization. Although this is an elegant approach, the combination with classical Finite Element formulations is not straight forward and computational expensive. *Gradient-extended damage formulations*, on the other hand, introduce an internal length scale

by means of an additional partial differential equation describing the diffusive nature of the damage field itself. Based on this idea, *phase field models of fracture* (see Francfort and Marigo [1998]; Bourdin et al. [2000]) as well as *micromorphic damage models* (Dimitrijevic and Hackl [2008, 2009]; Forest [2009, 2016]) have been developed and successfully applied for various situations (see e.g. Brepols et al. [2017*a*,*b*]; Fassin et al. [2019]).

Besides viscoelastic effects, many materials also tend to show a rate-dependent damage response. A famous example is the *creep damage* response of polymers. Classical, rate-independent damage models unfortunately are not able to cover this kind of behaviour properly (see Lamm et al. [2023]). Various approaches for modelling of rate-dependent damage behaviour already exist in the literature, which can be devided into micromechanically motivated and continuum based models. In the case of polymeric materials the class of micromechanically based models is usually based on chain statistics and scission kinematics of the polymeric network (see e.g. Shaw et al. [2005]; Wineman and Shaw [2007]; Wineman [2009]; Vernerey et al. [2018]; Guo and Zaïri [2021]; Lavoie et al. [2016]. Continuum based models are usually motivated by phenomenological observations made in experiments. When cosidering the simulation of structures subjected to small deformations, a variety of rate-dependent damage models have been developed over the years. Some examples of such models are Murakami and Ohno [1981]; Lemaitre [1985*a*]; Wang et al. [2013]; Pandey et al. [2019]; Pereira et al. [2017]; Shlyannikov and Tumanov [2019]; Nahrmann and Matzenmiller [2021]; Kou et al. [2022] among others. The literature on rate-dependent damage models covering also finite deformations is up to now, however, relatively sparse. The works of Lion [1996]; Miehe [2000]; Lin and Schomburg [2003]; Aboudi [2011] build on the ideas from small strain theory and extends it to the finite strain regime. These models are based on the explicitly definitiion of an evolution equation considering the rate of a strain like quantity as the main driving force for the damage process. The approach of Khaleghi et al. [2022] uses a damage evolution law based on the work of Lemaitre [1985*a*] and adapts it to the finite strain regime. Lamm et al. [2023] use a classical damage formulation and introduce the rate-dependent material response by means of an modified Perzyna [1963] type Ansatz.

For completeness, it should be mentioned that there exist also other approaches for the modelling of damage besides the CDM theory. Various authors have also worked on approaches using *cohesive zone theory* (see e.g. Dugdale [1960]; Barenblatt [1962]; Bayat et al. [2020]) or X-FEM (see e.g. Pezeshki et al. [2017]). Within this dissertation, an isotropic, gradient extended, CDM model based on the work of Brepols et al. [2017*a*] is used and adapted to account for rate-dependent damage evolutions by using a modified Perzyna-type ansatz.

1.3 Outline of the dissertation

The cumulative dissertation presented here consists of three peer-reviewed journal articles (Chapters 2, 4 and 5) and one conference proceeding (Chapter 3). It is structured as follows:

Article 1 (Chapter 2) considers a novel modelling approach for the description of volumetric growth processes in artificially grown biological tissues. The main assumption for this model is that the tissue is able to actively contract or expand in order to approach a desired internal stress state. Such a state is called homeostatic state and is subsequently described in terms of an inelastic pseudo potential. The framework is based on the multiplicative decomposition of the deformation gradient into elastic and growth related parts. Instead of a-priori defining a fixed structure of the growth related deformation gradient, this formulation bases the evolution of the inelastic, growth related contributions to the deformation on a Perzyna-type evolution law which uses the homeostatic potential. This gives the model much more flexibility than previous modelling approaches and leads in general to an anisotropic deformation due to the growth process itself. The overall formulation is derived in thermodynamically consistent manner.

Article 2 (Chapter 3) presents a novel framework for the description of rate-dependent damage occuring in polymeric materials. In this conference proceeding, a fully elastic, isotropic damage model for finite strains is introduced. To account for the temporal effects arising from the damage process, a Perzyna-type Ansatz for the definition of the damage evolution equation is used. All quantities used in the model are derived in a thermodynamically consistent manner by fulfilling the restrictions arising from the Clausius-Planck inequality.

Article 3 (Chapter 4) builds upon the previous chapter and extends the rate-dependent damage model to also account for viscoelastic effects. The viscous part of the model is based on the multiplicative decomposition of the deformation gradient into elastic and inelastic parts. For the description of the evolution of viscous state variables, a viscoelastic pseudo potential is introduced. The whole model is derived in a thermodynamically consistent manner. Within extensive studies, the differences in the material response between viscoelasticity and rate-dependent damage are investigated. It is furthermore shown, that a combination of viscous effects and rate-dependent damage is capable of predicting creep damage processes accurately. This is a great advantage over classical damage models, since they are in general not capable of capturing this effect properly.

Article 4 (Chapter 5) describes the thermodynamically consistent extension of the aforementioned model for rate-dependent damage to also capture thermo-mechanical effects. For this, an additional decomposition of the deformation gradient into mechanical and thermal parts is utilized. The thermal expansion is assumed to be isotropic, which yields the thermal part of the deformation gradient being proportional to the identity tensor. For the influence of the temperature field on the mechanical response, a linear relation of the material parameters with respect to the current temperature is assumed. Subsequently, all thermodynamic driving forces, heat sources and thermal coupling terms are derived in a thermodynamically sound manner.

Finally, Chapter 8 draws a conclusion to the work presented here and gives an outlook on further potential research opportunities.

2 Article 1: A macroscopic approach for stress-driven anisotropic growth in bioengineered soft tissues

This article was published as:

Lamm, L.; Holthusen, H.; Brepols, T.; Jockenhövel, S.; Reese, S. [2022], 'A macroscopic approach for stress driven anisotropic growth in bioengineered soft tissues', *Biomechanics and modeling in mechanobiology* **21**, 627 – 645.

Disclosure of the individual authors' contributions to the article:

L. Lamm reviewed the relevant existing literature, performed all simulations, interpreted the results and wrote this article. L. Lamm and H. Holthusen worked out the theoretical material model and impemented it into the finite element software FEAP. H. Holthusen, T. Brepols, S. Jockenhövel and S. Reese gave conceptual advice, contributed in the discussion of the results, read the article and gave valuable suggestions for improvement. All authors approved the publication of the manuscript.

2.1 Abstract

The simulation of growth processes within soft biological tissues is of utmost importance for many applications in the medical sector. Within this contribution we propose a new macroscopic approach for modelling stress-driven volumetric growth occurring in soft tissues. Instead of using the standard approach of a-priori defining the structure of the growth tensor, we postulate the existence of a general growth potential. Such a potential describes all eligible homeostatic stress states that can ultimately be reached as a result of the growth process. Making use of well established methods from visco-plasticity, the evolution of the growth-related right Cauchy-Green tensor is subsequently defined as a time dependent associative evolution law with respect to the introduced potential. This approach naturally leads to a formulation that is able to cover both, isotropic and anisotropic growth-related changes in geometry. It furthermore allows the model to flexibly adapt to changing boundary and loading conditions. Besides the theoretical development, we also describe the algorithmic implementation and furthermore compare the newly derived model with a standard formulation of isotropic growth.

2.2 Introduction

The production and use of artificially grown biological tissue has become an important research topic in the medical context over the last two decades. Great progress has been made in implant research in particular, with the cultivation of biohybrid heart valves being just one example among many (Fioretta et al. [2019]). Designing and constructing highly complex medical implants is a big challenge due to the biomechanical properties of the underlying cultivated tissue. Early works in the field of biomechanics have already pointed out that biological tissues adapt dynamically to the environment they are exposed to (see e.g. Fung [1995] and references therein). The goal of this process is to reach a homeostatic state in which e.g. a certain critical stress state is neither exceeded nor fallen below. From a physiological point of view this process, which we will call growth in the following, is mainly driven by a change in mass and internal structure of the given biological material. It is important to notice that since the model presented in this paper is a purely phenomenological approach, we disregard the micromechanical effects of remodelling in the following and concentrate exclusively on the description of volumetric growth. Subsequently, the growth process leads to a change in the mechanical behaviour, which usually has a large influence on the performance of the given implant. In contrast to native tissue, these adaptive effects are particularly pronounced during the cultivation period of bioengineered tissues and must therefore be taken into account from

the beginning of the design process. Within this context, computational modelling contributes to a deeper understanding and prediction of such adaptation processes. An important aspect of modelling the mechanics of growth is the description of geometry changes which are due to contraction and expansion of the material, respectively. Starting from the works of Skalak [1981], Skalak et al. [1982] and Rodriguez et al. [1994], many models have been developed over the last decades in order to describe such finite volumetric growth effects. Although being already successfully applied e.g. in the modelling of finite plasticity (see e.g. Eckart [1948], Kröner [1959], Lee [1969]), it was the contribution of Rodriguez et al. [1994] which first adapted the multiplicative split of the deformation gradient to describe the inelastic nature of finite growth processes. For a detailed overview on the various modelling strategies, the interested reader is referred to the comprehensive overviews given e.g. by Goriely [2018] and Ambrosi et al. [2019]. Most of the approaches based on the conceptually simple and computationally efficient framework by Rodriguez et al. [1994] can be roughly divided into two different groups, isotropic (e.g. Lubarda and Hoger [2002], Himpel et al. [2005]) and anisotropic growth models (e.g. Menzel [2005], Göktepe et al. [2010], Soleimani et al. [2020]). It is important to outline that the terms *isotropic* and *anisotropic* which are used here in the context of describing the volumetric growth response must not be confused with the similar terminology of the underlying basic continuum mechanical models, where *anisotropy* is often used to denote an initially preferred direction within the material. In case of isotropic growth, the growth-related part of the deformation gradient tensor is often assumed to be proportional to the identity tensor (e.g. Lubarda and Hoger [2002]), which yields a uniform expansion of a referential volume element. On the other hand, the term anisotropic growth describes a geometry change of a given volume element that is not uniform in all three spatial dimensions but rather has a distinct growth direction (e.g. Göktepe et al. [2010]). Despite its widespread use, the approach of isotropic growth modelling has strong limitations with regard to describing the mechanical behaviour of complex structures. Recently, Braeu et al. [2017, 2019] pointed out that in the context of relevant applications, anisotropic growth behaviour is more the standard case than an isotropic response. Classically, this intrinsically anistropic growth behaviour is modelled using heuristic assumptions on the definition of preferred growth directions. This, unfortunately, yields the need to a-priori prescribe a certain structure of the growth-related deformation gradient. Whilst this approach might be feasible for relatively simple problems such as e.g. fibre elongation and contraction, it is not well applicable for more complex applications. In order to cure the need for describing the structure of the growth-related deformation gradient a-priori, more recent works (e.g. Zahn and Balzani [2017]) have developed formulations in which the growth-related deformation gradient tensor is constructed

with respect to the eigenvectors corresponding to the principal stress state. Nevertheless, defining general and flexible formulations that can adapt to various boundary value problems remains a challenging task and ongoing topic of research, as pointed out already by e.g. Menzel [2005] or Soleimani et al. [2020].

In addition to the phenomenologically motivated models described above, another class of models was established for describing growth processes. Originating from the theory of mixtures, Humphrey and Rajagopal [2002], among others, developed the constrained mixture theory. Instead of assuming that the volume as a whole is deformed during the growth process, this modelling approach describes the change of volume in terms of a continuous deposition and removal of mass increments. Since this approach is computationally very expensive, Cyron et al. [2016] and Cyron and Humphrey [2017] developed a homogenized version of the constrained mixture model. This is achieved by using a temporal homogenization of the mass increments alongside with the same multiplicative split as described by Rodriguez et al. [1994]. Although this approach overcomes the limitations of the classical constrained mixture theory in terms of computational costs, it still suffers from the need to a-priori define the structure of the growth tensor. Recent versions of this framework, as described e.g. in the work of Braeu et al. [2019], were able to modify this approach such that the growth tensor adapts automatically to the given boundary value problem.

As an alternative to the just mentioned promising approach, this contribution presents a different way on tackling the issue of predefined growth tensors. This novel and flexible framework for the description of stress driven volumetric growth is able to cover both, isotropic and anisotropic growth behaviour, naturally. Section 2.3 covers the theoretical modelling ideas behind the proposed model. The numerical implementation of the derived material model is described in Section 2.4. Finally, numerical examples are given in Section 2.5.

2.3 Continuum mechanical modelling of finite growth

Let us first introduce the well established multiplicative split of the deformation gradient $\mathbf{F}$ into an elastic and a growth-related part (see e.g. Rodriguez et al. [1994]), i.e.

$$\mathbf{F} = \mathbf{F}_e \mathbf{F}_g. \tag{2.1}$$

Using this equation, the determinant of $\mathbf{F}$, abbreviated by $J := \det \mathbf{F} = \det \mathbf{F}_e \det \mathbf{F}_g$, is also multiplicatively split into two parts. Whilst the change of volume due to elastic deformations is described by $J_e = \det \mathbf{F}_e$, the growth-related volume changes are represented by $J_g = \det \mathbf{F}_g$.

In analogy to the right Cauchy-Green tensor $\mathbf{C} = \mathbf{F}^T\mathbf{F}$ as well as the left Cauchy-Green tensor $\mathbf{B} = \mathbf{F}\mathbf{F}^T$, the elastic right Cauchy-Green tensor and the growth-related right and left Cauchy-Green tensor can be defined as

$$\begin{aligned} \mathbf{C}_e &:= \mathbf{F}_e^T\mathbf{F}_e = \mathbf{F}_g^{-T}\mathbf{C}\mathbf{F}_g^{-1} \\ \mathbf{C}_g &:= \mathbf{F}_g^T\mathbf{F}_g \\ \mathbf{B}_g &:= \mathbf{F}_g\mathbf{F}_g^T. \end{aligned} \tag{2.2}$$

Furthermore, the growth-related velocity gradient $\mathbf{L}_g$ is introduced as

$$\mathbf{L}_g = \dot{\mathbf{F}}_g\mathbf{F}_g^{-1}. \tag{2.3}$$

2.3.1 Balance relations

Growth processes within biological systems in general lead to a change of the systems mass as well as a change of its shape and volume, respectively. Within this contribution, the focus lies on the macroscopic description of changes in shape rather than a change of the systems mass. We therefore neglect the description of the balance of mass in terms of production or flux terms and assume that this balance relation is fulfilled implicitly. It is furthermore well established to assume that growth processes take place on a significantly larger time scale than mechanical deformations do. This standard argument is known as the *slow growth assumption* and yields a quasi-static setup of the well known balance of linear momentum

$$\mathrm{Div}\,(\mathbf{F}\mathbf{S}) + \mathbf{b}_0 = \mathbf{0}. \tag{2.4}$$

Here $\mathbf{S}$ and $\mathbf{b}_0$ denote the second Piola-Kirchhoff stress tensor and the referential body force vector per reference volume, respectively. Following the idea of open system thermodynamics (see e.g. Kuhl and Steinmann [2003] and references therein), we describe the entropy production $\dot{\gamma}$ in terms of the Clausius-Duhem inequality

$$\dot{\gamma} = \mathbf{S} : \frac{1}{2}\dot{\mathbf{C}} - \dot{\psi} + \mathcal{S}_0 \geq 0, \tag{2.5}$$

with the volume specific Helmholtz free energy density ψ defined more precisely in the following section. The additional referential entropy contribution $\mathcal{S}_0$ is capturing both, entropy fluxes through the boundary as well as entropy sources within the system itself. It is important to notice, that we do not explicitly compute this particular contribution but introduce it to allow e.g. for a decrease in entropy due to the growth process itself.

2.3.2 Helmholtz free energy

We start from the general continuum mechanical framework laid down in Svendsen [2001]. Within this context, the constitutive equations are described with respect to a given but otherwise arbitrary configuration of the material body in question. Similar to the approaches made by Bertram [1999] and Svendsen [2001] in the context of finite plasticity, we choose the elastic part of the Helmholtz free energy to be stated in terms of quantities defined within the so-called grown intermediate configuration.

When modelling finite volumetric growth, it is important to ensure that the growth process will ultimately reach a homeostatic state. This must be the case even under the absence of growth restricting boundary conditions, since, otherwise, the growth process would continue ad infinitum. A common approach to limit the growth response is to introduce a set of material parameters, which can be interpreted as the maximum possible growth induced stretches (see e.g. Lubarda and Hoger [2002]). Such approaches may give computationally reasonable results, however, in the authors' opinion, cannot be easily motivated by physical arguments. Within this contribution we much rather assume that an internal force must evolve during the growth process that consequently counteracts the deformation process and ultimately yields it to stop. Since (engineered) biological tissue consists of high amounts of bound water, it is reasonable to assume that a growth-related change in volume is always accompanied by a change in internal pressure. Such pressure accumulations are consequently counteracting the expansion and contraction process, respectively. This growth-related internal pressure can be described by including an additional dependency on either $\mathbf{C}_g$ or $\mathbf{B}_g$. Using the idea of interpreting $\mathbf{F}_g$ as a so-called *material isomorphism* (see e.g. Noll [1958], Svendsen [2001]), it follows that one has to choose $\mathbf{B}_g$ in order to ensure that the kinematic quantities are located within the same configuration, i.e.

$$\psi := \tilde{\psi}\left(\mathbf{C}_e, \mathbf{B}_g\right).$$

Note that this choice is strongly related to the general concept of structural tensors. In the present case, namely by choosing the structural tensor equal to $\mathbf{B}_g$, the relation to linear kinematic hardening becomes obvious. This is worked out in the paper of Dettmer and Reese [2004], where linear kinematic hardening is a special case of the so-called Armstrong-Frederick type of kinematic hardening. In the following, we choose an additive format, i.e.

$$\tilde{\psi} := \psi_e(\mathbf{C}_e) + \psi_g(\mathbf{B}_g), \tag{2.6}$$

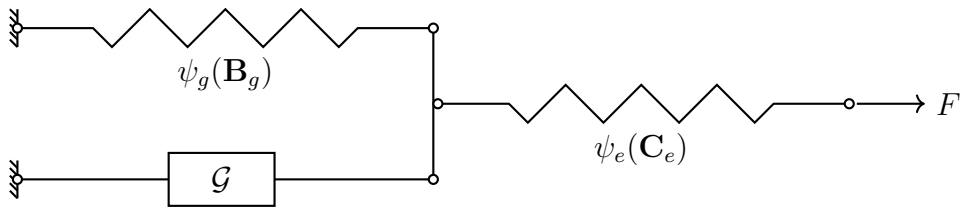

Figure 2.1: Rheological model corresponding to the given volumetric growth model. Growth is denoted by the element including the character $\mathcal{G}$.

for the Helmholtz free energy, which can be motivated easily by the rheological model shown in Figure 2.1. This model illustrates nicely that a growth-related expansion or contraction directly results in an accumulation of the growth-related energy ψ_g due to the loading of the associated spring element. Such an increase in growth-related energy clearly counteracts the growth deformation and ultimately leads to a decaying growth response. Please notice that the general idea of an energy contribution counteracting the growth process can also be found e.g. in Braeu et al. [2019]. In the above publication, however, this is achieved by a change in elastic energy, which is enforced by an additional term considering the change in volume directly. The elastically stored energy ψ_e is represented within this rheological model by the second spring element. It is obvious that this particular spring is influenced by both, growth-related and purely elastic deformations.

2.3.3 Thermodynamic considerations

To derive the constitutive equations representing finite volumetric growth, we next consider the isothermal Clausius-Duhem inequality as given in Equation (2.5). Inserting the Helmholtz free energy (Equation (2.6)) and differentiating with respect to time yields

$$\mathbf{S} : \frac{1}{2}\dot{\mathbf{C}} - \left(\frac{\partial \psi_e}{\partial \mathbf{C}_e} : \dot{\mathbf{C}}_e + \frac{\partial \psi_g}{\partial \mathbf{B}_g} : \dot{\mathbf{B}}_g \right) + \mathcal{S}_0 \geq 0. \tag{2.7}$$

By using the product rule as well as utilizing the identities $\dot{\overline{\mathbf{F}_g^{-T}}} = -\mathbf{F}_g^{-T}\dot{\overline{\mathbf{F}_g^{T}}}\mathbf{F}_g^{-T}$ and $\dot{\overline{\mathbf{F}_g^{-1}}} = -\mathbf{F}_g^{-1}\dot{\mathbf{F}}_g\mathbf{F}_g^{-1}$, the elastic deformation rate can be expressed as

$$\dot{\mathbf{C}}_e = \mathbf{F}_g^{-T}\dot{\mathbf{C}}\mathbf{F}_g^{-1} - \mathbf{L}_g^T\mathbf{C}_e - \mathbf{C}_e\mathbf{L}_g. \tag{2.8}$$

With the definition of the growth velocity gradient given in Equation (2.3), the growth-related deformation rate can similarly be found as

$$\dot{\mathbf{B}}_g = \mathbf{L}_g \mathbf{B}_g + \mathbf{B}_g \mathbf{L}_g^T. \tag{2.9}$$

As shown in detail in Appendix 2.7.1, the thermodynamically consistent definition of the second Piola-Kirchhoff stress tensor can be derived by combining the equations above and making use of the standard procedure of Coleman and Noll [1963], such that

$$\mathbf{S} = 2\mathbf{F}_g^{-1} \frac{\partial \psi}{\partial \mathbf{C}_e} \mathbf{F}_g^{-T}. \tag{2.10}$$

With this definition at hand, the reduced version of the Clausius-Duhem inequality is given as $\dot{\gamma}_{red} = \frac{\partial \psi_e}{\partial \mathbf{C}_e} : \left(\mathbf{L}_g^T \mathbf{C}_e + \mathbf{C}_e \mathbf{L}_g\right) - \frac{\partial \psi_g}{\partial \mathbf{B}_g} : \left(\mathbf{L}_g \mathbf{B}_g + \mathbf{B}_g \mathbf{L}_g^T\right) + \mathcal{S}_0 \geq 0$. If we furthermore let ψ_e and ψ_g only depend on the invariants of $\mathbf{C}_e$ and $\mathbf{B}_g$, their derivatives $\frac{\partial \psi_e}{\partial \mathbf{C}_e}$ and $\frac{\partial \psi_g}{\partial \mathbf{B}_g}$ are symmetric and commute with either $\mathbf{C}_e$ or $\mathbf{B}_g$. Combining this with the properties of the double contracting product, the reduced Clausius-Duhem inequality can be written only in terms of the symmetric part $\mathbf{D}_g = \operatorname{sym} \mathbf{L}_g$ of the growth velocity gradient, i.e.

$$\dot{\gamma}_{red} = [\mathbf{M} - \boldsymbol{\chi}] : \mathbf{D}_g + \mathcal{S}_0 \geq 0, \tag{2.11}$$

where the Mandel stress tensor is denoted by $\mathbf{M} = 2\mathbf{C}_e \frac{\partial \psi_e}{\partial \mathbf{C}_e}$ and the back-stress tensor is given as $\boldsymbol{\chi} = 2\mathbf{B}_g \frac{\partial \psi_g}{\partial \mathbf{B}_g}$. Similar to classical plasticity theory, see e.g. Vladimirov et al. [2008], one can identify the difference of the Mandel stress tensor $\mathbf{M}$ and the back-stress tensor $\boldsymbol{\chi}$ as the conjugated driving force for the evolution of growth. It is therefore natural to describe the evolution equation for $\mathbf{D}_g$ in terms of these quantities. Notice that $\mathbf{M}$ and $\boldsymbol{\chi}$ are located within a grown intermediate configuration, where they can be clearly identified as stress like quantities. This becomes clear by the fact that $\mathbf{M}$ has the same invariants as the Kirchhoff stress tensor $\boldsymbol{\tau}$ and, thus, has a clear physical meaning (see Appendix 2.7.2). Pulling $\mathbf{M}$ and $\boldsymbol{\chi}$ back to the reference configuration will yield a loss of such clear physical interpretation. Nevertheless, from a conceptual and computational point of view, a pull back of these quantities to the reference configuration is desirable (for details see e.g. Dettmer and Reese [2004] and Vladimirov et al. [2008]). Taking into account the relation $\mathbf{D}_g = \frac{1}{2}\mathbf{F}_g^{-T} \dot{\mathbf{C}}_g \mathbf{F}_g^{-1}$ one can rewrite the Clausius Duhem inequality purely in terms of quantities located within the reference

configuration, i.e.

$$\begin{aligned}\dot{\gamma}_{red} &= \left(\mathbf{F}_g^{-1}\mathbf{M}\mathbf{F}_g^{-T} - \mathbf{F}_g^{-1}\boldsymbol{\chi}\mathbf{F}_g^{-T}\right) : \frac{1}{2}\dot{\mathbf{C}}_g + \mathcal{S}_0 \\ &= (\boldsymbol{\Gamma} - \mathbf{X}) : \frac{1}{2}\dot{\mathbf{C}}_g + \mathcal{S}_0 \\ &= \boldsymbol{\Sigma} : \frac{1}{2}\dot{\mathbf{C}}_g + \mathcal{S}_0 \geq 0.\end{aligned} \tag{2.12}$$

Similar to the formulation given with respect to the grown intermediate configuration, it is reasonable to define the evolution of the growth-related right Cauchy-Green tensor $\mathbf{C}_g$ in terms of the thermodynamically conjugated driving forces $\boldsymbol{\Gamma} = \mathbf{C}_g^{-1}\mathbf{C}\mathbf{S}$ and $\mathbf{X} = 2\frac{\partial \psi_g}{\partial \mathbf{C}_g}$. It is important to mention that using $\mathbf{C}_g$ as the internal variable yields the fact that $\mathbf{F}_g$ must never be computed in the first place. Such an approach is in clear contrast to the standard formulations in volumetric growth modelling, where the growth tensor itself is usually explicitly prescribed.

2.3.4 Evolution of growth

Up to this point, the framework presented is very general and could be used to describe a wide variety of inelastic phenomena in finite deformations. It is therefore the choice of evolution equations for $\mathbf{C}_g$ that explicitly defines a particular kind of inelastic material model. For the most simple modelling assumption of a purely isotropic growth response, the inelastic part of the deformation gradient is usually defined as $\mathbf{F}_g = \vartheta\mathbf{I}$, where ϑ describes the growth induced stretch (see e.g. Lubarda and Hoger [2002], Himpel et al. [2005], Göktepe et al. [2010]). Using the thermodynamic framework described above, this assumption naturally leads to an evolution equation of $\mathbf{C}_g$, which can be written as

$$\dot{\mathbf{C}}_g := 2\frac{\dot{\vartheta}}{\vartheta}\mathbf{C}_g. \tag{2.13}$$

Within this context, a scalar valued evolution equation $\dot{\vartheta} = f(\vartheta, \mathbf{M}, \boldsymbol{\chi}, ...)$ is used to determine the overall growth response (see Appendix 2.7.3 for a more detailed example). Although the a priori assumption of $\mathbf{F}_g$ being a diagonal tensor is tempting due to its computational simplicity, it was already pointed out in various publications that such an assumption is not reasonable for many applications (see e.g. Soleimani et al. [2020], Braeu et al. [2019], Braeu et al. [2017]). This is especially the case for scenarios in which the body cannot grow freely but is restricted by complex boundary conditions. To overcome this issue, a new volumetric growth model is proposed in the following.

2.3.4.1 Finite growth using a growth potential

As described in the introduction, cell mediated expansion or compaction of engineered tissues takes place in such a way that a preferred homeostatic stress state is reached within the material. In the present work, it is assumed that this homeostatic state can be described in terms of a scalar equivalent stress. Thus, growth always takes place, if this equivalent stress is not equal to the preferred stress state of the biological material. These considerations lead us to the introduction of a general growth potential

$$\Phi := \tilde{\Phi}\left(\mathbf{M}, \boldsymbol{\chi}, \alpha_1, ..., \alpha_n\right), \tag{2.14}$$

which is a function of the conjugated driving forces as well as a set of material parameters α_i. Similar to the representation used in classical plasticity theory, this potential can be represented as a surface, located within the principal stress space, which contains all eligible homeostatic stress states. It will therefore be named *homeostatic surface* in the following. An example for such a homeostatic surface can be found in Figure 2.2. The overall goal of this process is to approach $\Phi = 0$ over time and therefore reach a stress state that lies on the homeostatic surface. Furthermore, it seems natural that such growth processes always try to minimize the amount of energy needed to reach the homeostatic state. Hence, the direction of growth response will be described by the derivative of the growth potential, i.e. $\mathbf{N} = \frac{\partial \Phi}{\partial \mathbf{M}}$. It is furthermore obvious that homeostasis is never reached instantaneously but rather approached over a certain period of time. To account for this temporal effect, we introduce the growth multiplier $\dot{\lambda}_g := \dot{\lambda}_g\left(\Phi, \eta, \beta_1, ..., \beta_n\right)$ defined as an explicit function of the growth potential, the growth velocity η and a set of material parameters β_i. Subsequently, the considerations above lead us to an associative growth evolution law that is postulated as

$$\mathbf{D}_g := \dot{\lambda}_g \frac{\mathbf{N}}{||\mathbf{N}||}. \tag{2.15}$$

In general, we do not want to restrict the choice of Φ to only positive homogeneous potentials of degree one. This has the side effect that $||\mathbf{N}|| = 1$ can not be guaranteed, which yields the need to normalize the growth direction tensor to assure that only $\dot{\lambda}_g$ has an influence on the amount of accumulated growth deformations. As before, we furthermore can define the given evolution equation in terms of quantities located purely within the reference configuration. To achieve this, a pull back operation is performed that yields

$$\dot{\mathbf{C}}_g = \frac{2\dot{\lambda}_g}{||\mathbf{N}||} \mathbf{F}_g^T \mathbf{N} \mathbf{F}_g = \dot{\lambda}_g \mathbf{f} = \dot{\lambda}_g \mathbf{g} \mathbf{C}_g, \tag{2.16}$$

including the general second order tensors $\mathbf{f} = \frac{2}{||\mathbf{N}||}\mathbf{F}_g^T\mathbf{N}\mathbf{F}_g$ as well as $\mathbf{g} = \mathbf{f}\mathbf{C}_g^{-1}$.

Remark. *The same result for Equation* (2.16) *could also be obtained following Reese et al. [2021] and the procedures proposed therein. Therefore, this evolution law could be interpreted in the broader context of a theory describing the evolution of general structural tensors.*

Since this approach is very similar to the classical models of visco-plasticity, the attentive reader may ask how far these approaches differ. In the case of plasticity, the yield criterion is used to clearly distinguish between the purely elastic and elasto-plastic state, i.e. the yield criterion must always be less than or equal to zero. In contrast, the growth potential Φ does not serve to distinguish between an elastic and inelastic region, since an 'elasto-growth' state is present for both $\Phi < 0$ and $\Phi > 0$. Only in case of $\Phi = 0$ no further growth has to take place, since homeostasis has already been reached. This behaviour is also reflected by the growth multiplier, which in contrast to plasticity can also have negative values. In the authors opinion this modelling approach has several advantages: (i) As stated earlier, the direction of growth does not have to be prescribed a priori, (ii) the complexity of the material model is reduced and (iii) due to the strong similarities to plasticity, one can rely on a large repertoire of knowledge from this field, both from a modeling and numerical point of view. For instance, one could argue that the preferred stress can not only be described by only one smooth growth potential. Having e.g. the concept of multisurface plasticity in mind, it would be easy to adopt the growth potential by a more sophisticated approach. In addition, it is also possible, for instance, to take into account a changing preferred stress using an approach similar to the concept of isotropic hardening.

Remark. *It is important to point out that while the model developed here is strongly inspired by the methods of classical plasticity theory, the micromechanical intepretations of these purely phenomenological approaches do not correspond to each other in any way. Furthermore, it is important to note that in reality, instead of a sharply defined homeostatic state, a fuzzy state or possibly even a multitude of such states might occur.*

Before defining a specific form of the growth potential, we first take a closer look at the structure of such a potential. It has already been pointed out above that it is reasonable to assume that growth in biological tissues tends to be of isotropic nature only in the absence of restricting boundary conditions. This idea leads us to the definition of the growth potential as a function of the volumetric invariant $I_1 := \operatorname{tr}(\mathbf{M} - \boldsymbol{\chi}) = \operatorname{tr}(\boldsymbol{\Sigma}\mathbf{C}_g)$. To allow also for an anisotropic growth response, we furthermore include the deviatoric invariant $J_2 := \frac{1}{2}\operatorname{tr}\left(\operatorname{dev}(\mathbf{M} - \boldsymbol{\chi})^2\right) = \frac{1}{2}\operatorname{tr}\left(\operatorname{dev}(\boldsymbol{\Sigma}\mathbf{C}_g)^2\right)$ (see Appendix 2.7.4), where we use the deviatoric

projection given as $\mathrm{dev}\,(\bullet) = (\bullet) - \frac{1}{3}\,\mathrm{tr}\,(\bullet)\,\mathbf{I}$. With theses considerations at hand, we propose a general form for the growth potential as

$$\Phi := \Phi\left(I_1, J_2, \omega_{hom}\right) = \phi_1\left(I_1\right) + \phi_2\left(J_2\right) - \omega_{hom}. \tag{2.17}$$

Here, the material parameter ω_{hom} describes a stress like quantity defining the state of homeostasis. It is important to emphasize that the combination of I_1 and J_2 is crucial for the proposed material model. If the potential was merely defined in terms of the volumetric invariant I_1, the growth direction tensor would become proportional to the identity tensor which consequently yields an evolution equation that is similar to the isotropic evolution law given in Equation (2.13). It is the dependency on J_2 that introduces an anisotropic growth behaviour, since the growth direction tensor no longer necessarily has to correspond to the identity. Nevertheless, in case of purely volumetric stress states, the dependency on I_1 ensures the desired isotropic growth response. This consideration yields an exclusion of any purely deviatoric potential, e.g. of von Mises type potentials. Furthermore, any suitable potential must fulfill $\frac{\partial \Phi}{\partial \mathbf{M}} \neq \mathbf{0}$ for all $(\mathbf{M} - \boldsymbol{\chi}) \in (\mathbb{R}^3 \times \mathbb{R}^3)$ in order to guarantee a well-defined growth direction for any arbitrary loading condition.

2.3.4.2 Choice of the growth potential and growth multiplier evolution

The form of a specific potential depends strongly upon the needs of the given application. Unfortunately, there is currently a lack of meaningful experimental data regarding the mechanics of volumetric growth. We therefore choose a potential that proofed to be able to predict our macroscopical observations and further satisfies the general requirements stated above. For this purpose, the quadratic potential as described e.g. by Stassi-D'Alia [1967] and Tschoegl [1971] is used in the following. This potential can be expressed in terms of $\omega_{hom} = m\sigma_g^2$ including the material parameters m and σ_g, i.e.

$$\Phi = 3J_2 - (1-m)\sigma_g I_1 - m\sigma_g^2. \tag{2.18}$$

As shown in Figure 2.2a, the homeostatic state defined by this particular growth potential forms a hyperbolic surface within the principal stress space. The tipping point of this parabola is located on the hydrostatic axis, where its precise location is determined by the parameter m (see Figures 2.2b and 2.2c). From Equation (2.18) it is obvious that both parameters must always be greater than zero. It is furthermore important to notice that the opening side of the parabolic potential lies within the compressive regime for $m < 1$ and in the tensional regime

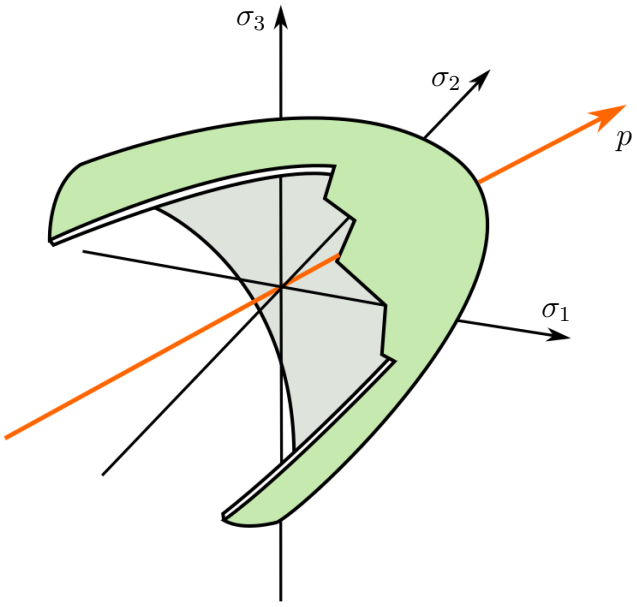

(a) Homeostatic surface located in principal stress space.

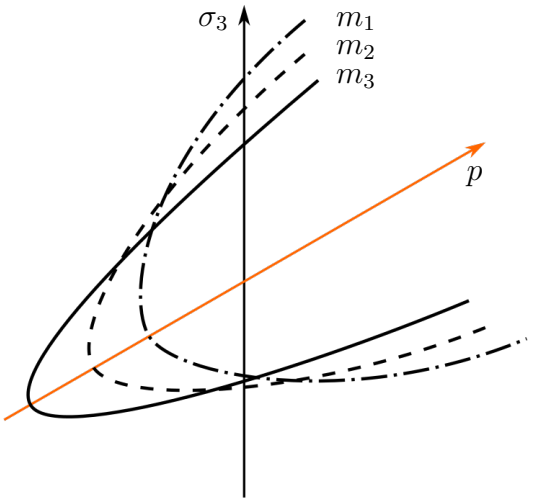

(b) Intersection of homeostatic surface with $\sigma_1 = \sigma_2$, showing the influence of the material parameter m for $m_i < 1$ with $m_1 < m_2 < m_3$.

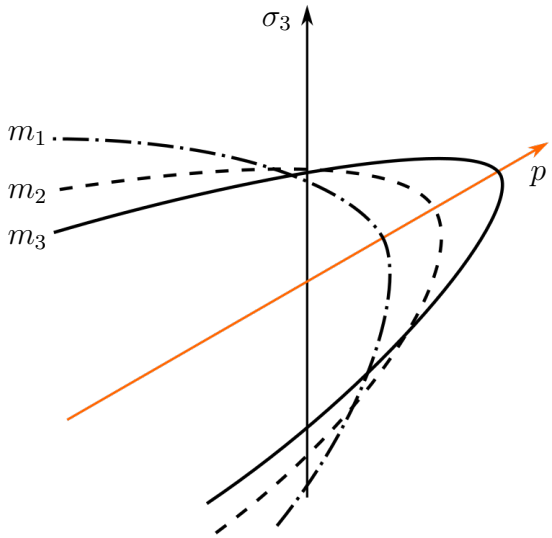

(c) Intersection of homeostatic surface with $\sigma_1 = \sigma_2$, showing the influence of the material parameter m for $m_i > 1$ with $m_1 < m_2 < m_3$.

Figure 2.2: Schematic representation of the homeostatic surface defined by Equation (2.18) displayed in principal stress space. The hydrostatic axis $p = \mathrm{tr}\,(\mathbf{M} - \boldsymbol{\chi})$ is shown in orange. The eigenvaules of $\mathbf{M} - \boldsymbol{\chi}$ are denoted by σ_i.

for $m > 1$, respectively. Since a choice of $m = 1$ describes a von-Mises type model such a choice of this parameters must be avoided. It is worth noticing from Figure 2.2 that this particular form of the growth potential leads to a different material response in the compressive and tensional regime, respectively. Using this form of the growth potential yields the growth direction tensor as

$$\mathbf{N} = 3\,\mathrm{dev}\,(\mathbf{M} - \boldsymbol{\chi}) - (1 - m)\,\sigma_g \mathbf{I}. \tag{2.19}$$

It is important to notice that this quantity can be reformulated with respect to quantities located within the reference configuration by using the identities from Appendix 2.7.4. In this case, Equation (2.16) can be written solely in terms of $\mathbf{C}_g$ since

$$\mathbf{F}_g^T \mathbf{N} \mathbf{F}_g = \mathbf{C}_g \left(3\,\mathrm{dev}\,(\boldsymbol{\Sigma}\mathbf{C}_g) - (1 - m)\,\sigma_g \mathbf{I}\right).$$

To complete the set of equations needed to describe the evolution of the growth-related right Cauchy-Green tensor, we furthermore define a particular form for the evolution of the growth multiplier $\dot{\lambda}_g$. From a physically motived point of view, it seems natural that the growth response increases with the deviation of the current stress state from homeostasis. We therefore assume the change in accumulated growth stretch is proportional to the current value of the growth potential. This furthermore ensures that the growth process stops as soon as homeostasis is reached. With these assumptions in mind, we choose the well established approach proposed in Perzyna [1966] and Perzyna [1971], i.e.

$$\dot{\lambda}_g := \frac{1}{\eta} \left(\frac{\Phi}{m \sigma_g^2} \right)^{\frac{1}{\nu}}. \tag{2.20}$$

Herein the growth multiplier is defined in terms of the growth relaxation time η as well as a non-linearity parameter ν.

2.3.4.3 Choice of Helmholtz free energy

Until this point, the constitutive framework presented herein has been described without defining a particular form of the Helmholtz free energy. In general, the choice of the energy potential depends upon the specific type of material one would want to model. For the time being, we choose a compressible Neo-Hookean type model to describe the elastic response of the material. Therefore, the elastic energy ψ_e is written in terms of the Lamé constants μ and Λ as

$$\psi_e = \frac{\mu}{2} \left(\mathrm{tr}\,\mathbf{C}_e - 3\right) - \mu \ln J_e + \frac{\Lambda}{4} \left(J_e^2 - 1 - 2 \ln J_e\right). \tag{2.21}$$

Following the argumentation in Section 2.3.2, we furthermore define the growth-related Helmholtz free energy ψ_g in terms of a stiffness like material parameter κ_g such that

$$\psi_g = \frac{\kappa_g}{2}\left(J_g^2 - 1 - 2\ln J_g\right). \tag{2.22}$$

This particular choice of the growth-related energy obviously fulfills the general requirements for the definition of a strain energy density, i.e. $\psi_g(J_g \to 0) \to \infty$ as well as $\psi_g(J_g = 1) = 0$ and $\psi_g(J_g \to \infty) \to \infty$. With these definitions at hand the second Piola-Kirchhoff stress tensor and the back-stress tensor can be derived as

$$\begin{aligned} \mathbf{S} &= \mu\left(\mathbf{C}_g^{-1} - \mathbf{C}^{-1}\right) + \frac{\Lambda}{2}\left(\left(\frac{J}{J_g}\right)^2 - 1\right)\mathbf{C}^{-1} \\ \mathbf{X} &= \kappa_g\left(J_g^2 - 1\right)\mathbf{C}_g^{-1} \end{aligned} \tag{2.23}$$

Notice that the conjugated driving force $\mathbf{\Gamma}$ can be easily computed, if $\mathbf{C}_g$ and $\mathbf{S}$ are known (see Section 2.3.3).

2.4 Numerical implementation

To incorporate the volumetric growth model at hand into a finite element simulation framework, a suitable time integration technique has to be used for evolution Equation (2.16). As shown for example by Weber and Anand [1990], Simo [1992], Reese and Govindjee [1998], Vladimirov et al. [2008] and discussed in further detail by Korelc and Stupkiewicz [2014], the exponential mapping algorithm is a very suitable choice for the treatment of the given evolution equation. We will therefore briefly describe this approach in the following.

Starting with the discrete time increments $\Delta t = t_{n+1} - t_n$, we introduce the growth increment $\Delta\lambda_{g_{n+1}} = \Delta t\dot{\lambda}_g$ as the discretized version of the growth multiplier. With this at hand, the exponential integration scheme for the evolution Equation (2.16) can be written in terms of the general second order tensors $\mathbf{g}$ and $\mathbf{f}$ as introduced in context of Equation (2.16), e.g.

$$\mathbf{C}_{g_{n+1}} = \exp\left(\Delta\lambda_g \mathbf{g}\right)\mathbf{C}_{g_n}. \tag{2.24}$$

Notice, that subscript $n+1$ will be dropped in the following for notational simplicity, which means that any discrete quantity without subscript will be associated with the current time step. Following the argumentation within Vladimirov et al. [2008] and Dettmer and Reese [2004] Equation (2.24) can be reformulated to ensure the symmetry of $\mathbf{C}_g$. Furthermore, the authors

mentioned above show that the exponential function within this equation can be expressed in terms of the growth-related right stretch tensor $\mathbf{U}_g = \sqrt{\mathbf{C}_g}$. Consequently, this leads to the discretized evolution equation given as

$$\mathbf{C}_{g_n}^{-1} = \mathbf{U}_g^{-1} \exp\left(\Delta\lambda_g \mathbf{U}_g^{-1} \mathbf{f} \mathbf{U}_g^{-1}\right) \mathbf{U}_g^{-1}. \tag{2.25}$$

In order to complete the set of discrete constitutive equations, the discrete growth multiplier $\Delta\lambda_g$ must determined. This can be achieved by reformulating Equation (2.20) (see e.g. Simo and Hughes [1998] and de Souza Neto et al. [2008]), i.e.

$$\Phi = m\sigma_g^2 \left(\Delta\lambda_g \eta\right)^\nu. \tag{2.26}$$

Since both of the discrete constitutive equations are non-linear in their arguments, a local iterative solution algorithm must be applied at integration point level to solve for both, the internal variable $\mathbf{U}_g^{-1}$ as well as the growth increment $\Delta\lambda_g$. It is convenient for such algorithms to write the evolution equations in terms of a set of coupled residual functions, which read in the case of this material model

$$\begin{aligned} \mathbf{r}_g &= -\mathbf{C}_{g_n}^{-1} + \mathbf{U}_g^{-1} \exp\left(\Delta\lambda_g \mathbf{U}_g^{-1} \mathbf{f} \mathbf{U}_g^{-1}\right) \mathbf{U}_g^{-1} = \mathbf{0} \\ r_\Phi &= \Phi - m\sigma_g^2 \left(\frac{\Delta\lambda_g}{\Delta t}\eta\right)^\nu = 0. \end{aligned} \tag{2.27}$$

Due to the symmetry of $\mathbf{U}_g$, the tensor valued residual function $\mathbf{r}_g$ can be transformed into Voigt notation, which is computationally more efficient than solving the full tensorial equation. When applying a Newton-Raphson procedure to solve Equations (2.27), the increments of the equations' arguments can be found by solving a linearized system of equations, i.e.

$$\begin{pmatrix} \frac{\partial \hat{\mathbf{r}}_g}{\partial \hat{\mathbf{U}}_g} & \frac{\partial \hat{\mathbf{r}}_g}{\partial \Delta\lambda_g} \\ \frac{\partial r_\Phi}{\partial \hat{\mathbf{U}}_g} & \frac{\partial r_\Phi}{\partial \Delta\lambda_g} \end{pmatrix} \Delta \begin{pmatrix} \hat{\mathbf{U}}_g \\ \Delta\lambda_g \end{pmatrix} = - \begin{pmatrix} \hat{\mathbf{r}}_{g_n} \\ r_{\Phi_n} \end{pmatrix}. \tag{2.28}$$

During the solution process, these increments are recomputed for every iteration step in which they are used to update the local iteration procedure. The partial derivatives used herein are not computed analytically but rather calculated by means of an algorithmic differentiation approach. For this, the software package *AceGen*, as described e.g. in Korelc [2002] and Korelc [2009], is being used to automatically generate source code for the computation of the tangent operators.

Since the local material response is implicitly included within the global material tangent

operator of a finite element simulation, we furthermore need to derive this tangent in a consistent manner. Otherwise, quadratic convergence of the global iteration scheme would not be reached. For this, one should bear in mind that the second Piola-Kirchhoff stress is a function of the right Cauchy-Green tensor as well as the internal variables. Within the given framework, the material tangent operator can be expressed as

$$\mathbb{C} = 2 \left(\left. \frac{\partial \mathbf{S}}{\partial \mathbf{C}} \right|_{\mathbf{U}_g} + \left. \frac{\partial \mathbf{S}}{\partial \mathbf{U}_g} \right|_{\mathbf{C}} : \frac{\partial \mathbf{U}_g}{\partial \mathbf{C}} \right). \tag{2.29}$$

Similar to the local tangent operator, these partial derivatives are computed using the software package *AceGen*. For this, the partial derivative of the growth-related stretch tensor $\mathbf{U}_g$ with respect to the right Cauchy Green tensor can be determined from the following relation

$$\Delta \begin{pmatrix} \hat{\mathbf{U}}_g \\ \Delta\lambda_g \end{pmatrix} = - \begin{pmatrix} \frac{\partial \hat{\mathbf{r}}_g}{\partial \hat{\mathbf{U}}_g} & \frac{\partial \hat{\mathbf{r}}_g}{\partial \Delta\lambda_g} \\ \frac{\partial r_\Phi}{\partial \hat{\mathbf{U}}_g} & \frac{\partial r_\Phi}{\partial \Delta\lambda_g} \end{pmatrix}^{-1} \begin{pmatrix} \frac{\partial \hat{\mathbf{r}}_g}{\partial \hat{\mathbf{C}}} \\ \frac{\partial r_\Phi}{\partial \hat{\mathbf{C}}} \end{pmatrix} \Delta\hat{\mathbf{C}}. \tag{2.30}$$

Here, we reuse the fully converged residual and Jacobian from the local solution process. Then, the desired partial derivative is given as the corresponding 6×6 submatrix located in the upper left corner of the right-hand side matrix product.

2.5 Numerical examples

In the following section, numerical examples are presented to examine and discuss various aspects of the material model introduced above. First, we show the influence of boundary conditions on the development of the volumetric growth process using a simple block model. For this purpose, volumetric growth in the absence of geometrically constraining boundary conditions is evaluated as well as the impact of both, temporal constant and time dependent constraining boundary conditions. Next, we investigate the influence of the introduced set of material parameters, before showing structural examples of a shrinking tissue stripe and comparing its growth-related response to an isotropic growth formulation. Finally, we show a qualitative comparison of our model with experimental data from the literature. For the finite element simulations, we implemented the presented material model as well as the element formulation itself into the *FEAP* software package (Taylor and Govindjee [2020]) in terms of a *user-element* routine. For meshing and visualization of the structural examples we have used the open source software tools *GMSH* (Geuzaine and Remacle [2009]) and *Paraview* (Ahrens et al. [2005]). Furthermore, the open source parallelisation tool *GNU Parallel* (Tange [2011])

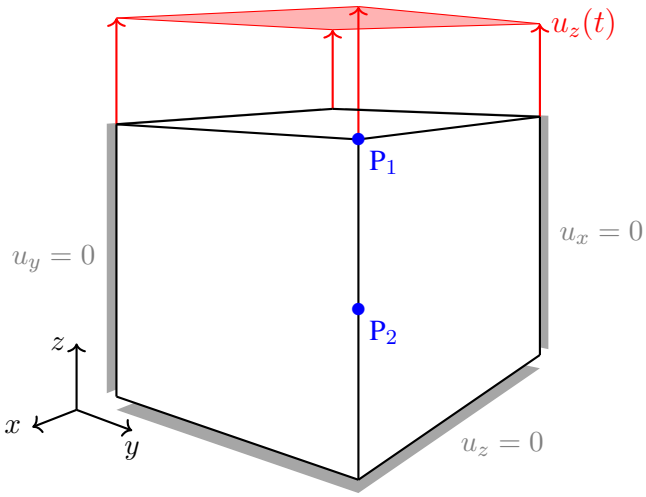

Figure 2.3: Geometrical block model with uniform side length of 1 mm. Uniaxial boundary conditions are given in gray and time dependent displacement $u_z(t)$ is denoted in red. Evaluation points $P_1 = (1, 1, 1)$ and $P_2 = (1, 1, 0.5)$ are given in blue.

	μ $\left[\frac{\text{N}}{\text{mm}^2}\right]$	Λ $\left[\frac{\text{N}}{\text{mm}^2}\right]$	κ_g $\left[\frac{\text{N}}{\text{mm}^2}\right]$	m $[-]$	σ_g $\left[\frac{\text{N}}{\text{mm}^2}\right]$	η [s]	ν $[-]$
Geom. unconstrained growth	40	400	150	1.2	70	20	1.0
Geom. constrained growth	40	400	250	1.2	200	100	1.0
Clamped tissue stripe	100	800	150	2.0	250	100	1.0

Table 2.1: Material parameters for numerical examples

was used during evaluations of the examples shown below.

2.5.1 Geometrically unconstrained growth

As a first example, we use the geometrical model shown in Figure 2.3 without applying any time dependent displacement boundary condition $u_z(t)$. Therefore, the specimen is able to expand or contract freely throughout the whole simulation, which should result in an isotropic growth response. We furthermore use the set of material parameters given in Table 2.1. The growth response for a choice of $m = 1.2$ is visualized in Figure 2.4. Shown by the stretches of point P_1 located in the upper corner of the given block geometry, it is obvious that the specimen contracts as expected. Since no constraining boundary conditions are applied, the overall stress within this system should always be equal to zero and therefore could never reach a state of tensional homeostasis. It is the additional growth-related free energy, which leads to the limitation of the otherwise infinite shrinking process. One can observe this influence really well in Figure 2.5a, where lower values of κ_g lead to a more pronounced shrinking of the

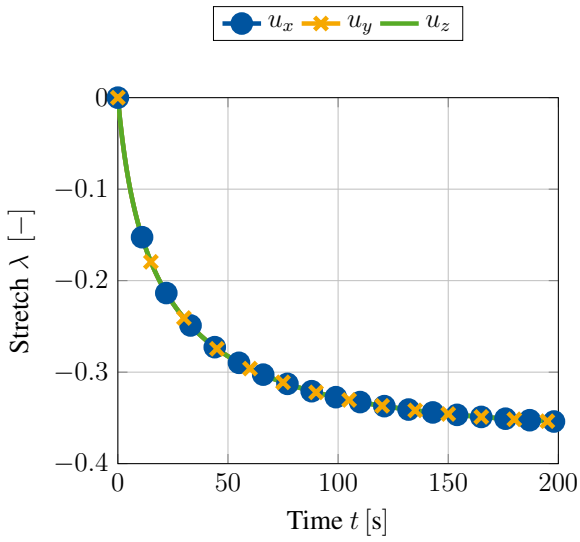

Figure 2.4: Isotropic growth behaviour resulting in a uniform contraction in all three spatial dimensions. No constraining boundary conditions are applied (i.e. no $u_z(t)$). Stretches are evaluated at point P_1 (see Figure 2.3).

specimen. It is worth noticing that $\kappa_g > 0$ must hold for any simulation, since neglecting the contribution of internal pressures would lead to non physical behaviour and consequently to an unstable simulation. It is furthermore shown in Figure 2.5d that the growth rate parameter η has only an impact on the speed at which the volumetric growth process approaches the desired homeostatic state but not on its magnitude. However, as shown in Figures 2.5b and 2.5c a change in magnitude of the homeostatic state can be achieved by variation of m and σ_g. As already described in Section 2.3.4.2, the material parameter m defines the location of the growth potential's tipping point on the hydrostatic axis. For values of $m < 1$ this point lies in the compressive regime, whilst a choice of $m > 1$ pushes this point into the tension regime. As a result, the specimen approaches homeostasis either by expansion or by shrinkage. This behaviour is really well reflected within Figure 2.5b. It is furthermore important to point out that for a choice of $m = 1$ the homeostatic potential introduced in Equation (2.18) becomes a *von Mises* type criterion, which must not be applied due to its purely deviatoric nature. Therefore, this particular choice of m should be avoided when using the potential introduced above.

2.5.2 Geometrically constrained growth

For the next example, we choose a stepwise time dependent displacement $u_z(t)$ to which the block given in Figure 2.3 is subjected. For the first 250 time steps, the displacement is

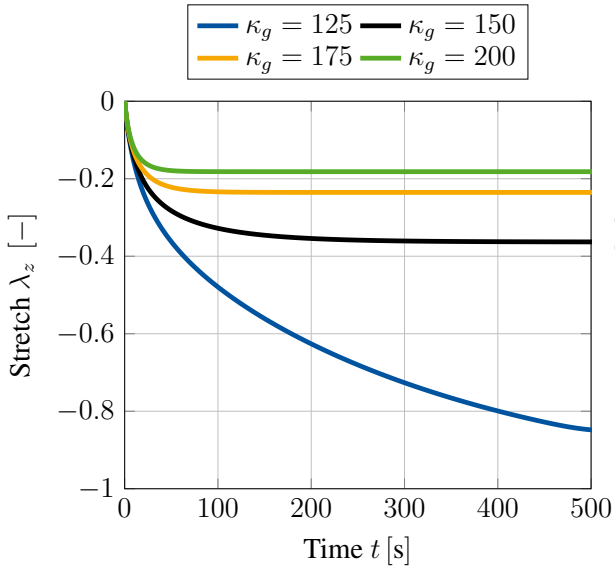

(a) Various choices of the material parameter κ_g.

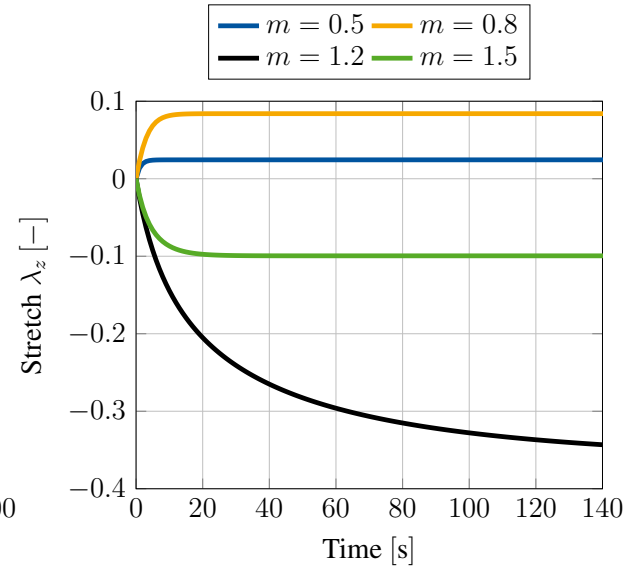

(b) Various choices of the material parameter m.

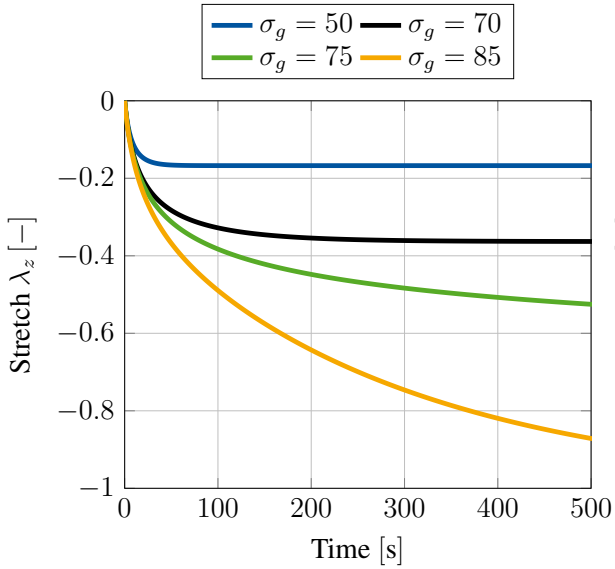

(c) Various choices of the material parameter σ_g.

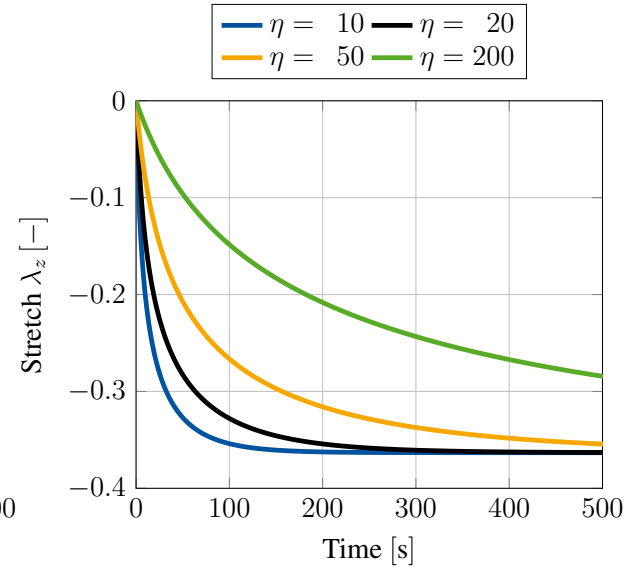

(d) Various choices of the material parameter η.

Figure 2.5: Growth induced stretch due to contraction of a block specimen for various sets of material parameters. No constraining boundary conditions are applied (i.e. no $u_z(t)$). Stretches are evaluated at point P_1 (see Figure 2.3).

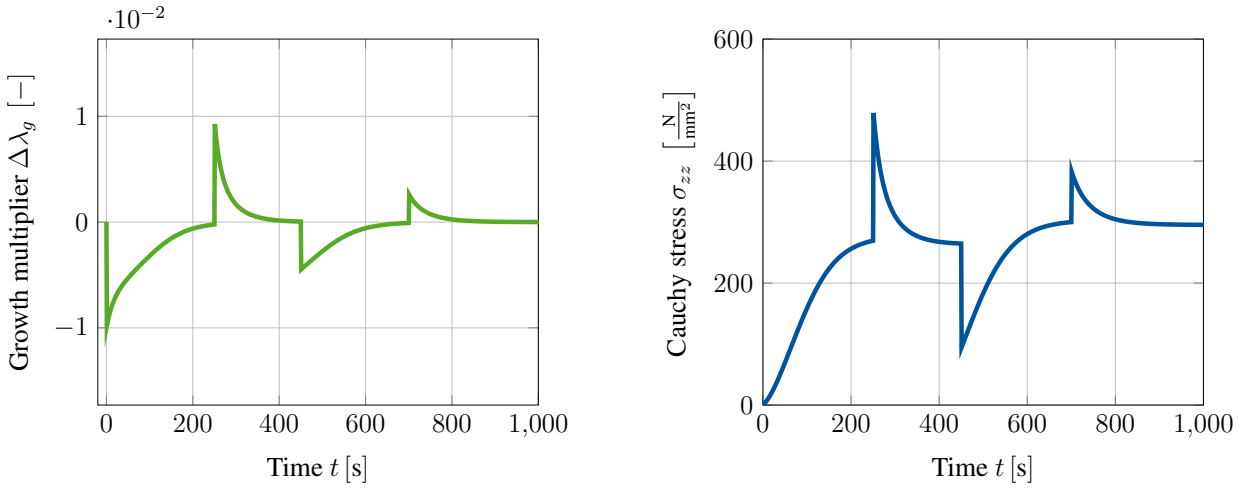

(a) Growth multiplier

(b) Cauchy stress in loading direction

Figure 2.6: Evolution of Cauchy stress σ_{zz} and growth multiplier $\Delta\lambda_g$ during stepwise loading of block specimen with $u_z(t)$. Both quantities are evaluated at point P_1(Figure 2.3). *Right*: The stress response is always converging towards a homeostatic state. This state is slightly different, after coming out of the compressive regime. This can be explained by the accumulted internal pressures described by the energy ψ_g. *Left*: Growth multiplier indicating, that the specimen is either expanding or shrinking to reach homeostasis.

held constant at $u_z(t) = 0$ mm before being raised to $u_z(t) = 0.3$ mm and held constant for another 200 time steps. Next, we apply compression by setting $u_z(t) = -0.1$ mm and holding it constant for another 250 time steps. At last, $u_z(t)$ is reset to zero again. The material parameters for this example are given in Table 2.1.

When applying this stepwise alternating stretch to the given block specimen, it can be seen in Figure 2.6 that the material shrinks and expands depending on the current loading state, respectively. During the first loading period, the accumulated Cauchy stress σ_{zz} rises to a value of approximately 300 MPa, which is due to a contraction induced by the volumetric growth process. This effect is represented by the evolution of the growth multiplier as shown in Figure 2.6a. Since the multiplier is negative, the specimen approaches homeostasis by shrinking. Once the displacement is raised to $u_z(t) = 0.3$ mm, the Cauchy stress σ_{zz} also rises abruptly before decaying and approaching the same homeostatic stress state as before. This kind of stress reduction is achieved by an expansion of the specimen, which is represented by a positive value of the growth multiplier. The following compression of the specimen causes a negative jump in the overall stress response. This again induces shrinkage of the specimen in order to regain the homeostatic state of approximately 300 MPa. It is important to notice that this homeostatic state is slightly higher than the state reached in the loading cycles before.

This change is due to the accumulated internal pressures described by the growth-related energy ψ_g. Consequently, this results in a shift of the homeostatic surface similar to kinematic hardening in plasticity. To what extent this effect corresponds to experimental studies is still unclear due to the lack of available data. However, there is no question that this effect can be adapted to any experimental data without further problems by extending the model, e.g. by a non-linear formulation. When setting $u_z(t) = 0$ mm in the last loading cycle, the Cauchy stresses overshoot this new homeostatic state slightly. This again results in an expansion of the specimen in order to release the excessive stresses.

2.5.3 Growth of a clamped tissue stripe

In the next example we consider the volumetric growth process within a tissue stripe that is clamped at both ends such that no stresses are induced at time $t = 0$. Under these conditions, the tissue stripe is expected to shrink, which induces a homeostatic stress state that is dominated by tension. Such effects have been shown experimentally e.g. by Ghazanfari et al. [2015] among others. As illustrated in Figure 2.7, symmetric properties are exploited such that only a quarter of the full specimen is used for the following simulations. The elastic and growth-related material parameters applied in this example are chosen in such a way that the desired shrinkage of the specimen is achieved. These parameters are given in Table 2.1. For the spatial discretisation, a standard linear (Q1) finite element formulation is adopted with various meshes containing 360, 408, 450, 1000 and 3000 elements (see Figure 2.8). Since the most pronounced stresses are expected to occur in the lower right corner of the symmetric specimen, the mesh is refined with a focus on this particular region. When considering the reaction force F_x evaluated over time at $z = 0$, Figure 2.9 shows good convergence behaviour for increasing number of elements within the mesh. Similar results can be obtained when evaluating the reaction forces in y and z direction, respectively. Although the solution of a mesh containing 450 elements has already reached convergence, for visualization purposes, the finest discretisation containing 3000 elements is used in the following.

To show the capabilities of the newly introduced material model, we next compare its response to the growth behaviour of a well established model for isotropic volumetric growth. For this, we adapted the model of Lubarda and Hoger [2002] such that it is capable of reaching a prescribed homeostatic state. Details about the evolution equations for this particular model are given in Appendix 2.7.3. Within this formulation, we use the material parameter $M_{crit} = 80$ MPa to describe the homeostatic stress state that shall ultimately be reached. For the positive and negative growth velocities $k^+ = 0.1$ and $k^- = 0.1$ are chosen, respectively. The upper and lower growth boundaries are set to $\vartheta^+ = 2.0$ and $\vartheta^- = 0.25$, while the shape

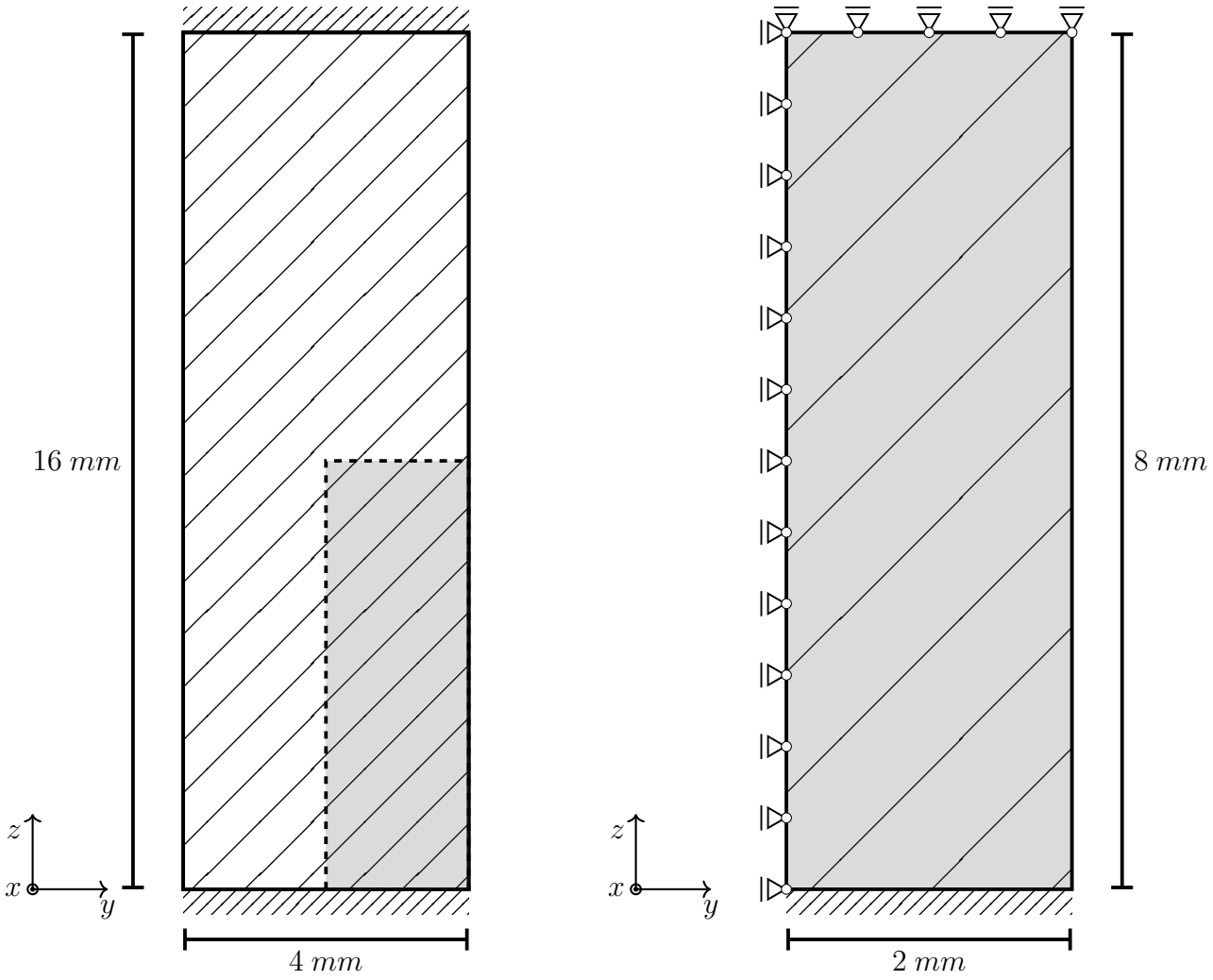

(a) Full structure

(b) Symmetric part

Figure 2.7: Geometric model of clamped tissue stripe with thickness of $t = 2$ mm. The overall structure is also supported in the x direction.

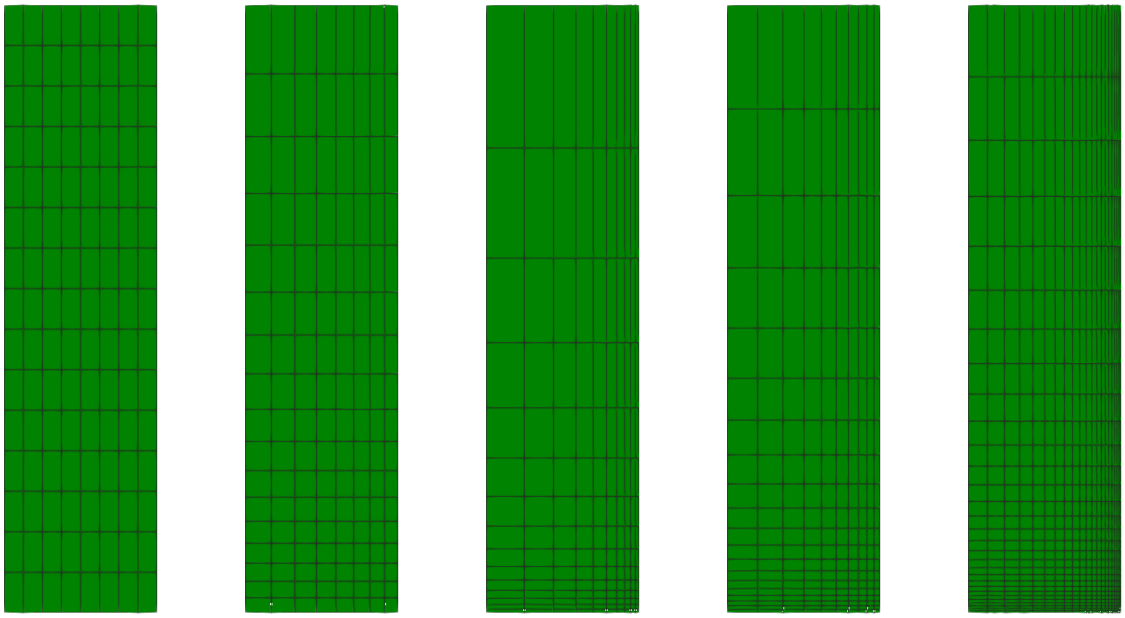

(a) 360 el. (b) 408 el. (c) 450 el. (d) 1000 el. (e) 3000 el.

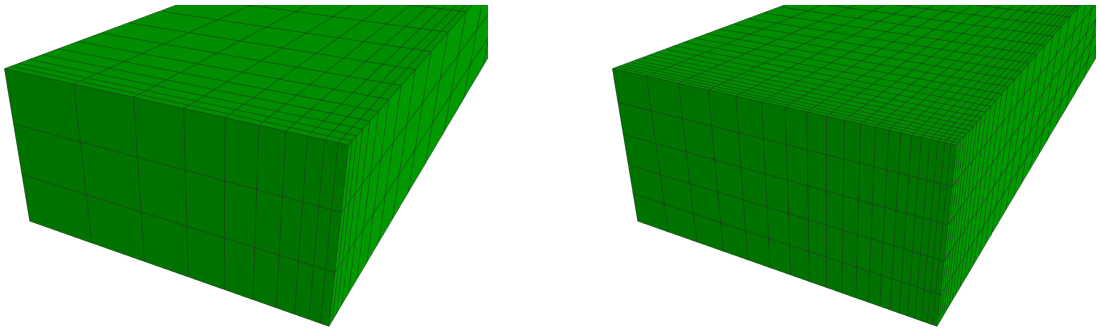

(f) Close up of right corner for 450 el. (g) Close up of right corner for 3000 el.

Figure 2.8: Mesh refinements for symmetric part of clamped tissue stripe.

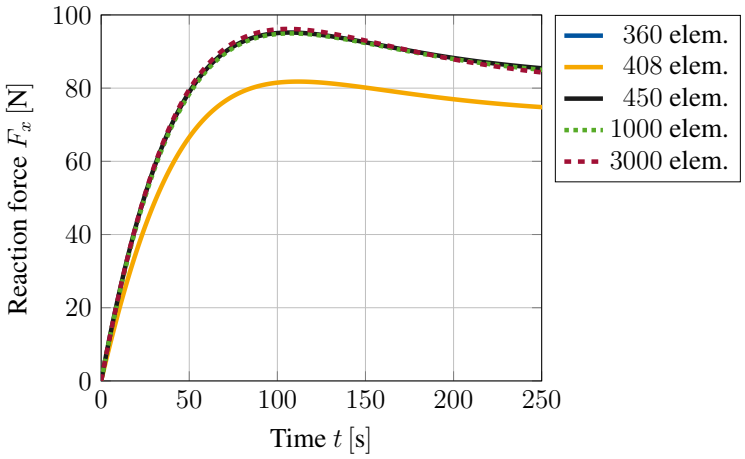

Figure 2.9: Reaction force of a clamped tissue stripe evaluated at $z = 0$ for various mesh sizes. Mesh convergence can be observed nicely.

factors are given as $\gamma^+ = 2$ and $\gamma^- = 3$. First of all it is important to notice that the given isotropic formulation shows severe stability problems for the example at hand. More precisely, as soon as material parameters are chosen such that a similar homeostatic stress state shall be reached within the specimen, the simulation becomes unstable after a finite number of time steps and eventually breaks. When taking a closer look at the evolution of the growth process as it is shown for three distinct time steps in Figure 2.10, it is obvious that the starting point of the instability can be located at the clamping of the tissue stripe. Due to the initial contraction of the overall tissue stripe, a multi-axial stress state is induced at the clamping. In this region, the stress state soon exceeds the desired homeostatic state which yields an expansion of the material in order to release excessive stresses. Whilst the newly derived growth model reduces this stress state by expanding anisotropically, the isotropic formulation seems not to be able to deal with this effect. This is due to the fact that an isotropic growth formulation can only predict expansion or shrinkage uniformly in all three spatial dimensions. Such a uniform expansion at the foot of the specimen results in a passive compression of the specimen's middle part, reducing the overall stress within this region and therefore inducing further contraction. This again triggers an increasing expansion in the foot of the specimen. A vicious cycle is born, which eventually leads to the hourglass like shape of the specimen as it is shown in Figure 2.10a. Ultimately, this leads to instabilities and a failing simulation at $t = 93$. For sure, it is possible to reduce such unwanted behaviour by variation of the material parameters. Nevertheless, the general problem of a non-physical expansion in the foot area could not be cured with such an approach. This example shows clearly how restrictive and, therefore, unsuitable the assumption of isotropic growth is, even for a relatively simple structure as the one shown in

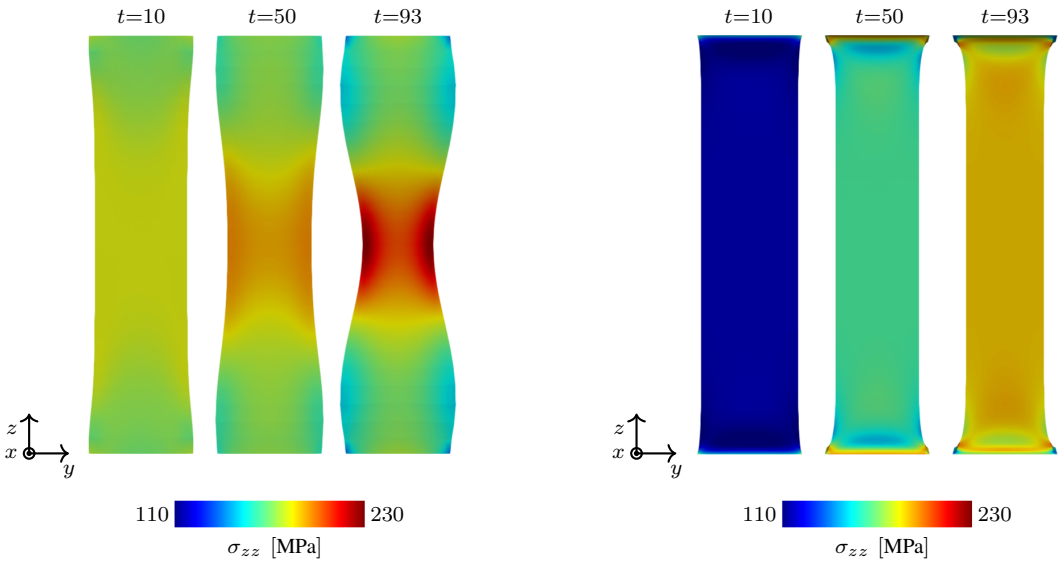

(a) Isotropic growth model using a modified version of Lubarda and Hoger [2002]

(b) New volumetric growth model using the general growth potential

Figure 2.10: Comparison of an isotropic growth model with the newly introduced formulation. The response of a clamped tissue stripe differs significantly in both, shape as well as the displayed stress response (Cauchy stresses σ_{zz}).

this example. Taking a closer look at the stress response of the newly derived model, one can observe the exceeding maximum principal Cauchy stresses σ_{max} located at the clamped foot of the specimen (see Figure 2.11) being released due to the anisotropic expansion process. This effect can also be observed in Figure 2.9, where the reaction forces reach a maximum at time $t = 100$ and decrease afterwards to approach a converged state. Unfortunately, this effect also leads to a pronounced distortion of the associated elements within the corners of the clamped stripe. Figure 2.11 shows that this artefact is even noticable for the finest mesh evaluated. Nevertheless, it is important to emphasize that this effect so far does not have an influence on the stability of the given simulation. Due to the incompressible nature of the material, it is possible that such behaviour is also amplified by shear or volumetric locking effects and would not occur in such a pronounced manner if locking would not play a role. However, the influence of possible locking effects is out of scope for this work.

2.5.4 Comparison with experimental data

Next, we are comparing our newly derived model to experimental data for the growth response of a clamped engineered tissue stripe. As an experimental reference, we are using the data published just recently in Eichinger et al. [2020], which was kindly provided to us by the

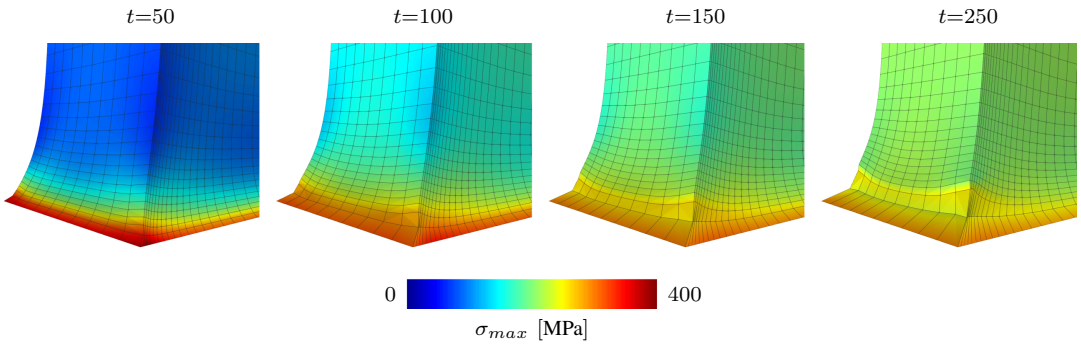

Figure 2.11: Pronounced distortion of elements at the clamped corner due to growth-related reduction of exceeding stresses. Maximum principal Cauchy stresses are plotted for four different snapshots in time.

authors. In this study, the authors used a cell seeded collagen gel to create the test specimens. For the experiment those specimens are clamped tension-free at the ends and are cultivated for 27 hours within a nutrient solution. After 17 hours, a positive or negative perturbation of the measured reaction force in longitudinal direction is applied. The displacement achieved by this perturbation is kept constant in the following course of the experiment. For our simulations we used a geometric representation of the clamped tissue stripe that is similar to the example shown in Figure 2.8 but has a width, hight and thickness of 10 mm, 60 mm and 2 mm. We again used only the symmetric part of the specimen in order to reduce computational effort. Since the microstructure of the collagen gel is somehow similar to polymeric materials, we decided to exchange the elastic strain energy density ψ_e in order to better capture the stress stiffening behaviour that can be observed within the experimental data. Here we used the well-known formulation of Arruda and Boyce [1993] (see Appendix 2.7.5 for details on the form of the energy).

Figure 2.12 shows a comparison of the measured normalized reaction force in longitudinal direction versus the results gained from our simulation. A perturbation of $\pm 10\%$ of the homeostatic reaction force at time $t = 17$h is shown in Figures 2.12a and 2.12b, respectively. Here it is clearly visible that the simulation is close to the experimental results both before and after perturbation and is mostly within the error tolerance. In particular, it can be observed in 2.12a that both the experiment and the simulation strive towards a new, somewhat higher homeostatic state after the perturbation. In contrast, the homeostatic state in Figure 2.12b settles back in approximately the same range as before, which also fits the behaviour observed in the experiment. Figures 2.12c and 2.12d show the results for a perturbation of $\pm 20\%$. Here, with the material data we use, the results of the experiment are also very well matched up to the point of perturbation. Only after that the simulation results do deviate quantitatively from

the measured data. Here it is particularly noticeable that a higher gradient is achieved in the result curve of the experiment directly after the perturbation. This leads to a faster convergence towards the new homeostatic state. This deviation could possibly be related to the fact that we assume a constant growth rate parameter η in our model. However, it cannot be ruled out that this parameter itself should be dependent on other constitutive variables such as e.g. the driving force $(\mathbf{M} - \boldsymbol{\chi})$. Overall, however, it can be stated that the simulation results represent the experimental data very well in a qualitative sense.

2.6 Conclusion and outlook

In this paper, we developed a novel model for the description of stress driven volumetric growth. This approach is based on the well established multiplicative split of the deformation gradient into an elastic and a growth related part. Furthermore, we made the assumption that the given material adapts to its surroundings such that a certain homeostatic stress state is induced within the material. For this homeostatic state, we assume that it can be described in terms of a scalar valued stress like quantity, which led us to the definition of a growth potential. With this idea in hand, we defined an evolution law for the growth related right Cauchy-Green tensor by means of a time dependent associative rule. This approach is similar but not identical to those often used in the field of finite visco-plasticity. To overcome the issue of infinite growth response, we made use of a similar idea as Braeu et al. [2019] and introduced an additional energy contribution that subsequently counteracts the growth process. In contrast to the latter approach, we use the inelastic part of the volume change, which leads us to a formulation similar to that of kinematic hardening. With these basic modelling assumptions, we were able to show that this approach is capable of simulating both, isotropic and anisotropic growth behaviour within one singular formulation. The distinction between isotropic and anisotropic response is merely a question of the applied boundary conditions and not a-priori prescribed by the structure of the growth tensor. The advantages of this approach have been shown by comparing it to a standard formulation of isotropic growth. In the authors' opinion, the results of the evaluations shown within this publication are very promising. We furthermore were able to show that our simulations are able to reproduce experimental results published in Eichinger et al. [2020] to a reasonable extend. Since the overall framework of the model is quiet general, it seems possible to easily adapt the growth behaviour to fit various experiments. For this, the choice of alternative descriptions for the growth potential as well as the evolution equation for the growth multiplier could be investigated. To this point, our formulation makes use of a purely isotropic elastic ground model, i.e. Neo-Hooke. Since biological tissue by

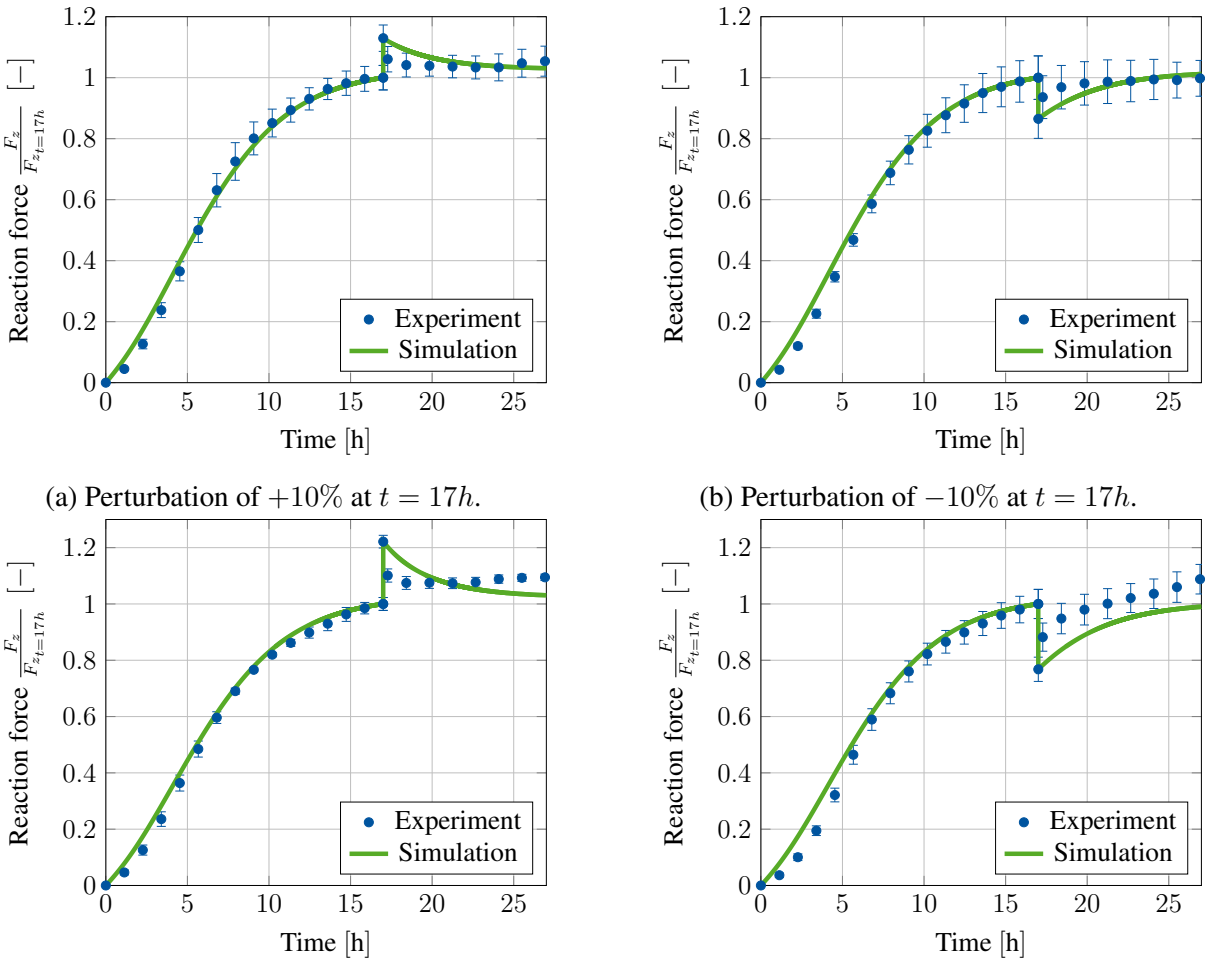

(a) Perturbation of $+10\%$ at $t = 17h$.

(b) Perturbation of -10% at $t = 17h$.

(c) Perturbation of $+20\%$ at $t = 17h$.

(d) Perturbation of -20% at $t = 17h$.

Figure 2.12: Comparison of simulation results with experimental data of an initially tension-free clamped tissue stripe that is perturbated at time $t = 17$h with $\pm 10\%$ and $\pm 20\%$ of the homeostatic reaction force measured at this point. Experimental data is plotted as the mean value of all experiments with error bars denoting the SEM (taken with permission from Eichinger et al. [2020]).

its very own nature is composed of various components, such as e.g. collagen and elastin, the assumption of material isotropy is not ideal. Therefore, we suggest that the given elastic ground model could be extended to also capture the anisotropic nature of the underlying material response properly. This could be achieved by introducing an additional dependency within the Helmholtz free energy that is defined by means of structural tensors describing e.g. the direction of collagen fibres. Furthermore, the investigation of locking effects triggered by the nearly incompressible material behaviour of biological tissues might also be of interest. Since standard low order finite element formulations are particularly vulnerable in this area, the finite element implementation should therefore be considered more closely. Investigating the influence of reduced integration finite elements seems to be of high benefit. Especially the element formulations Q1SP (see Reese [2005]) or Q1STx (see Schwarze and Reese [2011], Barfusz et al. [2021]) could improve the computation in terms of computational accuracy as well as computational speed.

2.7 Appendix

2.7.1 Derivation of stresses

To determine the second Piola-Kirchhoff stress tensor, we start with the isothermal Clausius-Duhem inequality as given in Equation (2.7), i.e.

$$\mathbf{S} : \frac{1}{2}\dot{\mathbf{C}} - \left(\frac{\partial \psi_e}{\partial \mathbf{C}_e} : \dot{\mathbf{C}}_e + \frac{\partial \psi_g}{\partial \mathbf{B}_g} : \dot{\mathbf{B}}_g \right) + \mathcal{S}_0 \geq 0.$$

When inserting the identities given in Equations (2.8) and (2.9) into the equation above, one can find

$$\mathbf{S} : \frac{1}{2}\dot{\mathbf{C}} - \frac{\partial \psi_e}{\partial \mathbf{C}_e} : \mathbf{F}_g^{-T}\dot{\mathbf{C}}\mathbf{F}_g^{-1} + \frac{\partial \psi_e}{\partial \mathbf{C}_e} : \left(\mathbf{L}_g^T \mathbf{C}_e + \mathbf{C}_e \mathbf{L}_g \right) - \frac{\partial \psi_g}{\partial \mathbf{B}_g} : \left(\mathbf{L}_g \mathbf{B}_g + \mathbf{B}_g \mathbf{L}_g^T \right) + \mathcal{S}_0 \geq 0$$

By reformulating the second term in this equation such that

$$\frac{\partial \psi_e}{\partial \mathbf{C}_e} : \mathbf{F}_g^{-T}\dot{\mathbf{C}}\mathbf{F}_g^{-1} = 2\mathbf{F}_g^{-1}\frac{\partial \psi_e}{\partial \mathbf{C}_e}\mathbf{F}_g^{-T} : \frac{1}{2}\dot{\mathbf{C}}$$

the Clausius-Duhem inequality becomes

$$\left(\mathbf{S} - 2\mathbf{F}_g^{-1}\frac{\partial \psi_e}{\partial \mathbf{C}_e}\mathbf{F}_g^{-T} \right) : \frac{1}{2}\dot{\mathbf{C}} + \frac{\partial \psi_e}{\partial \mathbf{C}_e} : \left(\mathbf{L}_g^T \mathbf{C}_e + \mathbf{C}_e \mathbf{L}_g \right) - \frac{\partial \psi_g}{\partial \mathbf{B}_g} : \left(\mathbf{L}_g \mathbf{B}_g + \mathbf{B}_g \mathbf{L}_g^T \right) + \mathcal{S}_0 \geq 0.$$

Following the standard argumentation of Coleman and Noll [1963] and assuming that the stress response shall be independent of the rate of $\mathbf{C}$, we find the second Piola-Kirchhoff stress tensor to be defined as

$$\mathbf{S} = 2\mathbf{F}_g^{-1}\frac{\partial \psi_e}{\partial \mathbf{C}_e}\mathbf{F}_g^{-T}.$$

2.7.2 Invariants of Mandel stress tensor and Kirchhoff stress tensor

The Kirchhoff stress tensor is defined as

$$\boldsymbol{\tau} = \mathbf{F}\mathbf{S}\mathbf{F}^T.$$

Making use of the identity $\mathbf{C}_e\mathbf{F}_g = \mathbf{F}_g^{-T}\mathbf{C}$ and using a push forward operation on the second Piola-Kirchhoff stress tensor $\mathbf{S}$, the definition of the Mandel stress tensor can be rewritten as

$$\begin{aligned}\mathbf{M} &= \mathbf{C}_e\mathbf{F}_g\mathbf{S}\mathbf{F}_g^T \\ &= \mathbf{F}_g^{-T}\mathbf{C}\mathbf{S}\mathbf{F}_g^T.\end{aligned}$$

With this at hand, it is easy to show that the main invariants J_α with $\alpha \in 1, 2, 3$ are identical for both, the Mandel and the Kirchhoff stress tensor, i.e.

$$\begin{aligned}J_\alpha &= \mathrm{tr}\left(\mathbf{M}^\alpha\right) \\ &= \mathrm{tr}\left(\left(\mathbf{F}_g^{-T}\mathbf{C}\mathbf{S}\mathbf{F}_g^T\right)^\alpha\right) \\ &= \mathrm{tr}\left((\mathbf{C}\mathbf{S})^\alpha\right) \\ &= \mathrm{tr}\left(\left(\mathbf{F}\mathbf{S}\mathbf{F}^T\right)^\alpha\right) \\ &= \mathrm{tr}\left(\boldsymbol{\tau}^\alpha\right).\end{aligned}$$

2.7.3 Isotropic growth model for comparison

The isotropic growth model used for comparison with the anisotropic growth model developed herein is based on the formulation of Lubarda and Hoger [2002]. It uses the multiplicative split of the deformation gradient, i.e.

$$\mathbf{F} = \mathbf{F}_e\mathbf{F}_g,$$

where the growth related deformation gradient is defined as

$$\mathbf{F}_g = \vartheta \mathbf{I},$$

with ϑ describing the growth induced stretch. The evolution equation of this particular model is defined in terms of the Mandel stress tensor $\mathbf{M}$ as well as a set of material parameters, i.e.

$$\dot{\vartheta} := k(\vartheta)\phi(\mathbf{M}).$$

Here the driving force ϕ is defined as

$$\phi := \operatorname{tr} \mathbf{M} - M_{crit},$$

where M_{crit} describes the desired homeostatic stress state that should be reached by the material. Furthermore, the growth velocity is described by

$$k(\vartheta) := \begin{cases} k^+ \left(\frac{\vartheta^+ - \vartheta}{\vartheta^+ - 1} \right)^{\gamma^+} & \text{if } \phi > 0 \\ k^- \left(\frac{\vartheta - \vartheta^-}{1 - \vartheta^-} \right)^{\gamma^-} & \text{if } \phi < 0, \end{cases}$$

with k^+, k^- denote the expansion and contraction speed, respectively. To restrict the growth process, the parameters ϑ^+ and ϑ^- are introduced as upper and lower thresholds of the growth induced stretch. Finally, two shape factors for the evolution are described by γ^+ and γ^-. For further information on this particular model, the reader is kindly referred to the original publication.

2.7.4 Transformation of invariants from intermediate to reference configuration

Reformulating the definition of the referential driving force, i.e.

$$\mathbf{M} - \boldsymbol{\chi} = \mathbf{F}_g \boldsymbol{\Sigma} \mathbf{F}_g^T,$$

directly yields the new definition for the volumetric invariant, i.e.

$$\begin{aligned} I_1 &= \operatorname{tr}\left(\mathbf{M} - \boldsymbol{\chi}\right) \\ &= \operatorname{tr}\left(\mathbf{F}_g \boldsymbol{\Sigma} \mathbf{F}_g^T\right) \\ &= \operatorname{tr}\left(\boldsymbol{\Sigma} \mathbf{C}_g\right). \end{aligned}$$

Making use of this relation, the deviatoric part of the driving force is given by

$$\begin{aligned} \operatorname{dev}\left(\mathbf{M} - \boldsymbol{\chi}\right) &= \operatorname{dev}\left(\mathbf{F}_g \boldsymbol{\Sigma} \mathbf{F}_g^T\right) \\ &= \mathbf{F}_g \boldsymbol{\Sigma} \mathbf{F}_g^T - \frac{1}{3} \operatorname{tr}\left(\mathbf{F}_g \boldsymbol{\Sigma} \mathbf{F}_g^T\right) \mathbf{I} \\ &= \mathbf{F}_g \boldsymbol{\Sigma} \mathbf{C}_g \mathbf{F}_g^{-1} - \frac{1}{3} \operatorname{tr}\left(\boldsymbol{\Sigma} \mathbf{C}_g\right) \mathbf{I} \\ &= \mathbf{F}_g \left(\boldsymbol{\Sigma} \mathbf{C}_g - \frac{1}{3} \operatorname{tr}\left(\boldsymbol{\Sigma} \mathbf{C}_g\right) \mathbf{I} \right) \mathbf{F}_g^{-1} \\ &= \mathbf{F}_g \operatorname{dev}\left(\boldsymbol{\Sigma} \mathbf{C}_g\right) \mathbf{F}_g^{-1}. \end{aligned}$$

Utilizing the properties of the trace operator, the deviatoric invariant can be rewritten as

$$J_2 = \frac{1}{2} \operatorname{tr}\left(\operatorname{dev}\left(\boldsymbol{\Sigma} \mathbf{C}_g\right)^2\right).$$

2.7.5 Arruda-Boyce model

By introducing the volumetric deviatoric split of the elastic right Cauchy Green tensor, i.e. $\mathbf{C}_e = J_e^{\frac{2}{3}} \bar{\mathbf{C}}_e$, one can describe the elastic energy of the well known hyperelastic material model of Arruda and Boyce [1993] as

$$\begin{aligned} \psi &= U(J_e) + W(\bar{\mathbf{C}}_e) \\ &= \frac{\kappa}{4} \left[J_e^2 - 1 - 2 \ln\left(J_e\right) \right] + \mu \sum_{k=1}^{K} \frac{C_k}{N^{k-1}} \left[\bar{I}_1^k - 3^k \right]. \end{aligned}$$

Here, κ, μ and N are material parameters and $C_k = \left[\frac{1}{2}, \frac{1}{20}, \frac{11}{1050}, \frac{19}{7000}, \frac{519}{673750}\right]$ are coefficients resulting from an approximation of the inverse Langevin function. Furthermore, $\bar{I}_1 = \operatorname{tr}\left(\bar{\mathbf{C}}_e\right)$ describes the first invariant of the deviatoric part of $\mathbf{C}_e$. For further information on this model, the reader is kindly referred to the comprehensive overview of Steinmann et al. [2012]

3 Article 2: Modelling and simulation of time-dependent damage and failure within silicone-based, polymeric adhesives

This article was published as:

Lamm, L.; Pfeifer, J. M.; Holthusen, H.; Brepols, T.; Reese, S. [2023], 'Modelling and simulation of time-dependent damage and failure within silicone-based, polymeric adhesives', *Proceeding in Applied Mathematics and Mechanics* **22** (1), e202200076.

Disclosure of the individual authors' contributions to the article:

L. Lamm worked out the theoretical material model and wrote this article. L. Lamm and J. M. Pfeifer implemented the model into the finite element software FEAP, reviewed the relevant existing literature, performed the simulations and interpreted the results. H. Holthusen, T. Brepols and S. Reese gave conceptual advice, contributed in the discussion of the results, read the article and gave valuable suggestions for improvement. All authors approved the publication of the manuscript.

3.1 Abstract

Hyperelastic adhesive joints are used successfully in many areas of industry. Besides all their inherent advantages, materials used for the construction of such bonds show a vast variety of non-linear effects in their response to mechanical loading, which poses a challenge in modelling and predicting their material response. Recent experiments have shown a strong temporal response when it comes to damage and failure within these materials. This contribution aims to propose a simple but yet flexible formulation to predict time-dependent damage effects within polymeric adhesives. Besides the main aspects of the thermodynamically consistent development, we also show numerical examples to demonstrate the capabilities of the model.

3.2 Introduction

Adhesives are widely used in the industrial context. Especially in the building industry, their use in the construction of glass façade systems is becoming increasingly important Klosowski and Wolf [2016]. To ensure safe application, the material behaviour under real load conditions must be predicted with high accuracy. Computational models have proven their worth for this purpose. In addition to the highly non-linear elastic material behaviour, such models must also be able to represent a wide range of inelastic, temperature-dependent and rate-dependent effects. Just recently Seewald et al. [2021] and Schaaf et al. [2020] found that such adhesives do show a pronounced time-dependent behaviour when it comes to damage and failure. These effects can not be described by a classical rate-independent viscoelastic damage model. Modelling time-dependent inelastic behaviour of solids is nothing new. In the field of damage modelling, however, approaches are often used which assume small deformations. The so called *creep damage model* developed by Kachanov [1958] and later modified by Rabotnov [1969] lays the ground for a variety of models used e.g. in the modelling of damage in rock or asphalt (see e.g. Geers et al. [1994], Wang et al. [2013] or Zeng et al. [2014]). Further approaches using *viscous regularization* as described in the work of Perzyna [1963] are e.g. Simo and Ju [1987], Cervera et al. [1996] or Ren and Li [2013]. The assumption of small deformations can no longer be assumed to be true for hyperelastic adhesives. Within this contribution we therefore follow an approach similar to *viscous regularization* but extend it to describe material responses at finite strains. The model proposed is simple yet powerful for modelling time-dependent isotropic damage. To study the effects of this modelling approach, we solely focus on this single type of temporal inelastic effect. For this, we derive a thermodynamically consistent material formulation based on the gradient extended micromorphic framework of

Brepols et al. [2020] and extend it with a Perzyna-type ansatz Perzyna [1963, 1966] to capture the temporal effects. We also show the algorithmic implementation strategy as well as selected numerical examples to evaluate the capabilities of the given model.

3.3 Continuum mechanical modelling

As frequently done within the modelling of hyperelastic polymeric materials, we start with the well-established multiplicative split of the deformation gradient $\mathbf{F}$ into volumetric and isochoric parts (see e.g. Lubliner [1985]; Simo and Taylor [1991]), i.e.

$$\mathbf{F} = \det \mathbf{F}^{\frac{1}{3}} \mathbf{I} \mathbf{F}^* = J^{\frac{1}{3}} \mathbf{F}^*. \tag{3.1}$$

With this at hand, the isochoric right Cauchy-Green tensor can be defined as $\mathbf{C}^* = J^{-\frac{2}{3}} \mathbf{F}^T \mathbf{F}$. To describe the damage behaviour within hyperelastic polymeric adhesives an isotropic evolution of damage within the material is assumed. Therefore, a scalar damage variable $D \in [0, 1]$ can be defined. The state of this variable determines the amount of accumulated damage. In this context, $D = 0$ describes the undamaged, virgin material whereas $D = 1$ means total failure of the material. Since the focus of this work is the investigation of time-dependent damage phenomena within polymeric adhesives, we assume the underlying basic material response to be hyperelastic. It is obvious that this is a strong assumption since polymers tend to show a pronounced time-dependent material response even within the purely elastic loading regime. For the sake of investigating the effects of time-dependent damage, it seems beneficial to isolate this modelling approach from further temporal dependencies and focus merely on the effects shown by the damage model itself. Therefore, the Helmholtz free energy can be defined by means of a damage degradation function $f_d(D) = (1 - D)^2$ such that

$$\psi := f_d(D) \psi_e(J, \mathbf{C}^*) + \psi_d(\xi_d) + \psi_{\bar{d}}(D, \bar{D}, \nabla \bar{D}). \tag{3.2}$$

Here, ψ_e is the elastically stored strain energy which is defined in terms of the symmetric right Cauchy-Green tensor $\mathbf{C} = \mathbf{F}^T \mathbf{F}$ with $\mathbf{F}$ being the deformation gradient. To describe damage hardening, we furthermore introduce the hardening variable ξ_d as well as the associated hardening energy ψ_d. It is well known that classical damage models tend to show pathological mesh dependencies accompanied by strong localization effects Rizzi and Loret [1997]. To avoid such effects, we make use of a gradient-extended ansatz as proposed by Brepols et al. [2020]. For this, the global damage variable $\bar{D}$ is introduced together with its associated free energy $\psi_{\bar{d}}$.

3.3.1 Thermodynamic considerations

In order to ensure physical correctness of the developed material model, the second law of thermodynamics must be fulfilled. Taking the given micromorphic extension into account it can be written in terms of the isothermal Clausius-Duhem inequality as

$$\mathbf{S} : \frac{1}{2}\dot{\mathbf{C}} - \dot{\psi} + \underbrace{a\dot{\bar{D}} + \mathbf{b} \cdot \nabla\dot{\bar{D}}}_{\text{micromorphic ext.}} \geq 0. \tag{3.3}$$

Here, $\mathbf{S}$ denotes the second Piola-Kirchhoff stress tensor whereas a and $\mathbf{b}$ describe the generalized stresses related to the non-local variable $\bar{D}$ and its gradient, respectively. For a more detailed elaboration the interested reader is kindly referred to Forest [2009]. Inserting Equation (3.2) into Equation (3.3) and applying the standard Coleman-Noll procedure Coleman and Noll [1963] yields the thermodynamically consistent definition of the second Piola-Kirchhoff stress tensor

$$\mathbf{S} = 2f_d \frac{\partial \psi_e}{\partial \mathbf{C}} \tag{3.4}$$

together with the generalized stresses $a = \frac{\partial \psi_{\bar{d}}}{\partial \bar{D}}$ and $\mathbf{b} = \frac{\partial \psi_{\bar{d}}}{\partial \nabla \bar{D}}$. Defining the thermodynamically conjugated driving forces for the damage variable D as well as the damage hardening variable ξ_d as $Y = -(\frac{\partial f_d}{\partial D}\psi_e + \frac{\partial \psi_{\bar{d}}}{\partial D})$ and $q_d = \frac{\partial \psi_d}{\partial \xi_d}$ leads to the reduced Clausius-Duhem inequality given by

$$Y\dot{D} - q_d\dot{\xi}_d \geq 0. \tag{3.5}$$

In order to ensure thermodynamical consistency, evolution equations for D and ξ_d must be found that fulfil this reduced inequality.

3.3.2 Evolution equations

In order to describe the onset of damage evolution within the material, we follow the standard approach of defining a scalar damage function as

$$\Phi_d = Y - (Y_0 + q_d), \tag{3.6}$$

which includes the damage threshold parameter Y_0. Next, we introduce the so-called damage multiplier $\dot{\lambda}_d$ and postulate an associative evolution law for both, the damage variable D as well as the hardening variable ξ_d, i.e.

$$\dot{D} = \dot{\lambda}_d \frac{\partial \Phi_d}{\partial Y} = \dot{\lambda}_d \qquad \text{and} \qquad \dot{\xi}_d = -\dot{\lambda}_d \frac{\partial \Phi_d}{\partial q_d} = \dot{\lambda}_d. \tag{3.7}$$

This particular choice of the evolution equations has the effect that the evolution of D and ξ_d are equivalent. It is important to notice that this is a rather simple assumption and by no means the only possible definition of associative evolution laws for D or ξ_d. For classical rate-independent isotropic damage, the definition of Equations (3.6) and (3.7) is sufficient and could be solved using Karush-Kuhn-Tucker conditions.

To introduce a temporal dependency into the damage model at hand, we adapt an ansatz made by e.g. Perzyna [1963, 1966] or Perić [1993] where we explicitly define an extra evolution equation for the damage multiplier $\dot{\lambda}_d$ such that

$$\dot{\lambda}_d = \begin{cases} \eta_d \, \Phi_d^{\frac{1}{\epsilon_d}} & \text{if} \quad \Phi_d \geq 0 \\ 0 & \text{if} \quad \Phi_d < 0 \end{cases} \tag{3.8}$$

Here, η_d describes a damage velocity and ϵ_d is the damage rate sensitivity.

3.3.3 Particular choice of the Helmhotz free energies

Depending on the material at hand, various hyperelastic ground models are applicable. For hyperelastic polymers which are showing pronounced strain-stiffening effects models such as Arruda and Boyce [1993] or Ogden [1972] seem to be a good choice. Since the focus of this study is merely the time-dependent damage behaviour and for the sake of simplicity, we make use of a classical Neo-Hookean type energy to describe the underlying elastic material response, i.e.

$$\psi_e(J, \mathbf{C}^*) := \frac{\mu}{2} \left(\operatorname{tr} \mathbf{C}^* - 3 \right) + \frac{\kappa}{4} \left(J^2 - 1 - 2 \ln J \right). \tag{3.9}$$

To describe the energy density associated with damage hardening, a combination of linear and nonlinear, Voce-type hardening Voce [1948] is used, i.e.

$$\psi_d(\xi_d) := \underbrace{\frac{1}{2} \, k \, \xi_d^2}_{\text{lin. hardening}} + \underbrace{r \left(\xi_d + \frac{1}{s} \left[\exp(-s \xi_d) - 1 \right] \right)}_{\text{Voce-type hardening}}. \tag{3.10}$$

Here, r, s and k are material parameters controlling the damage hardening behaviour. Regarding the energy density of the micromorphic gradient extension, we define $\psi_{\bar{d}}$ in accordance with Forest [2009] as

$$\psi_{\bar{d}}(D, \bar{D}, \nabla \bar{D}) := \frac{H}{2} \left(D - \bar{D} \right)^2 + \frac{A}{2} \nabla \bar{D} \cdot \nabla \bar{D}, \tag{3.11}$$

where the parameters H and A describe the coupling between local and non-local damage fields as well as the influence of the gradient of $\bar{D}$. These choices of the individual parts of the Helmholtz free energy yield for the thermodynamically conjugated driving forces the following expressions:

$$Y = -\left(2(1-D)\psi_e + H(D-\bar{D})\right) \qquad \text{and} \qquad q_d = k\,\xi_d + r - \exp(-s\xi_d) \tag{3.12}$$

3.4 Algorithmic implementation

The material formulation described above has been implemented into the multipurpose finite element program *FEAP*. For the solution of evolution Equation (3.7) together with Equation (3.8) we apply an implicit Euler integration scheme with time step size $\Delta t = t_{n+1} - t_n$, such that

$$r = D_{n+1} - D_n - \eta_d\, \Phi_d^{\frac{1}{\epsilon_d}} \Delta t \stackrel{!}{=} 0. \tag{3.13}$$

This non-linear residual equation can be solved using standard Newton-Raphson iteration, for which the local tangent operator $\frac{\partial r}{\partial D}$ must be computed. Within this contribution, we used the automatic differentiation framework *AceGen* (see Korelc [2002, 2009]) to obtain this derivative. With this at hand the current value of the local damage variable D can be iteratively determined for the kth iteration step via $D_{k+1} = D_k - \frac{\partial r}{\partial D}^{-1} r_k$.

The local material response is implicitly included within the global material tangent operator of the finite element simulation. We therefore need to derive this tangent in a consistent manner in order to achieve quadratic convergence of the global iteration scheme. Since the second Piola-Kirchhoff stress tensor is a function of the right Cauchy-Green tensor as well as the internal variables, the tangent operator can be expressed as

$$\mathbb{C} = 2\left(\left.\frac{\partial \mathbf{S}}{\partial \mathbf{C}}\right|_D + \left.\frac{\partial \mathbf{S}}{\partial D}\right|_{\mathbf{C}} : \frac{\partial D}{\partial \mathbf{C}}\right). \tag{3.14}$$

For the given choices of the Helmholtz free energies from the last section, the partial derivative of the second Piola-Kirchhoff stress tensor with respect to the right Cauchy-Green tensor can be computed easily using *AceGen*. For the partial derivative of the local damage variable D with respect to the right Cauchy-Green tensor $\mathbf{C}$ we make use of the relation

$$\Delta D = \frac{\partial D}{\partial \mathbf{C}} \Delta \mathbf{C} = -\frac{\partial r}{\partial D}^{-1} \frac{\partial r}{\partial \mathbf{C}} \Delta \mathbf{C}, \tag{3.15}$$

where we use the fully converged residual and jacobian from the local solution process.

3.5 Numerical examples

In the following, we demonstrate the behaviour of the model described above showing some numerical studies conducted at integration point level. For this, a uniaxial loading state is applied whilst the damage associated material parameters are varied. For the elastic parameters we choose the shear modulus to be $\mu = 6.0$ MPa whilst the bulk modulus is set to $\kappa = 10000\mu$ which enforces nearly incompressible material behaviour. In order to avoid locking effects, we adapted a reduced integration finite element formulation with adaptive hourglass stabilization as described in Barfusz et al. [2021].

3.5.1 Linear displacement simulation

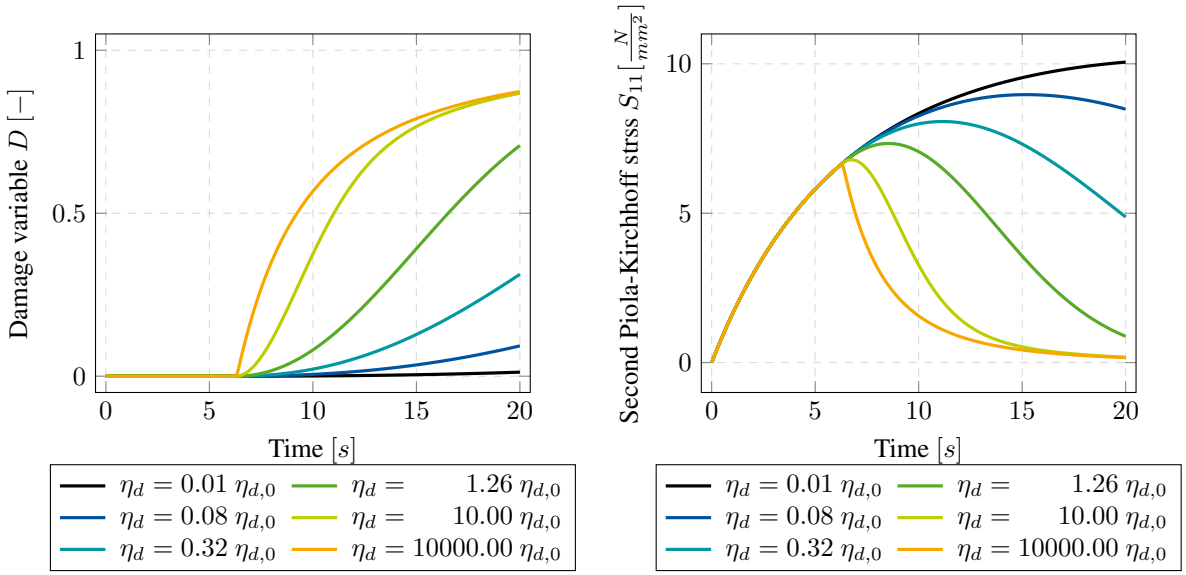

(a) Evolution of damage variable D.

(b) Evolution of stress in loading direction.

Figure 3.1: Results of linear displacement applied uniaxially to a single element. Showing the influence of the damage relaxation velocity η_d with reference $\eta_{d,0} = 10^{-2}$. Reaction force normalized wrt. $F_{max} = 20.25$ N.

The first example given in Figure 3.1 shows the results from a uniaxially loaded single element simulation over time. Here, a displacement $u(t)$ is applied at a constant rate $\frac{\mathrm{d}u}{\mathrm{d}t}$. Figures 3.1a and 3.1b clearly show the pronounced time dependency of the damage response with respect to time. For small values of the relaxation velocity η_d the model shows nearly no damage at all resulting in a response similar to classical Neo-Hookean elasticity. In case of high values

of η_d we observe results similar to what is expected from a rate-independent model. Values of η_d in between these two edge case are able to interpolate the time-dependency nicely.

3.5.2 Relaxation simulation

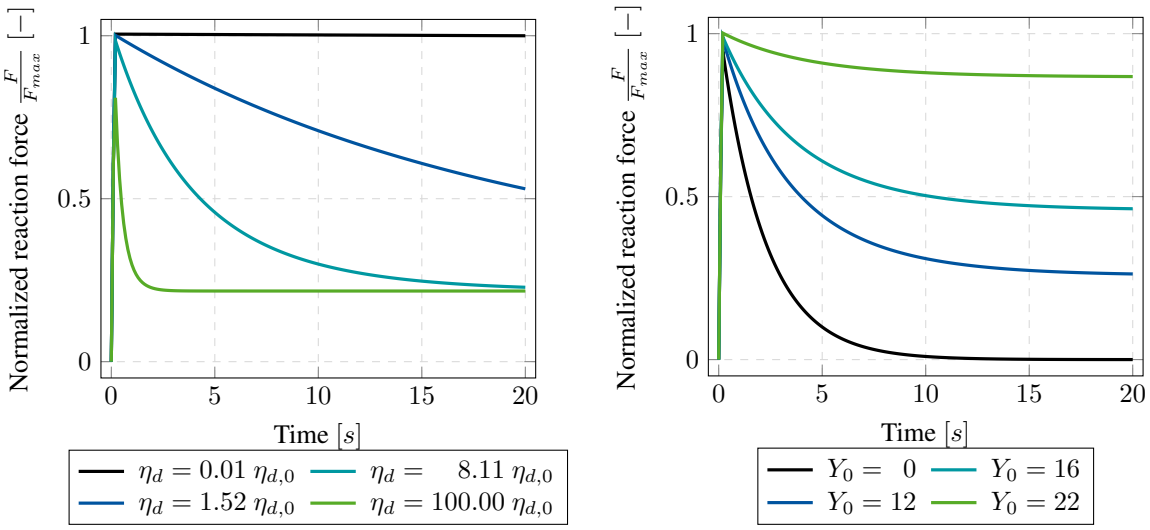

(a) Influence of damage relaxation velocity η_d.

(b) Influence of damage threshold Y_0.

Figure 3.2: Results of relaxation experiment applied uniaxially to a single element. Showing the influence of material parameters η_d and Y_0 with reference $\eta_{d,0} = 10^{-3}$. Reaction force normalized wrt. $F_{max} = 20.25$ N.

The next example considers a classical relaxation simulation where a constant displacement $u(t)$ is applied at time $t = 1$s and held constant for the remainder of the simulation. Figure 3.2 shows the influence of both, the relaxation velocity η_d as well as the damage threshold Y_0. As already discussed in the previous example, the relaxation velocity as shown in Figure 3.2a is able to produces smooth interpolations between the pure elastic response for small values of η_d and the nearly rate-independent damage response for large values. Figure 3.2b shows the influence of Y_0 on the damage progression. Here it is obvious that smaller values lead to a more pronounced damage behaviour whereas larger values result in a more subtle damage progression and consequently in a higher residual reaction force. This behaviour is as expected, since the damage related driving force Y decreases with increasing damage progression and consequently falls below Y_0 faster for a higher threshold.

3.5.3 Creep simulation

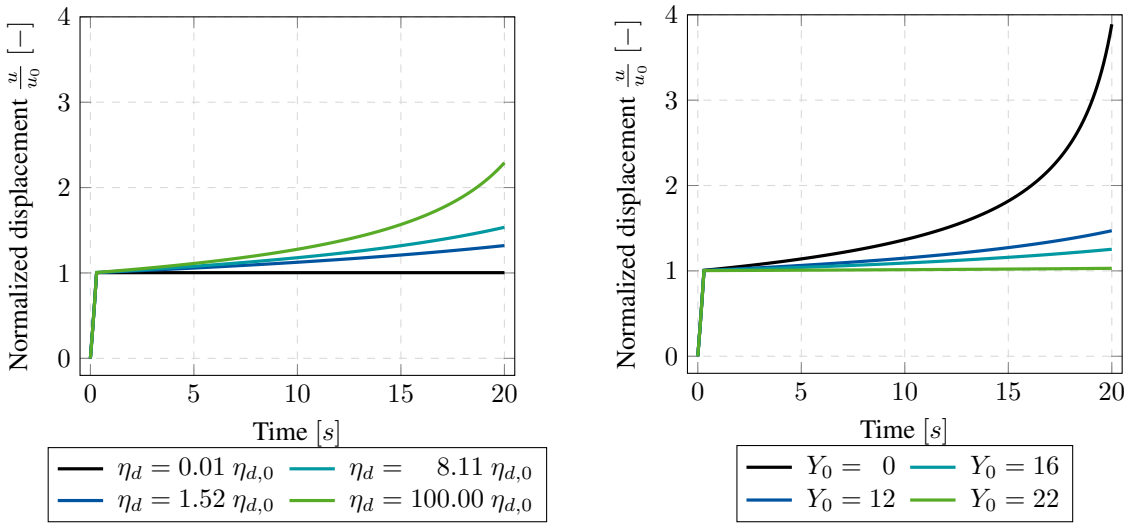

(a) Influence of damage relaxation velocity η_d.

(b) Influence of damage threshold Y_0.

Figure 3.3: Results of creep experiment applied uniaxially to a single element. Showing the influence of material parameters η_d and Y_0 with reference $\eta_{d,0} = 10^{-3}$. Displacement normalized wrt. $u_0 = 0.125$ mm.

In the last example, we take a closer look at a classical creep simulation setup. For this, a constant force F_x is applied uniaxially at time $t = 1s$ and held constant over the rest of the simulation. Figure 3.3 shows the influence of the damage relaxation time η_d as well as of the damage threshold Y_0. Both evaluations shown in Figures 3.3a and 3.3b show the expected damage behaviour. For small relaxation velocities η_d, the quasi-elastic response is achieved, whereas for large η_d an exponential growth in the displacement can be measured. This effect is even more pronounced when looking at the influence of the damage threshold Y_0. Since this measure describes the amount of energy that must be present in order to trigger damage effects, lower values of Y_0 lead to a faster and more pronounced damage progression.

3.6 Conclusion and outlook

In this work, we have presented a simple yet flexible approach to modelling rate-dependent isotropic damage at finite deformation. To account for the temporal dependence of the material, we used a Perzyna-type approach to describe the evolution equations of damage. With this at hand, we were able to briefly demonstrate the reasonability of the material response for

three different use-cases. Besides uniaxial linear deformation, also relaxation and creep simulations were shown. From a qualitative point of view, these studies gave reasonable results. Nevertheless, the model must still be validated using experimental data. Unfortunately, time-dependent damage is usually not observed as an isolated effect in real world materials but rather coupled with other inelastic effects, such as viscoelasticity in polymeric materials. Therefore, an extension of the given model to capture also viscoelasticity must be done before proceeding with the experimental validation of the model. Since polymers are known for their strongly temperature-dependent material behaviour, an extension of the model into a thermomechanically coupled formulation seems reasonable.

4 Article 3: Gradient-extended damage modelling for polymeric materials at finite strains: Rate-dependent damage evolution combined with viscoelasticity

This article was published as:

Lamm, L.; Pfeifer, J. M.; Holthusen, H.; Schaaf, B.; Seewald, R.; Schiebahn, A.; Brepols, T.; Feldmann M.; Reisgen, U.; Reese, S. [2023], 'Gradient-extended damage modelling for polymeric materials at finite strains: Rate-dependent damage evolution combined with viscoelasticity', *European Journal of Mechanics / Part A: Solids* **103**, 105121

Disclosure of the individual authors' contributions to the article:

L. Lamm worked out the theoretical material model and wrote this article. L. Lamm and J. M. Pfeifer implemented the model into the finite element software FEAP, reviewed the relevant existing literature, performed the simulations and interpreted the results. B. Schaaf and R. Seewald designed and conducted the experiments used for experimental comparison of the material model. A. Schiebahn, M. Feldmann, U. Reusgen, H. Holthusen, T. Brepols and S. Reese gave conceptual advice, contributed in the discussion of the results, read the article and gave valuable suggestions for improvement. All authors approved the publication of the manuscript.

4.1 Abstract

While the strong rate-dependent effects of polymeric materials in the elastic regime are well studied, the time-dependent effects that arise in the inelastic damage regime are still difficult to model and are therefore the subject of investigation. In this work, we propose a simple but flexible formulation for the description of rate-dependent damage combined with viscoelasticity at finite strains. This model is based on a finite viscoelastic material formulation combined with a Perzyna-type approach to describe the damage evolution equation. With this formulation we are able to describe both damage due to creep and relaxation of the polymer matrix in both a qualitative and quantitative manner. Besides the main aspects of thermodynamic consistency, we describe the numerical implementation into finite elements and present numerical examples to demonstrate the capabilities of the proposed model. At last, we compare the model with experimental data and show the good predictive capabilities of this newly developed material model.

4.2 Introduction

Highly deformable silicone-based polymeric adhesives play an important role in industrial applications such as building construction and the automotive industry. One particular example is their use in the construction of structural glazing façades. Here, the glass façade component is bonded directly to the load-bearing substructure using adhesives (see e.g. Hagl [2002]). To ensure the stability of such constructions, the mechanical behaviour of these bonded joints under load must be accurately predicted. Sophisticated computational models of material response are required to make such predictions. Within such models a vast variety of elastic and inelastic effects must be considered. In addition to their highly non-linear elastic behaviour, polymers typically exhibit strong rate dependencies. Viscoelasticity is classically considered to be the dominant rate-dependent effect in polymeric materials. Its modelling has long been a major research focus of the computational mechanics community. This has resulted in a large number of different models for the viscoelastic response of materials under finite deformation. A comprehensive list of the majority of publications in this field is not possible within the scope of this paper due to the sheer volume of publications. In the following, we will therefore limit ourselves to a brief overview of what we consider to be the most influential works at present. In general, these modelling approaches can be roughly divided into two classes. On the one hand, there is work by e.g. Simo [1987]; Holzapfel and Simo [1996]; Bonet [2001] which focuses on finite viscoelasticity considering a linear relation between stress and strain

rate. While these works only allow for small deviations from thermodynamic equilibrium, the works of e.g. Reese and Govindjee [1998]; Bergström [1998]; Haupt et al. [2000] also include the intrinsic non-linearity of the viscoelastic rates. These approaches leads to a generalised form of the description of viscoelastic behaviour. It has been shown, that such approaches can also be easily reduced to the linear theory, if needed. More recent modelling approaches and applications in this regard can be found e.g. in Fancello et al. [2006]; Kumar and Lopez-Pamies [2016]; Wang and Chester [2018] and Rambausek et al. [2022], among others.

In addition to their visco-elastic behaviour, polymeric adhesives also clearly show a strong rate dependence of the damage process itself. This is particularly evident in the high strain regime under finite deformation. We have been able to demonstrate this effect in experimental studies for the case of damage occuring under creep (*creep damage*) as well as during relaxation. Some of the results from these investigations will be presented within this paper. The main focus of this publication, however, is on the development of a material model that is able to account for both, viscoelasticity and rate-dependent damage effects. Various approaches for describing rate-dependent damage behaviour already exist in the literature. On the one hand side, there are micromechanically motivated models which are usually based on chain statistics and scission kinematics of the polymeric network. Examples for such works in the case of isotropic damage are Shaw et al. [2005]; Wineman and Shaw [2007]; Wineman [2009]; Vernerey et al. [2018]; Guo and Zaïri [2021]. Based on some of these ideas, Lavoie et al. [2016] extended the idea of scission kinematics to a general damage model that is also able to cover anisotropic damage behaviour. On the other side, there are models based on the phenomenological observations made in experiments. This category contains modelling approaches made either in the field of continuum damage or phase field modelling. Miehe and Schänzel [2014] and Miehe et al. [2015], for example, introduced a *viscous damage equation covered by "over force"* to stabilize their numerical algorithms. Loew et al. [2019] later took this idea and extended it to model fully rate-dependent damage and failure of polymeric materials. When cosidering classical isotropic continuum damage modelling, rate-independent models such as the one by Brepols et al. [2020] are usually not capable of properly covering effects such as creep damage, for example. This is due to the fact that they assume an instantaneous accumulation of damage once a certain damage threshold is reached and the underlying damage criterion is violated. If no further loading is applied, no additional damage can be accumulated within the material. In contrast to this, a model that could capture the rate-dependent nature of damage taking place in polymeric materials must be able to describe a contiunous accumulation of damage over time. When dealing with problems associated with structures subjected to small deformations, a variety of rate-dependent damage models have been developed for various applications and

materials. Some examples of such models are Murakami and Ohno [1981]; Lemaitre [1985*a*]; Wang et al. [2013]; Pandey et al. [2019]; Pereira et al. [2017]; Shlyannikov and Tumanov [2019]; Nahrmann and Matzenmiller [2021]; Kou et al. [2022] among others. In case of materials and structures subjected to finite deformation, such as the glass façade components mentioned above, the selection of relevant scientific literature is relatively sparse. Lion [1996] builds on the ideas from small strain theory, as described e.g. in Simo [1987], and extends it to finite deformation. While this model aims to describe stress softening and the Mullins effect, the models of Miehe [2000]; Lin and Schomburg [2003]; Aboudi [2011], use the same idea to more generally describe rate-dependent damage processes arising in polymeric materials. All of these models are based on an explicitly defined evolution equation considering the rate of a strain like quantity as a driving force for the damage process. Another approach published just recently in Khaleghi et al. [2022] uses a damage evolution law based on Lemaitre [1985*a*] and extends it to the finite strain regime.

Within this work we propose a simple yet flexible model for the description of rate-dependent non-local damage combined with viscoelasticy at finite deformations. Our model is based on the gradient-extended but rate-dependent micromorphic damage formulation for large deformations developed by Brepols et al. [2020]. For the viscoelastic material formulation we adapt the well-known model of Reese and Govindjee [1998] and formulate it in a co-rotated intermediate configuration as proposed recently by Holthusen et al. [2023]. In order to describe the rate-dependency of the damage evolution, we use the approach described in Lamm, Pfeifer, Holthusen, Brepols and Reese [2023] and adapt a Perzyna-type ansatz (see Perzyna [1966, 1971]) for the corresponding evolution law. Similar approaches have already successfully been used when modelling rate-dependent inelastic phenomena of various origin (see e.g. Lamm et al. [2021, 2022]; Holthusen et al. [2023] and references therein).

The overall work is structured as follows. In Section 4.3, we cover the theoretical modelling ideas behind the proposed model before describing its numerical implementation within Section 4.4. Numerical examples and validation using experimental data are given in Section 4.5.

4.3 Modelling of viscoelastic rate-dependent damage

4.3.1 Gradient extended damage formulation

For the sake of simplicity, we assume damage to occur isotropically, i.e. the material at hand is weakened equally with respect to all spacial dimensions. In order to model this kind of damage behaviour, we introduce a scalar damage variable $D \in [0, 1]$, which describes the

amount of accumulated damage. In this context, $D = 0$ refers to a virgin state of the material whereas $D = 1$ means total failure. Such an approach is called *local damage model*. It is well-known from the literature that local models show non-physical localization effects, resulting in pathological mesh dependencies (see e.g. Bažant et al. [1984], de Borst et al. [1993], Rizzi and Loret [1997]). To overcome these major problems, we use the gradient extended damage formulation of Brepols et al. [2020] which is based on the micromorphic framework of Forest [2009]. Here, an addition global field variable $\bar{D}$ is introduced as the so-called *global damage variable*. Due to this additional field, the classical balance of linear momentum has to be solved together with the micromorphic balance relation

$$\mathrm{Div}\,(\mathbf{b}_{0_i} - \mathbf{b}_{0_e}) - a_{0_i} + a_{0_e} = 0 \tag{4.1}$$

in a coupled sense. Here, $\mathbf{b}_{0_i}$, $\mathbf{b}_{0_e}$ are the internal forces related to the global damage variable as well as its gradient. Furthermore, a_{0_i} and a_{0_e} describe generalized body forces resulting from the micromorphic extension. For further details on the gradient extended approach, the interested reader is kindly referred to Brepols et al. [2017*a*, 2020].

Since polymer materials usually behave incompressibly, the use of a standard finite element formulation with linear shape functions can lead to spurious locking effects, resulting in an non-physical material response. To avoid this, we use a finite element formulation with reduced integration and hourglass stabilisation. Its derivations for gradient-extended micromorphic damage modelling can be found in Barfusz et al. [2021]. In addition to the avoidance of locking effects, this formulation is characterised in particular by its high computational efficiency, since the evaluation of the material routine only has to take place at a single Gaussian point per element. Other well established methods to deal with locking effects can be found e.g. in Reese [2005], Schwarze and Reese [2011] and references therein.

4.3.2 Continuum mechanical modelling

In order to describe the viscoelastic properties of the given material, we need to define the viscous part of the deformation of a given continuum body. We therefore start with the well established multiplicative decomposition of the deformation gradient $\mathbf{F}$ into an elastic and viscous part, i.e.

$$\mathbf{F} = \mathbf{F}_e \mathbf{F}_v \tag{4.2}$$

This particular choice is by no means the only possible option but is well established in the modelling of inelastic phenomena at finite strains (see e.g. Sidoroff [1974]). Possible

variations of this multiplicative split are investigated in more detail in Bahreman et al. [2022]. Furthermore, we define the Green-Lagrange strain tensor $\mathbf{E} = \frac{1}{2}(\mathbf{C} - \mathbf{1})$ together with the right Cauchy-Green tensor $\mathbf{C} := \mathbf{F}^T\mathbf{F}$ as well as its viscous and elastic counterparts as

$$\begin{aligned} \mathbf{C}_v &:= \mathbf{F}_v^T\mathbf{F}_v \\ \mathbf{C}_e &:= \mathbf{F}_e^T\mathbf{F}_e = \mathbf{F}_v^{-T}\mathbf{C}\mathbf{F}_v^{-1}. \end{aligned} \tag{4.3}$$

Following the argumentation of Holthusen et al. [2023], we utilize the polar decomposition of the viscous deformation gradient $\mathbf{F}_v = \mathbf{R}_v\mathbf{U}_v$ to define the co-rotated elastic right Cauchy-Green tensor as

$$\tilde{\mathbf{C}}_e = \mathbf{R}_v^{-1}\mathbf{C}_e\mathbf{R}_v = \mathbf{U}_v^{-1}\mathbf{C}\mathbf{U}_v^{-1}. \tag{4.4}$$

In this context $\mathbf{U}_v$ is the viscous stretch tensor and $\mathbf{R}_v$ describes a proper orthogonal non-unique viscous rotational tensor. With the definition of the co-rotated velocity gradient $\tilde{\mathbf{L}}_v = \dot{\mathbf{U}}_v\mathbf{U}_v^{-1}$, the associated rate of the co-rotated elastic right Cauchy Green tensor can be derived as shown in Appendix 4.7.1, i.e.

$$\begin{aligned} \overset{\nabla}{\tilde{\mathbf{C}}}_e &= \frac{\mathrm{d}}{\mathrm{d}t}\left(\mathbf{U}_v^{-1}\mathbf{C}\mathbf{U}_v^{-1}\right) \\ &= \mathbf{U}_v^{-1}\dot{\mathbf{C}}\mathbf{U}_v^{-1} - \left(\tilde{\mathbf{L}}_v^T\tilde{\mathbf{C}}_e + \tilde{\mathbf{C}}_e\tilde{\mathbf{L}}_v\right). \end{aligned} \tag{4.5}$$

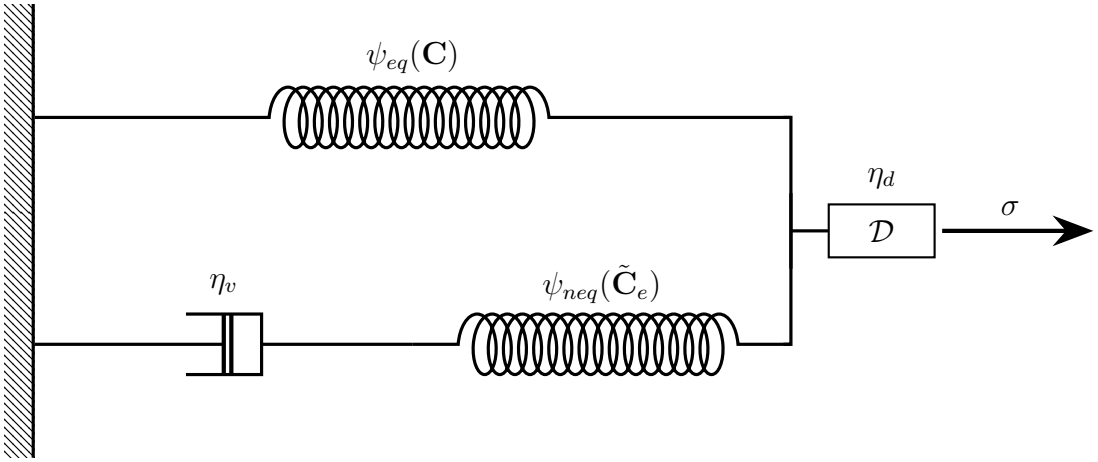

Figure 4.1: Rheological model motivating the proposed viscoelastic model including rate-dependent damage. Damage is denoted by the element including the character $\mathcal{D}$. Viscous relaxation and damage velocities are denoted by η_v and η_d, respectively.

4.3.2.1 General structure of the Helmholtz free energy

Within this contribution, we define the Helmholtz free energy as an energy density per unit reference volume and assume it to be additively split into

$$\psi := f_d(D) \underbrace{\left(\psi_{eq}(\mathbf{C}) + \psi_{neq}(\tilde{\mathbf{C}}_e)\right)}_{\psi_0} + \psi_d(\xi_d) + \psi_{\bar{d}}(D, \bar{D}, \nabla\bar{D}). \tag{4.6}$$

Here, the degradation function $f_d(D) = (1 - D)^2$ describes how the effective strain energy ψ_0 is decreased due to damage of the material. Motivated by the rheological model shown in Figure 4.1, we follow the ansatz of Reese and Govindjee [1998] and split the effective strain energy density of the undamaged viscoelastic material additively into an equilibrium and a non-equilibrium part, respectively. Within this approach, the equilibrium energy ψ_{eq} describes the time-independent part of the elastic energy, whereas the non-equilibrium part ψ_{neq} is related to the viscous response of the material. For a more flexible damage formulation, ψ_d is introduced as a damage hardening energy, which acts similar to isotropic hardening in the field of plasticity (see e.g. Chow and Wang [1987]; Chow and Lu [1989] among others). In order to make use of the micromorphic damage extension, an additional penalty energy contribution $\psi_{\tilde{d}}$ is required to couple the local and global damage fields with each other.

4.3.2.2 Thermodynamic considerations

In order to ensure that the constitutive relations of the model lead to physically reasonable results, we need to ensure that they do not violate the second law of thermodynamics which can be written in terms of the micromorphically extended isothermal Clausius-Duhem inequality, i.e.

$$\mathbf{S} : \frac{1}{2}\dot{\mathbf{C}} - \dot{\psi} + \underbrace{a_{0_i}\dot{\bar{D}} + \mathbf{b}_{0_i} \cdot \nabla\dot{\bar{D}}}_{\text{micromorphic extension}} \geq 0. \tag{4.7}$$

Here, $\mathbf{S}$ denotes the second Piola-Kirchhoff stress tensor. The latter terms in this equation result from the micromorphic extension of the model (see Forest [2009] for further details). By inserting the Helmholtz free energy from Equation (4.6) into the inequality and applying the standard Coleman-Noll procedure (see Coleman and Noll [1963]), the thermodynamically consistent definition of the second Piola-Kirchhoff stress tensor is given by

$$\mathbf{S} = 2f_d \left(\frac{\partial \psi_{eq}}{\partial \mathbf{C}} + \mathbf{U}_v^{-1} \frac{\partial \psi_{neq}}{\partial \tilde{\mathbf{C}}_e} \mathbf{U}_v^{-1} \right) \tag{4.8}$$

alongside with the generalized micromorphic stresses $a_{0_i} = \frac{\partial \psi_{\bar{d}}}{\partial D}$ and $\mathbf{b}_{0_i} = \frac{\partial \psi_{\bar{d}}}{\partial \nabla D}$. We furthermore assume that both, ψ_{eq} as well as ψ_{neq} are isotropic functions of their arguments. In this way their derivatives $\frac{\partial \psi_{eq}}{\partial \mathbf{C}}$ and $\frac{\partial \psi_{neq}}{\partial \tilde{\mathbf{C}}_e}$ become symmetric and commute with either $\mathbf{C}$ or $\tilde{\mathbf{C}}_e$, respectively. Consequently, also the co-rotated Mandel stress tensor $\tilde{\boldsymbol{\Sigma}} = 2 f_d \tilde{\mathbf{C}}_e \frac{\partial \psi_{neq}}{\partial \tilde{\mathbf{C}}_e}$ is symmetric. If we exploit the properties of the double contracting product, we can write the reduced form of the Clausius-Duhem Inequality (4.7) in terms of the symmetric part $\tilde{\mathbf{D}}_v := \operatorname{sym} \tilde{\mathbf{L}}_v$ of the co-rotated viscous velocity gradient such that

$$Y \dot{D} - q_d \dot{\xi}_d + \tilde{\boldsymbol{\Sigma}} : \tilde{\mathbf{D}}_v \geq 0. \tag{4.9}$$

The thermodynamically conjugate driving forces for damage and damage hardening are given in this equation by

$$Y := -\left(\frac{\partial f_d}{\partial D} \psi_0 + \frac{\partial \psi_{\bar{d}}}{\partial D} \right) \qquad \text{and} \qquad q_d := \frac{\partial \psi_d}{\partial \xi_d}. \tag{4.10}$$

Further details of the derivation can be found in Appendix 4.7.2.

4.3.2.3 Evolution equations

In order to fulfill the reduced inequality, we must formulate thermodynamically consistent evolution laws for the damage related quantities $\dot{D}$ and $\dot{\xi}_d$ as well as the symmetric part of the co-rotated viscous velocity gradient $\tilde{\mathbf{D}}_v$. To stay consistent with the thermodynamical considerations above, these laws must be formulated in terms of their corresponding conjugate driving forces Y, q_d and $\tilde{\boldsymbol{\Sigma}}$, respectively. Following the considerations of e.g. Simo and Miehe [1992] or Reese and Govindjee [1998], we postulate the existence of a viscoelastic potential that is written in terms of the viscous bulk modulus κ_v as well as the viscous shear modulus μ_v, i.e.

$$\Phi_v(\tilde{\boldsymbol{\Sigma}}_0) := \frac{1}{4\mu_v} \operatorname{tr}\left(\operatorname{dev}\left(\tilde{\boldsymbol{\Sigma}}_0 \right)^2 \right) + \frac{1}{18\kappa_v} \operatorname{tr}\left(\tilde{\boldsymbol{\Sigma}}_0 \right)^2. \tag{4.11}$$

Here, $\operatorname{tr}(\bullet)$ is the trace operator while $\operatorname{dev}(\bullet) = (\bullet) - \frac{1}{3}\operatorname{tr}(\bullet)$ is the deviatoric projection operator. We choose the potential to be a function of the co-rotated effective Mandel stress tensor $\tilde{\boldsymbol{\Sigma}}_0 = f_d^{-1} \tilde{\boldsymbol{\Sigma}}$ rather than the original Mandel stress tensor. This concept of using effective stresses is already well established in the field of plasticity modelling (see e.g. Lemaitre [1971]; Simo and Ju [1987]) as well as in the field of viscoelasticity (see e.g. Abdel-Tawab and Weitsman [2000]). We adapt this idea to ensure that the viscoelastic response of the material is not reduced due to the evolution of damage. From the potential defined above we can easily

define an associative evolution law for the symmetric part of the co-rotated viscous velocity gradient by means of a relaxation velocity η_v that reads

$$\tilde{\mathbf{D}}_v := \eta_v \frac{\partial \Phi_v(\tilde{\boldsymbol{\Sigma}}_0)}{\partial \tilde{\boldsymbol{\Sigma}}}. \tag{4.12}$$

By using the identity $\dot{\mathbf{C}}_v = 2\mathbf{U}_v \tilde{\mathbf{D}}_v \mathbf{U}_v$ (see Appendix 4.7.3 for the detailed derivation), we can reformulate Equation (4.12) and use an evolution equation in terms of the viscous right Cauchy-Green tensor $\mathbf{C}_v$ instead, i.e.

$$\dot{\mathbf{C}}_v = \frac{\eta_v}{f_d} \mathbf{U}_v \left(\frac{1}{2\mu_v} \operatorname{dev}\left(\tilde{\boldsymbol{\Sigma}}_0\right) + \frac{2}{3\kappa_v} \operatorname{vol}\left(\tilde{\boldsymbol{\Sigma}}_0\right) \right) \mathbf{U}_v. \tag{4.13}$$

For more details on this derivation, the interested reader is kindly referred to Appendix 4.7.4.

To model isotropic damage within the material at hand, we choose a scalar damage function which is defined in terms of the driving forces for damage Y and damage hardening q_d as well as the material parameter Y_0 which acts as a threshold for the damage process, i.e.

$$\Phi_d := Y - (Y_0 + q_d). \tag{4.14}$$

Remark. *Although it is the most simple and obvious, Equation* (4.14) *is not the only possible choice for the definition of an appropriate damage function. Without any doubt, the use of more complex (e.g. nonlinear) functions is possible and strongly depends on the type of material being modelled.*

With this at hand, the damage related evolution equations for the local damage variable D and the damage hardening variable ξ_d can be written as

$$\dot{D} := \dot{\lambda}_d \frac{\partial \Phi_d}{\partial Y} = \dot{\lambda}_d \qquad \text{and} \qquad \dot{\xi}_d := -\dot{\lambda}_d \frac{\partial \Phi_d}{\partial q_d} = \dot{\lambda}_d. \tag{4.15}$$

It is important to note that this particular choice of the associative evolution equations yields the same result for both, the local damage variable D and the damage hardening variable ξ_d. Such a relatively simple approach is by no means the only feasible option. For isotropic damage it has the computational and algorithmic advantage that only one of these variables must be stored in memory and only one evolution equation must be solved. In the case of a classical rate-independent damage model, $\dot{\lambda}_d$ would serve as a Lagrangian multiplier which has to be solved using the Karush-Kuhn-Tucker conditions. In contrast to that, we introduce an explicit

formulation for $\dot{\lambda}_d$, i.e.

$$\dot{\lambda}_d := \begin{cases} \eta_d \left(\frac{\Phi_d}{Y_0 + q_d} \right)^{\frac{1}{\varepsilon_d}} & \text{if} \quad \Phi_d \geq 0 \\ 0 & \text{else} \end{cases} \tag{4.16}$$

in order to introduce a temporal dependence into our model (see e.g. Perzyna [1963, 1966]; Perić [1993]). Similar to the viscoelastic part of this model, η_d describes the damage velocity. Furthermore, ε_d is the so-called damage sensitivity parameter.

Remark. *It has been shown recently by Satouri et al. [2022] that it makes a clear difference whether the local damage field D or the local hardening variable ξ_d is used for the non-local, gradient-extended regularization strategy. In their case, using the hardening variable rendered better results than the usage of D. In our modelling case, however, the damage variable D and hardening variable ξ_d evolve in the same manner as given in Equations* (4.15) *and* (4.16)*. Coupling either of these local variables therefore renders the same regularization effect. It is clear that this is no longer the case, if different evolution equations are used for D and ξ_d. In such a case, a detailed investigation on the influence of the choice of the coupling variable must be performed.*

4.3.2.4 Particular choices of the Helmholtz free energy

Up to this point, the constitutive framework presented herein is very generic and is not complete without the definition of a particular form of individual parts of the Helmholtz free energy. The choice of the individual energy potentials depends strongly upon the specific type of material which one aims to model. Especially for hyperelastic materials at finite strains, various energy models exist, which all have their own advantages and disadvantages (see e.g. Steinmann et al. [2012] for a detailed overview). Not least for simplicity reasons, we choose a Neo-Hookean type model as an elastic ground model for both, the equilibrium energy part ψ_{eq} as well as the non-equilibrium part ψ_{neq}. Written in terms of the well-known volumetric-isochoric split and with $\mathbf{C}_*$ referring either to $\mathbf{C}$ or $\tilde{\mathbf{C}}_e$ depending on the individual energy, this form can be written as

$$\psi_* := \frac{\mu_*}{2} \left[\operatorname{tr} \left(J_*^{-\frac{2}{3}} \mathbf{C}_* \right) - 3 \right] + \frac{\kappa_*}{4} \left(J_*^2 - 1 - 2 \ln J_* \right), \tag{4.17}$$

with $J_* = \sqrt{\det \mathbf{C}_*}$. Here, μ_* and κ_* refer to the shear and bulk modulus of the individual energy contribution, respectively. For the energy density of the damage hardening contribution, we choose a combination of a Voce-type hardening (see Voce [1948]) and a classical linear

hardening law including the material paramters k, r and s, i.e.

$$\psi_d(\xi_d) := \underbrace{\frac{1}{2}\, k\, \xi_d^2}_{\text{linear hardening}} + \underbrace{r\left(\xi_d + \frac{1}{s}\left[\exp(-s\xi_d) - 1\right]\right)}_{\text{Voce-type hardening}}. \tag{4.18}$$

Regarding the energy density of the micromorphic damage extension, we follow the choice of e.g. Forest [2009] or Brepols et al. [2017*b*, 2020] and define it such that

$$\psi_{\bar{d}}(D, \bar{D}, \nabla\bar{D}) := \frac{H}{2}\left(D - \bar{D}\right)^2 + \frac{A}{2}\nabla\bar{D}\cdot\nabla\bar{D}. \tag{4.19}$$

Here, H acts as a penalty parameter to couple the local and non-local damage fields whereas A describes the influence of the non-local damage gradient. With these definitions, the overall model consists of the material parameters as shown in Table 4.1.

Table 4.1: List of all material parameters included in the proposed material model.

Symbol	Units	Description
μ_{eq}	$\mathrm{N/mm^2}$	Elastic shear modulus
κ_{neq}	$\mathrm{N/mm^2}$	Elastic bulk modulus
μ_v	$\mathrm{N/mm^2}$	Viscous shear modulus
κ_v	$\mathrm{N/mm^2}$	Viscous bulk modulus
η_v	$\mathrm{s^{-1}}$	Viscoelastic relaxation velocity
η_d	$\mathrm{s^{-1}}$	Damage evolution velocity
Y_0	$\mathrm{N/mm^2}$	Damage threshold
ε_d	$-$	Damage evolution shape parameter
k	$\mathrm{N/mm^2}$	Linear damage hardening parameter
r	$\mathrm{N/mm^2}$	Voce-type damage hardening parameter 1
s	$-$	Voce-type damage hardening parameter 2
H	$\mathrm{N/mm^2}$	Micromorphic coupling between local an non-local damage fields
A	$\mathrm{N\,mm^2}$	Micromorphic influence of non-local damage gradient

4.4 Algorithmic implementation

For numerical investigations, we implemented the material model at hand into a finite element framework. Within this context, the evolution equations descibed in Section 4.3.2.3 have to be solved in a discrete manner. For this purpose, let us introduce the discrete time increment $\Delta t = t_{n+1} - t_n$, where subscipts $n+1$ and n denote the current and previous timestep, respectively.

In order to find a solution to the viscoelastic evolution equation given in Equation (4.13), we follow the approach of an exponential mapping algorithm as described in detail e.g. in Weber and Anand [1990]; Simo [1992]; Reese and Govindjee [1998]; Dettmer and Reese [2004]; Vladimirov et al. [2008] and Korelc and Stupkiewicz [2014]. To apply this particular integration scheme, we first rewrite Equation (4.13) in terms of the newly introduced second-order tensorial quantities $\mathbf{f}$ and $\mathbf{g}$, i.e.

$$\dot{\mathbf{C}}_v = \underbrace{\frac{\eta_v}{f_d}\mathbf{U}_v\left(\frac{1}{2\mu_v}\operatorname{dev}\left(\tilde{\boldsymbol{\Sigma}}_0\right)+\frac{2}{3\kappa_v}\operatorname{vol}\left(\tilde{\boldsymbol{\Sigma}}_0\right)\right)\mathbf{U}_v}_{\mathbf{f}} = \underbrace{\mathbf{f}\mathbf{C}_v^{-1}}_{\mathbf{g}}\mathbf{C}_v = \mathbf{g}\mathbf{C}_v. \tag{4.20}$$

The exponential map algorithm yields then the viscoelastic evolution law in its discretized form as

$$\mathbf{C}_{v_{n+1}} = \exp\left(\Delta t \mathbf{g}_{n+1}\right)\mathbf{C}_{v_n} \tag{4.21}$$

For notational simplicity, subscripts $n+1$ will be droped in the following. This means that any discrete quantity without subscript is associated with the current time step. Depending on the particular choice of the viscoelastic potential, $\mathbf{g}$ must not necessarrily be symmetric, which yields the implementation of the matrix eponential to be a non-trivial task (see e.g. Moler and van Loan [2003]). Following the argumentations in Dettmer and Reese [2004] and Vladimirov et al. [2008] we simplify the calculation of the matrix exponential by transformation such that

$$\mathbf{U}_{v_n}^{-2} = \mathbf{U}_v^{-1}\exp\left(\Delta t \mathbf{U}_v^{-1}\mathbf{f}\mathbf{U}_v^{-1}\right)\mathbf{U}_v^{-1}. \tag{4.22}$$

Notice that we exploit the identity $\mathbf{C}_v = \mathbf{U}_v^2$ within this relation and subsequently use the symmetric inverse of the viscous stretch tensor $\mathbf{U}_v^{-1}$ as the internal variable to solve for. Further details on this particular choice are ommited here but can be found in detailed manner in the original works by Dettmer and Reese [2004] and Vladimirov et al. [2008].

For the solution of the damage evolution equation given by Equations (4.15) and (4.16), we

apply a standard implicit Euler method which yields the discretized evolution law as

$$D = D_n + \Delta t\, \eta_d \left(\frac{\Phi_d}{Y_0 + q_d} \right)^{\frac{1}{\varepsilon_d}} . \tag{4.23}$$

Since both discrete evolution equations are coupled and highly non-linear in their arguments, we apply a Newton-Raphson iteration scheme in order to solve these equations. For this, we rewrite the evolution laws as a set of coupled residual functions, which reads

$$\begin{aligned} \mathbf{r}_v &= \mathbf{U}_{v_n}^{-2} - \mathbf{U}_v^{-1} \exp\left(\Delta t \mathbf{U}_v^{-1} \mathbf{f} \mathbf{U}_v^{-1} \right) \mathbf{U}_v^{-1} = \mathbf{0} \\ r_d &= D - D_n - \Delta t\, \eta_d \left(\frac{\Phi_d}{Y_0 + q_d} \right)^{\frac{1}{\varepsilon_d}} = 0. \end{aligned} \tag{4.24}$$

Due to the symmetry of $\mathbf{U}_v^{-1}$, we can transform it together with the residual function $\mathbf{r}_v$ into Voigt notation, which yields the residual vector $\mathbf{r} := [\hat{\mathbf{r}}_v, r_d]^T$ alongside the vector of arguments $\mathbf{x} := [\hat{\mathbf{U}}_v^{-1}, D]^T$. Here, $\hat{(\bullet)}$ denotes the Voigt notation of the tensorial quantity at hand. The increment $\Delta\mathbf{x} = [\Delta\hat{\mathbf{U}}_v^{-1}, \Delta D]^T$ used in the iteration process can be found by solving the linearized system of equations that is given by $\mathbf{J}_1 \Delta\mathbf{x} = -\mathbf{r}$. Herein, the jacobian $\mathbf{J}_1$ is explicitly given in terms of the partial derivatives of the residual vector with respect to the vector of arguments, i.e.

$$\mathbf{J}_1 = \begin{bmatrix} \frac{\partial \hat{\mathbf{r}}_v}{\partial \hat{\mathbf{U}}_v^{-1}} & \frac{\partial \hat{\mathbf{r}}_v}{\partial D} \\ \frac{\partial r_d}{\partial \hat{\mathbf{U}}_v^{-1}} & \frac{\partial r_d}{\partial D} \end{bmatrix} . \tag{4.25}$$

During the solution process, the current state of $\mathbf{x}$ is updated such that $\mathbf{x}_{k+1} = \mathbf{x}_k + \Delta\mathbf{x}$, where $k+1$ and k denote the current and previous iteration step, respectively. It is important to mention that the partial derivatives used for the computation of $\mathbf{J}_1$ are not computed analytically by hand but rather automatically by means of algorithmic differentiation. For this, we used the commercial software package *AceGen* (see e.g. Korelc [2002, 2009]).

Within the global iteration scheme of the finite element method used in this contribution, the material tangent operators $\partial\mathbf{S}/\partial\mathbf{E}$, $\partial\mathbf{S}/\partial\bar{D}$ and $\partial D/\partial\mathbf{E}$ are being used. Since these material tangents implicitly depend on the local material response, we must derive those quantities in an algorithmically consistent manner in order to ensure the best possible convergence behaviour of our global iteration scheme, i.e.

$$\frac{\partial \mathbf{S}}{\partial \mathbf{E}} = 2 \left(\frac{\partial \mathbf{S}}{\partial \mathbf{C}} + \frac{\partial \mathbf{S}}{\partial \mathbf{U}_v^{-1}} : \frac{\partial \mathbf{U}_v^{-1}}{\partial \mathbf{C}} + \frac{\partial \mathbf{S}}{\partial D} \otimes \frac{\partial D}{\partial \mathbf{C}} \right) \tag{4.26}$$

$$\frac{\partial \mathbf{S}}{\partial \bar{D}} = \frac{\partial \mathbf{S}}{\partial \mathbf{U}_v^{-1}} : \frac{\partial \mathbf{U}_v^{-1}}{\partial \bar{D}} + \frac{\partial \mathbf{S}}{\partial D} : \frac{\partial D}{\partial \bar{D}}, \quad \text{and} \quad \frac{\partial D}{\partial \mathbf{E}} = 2\,\frac{\partial D}{\partial \mathbf{C}}. \tag{4.27}$$

The green partial derivatives can be calculated directly from the introduced quantities by means of algorithmic differentiation. For the calculation of the red partial derivatives we introduce $\mathbf{y} = [\hat{\mathbf{C}}, \bar{D}]$ with $\hat{\mathbf{C}}$ being the Voigt-notation of the right Cauchy-Green tensor. By calculating $\mathbf{J}_2 = \partial \mathbf{r}/\partial \mathbf{y}$ we can make use of the chain rule and find the following relation, i.e.

$$\mathbf{J}_3 := \frac{\partial \mathbf{x}}{\partial \mathbf{y}} = -\mathbf{J}_1^{-1}\mathbf{J}_2 = \begin{bmatrix} \frac{\partial \hat{\mathbf{U}}_v^{-1}}{\partial \hat{\mathbf{C}}} & \frac{\partial \hat{\mathbf{U}}_v^{-1}}{\partial \bar{D}} \\ \frac{\partial D}{\partial \hat{\mathbf{C}}} & \frac{\partial D}{\partial \bar{D}} \end{bmatrix}. \tag{4.28}$$

It is important to notice that $\mathbf{J}_1$ and $\mathbf{J}_2$ are computed from the fully converged solution of the local Newton iteration scheme. The partial derivatives needed for the calculation of the material tangent operator are now directly given as the submatrices of $\mathbf{J}_3$. An overview on the overall algorithm of the local material model is given as pseudo-code in Figure 4.2.

4.5 Numerical examples

Within the following section, we present selected numerical examples to examine and discuss various aspects of the rate-dependent model introduced above. We start with a general parameter study for the purely viscoelastic, the pure rate-dependent damage model as well as the combined model. Here, we show the influence of the given material parameters, investigate the differences of the individual approaches and elaborate on the limiting cases for each of these models. Next, we show structural examples of a uniaxially loaded double notched specimen as well as clamped cylindrical test specimen. For the simulations shown below, the model was implemented into the general purpose finite element software package *FEAP* (see Taylor and Govindjee [2020]). For meshing and visualization, we used the open source software tools *GMSH* (see Geuzaine and Remacle [2009]) and *Paraview* (see Ahrens et al. [2005]).

4.5.1 Parameter studies

For the following studies, we use the simulation of a uniaxially loaded single element and vary the individual material parameters of the model according to the investigations at hand. For the viscoelastic material response, we choose an elastic Neo-Hookean ground model (see Equation (4.17)) with the same parameters for both, the equlibrium and the non-equilibrium part of the Helmholtz free energy given in Equation (4.6). These are given by $\mu_* = 6.0\ \frac{\mathrm{N}}{\mathrm{mm}^2}$ and $\kappa_* = 300.0\ \frac{\mathrm{N}}{\mathrm{mm}^2}$. The damage evolution shape parameter is set to $\varepsilon_d = 1$ for the following

Time-dependent viscoelastic damage model routine

Input: $\hat{\mathbf{C}}$, $\bar{D}$, $\hat{\mathbf{U}}_{v_n}^{-1}$, D_n
Output: $\hat{\mathbf{S}}$, $\hat{\mathbf{U}}_v^{-1}$, D, $\frac{\partial \hat{\mathbf{S}}}{\partial \hat{\mathbf{E}}}$, $\frac{\partial \hat{\mathbf{S}}}{\partial \bar{D}}$, $\frac{\partial D}{\partial \hat{\mathbf{E}}}$, $\frac{\partial D}{\partial \bar{D}}$

$\hat{\mathbf{U}}_v^{-1} \leftarrow \hat{\mathbf{U}}_{v_n}^{-1}$, $D \leftarrow D_n$
$\Delta\lambda_d \leftarrow 0$
$\Phi_d \leftarrow$ getPhiD()

if $\Phi_d \leq 0$ **then**
  `// Enforce purely viscoelastic step without damage`
  $\eta_d \leftarrow 0$
end if
`// Solve local Newton iteration`
$\left\{\hat{\mathbf{U}}_v^{-1}, D, \mathbf{J}_1, \mathbf{J}_2\right\} \leftarrow$ doLocalNewtonRaphsonIteration()
$\mathbf{J}_3 \leftarrow -\mathbf{J}_1^{-1}\,\mathbf{J}_2$
$\frac{\partial \hat{\mathbf{U}}_v^{-1}}{\partial \hat{\mathbf{C}}} \leftarrow \mathbf{J}_3$[1:6, 1:6]
$\frac{\partial \hat{\mathbf{U}}_v^{-1}}{\partial \bar{D}} \leftarrow \mathbf{J}_3$[1:6, 7]
$\frac{\partial D}{\partial \hat{\mathbf{C}}} \leftarrow \mathbf{J}_3$[7, 1:6]
$\frac{\partial D}{\partial \bar{D}} \leftarrow \mathbf{J}_3$[7, 7]
$\left\{\hat{\mathbf{S}}, \frac{\partial \hat{\mathbf{S}}}{\partial \hat{\mathbf{C}}}, \frac{\partial \hat{\mathbf{S}}}{\partial \hat{\mathbf{U}}_v^{-1}}, \frac{\partial \hat{\mathbf{S}}}{\partial D}\right\} \leftarrow$ getPK2andPartialTangents()
$\frac{\partial \hat{\mathbf{S}}}{\partial \hat{\mathbf{E}}} \leftarrow 2\left(\frac{\partial \hat{\mathbf{S}}}{\partial \hat{\mathbf{C}}} + \frac{\partial \hat{\mathbf{S}}}{\partial \hat{\mathbf{U}}_v^{-1}}\frac{\partial \hat{\mathbf{U}}_v^{-1}}{\partial \hat{\mathbf{C}}} + \frac{\partial \hat{\mathbf{S}}}{\partial D}\frac{\partial D}{\partial \hat{\mathbf{C}}}\right)$
$\frac{\partial \hat{\mathbf{S}}}{\partial \bar{D}} \leftarrow \frac{\partial \hat{\mathbf{S}}}{\partial \hat{\mathbf{U}}_v^{-1}}\frac{\partial \hat{\mathbf{U}}_v^{-1}}{\partial \bar{D}} + \frac{\partial \hat{\mathbf{S}}}{\partial D}\frac{\partial D}{\partial \bar{D}}$
$\frac{\partial D}{\partial \hat{\mathbf{E}}} \leftarrow 2\frac{\partial D}{\partial \hat{\mathbf{C}}}$

Figure 4.2: Pseudo-code for the implementation of the material model at integration point level. Quantities given in Voigt notation are denoted by $\hat{(\bullet)}$. The local Newton iteration as well as the calculation of the second Piola-Kirchhoff stress tensor and its partial derivatives is performed using custom *AceGen* implementations.

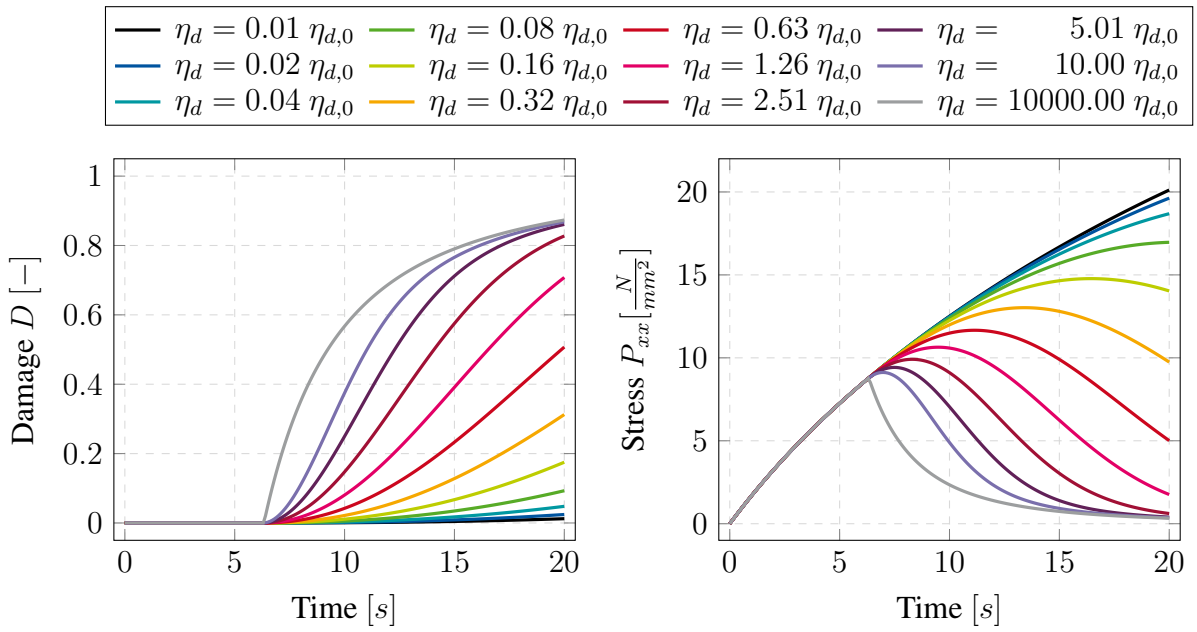

(a) Evolution of damage variable D.

(b) Evolution of stress in loading direction.

Figure 4.3: Results of a constant deformation rate applied uniaxially to a single element for pure rate-dependent damage, i.e. $\eta_v = 0$. The influence of the damage relaxation velocity η_d with reference $\eta_{d,0} = 10^{-2}$ s^{-1} is shown. Stress is given as the first Piola-Kirchhoff stress $\mathbf{P}$ evaluated in loading direction.

investigations. Since this study is based on the simulation of a single finite element, the micromorphic parameters A and H are set to zero and do not play any role within this investigation.

4.5.1.1 Constant deformation rate

In the first example, we study the influence of the damage relaxation velocity η_d on the temporal evolution of the damage variable D. For this, we apply a constant deformation rate of $\dot{u}_x = 0.5\ \frac{\text{mm}}{\text{s}}$ to the uniaxially loaded specimen and focus only on the temporal damage response, i.e. the viscous relaxation time is set to $\eta_v = 0\ \text{s}^{-1}$. The damage threshold for this simulation is set to $Y_0 = 3.0\ \frac{\text{N}}{\text{mm}^2}$ and damage hardening is turned off by setting $k = r = 0\ \frac{\text{N}}{\text{mm}^2}$. Figure 4.3 shows the evolution of both, the damage variable D and the first Piola-Kirchhoff stress in loading direction P_{11} for variations of η_d. First, we take a look at the edge cases, i.e. very low and very high values for η_d, respectively. In the first case, the damage progression observed during the simulation is almost negligible. This leads approximately to a purely elastic stress response. For very high values of the damage relaxation velocity the response approaches

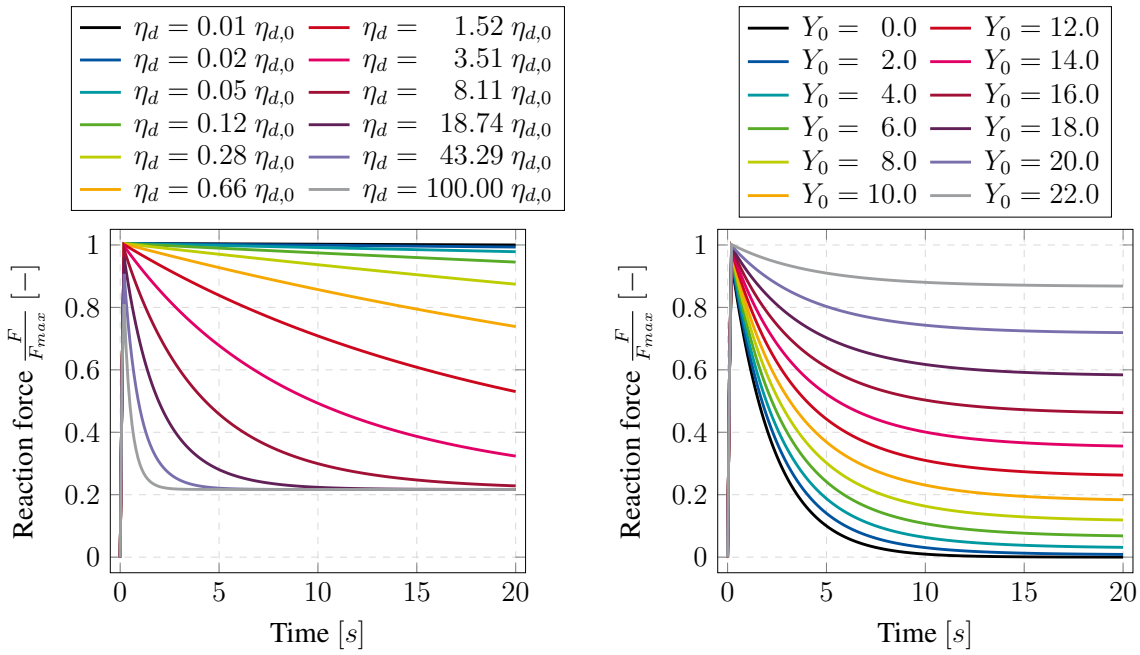

(a) Influence of damage relaxation velocity η_d.

(b) Influence of damage threshold Y_0.

Figure 4.4: Results of relaxation experiment applied uniaxially to a single element for pure rate-dependent damage, i.e. $\eta_v = 0\ \mathrm{s}^{-1}$. Left: Influence of damage relaxation velocity η_d with reference $\eta_{d,0} = 10^{-3}\ \mathrm{s}^{-1}$. Right: Influence of damage threshold Y_0. Here, a damage velocity of $\eta_d = 0.01\ \mathrm{s}^{-1}$ is chosen. The reaction force is normalized with respect to $F_{max} = 20.52$ N.

the well-investigated rate-independent isotropic damage formulation. Choices of η_d which lie in-between are able to interpolate smoothly between these edge cases. This examples clearly shows how the approach to model rate-dependent damage behaviour is a generalized version of the classical rate-independent modelling approach, thus giving the simulations much more flexibility.

4.5.1.2 Relaxation

Next, we take a look at the simulation of a one-dimensional relaxation experiment. For this, we apply a constant displacement $u_x = 1$ mm almost instantaneously and hold it fixed over the remainder of the simulation. The damage threshold for this simulation is set to $Y_0 = 11.0\ \left[\frac{\mathrm{N}}{\mathrm{mm}^2}\right]$. Similar to the simulation above, damage hardening is again ommited for the sake of simplicity.

Figure 4.4 shows the influence of both the damage relaxation velocity η_d and the damage threshold Y_0 on the reaction force over time for a purely rate-dependent damage model, i.e.

$\eta_v = 0$ s^{-1}. Similar to the example of a constant deformation rate from Section 4.5.1, the damage relaxation velocity determines how fast damage is accumulated within the material. Since the damage threshold Y_0 is held constant during the simulation shown in Figure 4.4a, the reaction force is not going down to zero but rather converges to a residual value. This limit state is ultimately reached for all non-zero choices of η_d and reflects the same state a rate-independent model would reach instantaneously rather than over time. This influence of the damage threshold on the residual value of the reaction force can further be studied in Figure 4.4b, where it is obvious that lower values lead to more damage being accumulated over time. At first glance, this behaviour might seem counterintuitive, but on closer inspection it is easy to explain. As damage progresses, the thermodynamic driving force Y given by Equation (4.10) also decreases steadily until it falls below the damage threshold Y_0, yielding the damage function to be $\Phi_d \leq 0$. This causes the damage process to gradually come to a standstill. The lower the threshold is selected, the longer the damage function is greater than zero, which leads to a continuation of the corresponding damage process. In the classical rate-independent damage formulation, this behaviour is of course not observed, since damage always occurs instantaneously in such a way that $\Phi_d = 0$ is directly given rather than approached over a finite period of time. The attentive reader will have noticed that the initial peak in the reaction force varies in height between the individual curves. This effect is very clearly visible in Figure 4.4a. The reaction force shown at this point takes on lower values for very high values of η_d than for low values of η_d. This is due to the fact that a high damage velocity already leads to damage accumulation during load application.

From the observations that can be made in Figure 4.4, the question arises as to how far this behaviour differs from pure viscoelastic behaviour. This difference can be seen in Figure 4.5. Here, after $t = 50$s, an additional jump in the displacement of the system was applied, which was kept constant until the end of the simulation. Whilst Figure 4.5a shows the purely viscoelastic response (i.e. $\eta_d = 0$), Figure 4.5b shows the pure rate-dependent damage response (i.e. $\eta_v = 0$). In both figures, a jump in displacement results in a jump in reaction force. After that, the purely viscoelastic model converges as expected towards a residual force that is higher than that of the previous displacement state, while the behaviour of the rate-dependent damage model is exactly the opposite. This behaviour can be explained if one takes into account that the additional displacement applied also introduces more elastic energy into the system, which increases the thermodynamic driving force Y and subsequently triggers the damage process more strongly than before.

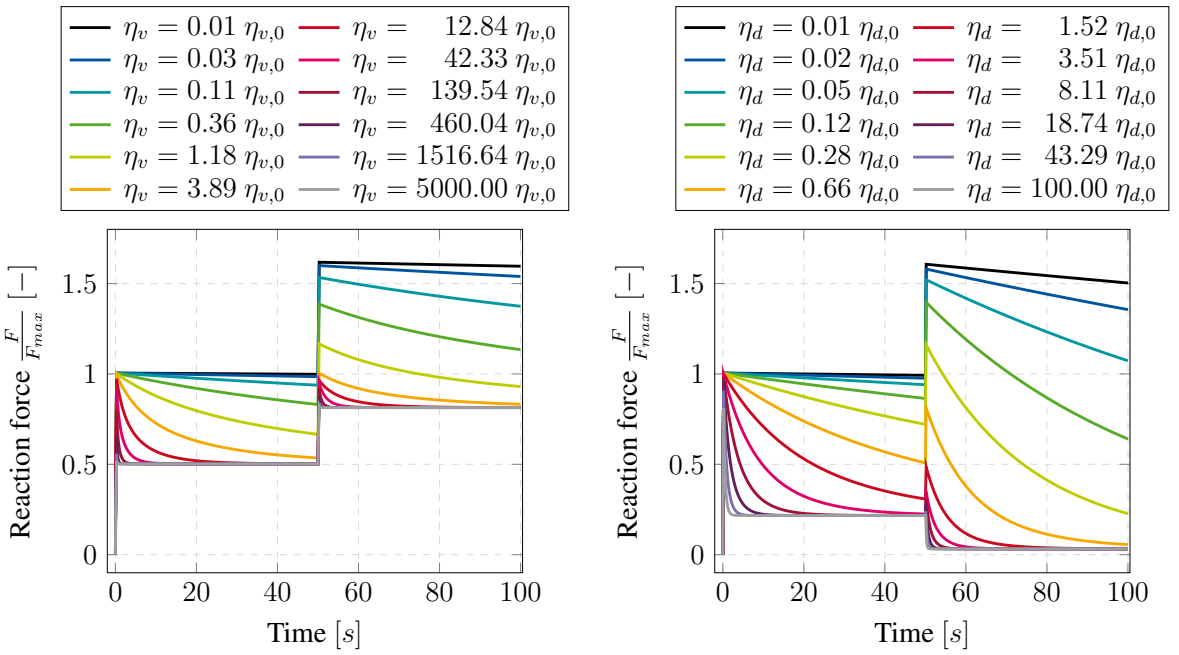

(a) Influence of viscous relaxation velocity η_v without damage, i.e. $\eta_d = 0\ \mathrm{s}^{-1}$.

(b) Influence of damage relaxation velocity η_d for pure rate-dependent damage, i.e. $\eta_v = 0\ \mathrm{s}^{-1}$.

Figure 4.5: Results of relaxation experiment with stepwise loading applied uniaxially to a single element. Left: Influence of viscous relaxation velocity η_v with reference $\eta_{v,0} = 10^{-2}\ \mathrm{s}^{-1}$. The damage velocity is set to $\eta_d = 0\ \mathrm{s}^{-1}$. Right: Influence of damage relaxation velocity η_d with reference $\eta_{d,0} = 10^{-3}\ \mathrm{s}^{-1}$. The relaxation velocity is set to $\eta_v = 0\ \mathrm{s}^{-1}$. The reaction forces are normalized with respect to $F_{max} = 20.52\ \mathrm{N}$.

4.5.1.3 Creep

Within the next study, we investigate the material response using the simulation of a one-dimensional creep experiment. We apply a constant force $F_x = 6.4\ \mathrm{N}$ at the beginning of the experiment and hold it fixed in the following. The damage threshold is set to $Y_0 = 11.0\ \left[\frac{\mathrm{N}}{\mathrm{mm}^2}\right]$ and damage hardening is again ommited. It is important to notice that for this creep simulation the relation between F_x and Y_0 is very important. If the loading force is too compared to the damage threshold, no damage is triggered and only a purely viscoelastic response will be observed. In this context, the differences between the purely viscoelastic model and the purely rate-dependent damage model are particularly interesting. As shown in Figure 4.6, we again observe nearly perfect elastic behaviour for very low choices of the corresponding relaxation velocities η_d and η_v, respectively. In contrast to that, we can see a clearly different progression of the displacement for higher choices of the relaxation velocities. Whilst the

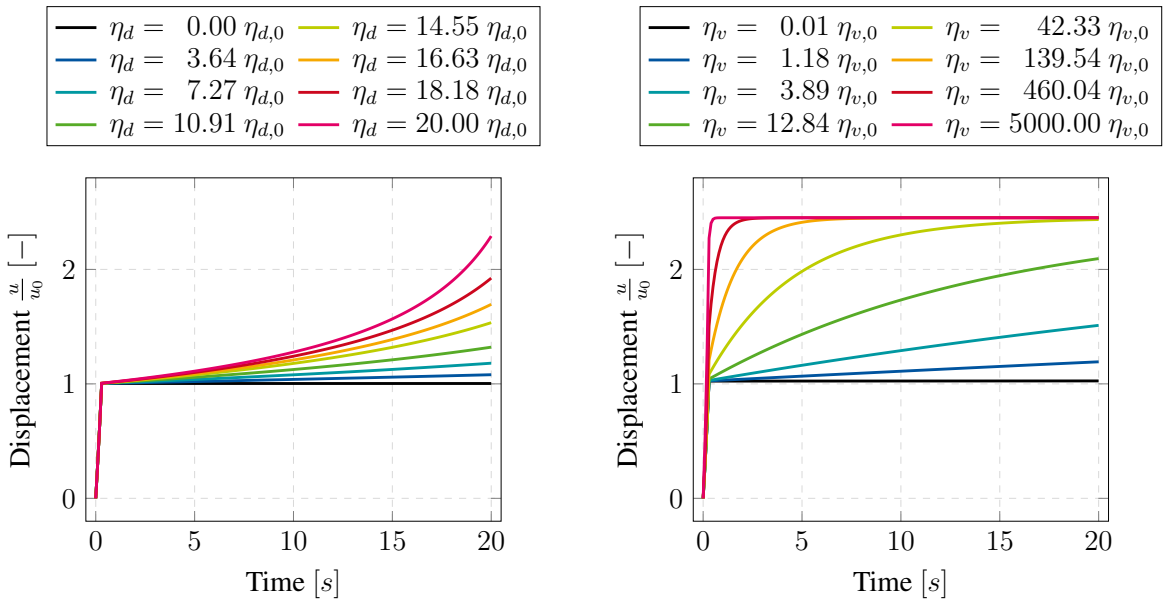

(a) Influence of damage relaxation velocity η_d for pure rate-dependent damage, i.e. $\eta_v = 0\ \mathrm{s}^{-1}$.

(b) Influence of viscous relaxation velocity η_v for pure viscoelasticity, i.e. $\eta_d = 0\ \mathrm{s}^{-1}$.

Figure 4.6: Results of creep experiment applied uniaxially to a single element. Left: Influence of damage relaxation velocity η_d with reference $\eta_{d,0} = 10^{-3}\ \mathrm{s}^{-1}$. The relaxation velocity is set to $\eta_v = 0\ \mathrm{s}^{-1}$. Right: Influence of viscous relaxation velocity η_v with reference $\eta_{v,0} = 10^{-2}\ \mathrm{s}^{-1}$. The damage velocity is set to $\eta_d = 0\ \mathrm{s}^{-1}$. The displacement is normalized with respect to $u_0 = 0.125$ mm.

results of the viscoelastic model converge towards a finite value, the displacements for the purely rate-dependent damage model grow exponentially. These observations are in line with what one would expect from a damage creep experiment (see Section 4.5.3). In contrast to this, the classical rate-independent damage formulation is usually not able to describe such kind of behaviour, since damage is instantaneously accumulated once the damage threshold Y_0 is reached. This effect becomes obvious when taking a look at the response of the combined viscoelastic rate-dependent damage model as shown in Figure 4.7 (i.e. $\eta_v \neq 0\ \mathrm{s}^{-1}, \eta_d \neq 0\ \mathrm{s}^{-1}$). Since the given model includes the rate-independent case for very high values of η_d, we are able to approximate this behaviour and show that this leads to an almost instantaneous accumulation of full damage within the material. The computation of a delayed evolution of damage as seen in experimental observations (see Section 4.5.3) is therefore not possible with a rate-independent approach. Within this example, the rate-dependent damage model is able to capture the distinct bahviour of creep damage in a qualitative manner.

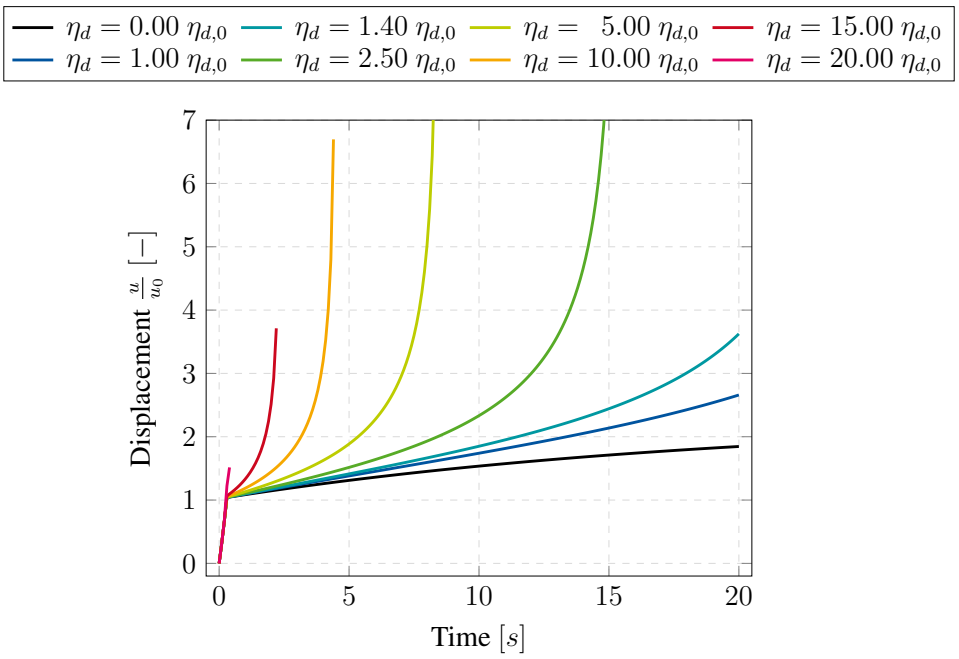

Figure 4.7: Results of creep experiment for the combined viscoelastic rate-dependent damage model. Influence of damage relaxation velocity η_d with reference $\eta_{d,0} = 10^{-2}\ \mathrm{s}^{-1}$. Here, the relaxation velocity is set to $\eta_v = 0\ \mathrm{s}^{-1}$.

4.5.1.4 Cyclic loading

In the last example of this section, we evaluate the behaviour of the given material model for cyclic loading as shown in Figure 4.8a. The rate of displacement $\dot{u}_x = 0.06\ \frac{\mathrm{mm}}{\mathrm{s}}$ is constant for all loading cycles. For this evaluation, we compare the response of the purely viscoelastic model (i.e. $\eta_d = 0\ \mathrm{s}^{-1}$) with results from both, the purely rate-dependent damage model (i.e. $\eta_v = 0\ \mathrm{s}^{-1}$) as well as the combined viscoelastic model for rate-dependent damage (i.e. $\eta_v \neq 0\ \mathrm{s}^{-1}$, $\eta_d \neq 0\ \mathrm{s}^{-1}$). Here, we use a damage threshold of $Y_0 = 2.5\ \frac{\mathrm{N}}{\mathrm{mm}^2}$ and again ommit damage hardening. If not set to zero, the viscoelastic relaxation time and the damage velocity are chosen to $\eta_v = 1.7\ \mathrm{s}^{-1}$ and $\eta_d = 0.01\ \mathrm{s}^{-1}$, respectively. Figures 4.8c and 4.8d show the corresponding material response for either the pure rate-dependent damage model (i.e. $\eta_v = 0\ \mathrm{s}^{-1}$) or the pure viscoelastic response (i.e. $\eta_d = 0\ \mathrm{s}^{-1}$). It is obvious that the stress-strain curves differ from each other both qualitatively and quantitatively. As expected, a corresponding hysteresis occurs in the case of pure viscoelasticity. With further loading, the material then returns to the same path as with a non-cyclic load. Furthermore, a residual viscous strain can be observed upon unloading. In the pure damage model, it can be seen that no damage occurs during the first loading cycle and thus a purely elastic material behaviour is

present. This is due to the fact that the damage threshold Y_0 for the load applied here has not yet been exceeded. As expected, a gradual stiffness reduction due to the accumulated damage can be observed for the further load cycles. Furthermore, there is no residual elongation when the load is removed. Figure 4.8b shows the response for a combined model with the velocities $\eta_d = 0.01\ \mathrm{s}^{-1}$ and $\eta_v = 1.7\ \mathrm{s}^{-1}$. Within the first two loading cycles, the model resembles the response of the pure viscoelastic material response whereas it is much closer to the pure damage response within the third cycle. This behaviour makes sense because no damage occurs in the first load cycle and damage develops slowly in the second cycle due to the low damage velocity η_d. Thus, the viscoelastic material behaviour dominates. In the third load cycle, however, the damage accumulation is now so significant that it becomes the predominant effect.

4.5.2 Structural example

In the following, we show a structural example of a double notched specimen (see Figure 4.9) subjected to a relaxation experiment using the combined viscoelastic rate-dependent damage model described above. For this investigation, we used the same bulk and shear moduli as in the examples above, namely $\mu_* = 6.0\ \frac{\mathrm{N}}{\mathrm{mm}^2}$ and $\kappa_* = 300.0\ \frac{\mathrm{N}}{\mathrm{mm}^2}$. The relaxation velocity is set to $\eta_v = 0.055\ \mathrm{s}^{-1}$ while the damage velocity is choosen to be $\eta_d = 0.002\ \mathrm{s}^{-1}$. For the damage threshold we use $Y_0 = 1.0\ \frac{\mathrm{N}}{\mathrm{mm}^2}$ whilst damage hardening is not activated here. The damage evolution shape parameter is set to $\varepsilon_d = 1.0$. Since we are now dealing with structural simulations containing multiple elements, we need to also consider the micromorphic extension and therefore the material parameters $A = 50.0$ N and $H = 10^5\ \frac{\mathrm{N}}{\mathrm{mm}^2}$. For the relaxation simulation, a displacement of $u_x = 15$ mm is applied within the first few seconds and then held fixed for the duration of the simulation. The notches located in the middle of the specimen are introduced to enforce this particular spot as the predeterminded point of damage initialization and failure. We therefore locally refined the mesh density within this area. Two examples of meshes with different element sizes are shown in Figure 4.9. By exposing symmetric boundary conditions, we are able to consider only a quarter of the full structure.

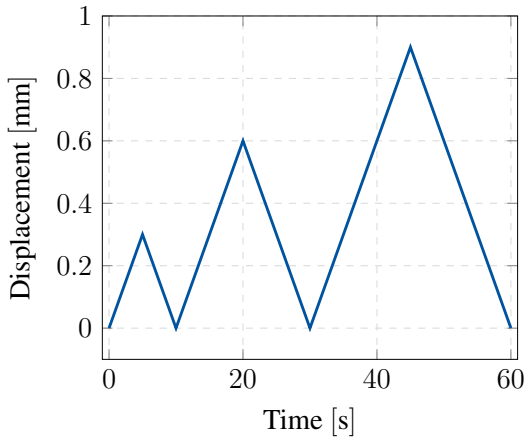

(a) Cyclic loading regime.

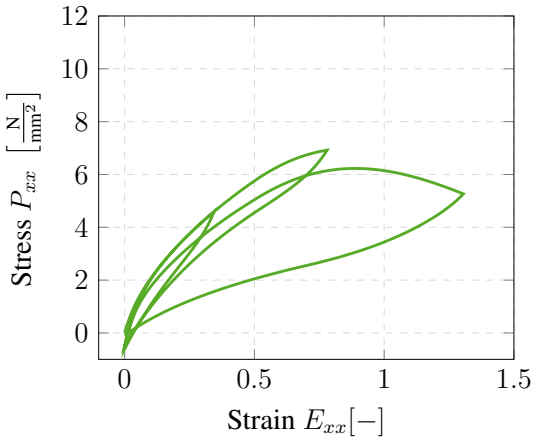

(b) Combined model, i.e. $\eta_d \neq 0\ \mathrm{s}^{-1}, \eta_v \neq 0\ \mathrm{s}^{-1}$.

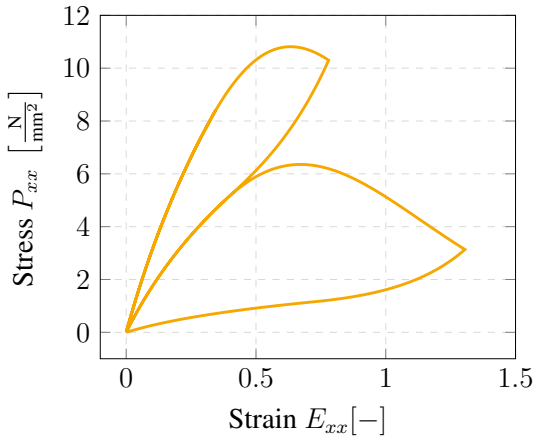

(c) Rate-dep. damage model, i.e. $\eta_v = 0\ \mathrm{s}^{-1}$.

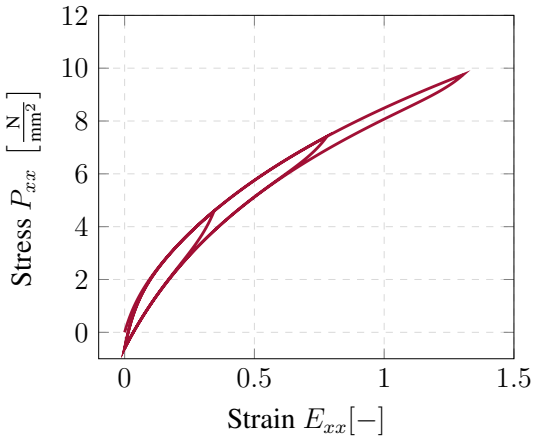

(d) Viscoelastic model, i.e. $\eta_d = 0\ \mathrm{s}^{-1}$.

Figure 4.8: Results of the simulation of a cyclic loading experiment applied uniaxially to a single element with material parameters $\eta_d = 0.01\ \mathrm{s}^{-1}$ and $\eta_v = 1.7\ \mathrm{s}^{-1}$. 4.8a) The cyclic loading process used in this simulation. 4.8b) Stress-strain response for the combined viscoelastic rate-dependent damage model. 4.8c) Stress-strain response for the purely rate-dependent damage model. 4.8d) Stress-strain response for the purely viscoelastic model. The stress in loading direction is given as the corresponding first Piola-Kirchhoff stress component.

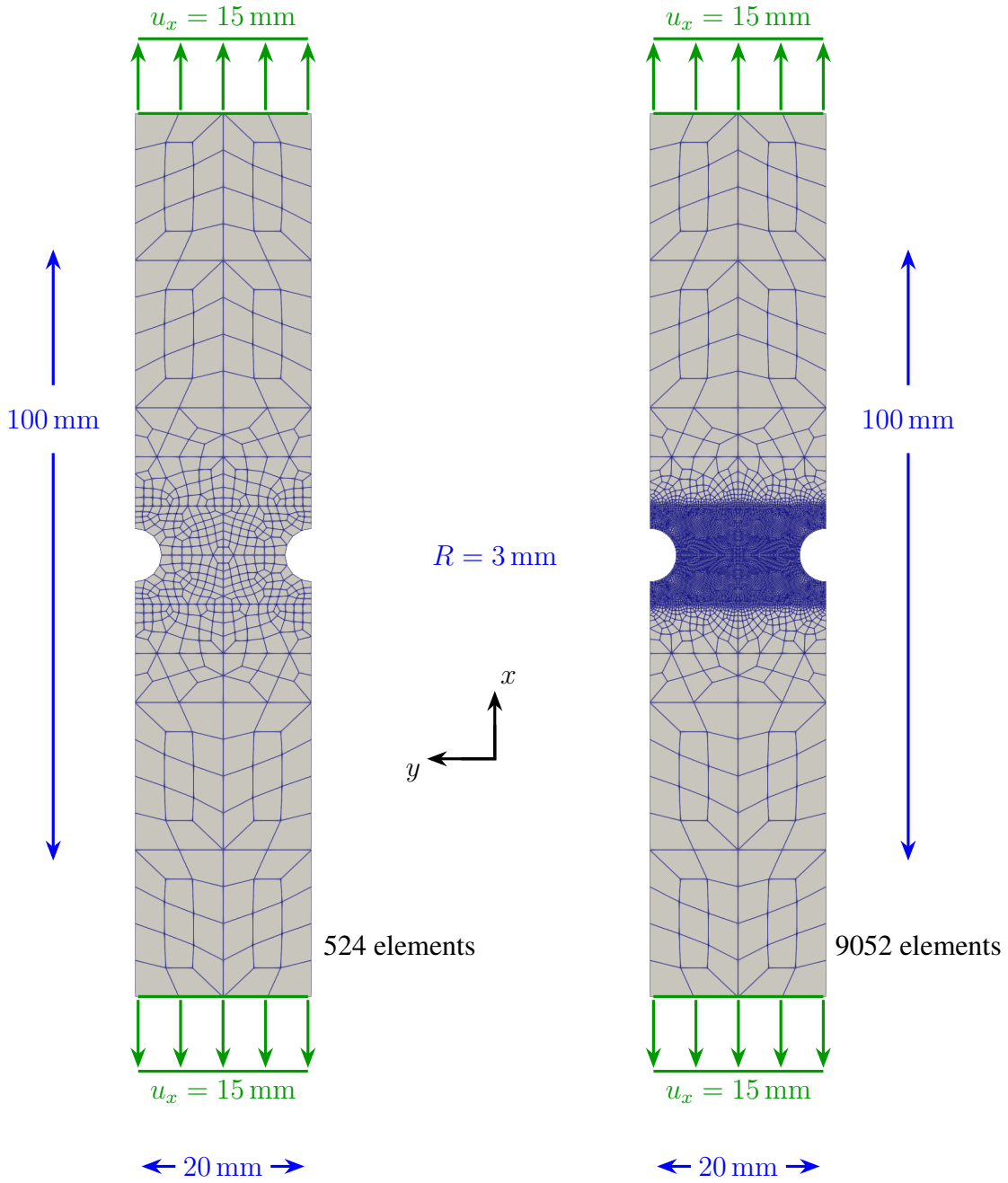

Figure 4.9: Two different discretizations for the model of a uniaxially loaded double notched specimen of thickness $t = 1\ mm$. For the simulation, only a quarter of the full structure is used by exposing symmetric boundary conditions.

Figure 4.10 shows the convergence behaviour of the solution to this problem given in terms of a diagram of the reaction forces. Here we evaluated different mesh sizes from really coarse with 524 elements to a relatively fine spatial discretization with 36316 elements. In the first area of the simulation, the curves lie exactly on top of each other. Similar to the example of cyclic

loading from the previous section, the viscoelastic material behaviour forms the predominant effect here. However, this does not seem to be particularly sensitive to the spatial discretisation. Only from about 40 seconds onwards does the cluster of curves fan out and converge for finer discretisations.

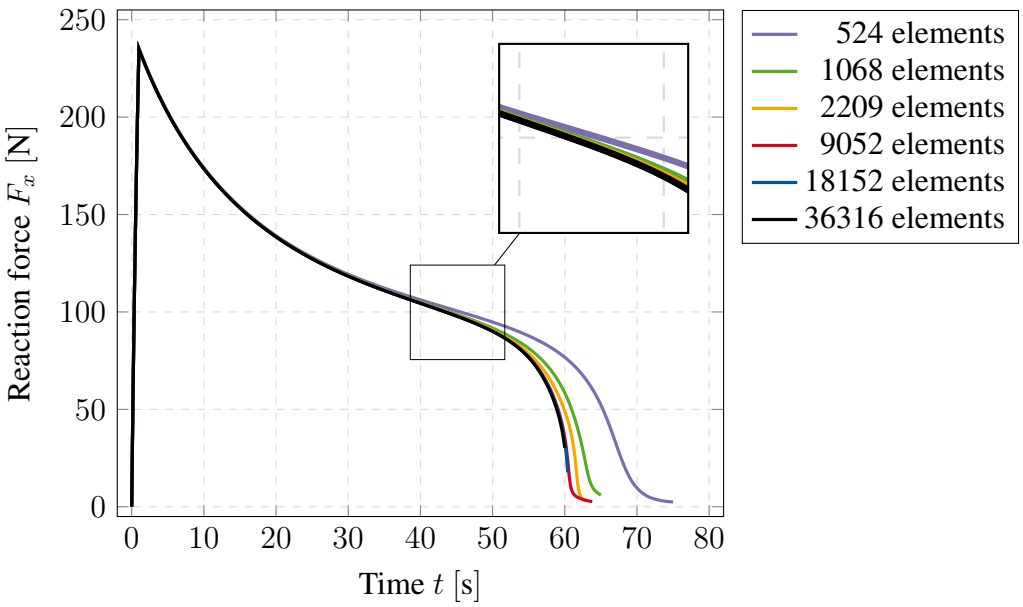

Figure 4.10: Reaction force over time for various mesh refinements of the uniaxially loaded double notched specimen given in Figure 4.9. Finer mesh discretizations yield successive convergence towards the unique solution.

The local distribution of the damage field for various snapshots in time is shown in Figure 4.11. Here, only the middle part of the specimen is shown, since this is the region where the damage response is triggered due to the imperfection associated with the double notch. Although the displacement is held constant, the evolution of damage starts slowly from the inner edges of the notches and gradually evolves from there over time. This distinct feature of the rate-dependent damage model is clearly visible here. Also the amount of accumulated damage within the structure correlates with the observations from the reaction force diagram, since the initialization of a crack is located roughly in the time period where the mesh sensitivity starts to occur. This observation is in line with what is already well known from the literature on rate-independent damage modelling.

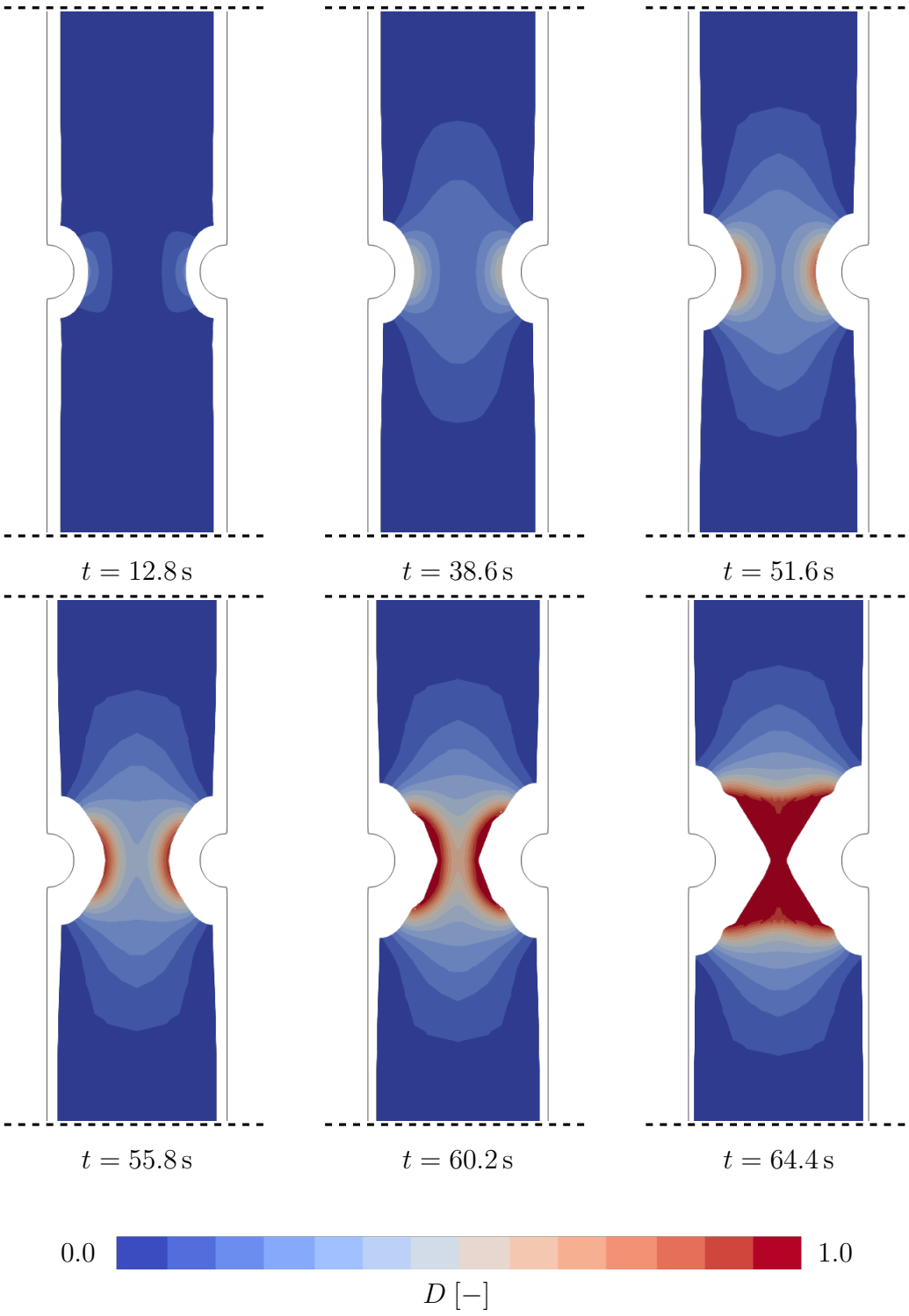

Figure 4.11: Contour plot of damage progression for uniaxially loaded double notched specimen subjected to the simulation of a relaxation experiment. Outlines of the initial geometry before loading is denoted by black solid lines. Only the middle part of the specimen is shown in order to give a closer look at the spatial domain of interest.

4.5.3 Comparison with experimental data

To demonstrate some of the models predictive capabilities, we conducted both, uniaxial relaxation and creep experiments. Based on these, we used one relaxation experiment to calibrate the material parameters of the elastic and viscoelastic domain. Next, we applied the parameter set found in the previous step to both, another relaxation experiment as well as the unixial creep problem. It is clear that this procedure is not comparable with a complete validation of the model. To achieve this, further experimental investigations would have to be used. For example, cyclic tests or montone tests at different strain rates could be considered. Due to the limited data basis on which we carry out this comparison, we would like to explicitly point out at this point that the following investigations only represent a first comparison of the predictive capability of the model with corresponding experimental data.

4.5.3.1 Experimental setup

For the experimental setup we choose the silicone-based adhesive *Koediglaze S* from *HB Fuller / Koemmerling* for the production of the test specimen. During production we stick to the specifications given in DIN [2012] for both, geometry and production protocol. More precisely, we select geometry type 1B according to section 6 of the given standard as the geometry for the test specimen. Figure 4.12b shows a schematic drawing of the geometry at hand. We chose a *Z100* testing device manufactured by *Zwick / Roell*. A picture of the testing setup is shown in Figure 4.12a. In both the creep test and the relaxation test, we apply a constant strain rate of 1.0 per minute until the desired target state of strain or stress is reached. In total, we apply two different loading scenarios within the relaxation experiment. In the first one, we choose a constant technical target strain of 0.75, whereas for the second one we set the target strain to 1.2. In the creep test we select the target condition corresponding to a constant technical stress of 1.5 MPa. Once reached, we keep the target state constant for the rest of the experiment. In the relaxation test, this is done for 4000 s. For the creep test, the maximum duration is 1300 s. Both, relaxation and creep experiments are repeated two times.

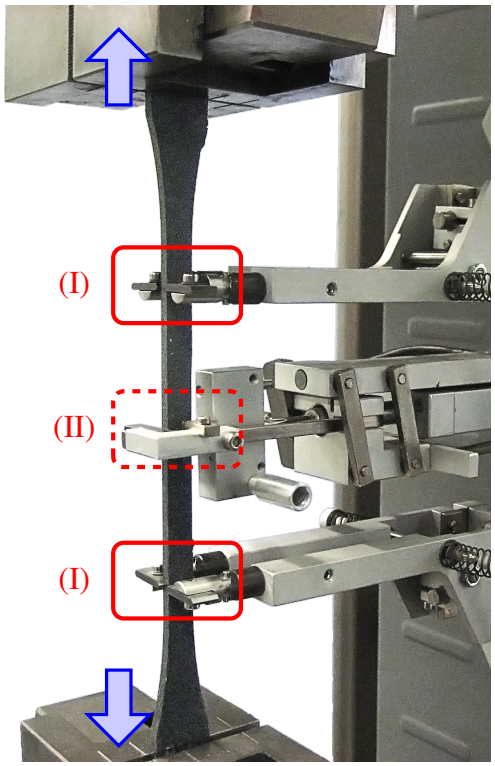

(a) Blue arrows denote the loading direction for the uniaxial loading applied during testing. (I) Elongation measuring system. (II) Thickness measuring system.

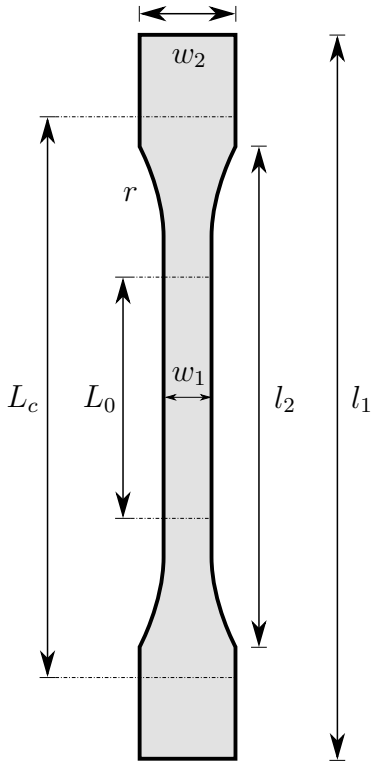

(b) Total length $l_1 = 150$ mm, inner length $l_1 = 108$ mm, outer width $w_2 = 10$ mm, inner width $w_1 = 20$ mm, clamping distance $L_c = 115$ mm, measurement distance $L_0 = 50$ mm, radius $r = 60$ mm, thickness $t = 4$ mm.

Figure 4.12: Setup for validation experiments as described in Section 4.5.3.1. Figure 4.12a: Setup of the test specimen within the testing device. Figure 4.12b: Geometrical specifications of test specimen according to standard DIN [2012] with geometry type 1B.

4.5.3.2 Comparison of numerical and experimental results

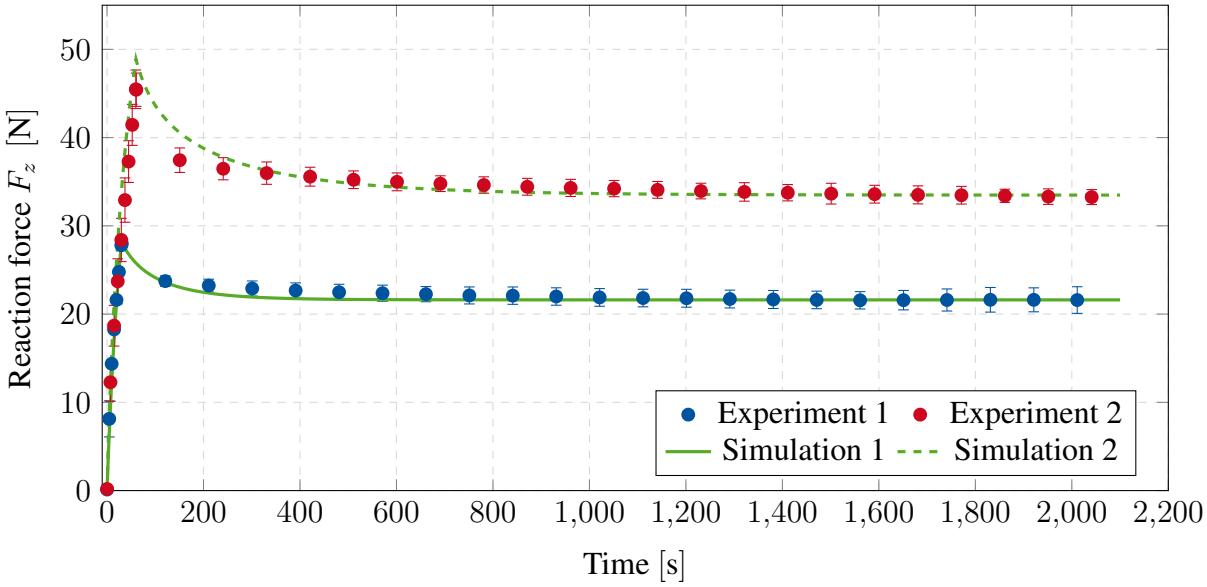

Figure 4.13: Results from two different uniaxially loaded relaxation experiments and simulations, respectively. Comparison of the reaction forces in loading direction. Experimental results are given as mean values. Errorbars show the standard mean error (SEM) of the experimental results. Material parameters were fitted for the Exp. 1 curve.

To adjust the parameters of the model for the comparison with experimental data presented here, we used a two-step approach. In a first step, the material parameters associated with the elastic or viscoelastic material behaviour were adjusted. For this purpose, we used the optimisation algorithm according to Levenberg [1944] and Marquardt [1963] in its implementation in the open source library SciPy (see Virtanen et al. [2020]). In order to be able to perform the optimisation, we implemented a corresponding routine in Python, which solves the given boundary value problem with the corresponding material parameters in the background and uses the results of this calculation for the optimisation. For this purpose, we used the data set labeled as *Exp. 1* in Figure 4.13. Next, we adjusted the parameters associated with the damage behaviour. Here, the hardening parameters were chosen so that no hardening occurs. Furthermore, the shape parameter $\varepsilon_d = 1.0$ was set. The remaining parameters were then adjusted by hand in order to reproduce the results in Figure 4.14 well. The use of an automated optimisation algorithm was not possible at this point due to the abrupt material failure in the experiment. The results of this adjustment process are given in Table 4.2.

Figure 4.13 shows the results from two different relaxation experiments and the correspond-

ing results predicted by the model. As described aboev, we use the experimental data of Exp. 1 for the calibration of the material model and afterwards apply the same set of material parameters to the simulation for the second loading scenario (see Exp. 2) as an example for the predictive capabilities of the model. Due to the calibration process itself, it is not surprising that the results from the first experiment are reproduced very well. But also the predictive results of the simulation of the second loading scenario are in good agreement with the data provided by the experiments. These results show how well the given material model generalizes for the case of pure viscoelastic material response.

Table 4.2: List of all material parameters included in the proposed material model. Values from the comparison experiments of Section 4.5.3 are given in the second column.

Symbol	Values	Units	Description
μ_{eq}	17.5	$\frac{\text{N}}{\text{mm}^2}$	Elastic shear modulus
κ_{neq}	300.0	$\frac{\text{N}}{\text{mm}^2}$	Elastic bulk modulus
μ_v	6.6	$\frac{\text{N}}{\text{mm}^2}$	Viscous shear modulus
κ_v	300.0	$\frac{\text{N}}{\text{mm}^2}$	Viscous bulk modulus
η_v	0.01	$\frac{1}{\text{s}}$	Viscoelastic relaxation velocity
η_d	10^{-5}	$\frac{1}{\text{s}}$	Damage evolution velocity
Y_0	45.0	$\frac{\text{N}}{\text{mm}^2}$	Damage threshold
ε_d	1.0	–	Damage evolution shape parameter
k	0.0	$\frac{\text{N}}{\text{mm}^2}$	Linear damage hardening parameter
r	0.0	$\frac{\text{N}}{\text{mm}^2}$	Voce-type damage hardening parameter 1
s	0.0	–	Voce-type damage hardening parameter 2
H	10^5	$\frac{\text{N}}{\text{mm}^2}$	Micromorphic coupling between local an non-local damage fields
A	50.0	N mm^2	Micromorphic influence of non-local damage gradient

In a next step, we used the same parameter set for the simulation of a uniaxial creep experiment and compared the results with the given experimental data. Figure 4.14 shows the corresponding results. In the beginning of the experiment, the experimental curve (red) shows the classical primary and secondary creep behaviour of polymeric materials. After an initial rise in displacement, the curve flattens. "*The last* [(tertiary)] *stage of the creep process is characterized by an increase of the creep strain rate due to microstructural damage mechanisms*" (Vladimirov et al. [2009]) and leads to rupture of the specimen at approximately 1300 s. Due to the sudden failure and the comparatively low temporal resolution of the measuring system, the failure path could not be captured in detail in the experiment. In Figure

4.14, the data point marked by the blue circle shows the point of failure observed in the experiment. When comparing the results from the simulation with the data points provided by the experiment, it becomes obvious that the model is well capable of predicting the creep damage behaviour of the polymeric adhesive under investigation.

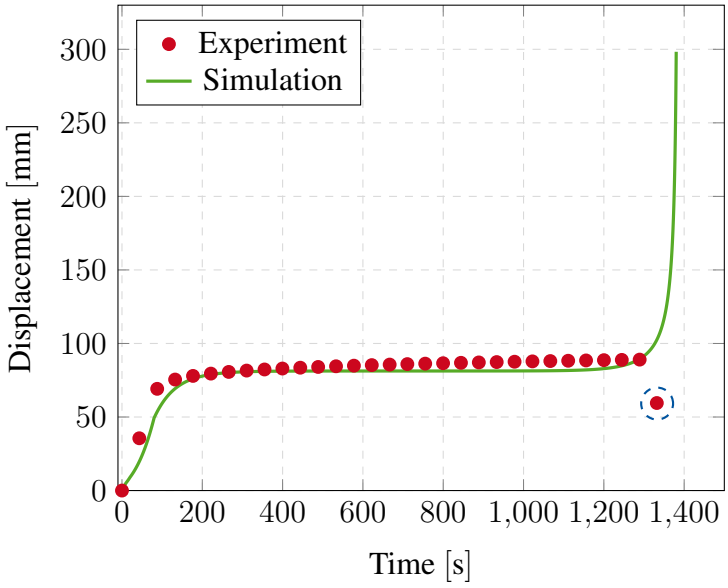

Figure 4.14: Results of validation simulation of a uniaxially loaded creep experiment using the material parameters fitted to the experimental results shown in Figure 4.13. Comparison of displacements in loading direction. Experimental data point marked by blue circle shows the abrupt rupture of the specimen due to creep damage. Here, the experimental setup was not able to capture this process in a detailed manner due to the low temporal resolution of the recorded signal.

4.6 Conclusion and outlook

In this paper, we have presented a model that combines viscoelasticity with rate-dependent damage for the case of finite deformations. This model makes use of a multiplicative split of the deformation gradient. Based on this, we have incorporated the viscoelastic effects by using an additive partition of the elastic Helmholtz free energy into equilibrium and nonequilibrium parts. Using the concepts of damage hardening and micromorphic damage extension, we were able to model the rate dependence of the damage behaviour by means of a modified Perzyna-type model. The entire model is derived in a thermodynamically consistent manner. In addition, we chose to describe the model in a novel corotated intermediate configuration, which allows for a straightforward implementation into computer code using automatic differentiation techniques.

In order to test the developed model, we carried out several numerical examples. Among them, we showed multi-parameter studies where we considered a single finite element of unit length subjected to a homogeneous stress state under tension. These parameter studies showed the influence of the material parameters on the response of the material. We were able to show how the rate-dependent damage approach differs from the purely viscoelastic material response. Furthermore, our results showed that damage associated with creep or relaxation can be well captured by the material formulation. We were able to demonstrate that this would not be the case for a rate-independent damage model. In addition, we presented selected structural examples. These include a double-notched specimen and a butt joint specimen. The developed model was able to resemble the standard viscoelastic relaxation and creep effects expected for a viscoelastic material.

Finally, we compared the model with a limited set of experimental data from uniaxial creep and relaxation experiments. We were able to show that the model is capable of predicting both, elastic relaxation as well as creep damage behaviour reasonably well. This gives confidence in the predictive capabilities of the model, although further investigations considering different loading scenarios must be performed in order to get a proper validation of the given model. Furthermore, an extension for thermo-mechanical coupling as shown for example in Reese [2003] or Felder et al. [2022] seems to be the next plausible step, as polymeric materials in particular are known for their temperature dependence.

4.7 Appendix

4.7.1 Total time derivative of the co-rotated elastic right Cauchy-Green tensor

Starting with the definition of the co-rotated elastic right Cauchy-Green tensor from Equation (4.4) and using the product rule of calculus, the total time derivative can written as

$$\dot{\tilde{\mathbf{C}}}_e = \dot{\mathbf{U}}_v^{-1}\mathbf{C}\mathbf{U}_v^{-1} + \mathbf{U}_v^{-1}\dot{\mathbf{C}}\mathbf{U}_v^{-1} + \mathbf{U}_v^{-1}\mathbf{C}\dot{\mathbf{U}}_v^{-1}.$$

With the relation $\dot{\mathbf{U}}_v^{-1} = -\mathbf{U}_v^{-1}\dot{\mathbf{U}}_v\mathbf{U}_v^{-1}$ as well as the definition of the viscous velocity gradient $\tilde{\mathbf{L}}_v = \dot{\mathbf{U}}_v\mathbf{U}_v^{-1}$, we can write the rate of the the co-rotated elastic right Cauchy-Green tensor as

$$\dot{\tilde{\mathbf{C}}}_e = \mathbf{U}_v^{-1}\dot{\mathbf{C}}\mathbf{U}_v^{-1} - \left(\tilde{\mathbf{L}}_v^T\tilde{\mathbf{C}}_e + \tilde{\mathbf{C}}_e\tilde{\mathbf{L}}_v\right).$$

4.7.2 Derivation of the reduced Clausius-Duhem inequality

In order to derive the reduced version of the Clausius-Duhem inequality (4.7) we need to calculate the total derivative of the Helmholtz free energy (see Equation (4.6)) with respect to time, i.e.

$$\begin{aligned}\dot{\psi} &= \dot{f}_d(D)\psi_0(\mathbf{C},\tilde{\mathbf{C}}_e) + f_d(D)\dot{\psi}_0(\mathbf{C},\tilde{\mathbf{C}}_e) + \dot{\psi}_d + \dot{\psi}_{\tilde{d}} \\ &= \left(\frac{\partial f_d}{\partial D}\psi_0 + \frac{\partial \psi_{\tilde{d}}}{\partial D}\right)\dot{D} + f_d\left(\frac{\partial \psi_{eq}}{\partial \mathbf{C}} : \dot{\mathbf{C}} + \frac{\partial \psi_{neq}}{\partial \tilde{\mathbf{C}}_e} : \dot{\tilde{\mathbf{C}}}_e\right) + \frac{\partial \psi_d}{\partial \xi_d}\dot{\xi}_d + \frac{\partial \psi_{\bar{d}}}{\partial \bar{D}}\dot{\bar{D}} + \frac{\partial \psi_{\bar{d}}}{\partial \nabla \bar{D}}\cdot\nabla\dot{\bar{D}}\end{aligned}$$

With the identity $\dot{\tilde{\mathbf{C}}}_e = \mathbf{U}_v^{-1}\dot{\mathbf{C}}\mathbf{U}_v^{-1} - \left(\tilde{\mathbf{L}}_v^T\tilde{\mathbf{C}}_e + \tilde{\mathbf{C}}_e\tilde{\mathbf{L}}_v\right)$ from Equation (4.5) we can rewrite the second term as

$$f_d\left(\frac{\partial \psi_{eq}}{\partial \mathbf{C}} : \dot{\mathbf{C}} + \frac{\partial \psi_{neq}}{\partial \tilde{\mathbf{C}}_e} : \dot{\tilde{\mathbf{C}}}_e\right) = f_d\left(\frac{\partial \psi_{eq}}{\partial \mathbf{C}} + \mathbf{U}_v^{-1}\frac{\partial \psi_{neq}}{\partial \tilde{\mathbf{C}}_e}\mathbf{U}_v^{-1}\right) : \dot{\mathbf{C}} - f_d\frac{\partial \psi_{neq}}{\partial \tilde{\mathbf{C}}_e} : \left(\tilde{\mathbf{L}}_v^T\tilde{\mathbf{C}}_e + \tilde{\mathbf{C}}_e\tilde{\mathbf{L}}_v\right)$$

Under the assumption that ψ_{neq} is an isotropic function of its arguments, we can exploit the symetric properties of the double contracting product which yields with the definition of the Mandel stress tensor $\tilde{\mathbf{\Sigma}} = 2f_d\tilde{\mathbf{C}}_e\frac{\partial \psi_{neq}}{\partial \tilde{\mathbf{C}}_e}$

$$f_d\left(\frac{\partial \psi_{eq}}{\partial \mathbf{C}} : \dot{\mathbf{C}} + \frac{\partial \psi_{neq}}{\partial \tilde{\mathbf{C}}_e} : \dot{\tilde{\mathbf{C}}}_e\right) = f_d\left(\frac{\partial \psi_{eq}}{\partial \mathbf{C}} + \mathbf{U}_v^{-1}\frac{\partial \psi_{neq}}{\partial \tilde{\mathbf{C}}_e}\mathbf{U}_v^{-1}\right) : \dot{\mathbf{C}} - \tilde{\mathbf{\Sigma}} : \tilde{\mathbf{D}}_v$$

With this at hand, we can include the derivative of the Helmholtz free energy in the Clausius-Duhem inequality (4.7) and arrive at

$$\left[\mathbf{S} - 2f_d\left(\frac{\partial \psi_{eq}}{\partial \mathbf{C}} + \mathbf{U}_v^{-1}\frac{\partial \psi_{neq}}{\partial \tilde{\mathbf{C}}_e}\mathbf{U}_v^{-1}\right)\right] : \dot{\mathbf{C}} \underbrace{- \left(\frac{\partial f_d}{\partial D}\psi_0 + \frac{\partial \psi_{\tilde{d}}}{\partial D}\right)}_{:=Y} \dot{D} - \underbrace{\frac{\partial \psi_d}{\partial \xi_d}}_{:=q_d}\dot{\xi}_d$$
$$+\tilde{\boldsymbol{\Sigma}} : \tilde{\mathbf{D}}_v + \left[a_{0_i} - \frac{\partial \psi_{\bar{d}}}{\partial \bar{D}}\right]\dot{\bar{D}} + \left[\mathbf{b}_{0_i} - \frac{\partial \psi_{\bar{d}}}{\partial \nabla \bar{D}}\right] \cdot \nabla \dot{\bar{D}} \geq 0$$

Under the assumption that the rates of the right Cauchy-Green tensor as well as the global damage variable and its gradient are arbitrary, the individual terms including these quantities should vanish (see [Coleman and Noll, 1963]). This yields the reduced Clausius-Duhem inequality (4.9), i.e.

$$Y\dot{D} - q_d\dot{\xi}_d + \tilde{\boldsymbol{\Sigma}} : \tilde{\mathbf{D}}_v \geq 0.$$

4.7.3 Total time derivative of the viscous right Cauchy-Green tensor

The rate of the viscous right Cauchy-Green tensor as given in Equation (4.3) can be derived as follows:

$$\begin{aligned}
\dot{\mathbf{C}}_v &= \dot{\mathbf{F}}_v^T\mathbf{F}_v + \mathbf{F}_v\dot{\mathbf{F}}_v^T \\
&= \left(\mathbf{F}_v^T\dot{\mathbf{F}}_v\mathbf{F}_v^{-1}\mathbf{F}_v\right)^T + \mathbf{F}_v^T\dot{\mathbf{F}}_v\mathbf{F}_v^{-1}\mathbf{F}_v \\
&= \left(\mathbf{F}_v^T\mathbf{L}_v\mathbf{F}_v\right)^T + \mathbf{F}_v^T\mathbf{L}_v\mathbf{F}_v \\
&= \mathbf{F}_v^T\left(\mathbf{L}_v^T + \mathbf{L}_v\right)\mathbf{F}_v \\
&= 2\mathbf{F}_v^T\mathbf{D}_v\mathbf{F}_v \\
&= 2\mathbf{U}_v^T\mathbf{R}_v^T\mathbf{D}_v\mathbf{R}_v\mathbf{U}_v \\
&= 2\mathbf{U}_v\tilde{\mathbf{D}}_v\mathbf{U}_v
\end{aligned}$$

4.7.4 Derivation of the viscoelastic evolution law

Considering the viscoelastic potential from Equation (4.11), the corresponding evolution law from Equation (4.12) can be written as

$$\begin{aligned}\tilde{\mathbf{D}}_v &:= \eta_v \frac{\partial \Phi_v}{\partial \tilde{\boldsymbol{\Sigma}}} \\ &= \eta_v \frac{\partial \Phi_v}{\partial \tilde{\boldsymbol{\Sigma}}_0} : \frac{\partial \tilde{\boldsymbol{\Sigma}}_0}{\partial \tilde{\boldsymbol{\Sigma}}} \\ &= \frac{\eta_v}{f_d} \left(\frac{1}{2\mu_v} \operatorname{dev}\left(\tilde{\boldsymbol{\Sigma}}_0\right) + \frac{1}{3\kappa_v} \operatorname{vol}\left(\tilde{\boldsymbol{\Sigma}}_0\right) \right).\end{aligned}$$

5 Article 4: A gradient-extended, thermomechanical model for rate-dependent damage and failure within rubberlike polymeric materials at finite strains

This article was published as:

Lamm, L.; A. Awad; Pfeifer, J. M.; Holthusen, H.; S. Felder; Reese, S.; Brepols, T. [2024], 'A gradient-extended, thermomechanical model for rate-dependent damage and failure within rubberlike polymeric materials at finite strains', *International Journal of Plasticity* **173**, 103883

Disclosure of the individual authors' contributions to the article:

L. Lamm worked out the theoretical material model and wrote this article. L. Lamm and J. M. Pfeifer implemented the model into the finite element software FEAP, reviewed the relevant existing literature, performed simulations and interpreted the results. A. Awad performed simulations and interpreted the results. H. Holthusen, S. Reese and T. Brepols gave conceptual advice, contributed in the discussion of the results, read the article and gave valuable suggestions for improvement. All authors approved the publication of the manuscript.

5.1 Abstract

Rate-dependencies play a crucial role in the mechanical response of polymeric materials. Besides viscoelasticity, many polymers also show pronounced rate-dependent behaviour with respect to damage accumulating within the material. Furthermore, thermal effects and large deformations have to be taken into account when modelling the mechanical behaviour of polymers. Within this work, we propose a novel fully thermomechanically coupled material model for the description of rate-dependent damage combined with viscoelasticity at finite strains. The model is based on the multiplicative decomposition of the deformation gradient into thermal and mechanical parts as well as a further decomposition of the mechanical part into equilibrium and non-equilibrium contributions. To describe the temporal dependencies of the damage evolution, we make use of a Perzyna-type approach. We furthermore show the thermodynamically consistent derivation of stresses and heat sources which arise due to energy dissipations triggered by the inelastic effects within the material. With the given material formulation, we are able to describe both, damage due to creep and due to relaxation in a precise manner. Besides the theoretical aspects, we describe the numerical implementation into finite element software and present numerical studies demonstrating the capabilities of the given model.

5.2 Introduction

Silicone based polymeric materials play a major role in today's industrial context. Load bearing adhesives are used e.g. in the automotive, mechanical engineering or construction industry to connect various components with each other. One example among many is the construction of glass façade systems using silicone bonding (see e.g. de Buyl [2001]). In such constructions, the glass panels are bonded directly to the load bearing structure below. In addition to improved load transfer and easier installation, this also ensures a better insulation effect. Another example for applications of silicone is its use in the field of biomedical engineering. In this sector, silicone is used in a variety of ways. Just recently it was even for the production of heart valve prosthetics replacing a crucial part of the native human heart (see Engelhardt et al. [2019]; Coulter et al. [2019], among others). In addition to these two examples, there are many other possible applications for silicone-based materials, whose description is beyond the scope of this paper. However, all these fields of application have in common that they have to deal with the highly complex mechanical behaviour of this particular type of material. In this respect, mathematical models can make a valuable contribution to a deeper

understanding of the material behaviour in addition to classical experimental investigations. However, an adequate mathematical description of this behaviour is not trivial. This is due to the many different inelastic and multiphysical effects that must be taken into account for a realistic description of the material. In addition to temperature dependence, incompressibility and entropy elasticity, these also include the strongly rate-dependent material behaviour, which takes place in both the elastic regime and in the limit range of damage and failure.

The description of the thermoelastic behaviour of polymeric materials has long been an important part of research in the field of continuum mechanics and differs fundamentally from that of other classical engineering materials, such as metals. Above their individual glass transition temperature, the stress response of polymers is mainly of entropic origin, whereas the energetic part is predominant in metals (see Chadwick [1974] for more details). Fortunately, silicone based polymeric materials often show a very low glass transition temperature which usually lies in a range that is not relevant for technical application. We therefore limit this modelling approach to the description of rubberlike behaviour. The modelling approaches capturing this behaviour can be roughly divided into two groups. On the one hand, there are works based on the idea of Lu and Pister [1975] which multiplicatively decompose the deformation of the body (represented by the deformation gradient) into a mechanical and a thermal part. The free energy is then described by a mechanical and a thermal part, which are added accordingly. In order to be able to represent the dominant entropic material behaviour of polymers well in this context, Holzapfel and Simo [1996] and Lion [1996, 1997] add an explicit dependence of the material parameters on the temperature. Due to the fundamental connection between the heat capacity and the Helmholtz free energy, this leads to the heat capacity becoming a complex, non-linear function of all internal variables. The thermal fraction of the free energy must therefore be chosen appropriately to avoid unwanted dependencies. This is usually not trivial, which is why various works implicitly assume that the heat capacity is constant and the thermal energy assumes an appropriate form that ensures this (see e.g. Canadija and Mosler [2011]; Aldakheel and Miehe [2017]; Dittmann et al. [2020]; Felder et al. [2022]). Other works use a different approach and are able to find an explicit form for the thermal fraction of the free energy on the basis of elaborate material tests (see e.g. Lion [1996, 1997]; Lion et al. [2017]). As an alternative to the models based on the split of the deformation gradient, the other side in this classification is based on the original ideas of Chadwick [1974]. Here, the double integration of the fundamental connection between the heat capacity and the Helmholtz free energy forms the basis for determining a general form of the free energy. This approach motivated e.g. Reese and Govindjee [1997] to develop a model which takes into account the temperature and deformation dependence of the heat capacity and thus leads

directly to a non-linear relationship between stress and temperature. One particular advantage of this method is that the material parameters not functions of the the temperature anymore and must therefore only be determined for a predefined reference temperature. More recent works using this approach are e.g. Xiao and Nguyen [2015]; Behnke et al. [2016]; Mehnert et al. [2017, 2018]; Dai et al. [2020], among others.

The rate-dependent behaviour of polymers can be described very well in the elastic range with the help of the viscoelasticity theory. Similar to thermomechanical coupling, a large number of modelling approaches exist in this area today. If finite deformations are considered, these approaches can be subdivided according to their dependence of the stresses on the strain rate. In classical approaches, e.g. by Simo [1987]; Holzapfel and Simo [1996]; Bonet [2001]; Österlöf et al. [2016]; Guo et al. [2018]; Wang et al. [2019], a linear relationship between the variables is assumed. While such work is only valid for small pertubations of thermodynamic equilibrium, the works of, for example, Reese and Govindjee [1998]; Bergström [1998]; Haupt et al. [2000] also consider the intrinsically non-linear nature of the relationship between stress and strain rate. These approaches lead to a more general formulation of the viscoelastic constitutive equations and can usually be reduced to the simpler case of the linear theory. Current works applying the approach of a non-linear theory can be found e.g. in Fancello et al. [2006]; Kumar and Lopez-Pamies [2016]; Wang and Chester [2018] and Rambausek et al. [2022], among others.

Another important effect that should not be neglected when describing the material behaviour of polymers is the behaviour in the event of damage or failure. In general, the damage behaviour of rubber-like polymers can be attributed to various microscopic effects. In addition to the well-known Mullins effect, the formation of cavities also plays a role. The latter occurs primarily in filled polymers when they are exposed to high hydrostatic tensile stresses. Both effects lead to a substantial reduction in the stiffness of the material, but are only indirectly responsible for the corresponding crack failure. In addition, another type of damage plays an important role, in which the molecular bonds between the individual polymer chains are successively broken, ultimately leading to crack failure in the material under high tensile stresses. It has already been shown in the literature that this crack failure is a rate-dependent effect (see e.g. Lamm et al. [2023]). In the present work, our focus is on the description of rate-dependent crack damage in rubber-like polymers. Other damage effects, such as the Mullins effect or cavity damage, are therefore not considered further in this work. A detailed modelling of the micromechanical effects is basically very complicated and often not necessary for the characterisation of the macroscopically visible material behaviour. A large amount of Continuum Damage Mechanics (CDM) models based on the work of Kachanov [1958] and

Rabotnov [1969] have been established in the literature. These approaches consider damage in an averaged sense by introducing one or more internal damage variables. These tensor- or scalar-valued variables are subsequently used to achieve a stiffness reduction. The simplest choice is that of isotropic damage, for which only one scalar damage variable is introduced (see Lemaitre [1984, 1985*a*]; de Souza Neto et al. [1998]; Saanouni [2009]; Jeridi et al. [2015]; Brepols et al. [2017*a*], among many others). More complex models also take into account an anisotropic development of damage by introducing a damage tensor (see Davison and Stevens [1973]; Krajcinovic and Fonseka [1981]; Murakami and Ohno [1981]; Pituba and Fernandes [2011]; Ayadi et al. [2016]; Reese et al. [2021]; Holthusen et al. [2022], among many others). It should be noted at this point that the literature on the subject of CDM is so extensive that a detailed listing of all modelling approaches would go beyond the scope of this paper.

When considering the damage behaviour of polymeric adhesives, it has been shown that also the damage process itself is depending on rate of deformation applied to the material at hand (see Lamm et al. [2023]). It is therefore desirable to also include this dependency within the modelling process. When considering small strains, a variety of models has been developed such as e.g. Voyiadjis et al. [2012]; Al-Rub and Darabi [2012]; Wang et al. [2013]; Zhu and Sun [2013]; Pandey et al. [2019]; Pereira et al. [2017]; Shlyannikov and Tumanov [2019]; Nahrmann and Matzenmiller [2021]; Xia et al. [2022]; Kou et al. [2022], among others. Unfortunately, the literature considering rate-dependent CDM approaches which are valid for large deformations is relatively sparse. Based on the work of Lion [1996], the models of Miehe [2000]; Lin and Schomburg [2003] and Aboudi [2011] describe a general rate-dependent damage process by defining an explicit damage evolution equation considering the rate of a strain-like quantity as the corresponding driving force. The approach of Khaleghi et al. [2022] extends the classical damage evolution formulation of Lemaitre [1985*a*] to the finite strain regime. Just recently, the approach by Lamm et al. [2023] proposes a Perzyna-type (Perzyna [1963]) approach to describe the rate-dependent evoution of the local damage variable in a simple yet effective fashion.

A fundamental problem in the field of CDM are the instabilities caused by localisations, which can lead to strong mesh dependence and potentially physically implausible results (see e.g. Bažant et al. [1984]; de Borst et al. [1993]; Cervera and Chiumenti [2006]; Jirásek and Grassl [2008]). To counteract this problem, a number of approaches have been developed based on the non-local extension of the otherwise local damage model (see Bažant [1976]; Bažant and Lin [1988]). This means that the evolution of the local damage variable at a single point is made explicitly dependent the damage state at surrounding points. The region of influence can generally be understood as an internal length limiting the localisation. A frequently used

method to realise this regularisation in the context of a non-local extension is the concept of gradient-extended damage, which can be, for example, based on the micromorphic framework of Forest [2009]. In this framework, an additional global variable is introduced whose diffusive nature is described by means of another partial differential equation (PDE). This results in the present case in a coupled problem of balance of linear momentum, energy balance and the mentioned PDE, which have to be solved in a meaningful way.

Within this work we introduce a flexible model for the description of thermomechanically coupled rate-dependent damage in polymeric adhesives. For this, we follow the approach of Lu and Pister [1975] and introduce the multiplicative decomposition of the deformation gradient into mechanical and thermal parts.For the viscoelastic ground model, a formulation for finite viscoelasticity is chosen as described by Reese and Govindjee [1998]. For the regularisation of the damage field, we base our model on the gradient-extended micromorphic damage formulation for large deformations introduced by Brepols et al. [2020]. To include the rate-dependencies into the damage response, we follow the approach of Lamm et al. [2023] and apply a Perzyna type ansatz for the description of the damage evolution equations (see Perzyna [1963, 1966, 1971]). This approach has shown to be an effective way of including rate-dependent material properties into various kinds of material descriptions (see e.g. Lamm et al. [2021, 2022]). To assure a straight forward implementation by means of automatic differentiation, we base the whole formulation on the theory of co-rotated intermediate configurations as described by Holthusen et al. [2023].

The overall structure of this work is as follows. In Section 5.3, we introduce the theoretical modelling ideas behind the proposed model before we come to the description of its numerical implementation within Section 5.4. Finally, we show numerical examples of selected parameter sensitivities as well as structural simulations in Section 5.5.

5.3 Modelling of thermo-viscoelastic rate-dependent damage

Within this contribution, we aim to solve a fully thermomechanically coupled problem considering inelastic deformations and damage within the finite strain regime. We therefore do not only need to consider the vector valued displacement field $\mathbf{u}$ as the global degrees of freedom but also the scalar valued temperature field Θ. To model the damage behaviour, we make use of a continuum damage approach and introduce the local internal damage variable $D \in [0, 1]$, which describes the amount of damage accumulated within a point of the continuum at hand.

Here, $D = 0$ refers to a virgin state of the material, while $D = 1$ describes total failure. For $D \to 1$ the material stiffness approaches zero, which could be interpreted as the formation of a macroscopic crack. It is obvious that we limit ourselves to isotropic damage evolutions with this choice. There are other approaches in the literature which deal with anisotropic evolutions of a damage tensor (see Murakami and Ohno [1981]; Pituba and Fernandes [2011]; Reese et al. [2021]; Holthusen et al. [2022], among others). In this work, we, however, stick to the assumption of isotropy, since we mainly want to study the influence of rate-dependencies arising in the damage evolution.

For the deformation of a continuum body $\mathcal{B}_0$ located within the reference configuration, we introduce the stationary version of the balance of linear momentum written in terms of the deformation gradient $\mathbf{F}$, the second Piola-Kirchhoff stress tensor $\mathbf{S}$, the general body force vector $\mathbf{b}_0$, the outward normal $\mathbf{n}_0$, the traction vector $\mathbf{t}_0$ as well as prescribed displacements $\tilde{\mathbf{u}}$, i.e.

$$\begin{aligned} \operatorname{Div}(\mathbf{F}\mathbf{S}) + \mathbf{b}_0 &= \mathbf{0} \qquad \text{in } \mathcal{B}_0 \\ \mathbf{F}\mathbf{S} \cdot \mathbf{n}_0 &= \mathbf{t}_0 \qquad \text{on } \partial\mathcal{B}_{0_t} \\ \mathbf{u} &= \tilde{\mathbf{u}} \qquad \text{on } \partial\mathcal{B}_{0_u}. \end{aligned} \tag{5.1}$$

In order to overcome pathological mesh dependencies (see e.g. Bažant et al. [1984]; de Borst et al. [1993]), we base our constitutive modelling approach on the general micromorphic approach as suggested by Forest [2009], which was applied for gradient-extended damage simulations at finite strains e.g. by Brepols et al. [2020]. In line with these works, we introduce an additional global micromorphic damage field $\bar{D}$. This additional global damage field is subsequently coupled with the local damage field D by introducing a contribution to the Helmholtz free energy (see Section 5.3.1.1). The development of the global damage field $\bar{D}$ is described by means of the micromorphic balance equation as

$$\begin{aligned} \operatorname{Div}(\mathbf{b}_{0_i} - \mathbf{b}_{0_e}) - a_{0_i} + a_{0_e} &= 0 \qquad \text{in } \mathcal{B}_0 \\ (\mathbf{b}_{0_i} - \mathbf{b}_{0_e}) \cdot \mathbf{n}_0 &= a_{0_c} \quad \text{on } \partial\mathcal{B}_{0_c} \\ \bar{D} &= \bar{\tilde{D}} \qquad \text{on } \partial\mathcal{B}_{0_D}. \end{aligned} \tag{5.2}$$

This equation describes the diffusion of the global state variable in terms of the micromorphic body forces a_{0_e} and $\mathbf{b}_{0_e}$ together with the internal micromorphic forces a_{0_i} and $\mathbf{b}_{0_i}$, respectively. The approach is directly derived from the extended version of the principle of virtual work, thermodynamic consistency is a priori given.

To describe the change in internal energy e within $\mathcal{B}$, we furthermore introduce an extended

balance of energy (see e.g. Forest [2009]; Felder et al. [2022]) in terms of the referential heat flux vector $\mathbf{q}_0$ and the external heat sources r_{ext} such that

$$\begin{aligned} -\dot{e} + \mathbf{S} : \frac{1}{2}\dot{\mathbf{C}} - \operatorname{Div} \mathbf{q}_0 + a_{0_i}\dot{\tilde{D}} + \mathbf{b}_{0_i} \cdot \operatorname{Grad} \dot{\tilde{D}} + r_{ext} = 0 \qquad & \text{in } \mathcal{B}_0 \\ \mathbf{q}_0 \cdot \mathbf{n}_0 = -q_0 \qquad & \text{on } \partial\mathcal{B}_{0_q} \\ \Theta = \tilde{\Theta} \qquad & \text{on } \partial\mathcal{B}_{0_\theta}. \end{aligned} \tag{5.3}$$

To account for the additional contributions of the gradient-extended approach on the internal energy, we must also include corresponding terms into the balance of energy. For more details on the derivation of the gradient-extended framework, the interested reader is kindly referred to the original works by Forest [2009] and Brepols et al. [2017*a*, 2020]; Felder et al. [2022].

Within Equations (5.1), (5.2) and (5.3) the corresponding Dirichlet boundary conditions are described on the boundaries $\partial\mathcal{B}_{0_u}$, $\partial\mathcal{B}_{0_D}$ and $\partial\mathcal{B}_{0_\theta}$. These parts of the boundary are exposed to the prescribed displacement $\tilde{\mathbf{u}}$, global damage variable $\tilde{\tilde{D}}$ and temperature $\tilde{\Theta}$, respectively. Furthermore, all relevant Neumann boundary conditions are given on the boudaries $\partial\mathcal{B}_{0_t}$, $\partial\mathcal{B}_{0_c}$ and $\partial\mathcal{B}_{0_q}$. The imposed values on these portions of the boundary are given by the tractions $\mathbf{t}_0$, a_{0_c} and the heat flux q_0. These equations described here form the basis of the solution of the thermomechanical problem and are completed in the following by the constitutive model we have developed.

5.3.1 Constitutive framework

We start the constitutive modelling process by following the argumentation of Lu and Pister [1975] and multiplicatively decompose the deformation gradient $\mathbf{F}$ such that

$$\mathbf{F} = \mathbf{F}_M \mathbf{F}_\theta, \tag{5.4}$$

where $\mathbf{F}_\theta$ describes the part of the deformation which is related to thermal expansion. Depending on the degree of anisotropy within the thermal material response, various explicit definitions of $\mathbf{F}_\theta$ can be found in literature (see e.g. Vujosevic and Lubarda [2002]; Lubarda [2004]). Within this work, we limit ourselves to purely isotropic heat expansion. By defining the heat expansion coefficient α_θ and a reference temperature Θ_0, we can therefore describe isotropic heat expansion of the continuum body at hand via the relation $\mathbf{F}_\theta = \vartheta(\Theta)\mathbf{I}$ using the heat expansion function $\vartheta(\Theta) = \exp(\alpha_\theta(\Theta - \Theta_0))$ (see e.g Lion [2000*b*]).

In order to describe inelastic material behaviour, we apply a further multiplicative decom-

position of the mechanical part of the deformation gradient $\mathbf{F}_M$ into an elastic part $\mathbf{F}_e$ and an inelastic part $\mathbf{F}_v$ (see e.g. Reese and Govindjee [1998]). The full decomposition of the deformation gradient consequently reads $\mathbf{F} = \vartheta(\theta)\mathbf{F}_e\mathbf{F}_v$. With this at hand, we can define the right Cauchy-Green tensor

$$\mathbf{C} = \vartheta^2\, \mathbf{F}_M^T\mathbf{F}_M = \vartheta^2\, \mathbf{C}_M \tag{5.5}$$

as well as its viscous counterpart, i.e. $\mathbf{C}_v = \mathbf{F}_v^T\mathbf{F}_v$. By following the argumentations made in Holthusen et al. [2023], we make use of the right polar decomposition of the viscous deformation gradient, i.e. $\mathbf{F}_v = \mathbf{R}_v\mathbf{U}_v$, to define the co-rotated elastic right Cauchy Green tensor $\tilde{\mathbf{C}}_e$, i.e.

$$\tilde{\mathbf{C}}_{e,\Theta} = \vartheta^{-2}\mathbf{U}_v^{-1}\mathbf{C}\mathbf{U}_v^{-1} = \vartheta^{-2}\tilde{\mathbf{C}}_e. \tag{5.6}$$

For details on the theory of co-rotated intermediate configurations, the interested reader is kindly referred to the original literature given in Holthusen et al. [2023]. Using the definition of the co-rotated velocity gradient $\tilde{\mathbf{L}}_v = \dot{\mathbf{U}}_v\mathbf{U}_v^{-1}$, we can derive the associated rate of the co-rotated elastic right Cauchy-Green tensor as

$$\dot{\tilde{\mathbf{C}}}_e = \mathbf{U}_v^{-1}\dot{\mathbf{C}}\mathbf{U}_v^{-1} - \left(\tilde{\mathbf{L}}_v^T\tilde{\mathbf{C}}_e + \tilde{\mathbf{C}}_e\tilde{\mathbf{L}}_v\right). \tag{5.7}$$

For details on the corresponding derivation, the reader if referred to Appendix 5.7.1.

5.3.1.1 General structure of the Helmholtz free energy

Motivated by the multiplicative decompositions made above, we postulate the Helmholtz free energy for the given material as

$$\psi = f_d(D)\underbrace{\frac{\Theta}{\Theta_0}\left[\psi_{eq}(\mathbf{C},\Theta) + \psi_{neq}(\tilde{\mathbf{C}}_e,\Theta)\right]}_{\psi_0} + \psi_d(\xi_d) + \psi_{\bar{d}}(D,\bar{D},\operatorname{Grad}\bar{D}) + \psi_\theta(\Theta), \tag{5.8}$$

where ψ_0 describes the undamaged viscoelastic energy. This energy further consists of a rate-independent elastic equilibrium energy ψ_{eq} as well as an inelastic non-equilibrium energy ψ_{neq} (see Reese and Govindjee [1998]). In order to describe the temperature dependency of the undamaged energy ψ_0, we choose a linear relation of the material parameters following the argumentations in Lion [1997]. It is important to mention that this is not the only feasible choice. One could also describe the material parameters as nonlinear functions of the temperature. The particular choice depends strongly on the individual behaviour of the material at hand. In order to describe the influence of damage on the stored energy, we introduce the quadratic function $f_d(D) = (1-D)^2$, which successively degrades the undamaged energy

while damage evolves. This effectively leads to a softening behaviour with zero stiffness for $D = 1$.

Remark. *Without any doubt there exist many different choices for a suitable definition of the damage degradation function. Among others, the most well-known are probably* $f_d = (1 - D)$ *(see Lemaitre [1971]) and* $f_d = (1 - D)^2$ *(see e.g. Cordebois and Sidoroff [1982]). Other authors even use an exponential formulation* $f_d = \exp(-D)$ *(see e.g. Dimitrijevic and Hackl [2008]). In case of the polynomial approaches, the linear approach can be directly derived from the hypothesis of strain equivalence, whereas the quadratic form follows from the hypothesis of energy equivalence (see e.g. the references mentioned above).*

To achieve more flexibility within the damage formulation, we introduce ψ_d as a damage hardening energy. This energy acts similar to isotropic hardening in the field of elasto-plasticity (see e.g. Chow and Wang [1987]; Chow and Lu [1989]). Finally, we introduce $\psi_{\bar{d}}$ denoting the energy associated with the micromorphic gradient-extension as well as the caloric energy ψ_θ.

5.3.1.2 Thermodynamic considerations & heat sources

One goal of major importance in the development of constitutive relations is to assure that the model developed fulfills the basic laws of thermodynamics. This is necessary to ensure physically reasonable results of the computations conducted with the given model. In the case of a thermomechanically coupled problem, both, the balance of energy as well as the Clausius Duhem inequality (CDI) must be fulfilled to construct a thermodynamically consistent material model. The former is given in Equation (5.3), whilst the CDI can be written in terms of the entropy η as

$$-\dot{\psi} + \mathbf{S} : \frac{1}{2}\dot{\mathbf{C}} + a_{0_i}\dot{\bar{D}} + \mathbf{b}_{0_i} \cdot \operatorname{Grad}\dot{\bar{D}} - \eta\dot{\Theta} - \frac{1}{\Theta}\mathbf{q}_0 \cdot \operatorname{Grad}\Theta \geq 0. \tag{5.9}$$

The fundamental relation between the specific free energy ψ, the internal energy e, the entropy η as well as the thermodynamic temperature Θ is given by means of the Legendre transformation $e = \psi + \Theta\eta$. By combining the temporal derivative of the Helmholtz free energy given in Equation (5.8) with the CDI and following the standard argumentation of Coleman and Noll [1963, 1974], we can find the thermodynamically consistent definitions of the second Piola-

Kirchhoff stress tensor, the entropy and the generalized micromorphic stresses as

$$\mathbf{S} = 2f_d \frac{\Theta}{\Theta_0}\left(\frac{\partial \psi_{eq}}{\partial \mathbf{C}} + \mathbf{U}_v^{-1}\frac{\partial \psi_{neq}}{\partial \tilde{\mathbf{C}}_e}\mathbf{U}_v^{-1}\right), \quad \eta = -\frac{\partial \psi}{\partial \Theta}, \quad \mathbf{b}_{0_i} = \frac{\partial \psi}{\partial \operatorname{Grad} \bar{D}}, \quad a_{0_i} = \frac{\partial \psi}{\partial \bar{D}}. \tag{5.10}$$

We furthermore can define the damage driving force Y, the hardening driving force q_d and the co-rotated Mandel stress tensor $\tilde{\mathbf{M}}$, i.e.

$$Y = -\left(\frac{\partial f_d}{\partial D}\psi_0 + \frac{\partial \psi_{\bar{d}}}{\partial D}\right), \qquad q_d = \frac{\partial \psi_d}{\partial \xi_d}, \qquad \tilde{\mathbf{M}} = 2f_d \frac{\Theta}{\Theta_0}\tilde{\mathbf{C}}_e \frac{\partial \psi_{neq}}{\partial \tilde{\mathbf{C}}_e}. \tag{5.11}$$

With this as well as the symmetric part of the corotated viscous velocity gradient $\tilde{\mathbf{D}}_v := \operatorname{sym} \tilde{\mathbf{L}}_v$, the reduced Clausius Duhem inequality reads

$$\tilde{\mathbf{M}} : \tilde{\mathbf{D}}_v - q_d \dot{\xi}_d + Y\dot{D} - \frac{1}{\Theta}\mathbf{q}_0 \cdot \operatorname{Grad} \Theta \geq 0. \tag{5.12}$$

For a detailed derivation, the interested reader is kindly referred to Appendix 5.7.2. In order to fulfill Equation (5.12) we have to define reasonable equations for the evolution of the internal variables as well as for the heat flux vector $\mathbf{q}_0$, which will be described in detail later in this text.

All inelastic processes occuring within the material at hand are directly associated with the dissipation of elastic energy. Be it the viscous response or the damage evolution, both effects transfer elastic energy into other forms of energy. Besides other forms of energies, the most predominant form in which the elastic energy is transformed is heat. This process can be interpreted as internal heat sources entering the balance of energy. To derive the internal heat sources in a thermodynamically consistent manner, we start with the Legendre transformation $e = \psi + \Theta\eta$, describing the relation between internal energy e and the Helmholtz free energy ψ as well as the temperature Θ and entropy η, respectively. By inserting the temporal derivative of the Legendre transformation into the balance of energy given by Equation (5.3) we can find a version of the balance of energy that is given solely in terms of quantities already introduced above, i.e.

$$-\dot{\psi} - \dot{\eta}\Theta - \eta\dot{\Theta} + \mathbf{S} : \frac{1}{2}\dot{\mathbf{C}} - \operatorname{Div} \mathbf{q}_0 + a_{0_i}\dot{\bar{D}} + \mathbf{b}_{0_i} \cdot \operatorname{Grad} \dot{\bar{D}} + r_{ext} = 0. \tag{5.13}$$

Subsequently, we insert the time derivative of the Helmholtz free energy (5.8) and the total time derivative of the entropy (5.10) into this relation. In this way, we arrive at a partial differential

equation describing the temperature field in terms of the internal heat generation r_{int}, i.e.

$$c\dot{\Theta} = r_{int} + r_{ext} - \operatorname{Div} \mathbf{q}_0. \tag{5.14}$$

Here, the specific heat capacity per reference volume is given by $c = -\Theta\partial^2\psi/\partial\Theta^2$. If we follow the procedures described in detail in Appendix 5.7.3, the internal heat source $r_{int} = r_e + r_v + r_d$ is given in terms of the thermoelastic coupling term r_e as well as the viscous heat source r_v and the damage related heat source r_d, i.e.

$$\begin{aligned} r_e &= \frac{1}{2}\frac{\partial \mathbf{S}}{\partial \Theta}\Theta : \dot{\mathbf{C}} \\ r_v &= \left(\tilde{\mathbf{M}} - \frac{\partial \tilde{\mathbf{M}}}{\partial \Theta}\Theta\right) : \tilde{\mathbf{D}}_v \\ r_d &= \left(Y - \frac{\partial Y}{\partial \Theta}\Theta\right)\dot{D} - \left(q_d - \frac{\partial q_d}{\partial \Theta}\Theta\right)\dot{\xi}_d + \frac{\partial a_{0_i}}{\partial \Theta}\Theta\dot{\bar{D}} + \frac{\partial b_{0_i}}{\partial \Theta}\Theta \cdot \operatorname{Grad}\dot{\bar{D}}. \end{aligned} \tag{5.15}$$

5.3.1.3 Heat flux & evolution equations

A well established approach of describing a thermodynamically consistent constitutive relation for the heat flux vector $\mathbf{q}_0$ is Fourier's law. Written in referential coordinates this relation often reads

$$\mathbf{q}_0 = -Jh\,\mathbf{C}^{-1}\operatorname{Grad}\Theta \tag{5.16}$$

and makes use of the thermal conductivity h to describe how heat flows from regions of higher to regions of lower temperature. Here, $J = \det\mathbf{F}$ denotes the determinant of the deformation gradient. If we consider a material undergoing damage, we cannot assume that the conductivity h is constant but must rather assume that it is dependent on the damage process itself. Following the approach introduced in Dittmann et al. [2020], we define the thermal conductivity in terms of the virgin conductivity h_0 as well as the damaged conductivity h_d, i.e.

$$k(D) = f_d(D)h_0 + (1 - f_d(D))h_d. \tag{5.17}$$

This definition ensures that a damaged material does no longer conduct heat in the same manner as a virgin material, which seems physically reasonable. It is obvious, that also other degradation functions could be used here, depending on the behaviour of the material under investigation.

Besides the heat flux, we also need to define how the internal variables, namely the damage variable D and the viscous right Cauchy-Green tensor $\mathbf{C}_v$, evolve. Following the ideas from

e.g. Simo [1992] and Reese and Govindjee [1998], we postulate the existence of a viscoelastic dissipation potential that is written as

$$\Phi_v(\tilde{\mathbf{M}}_0) := \frac{1}{4\mu_v}\,\mathrm{tr}\left(\mathrm{dev}\left(\tilde{\mathbf{M}}_0\right)^2\right) + \frac{1}{18\kappa_v}\,\mathrm{tr}\left(\tilde{\mathbf{M}}_0\right)^2, \tag{5.18}$$

where $\kappa_v = \kappa_v(\Theta)$ denotes the viscous bulk modulus and $\mu_v = \mu_v(\Theta)$ the viscous shear modulus. Here, the operators $\mathrm{tr}\,(\bullet)$ and $\mathrm{dev}\,(\bullet) = (\bullet) - \frac{1}{3}\,\mathrm{tr}\,(\bullet)\,\mathbf{I}$ denote the trace as well as the deviatoric operator, respectively. From Equation (5.11) it becomes obvious that the co-rotated Mandel stress tensor $\tilde{\mathbf{M}}$ gets degraded during damage evolution due to its explicit dependency on the degradation funtion f_d. This, however, is not desirable, since it would ultimately lead to a vanishing viscous driving force for $D \to 1$. We therefore follow the suggestion made e.g. in Abdel-Tawab and Weitsman [2000] and define the viscous potential in terms of the effective co-rotated Mandel stress tensor $\tilde{\mathbf{M}}_0 = f_d^{-1}\tilde{\mathbf{M}}$ instead. Based on these assumptions, we choose the evolution of the viscous velocity gradient $\tilde{\mathbf{D}}_v$ to being proportional to the derivative of the dissipative potential given above with respect to the viscous driving force. By using a pull-back operation, we can define the evolution of the viscous right Cauchy Green tensor such that

$$\begin{aligned}
\dot{\mathbf{C}}_v &= 2\mathbf{U}_v\tilde{\mathbf{D}}_v\mathbf{U}_v \\
&= 2\eta_v\mathbf{U}_v\frac{\partial\Phi_v(\tilde{\mathbf{M}}_0)}{\partial\tilde{\mathbf{M}}}\mathbf{U}_v \\
&= \frac{\eta_v}{f_d}\mathbf{U}_v\left(\frac{1}{\mu_v}\,\mathrm{dev}\left(\tilde{\mathbf{M}}_0\right) + \frac{2}{9\kappa_v}\,\mathrm{vol}\left(\tilde{\mathbf{M}}_0\right)\right)\mathbf{U}_v,
\end{aligned} \tag{5.19}$$

where $\eta_v = \eta_v(\Theta)$ is a (nonlinear) function of the temperature and acts as the relaxation velocity of the given material. Here, the operator $\mathrm{vol}\,(\bullet) = \frac{1}{3}\,\mathrm{tr}\,(\bullet)\,\mathbf{I}$ denotes the volumetric part of the given tensorial quantity.

In order to describe the onset of damage evolution, we introduce a damage threshold $Y_0 = Y_0(\Theta)$ and define the damage function as

$$\Phi_d := Y - (Y_0 + q_d)\,. \tag{5.20}$$

By interpreting this function as a damage related pseudo potential, we define the evolution of the damage variable D as well as the damage hardening variable ξ_d by means of a Perzyna type ansatz (see e.g. Perzyna [1963, 1966]). This idea yields the following damage evolution equations in terms of the damage velocity $\eta_d = \eta_d(\Theta)$ and the damage sensitivity parameter

ε_d, i.e.

$$\dot{D} := \dot{\xi}_d := \begin{cases} \eta_d \left(\frac{\Phi_d}{Y_0 + q_d} \right)^{\frac{1}{\varepsilon_d}} & \text{if} \quad \Phi_d \geq 0 \\ 0 & \text{else} \end{cases} \tag{5.21}$$

It is important to note that the choice of D and ξ_d evolving in the same manner is by no means the only one feasible but rather the most simple assumption for damage hardening. Due to simplicity, we however stick to this assumption within this work. Furthermore, it should be explicitly mentioned that all material parameters used in Equations (5.19) and (5.21) are in general described as nonlinear functions of the temperature.

Remark. *The relaxation and damage velocities η_v and η_d are often also known as the reciprocal relaxation time and the reciprocal time of damage evolution, respectively.*

5.3.1.4 Particular choices of the Helmholtz free energy

The constitutive framework presented so far is very generic and not complete without the specific definition of particular forms for the individual terms of the Helmholtz free energy (5.8). Within this contribution we choose a Neo-Hookean type energy model for both, the elastic equilibrium energy ψ_{eq} as well as the non-equilibrium energy ψ_{neq}. Using the well known volumetric-isochoric split (see Flory [1961]), we define both of these energy contributions as

$$\psi_* := \frac{\mu_*}{2} \left[\operatorname{tr} \left(J_*^{-\frac{2}{3}} \mathbf{C}_* \right) - 3 \right] + \frac{\kappa_*}{4} \left(J_*^2 - 1 - 2 \ln J_* \right). \tag{5.22}$$

Here, $\mathbf{C}_*$ is referring either to $\mathbf{C}_M$ or $\tilde{\mathbf{C}}_e$, depending on the individual energy. Furthermore, $J_* = \sqrt{\det \mathbf{C}_*}$ describes the Jacobian determinant and μ_* and κ_* refer to the shear and bulk modulus of the individual energy contribution, respectively. For the energy density associated with damage hardening, we choose a combined formulation that is composed of a linear and a Voce-type (Voce [1948]) hardening term. Defining the material parameters k, r and s, this energy contribution reads

$$\psi_d(\xi_d) := \underbrace{\frac{1}{2}\, k\, \xi_d^2}_{\text{linear hardening}} + \underbrace{r \left(\xi_d + \frac{1}{s} \left[\exp(-s\xi_d) - 1 \right] \right)}_{\text{Voce-type hardening}}. \tag{5.23}$$

It should be mentioned here that whilst plastic hardening might have a clear physical interpretation, e.g. in the case of metal plasticity, the situation remains less clear for damage hardening not just for polymeric materials but in general. Nevertheless, in line with the phenomenological approach pursued in this paper, we included damage hardening into the model in order to make

it much more flexible in adapting to experimental data. For a short study on the influence of damage hardening, please see Appendix 5.7.4.

For the definition of the energy related to the micromorphic damage extension, we follow the choice made, for example, by Brepols et al. [2017*a*, 2020] such that

$$\psi_{\bar{d}}(D, \bar{D}, \nabla\bar{D}) := \frac{H}{2}\left(D - \bar{D}\right)^2 + \frac{A}{2}\nabla\bar{D}\cdot\nabla\bar{D}, \tag{5.24}$$

where H acts as a penalty parameter coupling the local and non-local damage fields whereas A describes the influence of the non-local damage gradient.

In general the specific heat capacity $c = -\Theta\partial^2\psi/\partial\Theta^2$ is determined by means of the temperature dependence of the free energy function ψ. It therefore depends on a variety of quantities such as, for example, the current temperature and the deformation state. Within this contribution, however, we make the simplifying assumption that the specific heat capacity c is a constant. To achieve this, we further assume that the caloric energy ψ_Θ implicitly takes a suitable form which ensures this. Please note that in this way, the caloric energy does not need to be defined explicitly but remains undetermined (see e.g. Lion [2000*a*]; Felder et al. [2022], among others).

5.3.2 Summary of constitutive equations

All constitutive equations derived above can be expressed in terms of the symmetric strain-like tensors $\mathbf{C}$ and $\mathbf{U}_v$, the temperature Θ, the global damage variable $\bar{D}$ and the local damage variable D. The internal variables used within this context are $\mathbf{U}_v$ and D, since the evolution of the damage hardening variable ξ_d is by definition equivalent to the evolution of D. For convenience, we provide a summary of the constitutive equations below:

- Stresses and stress-like quantities:
  $\mathbf{S} = 2f_d(D)\frac{\Theta}{\Theta_0}\left(\frac{\partial\psi_{eq}}{\partial\mathbf{C}} + \mathbf{U}_v^{-1}\frac{\partial\psi_{neq}}{\partial\tilde{\mathbf{C}}_e}\mathbf{U}_v^{-1}\right), \quad \mathbf{b}_{0_i} = \frac{\partial\psi}{\partial\,\mathrm{Grad}\,\bar{D}}, \quad a_{0_i} = \frac{\partial\psi}{\partial\bar{D}}$
- Heat flux:
  $\mathbf{q}_0 = -\mathbf{K}\,\mathrm{Grad}\,\Theta$
  $\mathbf{K} = \left[f_d(D)h_0 + (1 - f_d(D))h_d\right]\mathbf{C}^{-1}\,\mathrm{Grad}\,\Theta$
- Thermodynamically conjugate driving forces:
  $\tilde{\mathbf{M}} = 2f_d(D)\frac{\Theta}{\Theta_0}\tilde{\mathbf{C}}_e\frac{\partial\psi_{neq}}{\partial\tilde{\mathbf{C}}_e}, \quad Y = -\left(\frac{\partial f_d}{\partial D}\frac{\Theta}{\Theta_0}(\psi_{eq} + \psi_{neq}) + \frac{\partial\psi_{\bar{d}}}{\partial D}\right), \quad q_d = \frac{\partial\psi_d}{\partial\xi_d}$
- Damage onset criterion:
  $\Phi_d := Y - (Y_0 + q_d)$

- Evolution equations of damage and viscous deformation:
$$\dot{D} = \dot{\xi}_d = \begin{cases} \eta_d \left(\frac{\Phi_d}{Y_0 + q_d} \right)^{\frac{1}{\varepsilon_d}} & \text{if} \quad \Phi_d \geq 0 \\ 0 & \text{else} \end{cases}$$
$$\dot{\mathbf{C}}_v = \frac{\eta_v}{f_d} \mathbf{U}_v \left(\frac{1}{2\mu_v} \operatorname{dev} \left(\tilde{\mathbf{M}}_0 \right) + \frac{2}{3\kappa_v} \operatorname{vol} \left(\tilde{\mathbf{M}}_0 \right) \right) \mathbf{U}_v.$$

- Internal heat generation:
$$r_e = \frac{1}{2} \frac{\partial \mathbf{S}}{\partial \Theta} \Theta : \dot{\mathbf{C}},$$
$$r_v = \left(\tilde{\mathbf{M}} - \frac{\partial \tilde{\mathbf{M}}}{\partial \Theta} \Theta \right) : \tilde{\mathbf{D}}_v,$$
$$r_d = \left(Y - \frac{\partial Y}{\partial \Theta} \Theta \right) \dot{D} - \left(q_d - \frac{\partial q_d}{\partial \Theta} \Theta \right) \dot{\xi}_d + \frac{\partial a_{0_i}}{\partial \Theta} \Theta \dot{\bar{D}} + \frac{\partial b_{0_i}}{\partial \Theta} \Theta \cdot \operatorname{Grad} \dot{\bar{D}}.$$

A brief summary and description of the material parameters used within this modelling approach is given in Table 5.1.

5.4 Algorithmic implementation

For the investigation of the performances of the given material model we implemented the equations derived above into the finite element framework *FEAP* (Taylor and Govindjee [2020]). For the efficient and easy computation of derivatives, we used automatic differentiation as provided by the *Wolfram Mathematica* package *AceGen* (Korelc [2002, 2009]). Within the context of the numerical implementation, we needed to find appropriate numerical strategies for the solution of the Equations described in Section 5.3. These strategies are described briefly in the following. For the derivation of the finite element formulation used for the gradient-extended thermomechanical problem at hand, the interested reader is kindly referred to Felder et al. [2022] and the derivations made therein.

First, we introduce the discrete time interval $\Delta t = t_n - t_{n-1}$ with subscripts n and $n+1$ denoting the previous and current time step, respectively. For notational simplicity, we drop the subscript for the current time step in the following. With this in hand, we can use the exponential mapping algorithm as described e.g. in Dettmer and Reese [2004] or Vladimirov et al. [2009] to approximate the solution to the viscous evolution given in Equation (5.19), i.e.

$$\mathbf{U}_{v_n}^{-2} = \mathbf{U}_v^{-1} \exp \left(\Delta t \frac{\eta_v}{f_d} \left(\frac{1}{2\mu_v} \operatorname{dev} \left(\tilde{\boldsymbol{\Sigma}}_0 \right) + \frac{2}{3\kappa_v} \operatorname{vol} \left(\tilde{\boldsymbol{\Sigma}}_0 \right) \right) \right) \mathbf{U}_v^{-1}. \tag{5.25}$$

Notice that we can now express the overall viscous evolution solely in terms of the viscous stretch tensor $\mathbf{U}_v$, which will be used in the following as the internal variable describing viscous deformations. For further details on the derivation of this particular form of the discretized

evolution equation, we kindly refer the interested reader to Lamm et al. [2023] as well as the original literature.

In order to derive a discretized equation for the evolution of damage, we use an implicit Euler method to discretize the associated evolution equation given in Equation (5.21). This leads to the following formulation:

$$D = D_n + \Delta t\, \eta_d \left(\frac{\langle \Phi_d \rangle}{Y_0 + q_d} \right)^{\frac{1}{\varepsilon_d}} . \tag{5.26}$$

Here, $\langle \bullet \rangle$ describes the Macauley bracket, i.e. all values of Φ_d that are less than zero are explicitly set to zero.

For the solution of the resulting set of discretized coupled differential equations, we make use of a Newton-Raphson iteration scheme for which we must rewrite the equations in terms of residuals, i.e.

$$\begin{aligned} \hat{\mathbf{r}}_v &= \hat{\mathbf{U}}_{v_n}^{-2} - \hat{\mathbf{U}}_v^{-1} \exp\left(\Delta t \frac{\eta_v}{f_d} \left(\frac{1}{\mu_v} \operatorname{dev}\left(\hat{\bar{\boldsymbol{\Sigma}}}_0 \right) + \frac{2}{9\kappa_v} \operatorname{vol}\left(\hat{\bar{\boldsymbol{\Sigma}}}_0 \right) \right) \right) \hat{\mathbf{U}}_v^{-1} = \mathbf{0} \\ r_d &= D - D_n - \Delta t\, \eta_d \left(\frac{\Phi_d}{Y_0 + q_d} \right)^{\frac{1}{\varepsilon_d}} = 0. \end{aligned} \tag{5.27}$$

Here, we chose to use the vector valued Voigt notation denoted by $\hat{(\bullet)}$ to describe symmetric tensorial quantities. We can therefore combine both residua into the residual vector $\mathbf{r} := [\hat{\mathbf{r}}_v, r_d]^T$. Using the vector of arguments $\mathbf{x} := \left[\hat{\mathbf{U}}_v, D \right]^T$, we can find the incremental solution $\Delta\mathbf{x}$ by solving the linearized system of equations given by $\mathbf{J}_1 \Delta\mathbf{x} = -\mathbf{r}$. Here, the jacobian $\mathbf{J}_1$ is directly given as the matrix of partial derivatives such that

$$\mathbf{J}_1 = \begin{bmatrix} \frac{\partial \hat{\mathbf{r}}_v}{\partial \hat{\mathbf{U}}_v^{-1}} & \frac{\partial \hat{\mathbf{r}}_v}{\partial D} \\ \frac{\partial r_d}{\partial \hat{\mathbf{U}}_v^{-1}} & \frac{\partial r_d}{\partial D} \end{bmatrix} . \tag{5.28}$$

With this at hand, the updated solution vector is computed by applying $\mathbf{x}_{k+1} = \mathbf{x}_k + \Delta\mathbf{x}$ iteratively until sufficient convergence is achieved. Within this context, k and $k+1$ denote the previous and current iteration step, respectively.

For the global iteration scheme of the finite element solver used by *FEAP* we need to further provide the material sensitivities by means of the algorithmically consistent tangent operators for both, the mechanical as well as the thermal subproblem. For this, let us start with the sensitivities of the second Piola Kirchhoff stress $\mathbf{S}$ with respect to the independent variables

$\mathbf{C}$, $\bar{D}$ and Θ, which can be written as

$$\begin{aligned}
\frac{\mathrm{d}\mathbf{S}}{\mathrm{d}\mathbf{C}} &= \frac{\partial \mathbf{S}}{\partial \mathbf{C}} + \frac{\partial \mathbf{S}}{\partial \mathbf{U}_v} : \frac{\partial \mathbf{U}_v}{\partial \mathbf{C}} + \frac{\partial \mathbf{S}}{\partial D} \otimes \frac{\partial D}{\partial \mathbf{C}} \\
\frac{\mathrm{d}\mathbf{S}}{\mathrm{d}\bar{D}} &= \frac{\partial \mathbf{S}}{\partial \mathbf{U}_v} : \frac{\partial \mathbf{U}_v}{\partial \bar{D}} + \frac{\partial \mathbf{S}}{\partial D} \frac{\partial D}{\partial \bar{D}} \\
\frac{\mathrm{d}\mathbf{S}}{\mathrm{d}\Theta} &= \frac{\partial \mathbf{S}}{\partial \Theta} + \frac{\partial \mathbf{S}}{\partial \mathbf{U}_v} : \frac{\partial \mathbf{U}_v}{\partial \Theta} + \frac{\partial \mathbf{S}}{\partial D} \frac{\partial D}{\partial \Theta}.
\end{aligned} \tag{5.29}$$

Here, the terms marked in green color can be computed directly using automatic differentiation. All terms marked in red on the other hand, must be found implicitly. An approach on how to deal with this will be described later in this text. Similar to the second Piola Kirchhoff stress tensor, we can also find the material sensitivities of the internal heat generation r_{int} with respect to the independent variables as

$$\begin{aligned}
\frac{\mathrm{d}r_{int}}{\mathrm{d}\mathbf{C}} &= \frac{\partial r_{int}}{\partial \mathbf{C}} + \frac{\partial r_{int}}{\partial \mathbf{U}_v} : \frac{\partial \mathbf{U}_v}{\partial \mathbf{C}} + \frac{\partial r_{int}}{\partial D} \frac{\partial D}{\partial \mathbf{C}} \\
\frac{\mathrm{d}r_{int}}{\mathrm{d}\bar{D}} &= \frac{\partial r_{int}}{\partial \bar{D}} + \frac{\partial r_{int}}{\partial \mathbf{U}_v} : \frac{\partial \mathbf{U}_v}{\partial \bar{D}} + \frac{\partial r_{int}}{\partial D} \frac{\partial D}{\partial \bar{D}} \\
\frac{\mathrm{d}r_{int}}{\mathrm{d}\Theta} &= \frac{\partial r_{int}}{\partial \Theta} + \frac{\partial r_{int}}{\partial \mathbf{U}_v} : \frac{\partial \mathbf{U}_v}{\partial \Theta} + \frac{\partial r_{int}}{\partial D} \frac{\partial D}{\partial \Theta}.
\end{aligned} \tag{5.30}$$

Finally, the sensitivities of the heat flux vector $\mathbf{q}_0$ are given as

$$\begin{aligned}
\frac{\mathrm{d}\mathbf{q}_0}{\mathrm{d}\mathbf{C}} &= \frac{\partial \mathbf{q}_0}{\partial \mathbf{C}} + \frac{\partial \mathbf{q}_0}{\partial D} \otimes \frac{\partial D}{\partial \mathbf{C}} \\
\frac{\mathrm{d}\mathbf{q}_0}{\mathrm{d}\bar{D}} &= \frac{\partial \mathbf{q}_0}{\partial D} \frac{\partial D}{\partial \bar{D}} \\
\frac{\mathrm{d}\mathbf{q}_0}{\mathrm{d}\Theta} &= \frac{\partial \mathbf{q}_0}{\partial \Theta} + \frac{\partial \mathbf{q}_0}{\partial D} \frac{\partial D}{\partial \Theta} \\
\frac{\mathrm{d}\mathbf{q}_0}{\mathrm{d}\,\mathrm{Grad}\,\Theta} &= -\mathbf{K}.
\end{aligned} \tag{5.31}$$

As mentioned above, the partial derivatives marked in red must be calculated using an implicit formulation that will be described next. For this, let us introduce the vector $\mathbf{y} = \left[\hat{\mathbf{C}}, \bar{D}, \Theta\right]$ and furthermore define the jacobian of the residual vector $\mathbf{r}$ with respect to $\mathbf{y}$, i.e. $\mathbf{J}_2 = \frac{\partial \mathbf{r}}{\partial \mathbf{y}}$. By applying the chain rule of differentiation, we can come up with the following

matrix of partial derivatives,

$$\mathbf{J}_3 := \frac{\partial \mathbf{x}}{\partial \mathbf{y}} = -\mathbf{J}_1^{-1}\mathbf{J}_2 = \begin{bmatrix} \frac{\partial \hat{\mathbf{U}}_v}{\partial \hat{\mathbf{C}}} & \frac{\partial \hat{\mathbf{U}}_v}{\partial D} & \frac{\partial \hat{\mathbf{U}}_v}{\partial \Theta} \\ \frac{\partial D}{\partial \hat{\mathbf{C}}} & \frac{\partial D}{\partial D} & \frac{\partial D}{\partial \Theta} \end{bmatrix}. \tag{5.32}$$

The partial derivatives needed for the computation of the material sensitivities are then given directly as the corresponding submatrices of $\mathbf{J}_3$. A summary of the overall algorithm for the material model proposed herein is shown in Figure 5.1.

Thermomechanical material routine for viscoelasticity and rate-dependent damage

Input: $\hat{\mathbf{C}}$, $\bar{D}$, Θ, $\hat{\mathbf{U}}_v$, D, matPars

Output: $\hat{\mathbf{S}}$, $\hat{\mathbf{U}}_v$, D, $\frac{\partial \hat{\mathbf{S}}}{\partial \hat{\mathbf{C}}}$, $\frac{\partial \hat{\mathbf{S}}}{\partial D}$, $\frac{\partial \hat{\mathbf{S}}}{\partial \Theta}$, $\frac{\partial D}{\partial \hat{\mathbf{C}}}$, $\frac{\partial D}{\partial D}$, $\frac{\partial D}{\partial \Theta}$, $\frac{\partial r_{int}}{\partial \hat{\mathbf{C}}}$, $\frac{\partial r_{int}}{\partial D}$, $\frac{\partial r_{int}}{\partial \Theta}$, $\frac{\partial \mathbf{q}_0}{\partial \hat{\mathbf{C}}}$, $\frac{\partial \mathbf{q}_0}{\partial D}$, $\frac{\partial \mathbf{q}_0}{\partial \Theta}$, $\frac{\partial \mathbf{q}_0}{\partial \mathrm{Grad}\,\Theta}$

$f_d \leftarrow (1-D)^2$

Define energy contributions ψ_{eq}, ψ_{neq} etc.

$Y \leftarrow -\left(\frac{\partial f_d}{\partial D}\frac{\Theta}{\Theta_0}(\psi_{eq}+\psi_{neq}) + \frac{\partial \psi_{\bar{d}}}{\partial D}\right)$

$q_d \leftarrow \frac{\partial \psi_d}{\partial \xi_d}$

if $(Y-(Y_0+q_d)) \leq 0$ **then**

```
// Enforce purely viscoelastic step without damage
```

$\eta_d \leftarrow 0$

end if

```
// Solve local Newton iteration
```

$\left\{\hat{\mathbf{U}}_v, D, \mathbf{J}_1, \mathbf{J}_2\right\} \leftarrow$ doLocalNewtonRaphsonIteration()

$\mathbf{J}_3 \leftarrow -\mathbf{J}_1^{-1}\,\mathbf{J}_2$

```
// Get stresses and partial tangent operators
```

$\left\{\hat{\mathbf{S}}, \frac{\partial \hat{\mathbf{S}}}{\partial \hat{\mathbf{C}}}, \frac{\partial \hat{\mathbf{S}}}{\partial \hat{\mathbf{U}}_v}, \frac{\partial \hat{\mathbf{S}}}{\partial D}, \frac{\partial \hat{\mathbf{S}}}{\partial \Theta}\right\} \leftarrow$ getPK2andPartialTangents()

```
// Assemble tangent operators
```

$\frac{\partial \hat{\mathbf{S}}}{\partial \hat{\mathbf{C}}} \leftarrow \frac{\partial \hat{\mathbf{S}}}{\partial \hat{\mathbf{C}}} + \frac{\partial \hat{\mathbf{S}}}{\partial \hat{\mathbf{U}}_v}\mathbf{J}_3[1{:}6,\,1{:}6] + \frac{\partial \hat{\mathbf{S}}}{\partial D} \otimes \mathbf{J}_3[7,\,1{:}6]$

$\frac{\partial \hat{\mathbf{S}}}{\partial D} \leftarrow \frac{\partial \hat{\mathbf{S}}}{\partial \hat{\mathbf{U}}_v}\mathbf{J}_3[1{:}6,\,7] + \frac{\partial \hat{\mathbf{S}}}{\partial D}\,\mathbf{J}_3[7,\,7]$

$\frac{\partial \hat{\mathbf{S}}}{\partial \Theta} \leftarrow \frac{\partial \hat{\mathbf{S}}}{\partial \Theta} + \frac{\partial \hat{\mathbf{S}}}{\partial \hat{\mathbf{U}}_v}\mathbf{J}_3[1{:}6,\,8] + \frac{\partial \hat{\mathbf{S}}}{\partial D}\mathbf{J}_3[7,\,8]$

$\frac{\partial r_{int}}{\partial \hat{\mathbf{C}}} \leftarrow \frac{\partial r_{int}}{\partial \hat{\mathbf{C}}} + \frac{\partial r_{int}}{\partial \hat{\mathbf{U}}_v}\mathbf{J}_3[1{:}6,\,1{:}6] + \frac{\partial r_{int}}{\partial D} \otimes \mathbf{J}_3[7,\,1{:}6]$

$\frac{\partial r_{int}}{\partial D} \leftarrow \frac{\partial r_{int}}{\partial \hat{\mathbf{U}}_v}\mathbf{J}_3[1{:}6,\,7] + \frac{\partial r_{int}}{\partial D}\,\mathbf{J}_3[7,\,7]$

$\frac{\partial r_{int}}{\partial \Theta} \leftarrow \frac{\partial r_{int}}{\partial \Theta} + \frac{\partial r_{int}}{\partial \hat{\mathbf{U}}_v}\mathbf{J}_3[1{:}6,\,8] + \frac{\partial r_{int}}{\partial D}\mathbf{J}_3[7,\,8]$

$\frac{\partial \mathbf{q}_0}{\partial \hat{\mathbf{C}}} \leftarrow \frac{\partial \mathbf{q}_0}{\partial \hat{\mathbf{C}}} + \frac{\partial \mathbf{q}_0}{\partial D} \otimes \mathbf{J}_3[7,\,1{:}6]$

$\frac{\partial \mathbf{q}_0}{\partial D} \leftarrow + \frac{\partial \mathbf{q}_0}{\partial D}\,\mathbf{J}_3[7,\,7]$

$\frac{\partial \mathbf{q}_0}{\partial \Theta} \leftarrow \frac{\partial \mathbf{q}_0}{\partial \Theta} + \frac{\partial \mathbf{q}_0}{\partial D}\mathbf{J}_3[7,\,8]$

$\frac{\partial \mathbf{q}_0}{\partial \mathrm{Grad}\,\Theta} \leftarrow -\mathbf{K}$

Figure 5.1: Pseudo code for the proposed material model at integration point level.

5.5 Numerical examples

Within the following section, we investigate the capabilities of the proposed material model using numerical simulations. For this, we start with a general parameter study conducted at integration point level in order to show the overall behaviour of the material model with respect to the individual material parameters. Afterwards, we show some structural examples including more complex geometries and boundary conditions. Here, we used the finite element formulation recently described by Felder et al. [2022], which uses a Q1 based discretisation of the fully coupled thermoelastic micromorphic damage formulation given above. For all the simulations shown herein, we used the general purpose finite element software *FEAP* (Taylor and Govindjee [2020]) together with the open source software tools *GMSH* (Geuzaine and Remacle [2009]) and *ParaView* for meshing and visualization, respectively.

5.5.1 Parameter studies

For the parameter studies conducted in the following, we use a three dimensional single element with edge length of $l_x = l_y = l_z = 1$ mm and apply the corresponding boundary conditions such that a uniaxial deformation state is achieved. For the viscoelastic energy contribution, we choose an elastic Neo-Hookean ground model with the same parameter sets for both, the equilibrium and the non-equilibrium parts. These are given by $\mu_* = 30\ \frac{\mathrm{N}}{\mathrm{mm}^2}$ and $\kappa_* = 3000\ \frac{\mathrm{N}}{\mathrm{mm}^2}$, respectively. Furthermore, the damage parameter is set to $\varepsilon_d = 1.0$. Since we do not consider a structural simulation at this stage of our investigations, the gradient extension parameters A and H are also set to zero. Additionally, we also choose the hardening parameters r, s and k to become zero in order to get a clearer view on the influence of the remaining parameters. For the referential temperature, the conductivity and the volume specific heat capacity we choose $\Theta_0 = 273.15$ K, $h_0 = h_d = 0.0\ \frac{\mathrm{W}}{\mathrm{mm\ K}}$ and $c = 3.588\ \frac{\mathrm{J}}{\mathrm{mm}^3\ \mathrm{K}}$. The thermal expansion coefficient is set to $\alpha_\Theta = 0.01\ \mathrm{K}^{-1}$. Since the focus of this work is on modelling rate-dependent damage, we will limit the parameter studies shown in the following sections to the influence of the parameters describing exactly this behaviour. For more detailed evaluations in the context of thermocoupled finite viscoelasticity, the interested reader is kindly referred to the existing extensive literature on this topic.

5.5.1.1 Constant deformation rate

The first example considers a displacement that is applied to the system at hand with a constant deformation rate of $\dot{u}_x = 0.5\ \frac{\mathrm{mm}}{\mathrm{s}}$. We first take a look at the influence of the damage velocity

parameter η_d with respect to the damage evolution as well as the internal heat generated due to dissipational effects. For this purpose, we set the relaxation velocity $\eta_v = 0.0\ \mathrm{s}^{-1}$ and only take a look at the pure damage behaviour.

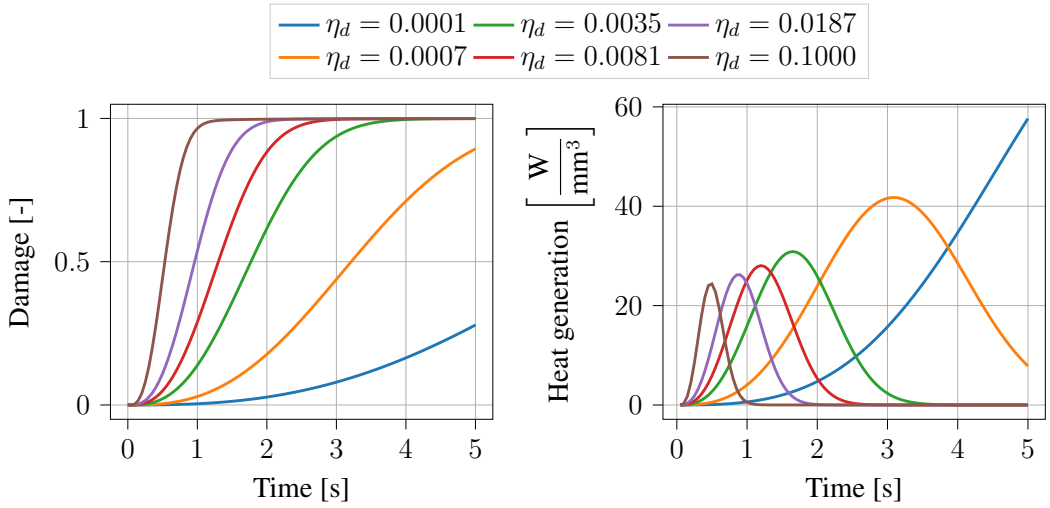

Figure 5.2: Influence of the damage velocity η_d on both, the evolution of the damage variable D (left) as well as the internal heat generation due to damage (right). Results are given for a viscous relaxation velocity of $\eta_v = 0\ \mathrm{s}^{-1}$.

Figure 5.2 shows the results of this investigation. It is clearly visible that higher values of η_d result in a faster evolution of damage and vice versa. Similarly, the heat generated due to the overall dissipation shows that a higher damage velocity also yields a faster release of energy. Furthermore, it is visible that lower values of η_d lead to more heat being generated throughout the damage process. If we take a look at the boundary conditions applied in this example, this result is as expected. Since we specify a constant deformation rate, more and more deformation related energy is introduced into the system over time. On the other hand, the damage progression in the material develops more slowly as the damage velocity η_d is decreased. This leads to the fact that for smaller values of η_d, more energy can be introduced into the system before being released again due to the damage process.

Next, we consider the influence of the damage threshold Y_0. For this, we set the damage velocity to $\eta_d = 0.01\ \mathrm{s}^{-1}$ and evaluate the same boundary value problem as above for a varying Y_0. Figure 5.3 shows the results of this variation. We can observe that a lower damage threshold lead to an earlier onset of the damage process. A similar behaviour is also reflected within the progression of the heat generation due to damage, which is depicted on the right plot in Figure 5.3. Here, higher values of Y_0 again yield a later damage onset together with more energy being released throughout the damage process. Similarly to the example above, this is mainly

due to the fact that, the later damage starts to evolve, the more energy is already stored in the system. This additional energy can then be released during the damage of the material.

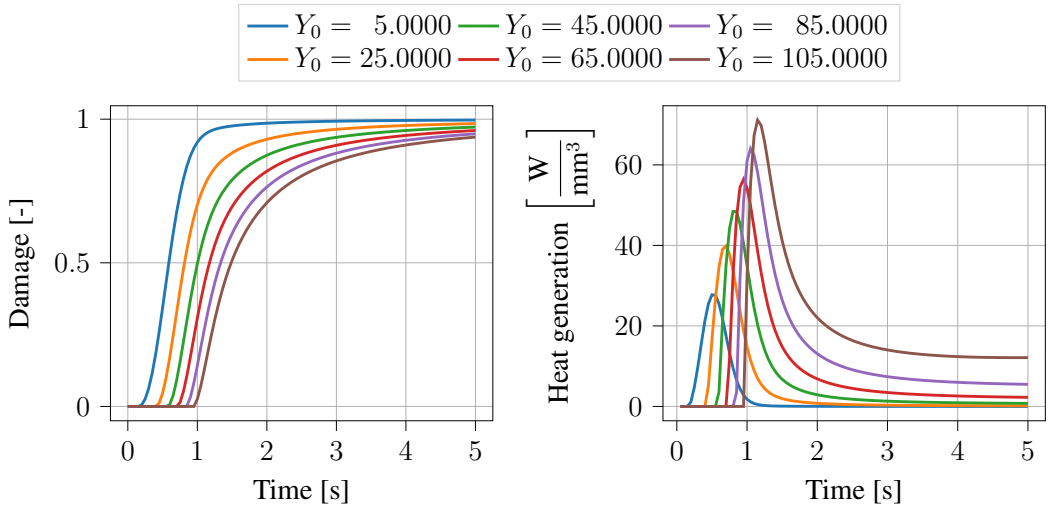

Figure 5.3: Influence of the damage threshold Y_0 on both, the evolution of the damage variable D (left) as well as the internal heat generation due to damage (right). Results are given for a viscous relaxation velocity of $\eta_v = 0\ \mathrm{s}^{-1}$ as well as a damage velocity of $\eta_d = 0.1\ \mathrm{s}^{-1}$.

5.5.1.2 Relaxation

For the next example, we consider the simulation of a uniaxial relaxation experiment. Here we increase the displacement within 0.2 s to $u_x = 0.5$ mm and then keep it constant. The influence of the damage velocity parameter η_d on the reaction force and the heat generated due to dissipation is shown in Figure 5.4a. As shown on the left side of Figure 5.4a, the reduction of the reaction force in the loading direction is faster with increasing η_d. For example, for $\eta_d = 0.0433\ \mathrm{s}^{-1}$, complete damage is reached after about one second, while for $\eta_d = 0.0001\ \mathrm{s}^{-1}$, about 90 per cent of the initial reaction force is still present even after $5\ s$. Furthermore, it can be seen that the peak value of the reaction force reduces with increasing η_d and shifts further forward. This effect is to be expected because the accumulated damage in the material under consideration can no longer be neglected at high damage speeds even in the ascending load branch. As a result, a correspondingly high initial reaction force can only build up at very low damage velocities. This behaviour is also reflected in the course of the heat development, as it is depicted on the right side of Figure 5.4a. A faster damage development leads here to a faster and higher increase in the generated heat at high values of η_d. For low

values of the damage rate, the high point of dissipation is shifted backwards in time and the heat curve flattens out.

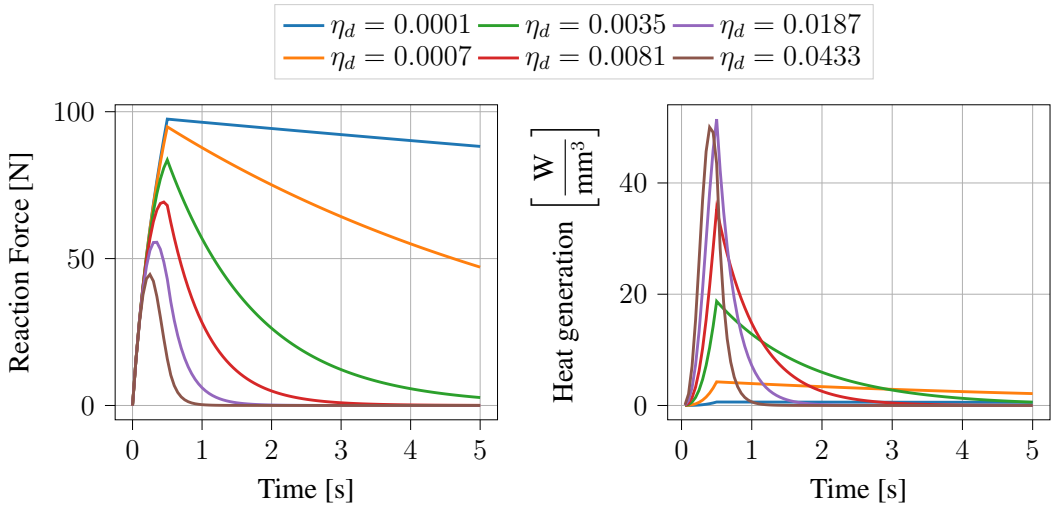

(a) Influence of the damage velocity η_d.

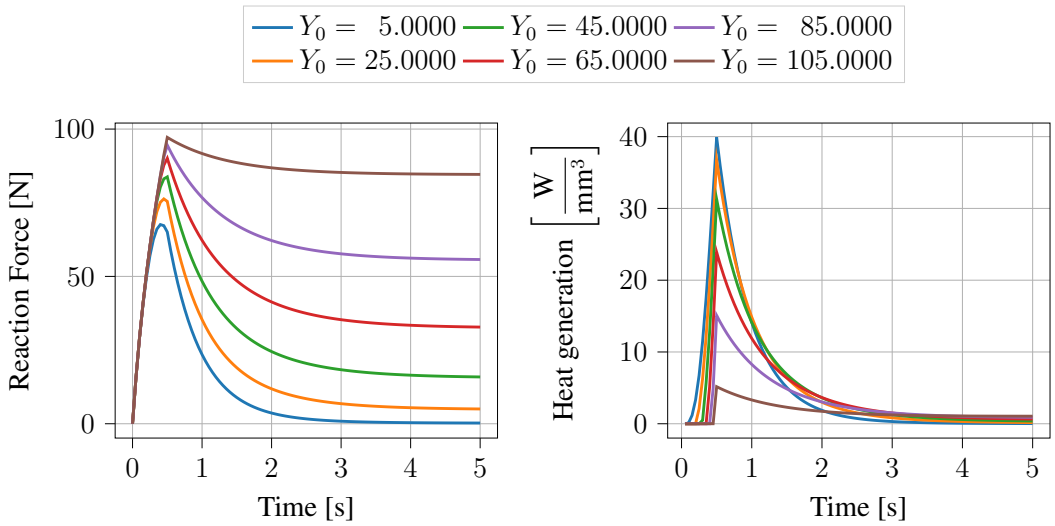

(b) Influence of the damage threshold Y_0. Results given for a damage velocity of $\eta_d = 0.01\ \mathrm{s}^{-1}$.

Figure 5.4: Influence of the damage velocity η_d and the damage threshold Y_0 on the internal heat generation for a relaxation simulation. Results are given for a viscous relaxation velocity of $\eta_v = 0\ \mathrm{s}^{-1}$.

Next, we take a look at the evolution of the damage response as well as the corresponding heat production for variations in the damage threshold Y_0. Figure 5.4b shows both of these quantities over time for a constant damage velocity $\eta_d = 0.01\ \mathrm{s}^{-1}$ and a viscous relaxation velocity $\eta_v = 0.0\ \mathrm{s}^{-1}$. These results show a different behaviour of the damage response as the ones given in Figure 5.4a. It is clearly visible that the damage process starts earlier for lower

values of Y_0. This effect is as expected, since the lower the threshold, the earlier it is overshot during loading and therefore triggers the damage process. Another interesting effect that can be seen in the results is the fact that for higher values of Y_0, the solution seems to converge towards a stationary value for the reaction force that is not equal to zero. Whilst such an effect might be unexpected at first sight, it can easily be explained and is in line with the theory lying behind the proposed model. If damage is triggered in the material, its stiffness and therefore also the stored energy is reduced gradually. For higher values of the damage threshold, this can lead to a point at which the damage driving force Y becomes smaller than the given threshold and the damage process comes to an end. This effect is also very well reflected in the heat generation due to damage shown on the right side of Figure 5.4b. The lower the value of Y_0, the earlier energy is dissipated due to the damage process and transformed into heat. Furthermore, the total amount of energy dissipated over time given by the integral of the heat curves is lower for higher values of the damage threshold. This is a clear indicator for the interpretation that in such cases not all of the elastically stored energy is dissipated leading to a residual stiffness of the material.

5.5.1.3 Creep

In the following example, we show the simulation of a simple creep experiment. For this, a force of $F = 5$ N was uniaxially applied within 0.1 s and kept constant for the rest of the simulation. We again considered the influence of the damage velocity η_d on the development of the displacement as well as the associated heat generation. The results of this investigation can be found in Figure 5.5a. It can be observed that, similarly to the results from in the investigations shown above, a higher value of η_d results in a faster accumulation of damage within the material. In the case of this creep simulation this yields an exponential growth of the measured displacement. Since a fully damaged material has effectively zero stiffness, this would ultimately lead to an infinite displacement. This behaviour is nicely reflected in the evaluation shown on the left side of Figure 5.5a. Considering the heat generation due to damage in the material, the right side of Figure 5.5a shows that the heat generation is directly proportional to the displacement measured and therefore also to the amount of damage accumulated. Here it is evident that a faster development of damage also leads to a higher initial heat release.

Furthermore, Figure 5.5b shows the results from a parameter study considering the influence of the damage threshold Y_0 on the same creep experiment. For this, we show both, the displacement as well as the generated heat over time for constant values of the damage velocity $\eta_d = 0.01$ s^{-1} and a viscous relaxation velocity of $\eta_v = 0.0$ s^{-1}. Here again, lower values of

Y_0 lead to a faster and more pronounced evolution of damage and therefore of the associated displacements as well as the heat generated due to dissipation.

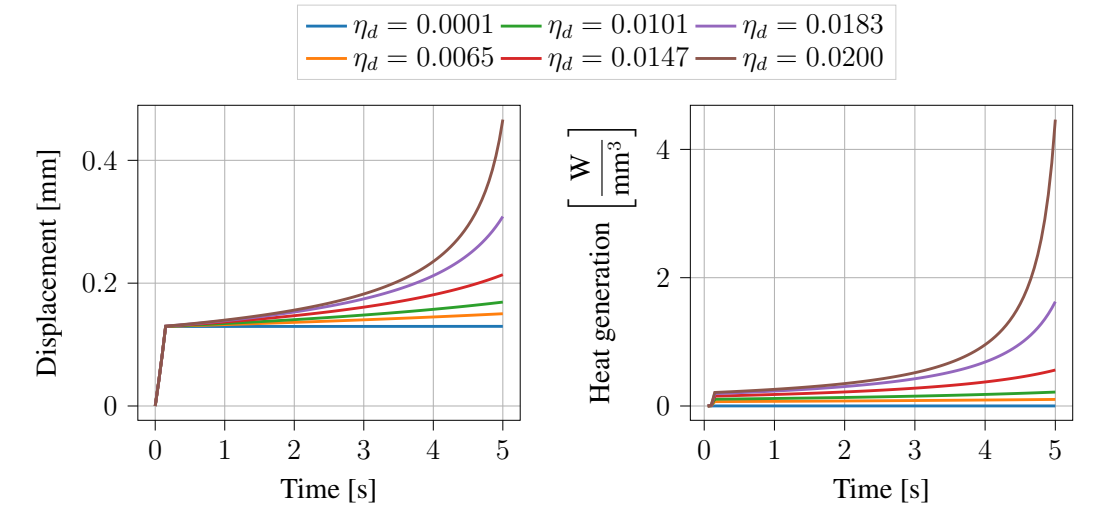

(a) Influence of the damage velocity η_d.

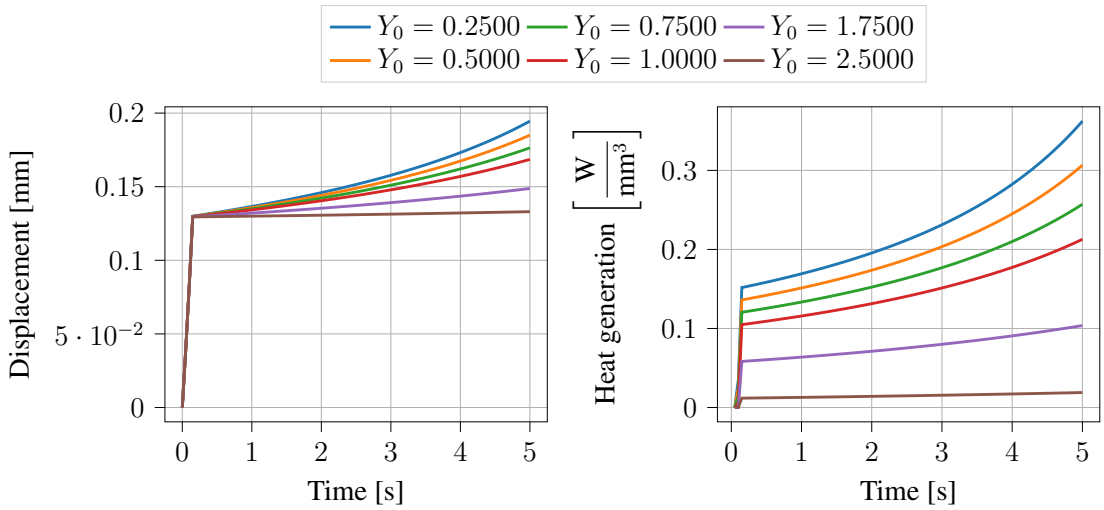

(b) Influence of the damage threshold Y_0. Results are given for a damage velocity of $\eta_d = 0.01\ \mathrm{s}^{-1}$.

Figure 5.5: Influence of the damage velocity η_d and of the damage threshold Y_0 on the evolution of the global displacements as well as the internal heat generation for a creep simulation. Results are given for a viscous relaxation velocity of $\eta_v = 0\ \mathrm{s}^{-1}$.

5.5.1.4 Cyclic loading

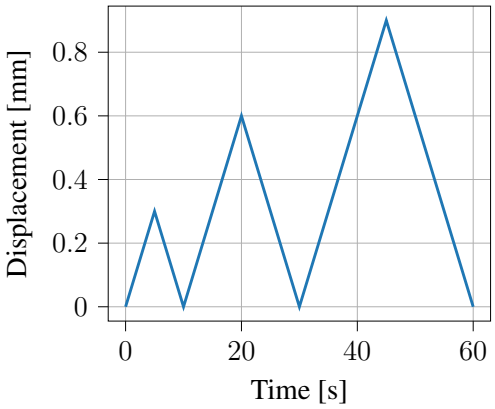

Figure 5.6: Loading pattern for cyclic loading simulation used in parameter study.

As a final example in this section on the influence of material parameters, we show the simulation of a displacement-driven cyclic loading experiment conducted under uniaxial loading conditions. For this, we linearly increased the displacement during the first 5 s to a value of $u_x = 0.3$ mm and decreased it afterwards to $u_x = 0$ mm. Two additional cycles were applied afterwards with the maximum values of the displacement of $u_x = 0.6$ mm at $t = 20$ s and $u_x = 0.9$ mm at $t = 45$ s (see Figure 5.6). For this investigation, we took a look at the influence of the damage velocity η_d as well as the damage threshold Y_0. The results showing their influence on the progression of damage as well as the associated heat generation are shown in Figures 5.7 and 5.8, respectively.

Figure 5.7 shows the progression of damage over time on the left as well as the development of the corresponding heat generation on the right for four different choices of the damage velocity η_d. The progression of the quantities of interest over time can be found in Appendix 5.7.5. Here it can be observed that damage only increases during the loading phases and remains constant during the unloading phases. This is also reflected in the heat generation in that the highest values occur at those points in time where the damage rate reaches its respective maximum value. Depending on the amount of newly accumulated damage during one loading cycle, the additional amount of generated heat also differs. For larger steps in the damage progression also more heat is generated and vice versa. This effect makes total sense from a qualitative point of view. Since the development of damage changes with a change in η_d, the corresponding maximum values in the heat generation are shifted in time. Furthermore, it can be observed that the curves for $\eta_d = 0.02$ s^{-1} and $\eta_d = 0.03$ s^{-1} strongly converge in the last load cycle.

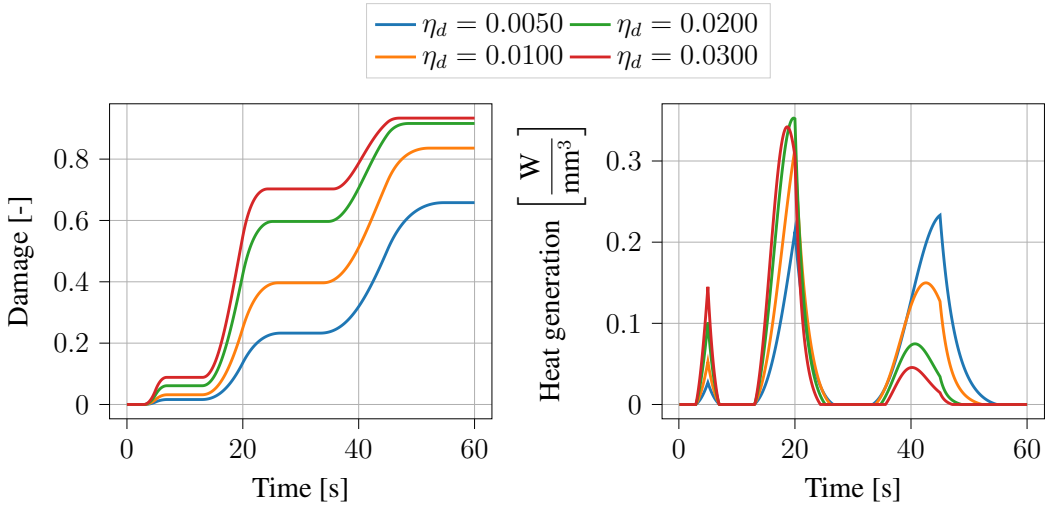

Figure 5.7: Influence of the damage velocity η_d on the internal heat generation for a cyclic loading simulation. Results are given for a viscous relaxation velocity of $\eta_v = 0\,\mathrm{s}^{-1}$.

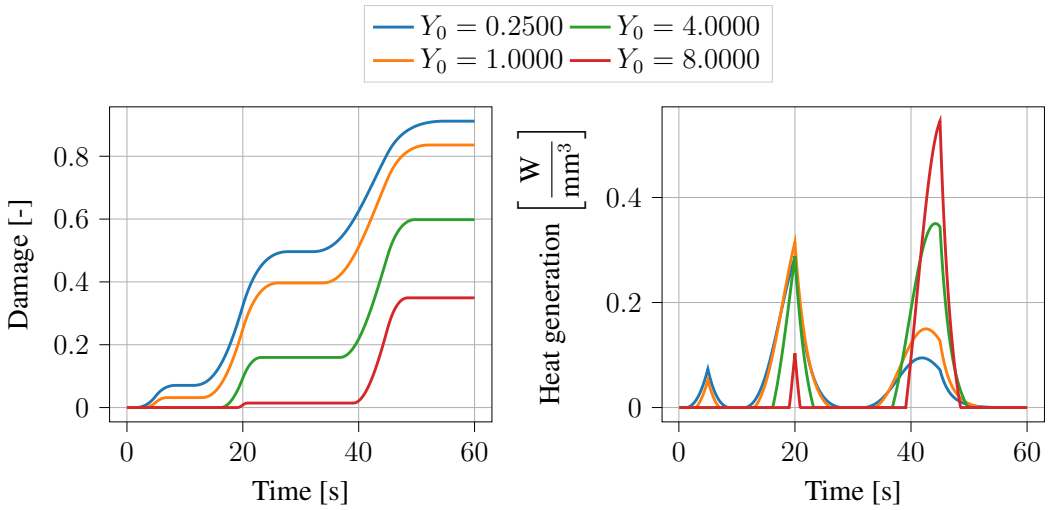

Figure 5.8: Influence of the damage velocity Y_0 on the internal heat generation for a cyclic loading simulation. Results are given for a viscous relaxation velocity of $\eta_v = 0\,\mathrm{s}^{-1}$ and a damage velocity of $\eta_d = 0.01\ \mathrm{s}^{-1}$.

Table 5.1: List of all material parameters that are included in the proposed material model and are used for the structural simulations.

Symbol	Value	Units	Description
μ_{eq}	6.0	$\frac{\text{N}}{\text{mm}^2}$	Elastic shear modulus
κ_{neq}	3000	$\frac{\text{N}}{\text{mm}^2}$	Elastic bulk modulus
μ_v	6.0	$\frac{\text{N}}{\text{mm}^2}$	Viscous shear modulus
κ_v	3000	$\frac{\text{N}}{\text{mm}^2}$	Viscous bulk modulus
η_v	0.055	$\frac{1}{\text{s}}$	Viscoelastic relaxation velocity
η_d	0.002	$\frac{1}{\text{s}}$	Damage evolution velocity
Y_0	1.0	$\frac{\text{N}}{\text{mm}^2}$	Damage threshold
ε_d	1.0	$-$	Damage evolution shape parameter
k	0.0	$\frac{\text{N}}{\text{mm}^2}$	Linear damage hardening parameter
r	0.0	$\frac{\text{N}}{\text{mm}^2}$	Voce-type damage hardening parameter 1
s	1.0	$-$	Voce-type damage hardening parameter 2
H	10^5	$\frac{\text{N}}{\text{mm}^2}$	Micromorphic coupling between local an non-local damage fields
A	50	N mm^2	Micromorphic influence of non-local damage gradient
Θ_0	293.15	K	Referential temperature
h_0	0.19	$\frac{\text{W}}{\text{mm K}}$	Undamaged heat conductivity
h_d	0.0	$\frac{\text{W}}{\text{mm K}}$	Damaged heat conductivity
c	3.588	$\frac{\text{J}}{\text{mm}^3\,\text{K}}$	Volume specific heat capacity
α_Θ	0.001	K^{-1}	Heat expansion coefficient

This can be attributed to the fact that the damage value of $D = 0.93$ represents the maximum damage level achievable under the given boundary conditions. This is also supported by the fact that the damage rate for $\eta_d = 0.03\ \text{s}^{-1}$ strongly decreases during this cycle. Figure 5.8 shows the influence of the damage threshold Y_0 on the development of both, damage (left) and the corresponding heat generation (right). These results were achieved with a viscous relaxation velocity of $\eta_v = 0\ \text{s}^{-1}$ and a damage velocity of $\eta_d = 0.01\ \text{s}^{-1}$. As described above, the corresponding force-displacement diagrams are given in Appendix 5.7.5. Especially for $Y_0 = 4.0$ and $Y_0 = 8.0$ the influence of the damage threshold is clearly visible, because here no damage is accumulated in the first loading cycle. Only in the last two cycles is the corresponding threshold exceeded at the specified load, such that damage can develop in the material. For a value of $Y_0 = 8.0$ this effect can be observed particularly well. The same behaviour can also be observed in the corresponding curves of the generated heat. If we compare the results from this investigation with those from Figure 5.7, it is immediately apparent that the choice of the damage threshold also has a direct influence on the amount of accumulated damage after three load cycles. For the same damage rate η_d, more damage can build up in the material if Y_0 is chosen smaller.

5.5.2 Structural examples

After having shown and evaluated the influences of some of the material parameters associated with the rate dependent behaviour of the proposed damage model, we will next show some examples of simulations using more complex boundary value problems. For this, we first show the results of a relaxation experiment conducted on a double notched specimen. Next, we show the behaviour of a creep simulation performed usind a plate with a singular hole at its center. We furthermore present results of the simulation of a silicone duckbill valve subjected to a cyclic loading scenario. If not stated otherwise for the individual example, the related material parameters parameters used for the simulation are given in Table 5.1. It is important to point out that we chose the parameters related to inelastic effects as constants. This rather strong assumption should be replaced with temperature related functions adjusted to experimental data once available. For the time being, we use this choice for demonstrative purpose only. Furthermore, we would like to point out that the choice of the viscous and elastic moduli having the same value is in this case arbitrary, since the parameters used in these examples were not determined using experimental data.

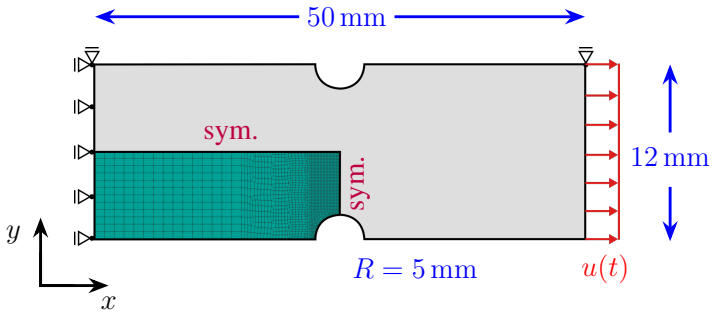

Figure 5.9: Schematic drawing of the double notched specimen geometry used for the simulation of a relaxation experiment. Due to symmetry, only a quarter of the whole geometry is used. The simulation is performed using a full three dimensional model.

5.5.2.1 Double notched specimen

We start with the example of a simulation of a symmetrically notched specimen subjected to uniaxial boundary conditions. Due to the symmetry of the given boundary value problem, we used only a quarter of the overall structure for the simulation. Figure 5.9 shows a schematic drawing of the boundary value problem used here. The time dependent displacement boundary condition is applied with a constant rate during the first 20 s and held constant afterwards at a

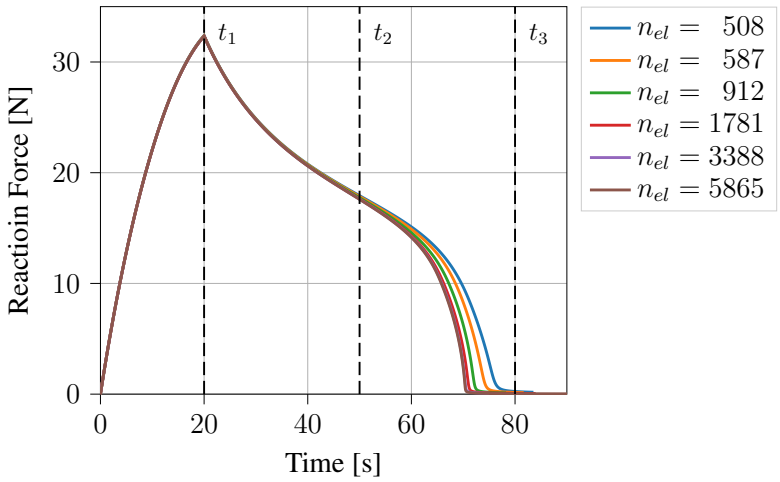

Figure 5.10: Results of the development of the reaction force recorded from the relaxation simulation of the double notched specimen. Evaluated for six different levels of refinement. The number of elements used is given by n_{el}. Convergence of the solution can be observed for finer discretizations.

value of $u_x = 10$ mm. The spatial discretization is refined in the region of the notches, since this is the place where damage is supposed to appear most predominantly.

In order to obtain a unique solution, we investigated the influence of the mesh size for the given problem. For this, we refined the mesh mainly within the region of interest around the notches. The results of this investigation are shown in Figure 5.10. Here, the reaction force due to the applied displacement boundary conditions is shown for six different levels of discretization. It can be observed that finer discretizations lead to a converged solution. Furthermore, it can be seen that the mesh dependencies only effect the solution in the high damage regime starting at around 55 s within this simulation. This is an important finding, since many applications do not need to take the high damage regime into account. This gives such applications the advantage of using coarser spatial discretisation and therefore saving computational costs. Figure 5.11 shows selected contour plots for the results of the damage variable D (left), the effective viscous stretch $U_{v,eff} = \sqrt{\mathbf{U}_v : \mathbf{U}_v}$ (right) and the overall temperature Θ (middle) at three different points in time. The original (undeformed) geometry is denoted by black lines and all elements with a damage value of $D > 0.99$ are removed from the pictures. At time $t = 20$ s the maximum displacement boundary condition is applied, which is kept constant in the following. Due to the relatively low damage velocity η_d, no significant damage accumulation can yet be observed in the structure at this point. The effective viscous strain, on the other hand, is already greater than zero throughout the structure at this point in time, with higher values observed in the area of the narrowest part of the cross-section. As

can be seen in the temperature distribution, this leads to a temperature increase in the same region of the sample. The temperature maximum can be observed, as expected, in the area of the largest viscous strains. This is reasonable since the most energy is dissipated at this point in space.

As already shown in Figure 5.10, viscous deformation dominates over damage in the initial phase of the relaxation process. Here, especially the area at the notch is influenced by viscoelastic deformation and leads to a corresponding heating of the material in this area. In the later course of the simulation, however, damage dominates as the main inelastic effect. This becomes very clear in the lower two rows of Figure 5.11. Here, damage starts in the area of the notch and develops gradually from there towards the middle symmetry axis of the structure. The energy released in this process contributes significantly to an increase in the temperature of the material in the area of the crack edge. As the crack progresses, the cross-sectional area available for load transfer is reduced and the overall stiffness of the structure decreases. This allows the upper part of the structure to contract more, inhibiting the viscous strain process in this area. As soon as the crack has moved completely through the material, the corresponding structure can be considered as completely unloaded under the given boundary conditions. From this point in time onwards, further heat production therefore only takes place in regions where the material relaxes towards its stress free configuration. Therefore, the viscous strains still existing in the material can now be gradually reduced, so that the original geometric dimensions of the structure are achieved again over time. Changes in termperature after this point are mainly due to the conduction of heat throughout the undamaged material.

Overall, it can be stated that the material behaviour observed here can be assessed as plausible from a qualitative point of view. In particular, the effect of damage related full relaxation as well as the coupling between the inelastic effects considered and the temperature development can be captured nicely in this structural simulation.

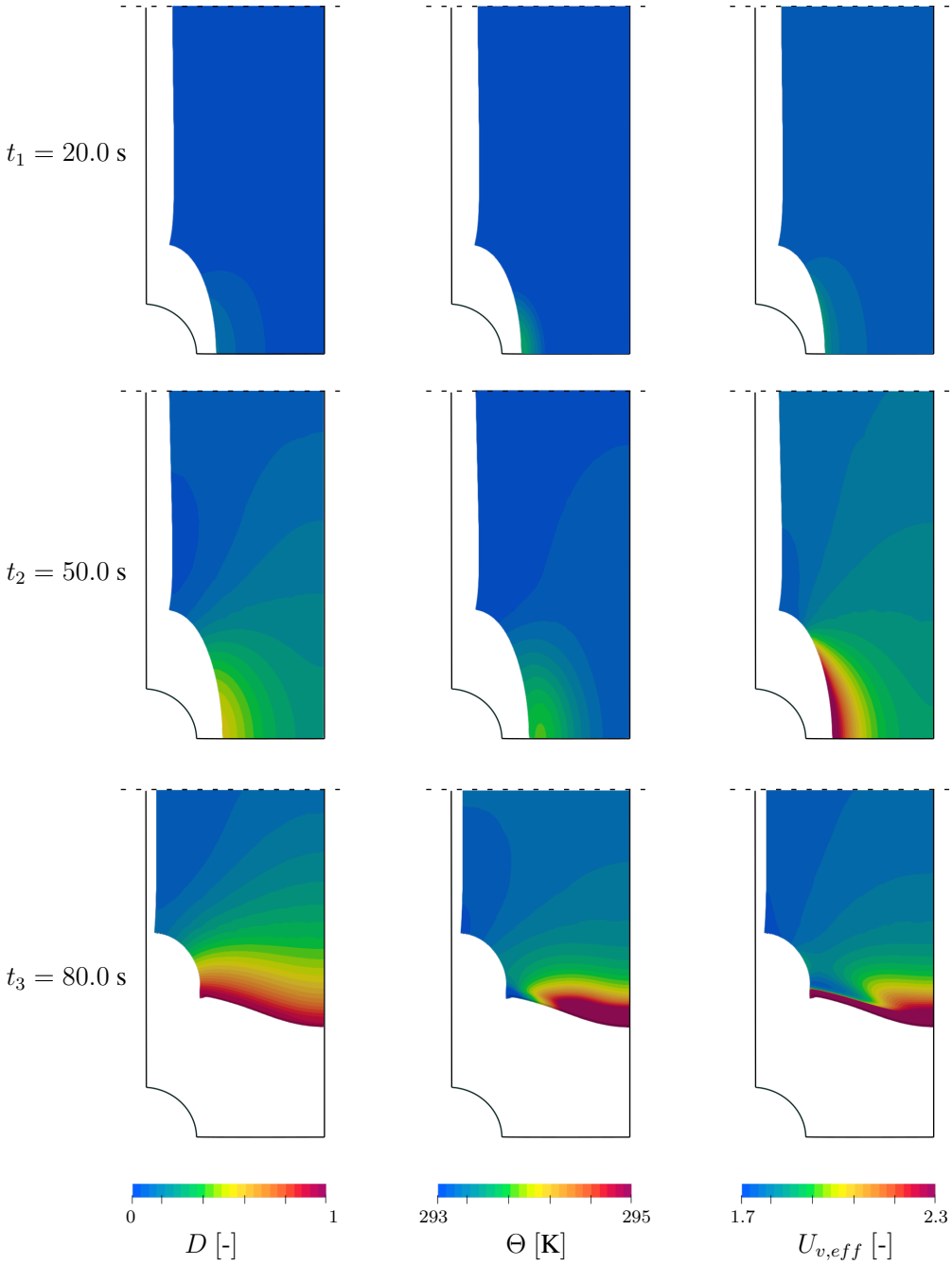

Figure 5.11: Selected results of the relaxation simulation at a double notched specimen. Only the middle of the symmetric part of the specimen is shown. The original (undeformed) geometry is denoted by black lines. Elements with a damage value of $D > 0.99$ are removed from the pictures. The effective viscous stretch is calculated as $U_{v,eff} = \sqrt{\mathbf{U}_v : \mathbf{U}_v}$. Points in time t_1, t_2 and t_3 are highlighted in Figure 5.10.

5.5.2.2 Plate with hole

In the second example, we consider the simulation of a plate with a singular hole located in its middle. Again, due to the symmetry of the given system, we used only a quarter of the overall structure for the simulation. The structure including boundary values is shown schematically in Figure 5.12. We applied a time dependent surface loading $q_x(t)$ on the outer left and right edges of the plate. This loading was linearly increased during the first 10 s until a value of $q_x = 0.5\ \frac{\mathrm{N}}{mm^2}$ was reached. During the remainder of the simulation, the load was held constant resulting in a classical creep setup. We chose to refine the spatial discretization at the symmetry plane that is perpendicular to the loading direction. This is the region where damage is supposed to mainly occur during the simulation which yields the need for a relatively fine mesh to capture the damage process precisely.

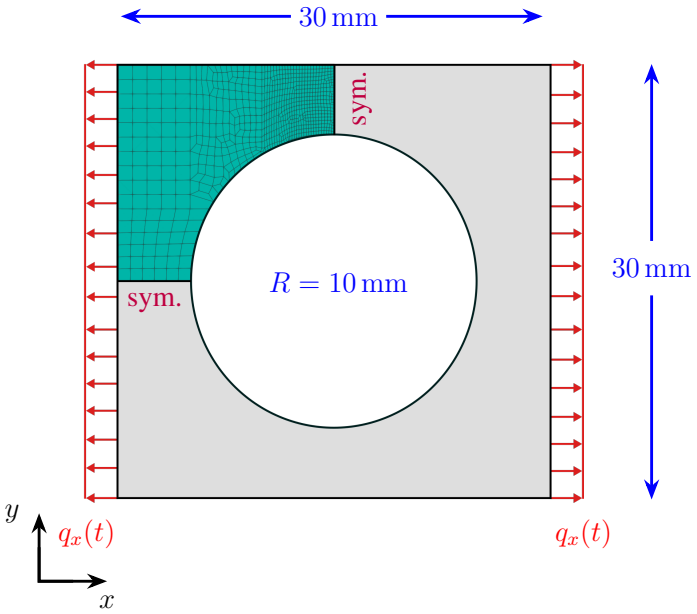

Figure 5.12: Schematic drawing of the plate with holeg eometry used for the simulation of a creep experiment. Due to symmetry, only a quarter of the whole geometry is used. The simulation is performed using a full three dimensional model.

We again investigated the influence of the spatial discretization on the uniqueness of the solution for this boundary value problem. Figure 5.13 shows the displacement over time for two different levels of discretization. It is clearly visible that the results for both discretizations yield the same solution even though the number of elements was nearly four times higher for the finer mesh than for the coarse mesh. This behaviour gives us confidence to assume that this simulation converges towards a unique solution.

Figure 5.13 furthermore shows a pronounced creep damage behaviour of the given structure. This behaviour can be observed for many materials and is characterised by an initial phase of viscous creep followed by abrupt crack propagation, leading to an exponential increase in the measured displacements. Classical rate-independent damage models are usually not able to reproduce this behaviour, as full damage always occurs at the time of the highest energy of the system. However, this is the case directly at the beginning of the creep process, which means that complete damage to the material would also occur at this point. In contrast, the model proposed by us in this paper is able to represent the desired behaviour in a qualitatively meaningful way.

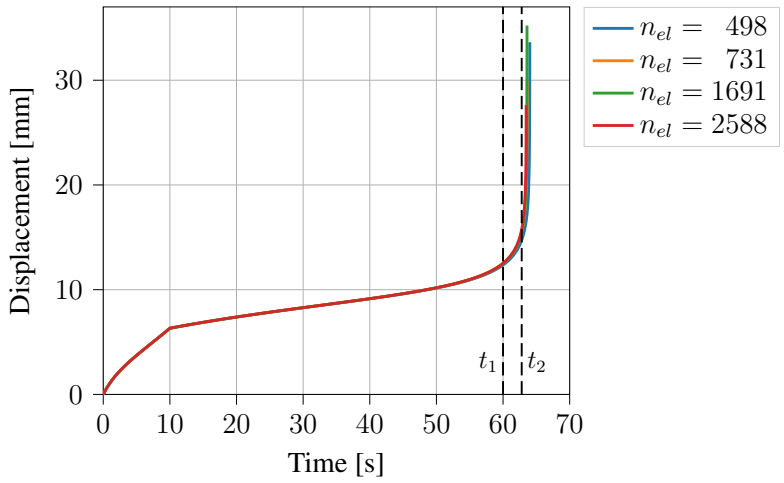

Figure 5.13: Results of the development of the displacement recorded from the creep simulation of the plate with a hole. Evaluated for two different levels of refinement. The number of elements used is given by n_{el}.

If we take a look at the development of the damage variable D, the effective viscous stretch $U_{v,eff}$ and the temperature Θ in Figure 5.14 at the end of the simulation, the rapid propagation of damage at this point in time becomes particularly visible. This is accompanied by a strong increase in temperature in the area where most of the damage is accumulated. Compared to this, the effective viscous stretch develops only relatively slowly at this point. This can be associated with creep process already progressing towards its end. In contrast to the previous structural example from Section 5.5.2.1, an increasing damage propagation does not automatically lead to a reduction of loading of the structure and, thus, does not necessarily reduce the development of viscous stretches.

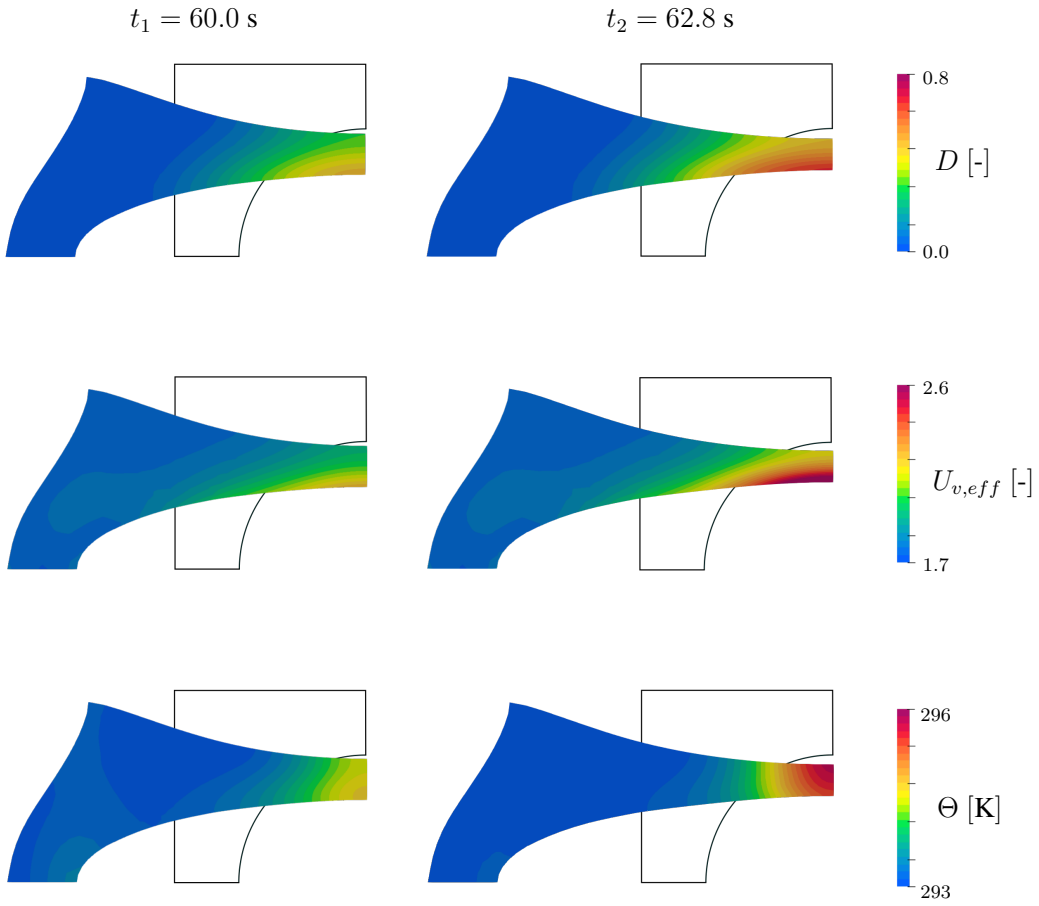

Figure 5.14: Selected results of the relaxation simulation of a plate with hole. Only the symmetric part of the specimen is shown. The original (undeformed) geometry is denoted by black lines. The effective viscous stretch is calculated as $U_{v,eff} = \sqrt{\mathbf{U}_v : \mathbf{U}_v}$.

5.5.2.3 Duckbill check valve

As a last structural example, we show the simulation of a cyclically loaded duckbill valve. These types of valves are often used as check valves to ensure a unidirectional fluid flow within a certain system, for example, in ventilation systems used for medical purpose. Due to the large amount of cycles such valves are subjected to, fatigue due to creep damage is a big issue. It is therefore of interest to identify the regions within the valve which are most susceptible for such damage effects.

Figure 5.15a shows the geometric representation of the duckbill valve used in this simulation.

Due to the symmetric properties of the system, we only used a quarter of the valve for the computation and applied the corresponding symmetric boundary conditions. During the whole simulation, the bottom surface at $z = 0$ mm of the valve was held fixed in all three spatial directions. A varying normal pressure with maximum value of $p_{max} = 2.7$ MPa was applied to the inner surface of the valve in a sawtooth pattern as shown in the upper graph of Figure 5.15b. The inital temperature is set to $\Theta_0 = 293.15$ K and no flux over the boundary of the valve is applied.

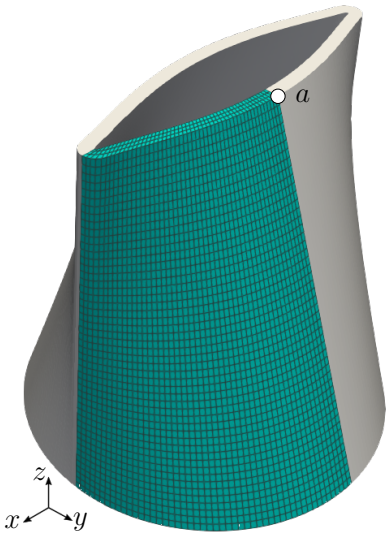

(a) Geometric representation of the valve. The bottom of the system ($z = 0$ mm) is held fixed in all spatial dimensions. Only a quarter of the overall geometry is used by exposing symmetric boundary conditions.

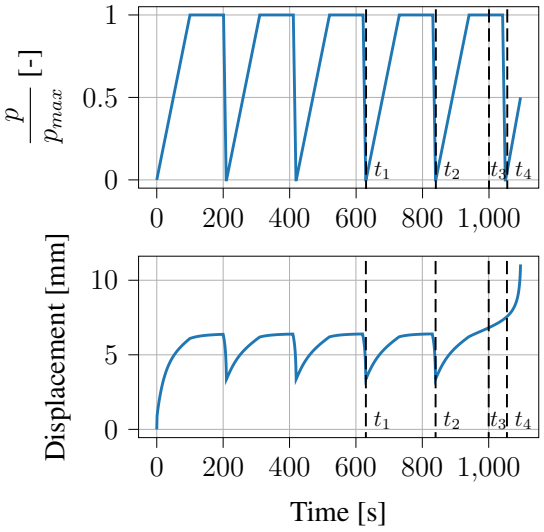

(b) *Top*: Loading path for pressure applied on the inside of the valve. *Bottom*: Displacement at point a in y-direction over time.

Figure 5.15: *Left*: Geometric representation of the duckbill valve showing the spatial discretisation of the symmetric part of the valve. The bottom surface of the valve is held fixed in all three spatial directions during the whole simulation. A varying normal pressure of $p_{max} = 2.7$ MPa is applied uniformly on the inner surface of the valve. *Right*: The loading path of the applied pressure p as well as the corresponding displacement of point a over time.

The bottom graph of Figure 5.15b shows the y-directional displacement response of the valve at point a (see Figure 5.15b) over time. During the first few loading cycles, the nonlinear, visco-elastic material response is clearly visible. The amount of damage within the valve does not yet play a role in the displacement response of the valves cusp. Within the last loading cycle, however, the damage response becomes the dominating inelastic effect and consequently

leads to a creep-like failure of the overall valve.

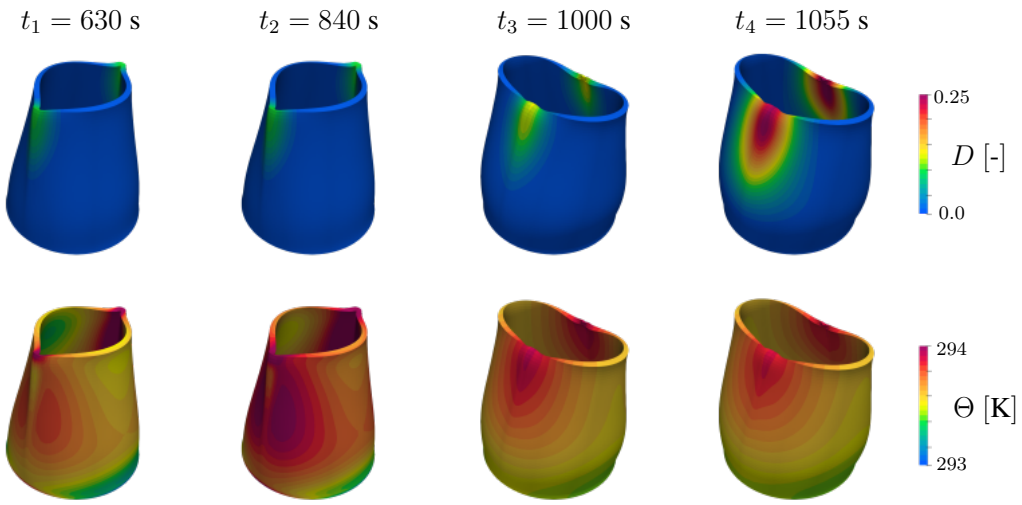

Figure 5.16: Selected results for the amount of accumulated damage (top) and the temperature distribution (bottom) for four destinct points in time.

This effect is reflected in both, the displacement response and the spatial distribution of the damage field as shown in Figure 5.16. Here, the damage response at four different points in time is shown together with the temperature distribution within the valve. It is obvious from these results that the folding edge of the valve is the most crucial part when it comes to damage of the material. While the value of accumulated damage within this region is still relatively low at the end of the third and fourth loading cycle, creep failure leads to a rapid increase in the amount of damage afterwards. The heat produced by the damage process within the region of interest consequently leads to a slight rise in temperature of the whole valve. Overall, based on this simulation, the statement can be made that especially the folded edge shows a great risk for incipient damage. It might therefore be of high interest to reinforce these areas to ensure longevity of the valve.

5.6 Conclusion and outlook

In this contribution, we introduced a fully thermomechanically coupled material model for damage and failure within polymeric materials subjected to finite strains. We made use of the multiplicative decomposition of the deformation gradient in mechanical and thermal parts as well as elastic and inelastic parts. Following well established models from the literature, we incorporated viscoelastic effects by introducing an additive decomposition of the free energy into equilibrium and non-equilibrium parts. The desired rate-dependent damage response was captured using a Perzyna-type ansatz for the evolution of the internal damage variable. To avoid pathological mesh dependencies, we furthermore introduced a gradient-extension of the damage field. Based on the balance of energy, we also derived all necessary source terms of internal heat generation for the given inelastic effects of the material. The entire model was derived in a thermodynamically consistent manner and implemented into finite element software making use of automatic differentiation for the calculation of all partial derivatives. To show the capabilities of the given model, we conducted and showed several numerical studies including investigations of the parameter influences as well as structural examples. Doing so, we were able to show that the model behaves as expected and gives qualitatively good results. Due to a current lack of experimental data capturing the thermal effects of rate-dependent damage within rubberlike polymers, we were not yet able to validate the given model. This should be a plausible next step for further investigations. For this, experimental setups similar to the ones used in Ovalle Rodas et al. [2016] or Hottin et al. [2023] could, for example, be used. Furthermore, it is well known that polymeric materials behave in a nearly incompressible way. This general material property can lead to undesired stiffening effects of the results due to locking effects of lower order finite element functions. To ensure that this model does not suffer from such problems, an extension of the finite element formulation using methods such as reduced integration might be benefitial (see e.g. Reese [2005]; Barfusz et al. [2021], among others).

5.7 Appendix

5.7.1 Total time derivative of the co-rotated elastic right Cauchy-Green tensor

The total time derivative of the co-rotated elastic right Cauchy-Green tensor can be written using the product rule of calculus as

$$\dot{\tilde{\mathbf{C}}}_e = \dot{\mathbf{U}}_v^{-1}\mathbf{C}\mathbf{U}_v^{-1} + \mathbf{U}_v^{-1}\dot{\mathbf{C}}\mathbf{U}_v^{-1} + \mathbf{U}_v^{-1}\mathbf{C}\dot{\mathbf{U}}_v^{-1}.$$

Using the relations $\dot{\mathbf{U}}_v^{-1} = -\mathbf{U}_v^{-1}\dot{\mathbf{U}}_v\mathbf{U}_v^{-1}$ and $\tilde{\mathbf{C}}_e = \mathbf{U}_v^{-1}\mathbf{C}\mathbf{U}_v^{-1}$ together with the definition of the viscous velocity gradient $\tilde{\mathbf{L}}_v = \dot{\mathbf{U}}_v\mathbf{U}_v^{-1}$, we can rewrite the rate of the co-rotated elastic right Cauchy-Green tensor as

$$\dot{\tilde{\mathbf{C}}}_e = \mathbf{U}_v^{-1}\dot{\mathbf{C}}\mathbf{U}_v^{-1} - \left(\tilde{\mathbf{L}}_v^T\tilde{\mathbf{C}}_e + \tilde{\mathbf{C}}_e\tilde{\mathbf{L}}_v\right).$$

5.7.2 Derivation of the reduced Clausius Duhem inequality

We start with the definition of the Helmholtz free energy as given in Equation (5.8) and take its temporal derivative, i.e.

$$\begin{aligned}\dot{\psi} = &\left(\frac{\partial f_d}{\partial D}\psi_0 + \frac{\partial \psi_{\bar{d}}}{\partial D}\right)\dot{D} \\ &+ f_d\frac{\Theta}{\Theta_0}\left(\frac{\partial \psi_{eq}}{\partial \mathbf{C}} : \dot{\mathbf{C}} + \frac{\partial \psi_{neq}}{\partial \tilde{\mathbf{C}}_e} : \dot{\tilde{\mathbf{C}}}_e\right) \\ &+ \left(\frac{f_d}{\Theta_0}\left(\psi_{eq} + \psi_{neq}\right) + \frac{\partial \psi_\Theta}{\partial \Theta}\right)\dot{\Theta} \\ &+ \frac{\partial \psi_d}{\partial \xi_d}\dot{\xi}_d + \frac{\partial \psi_{\bar{d}}}{\partial \bar{D}}\dot{\bar{D}} + \frac{\partial \psi_{\bar{d}}}{\partial\, \mathrm{Grad}\,\bar{D}} \cdot \mathrm{Grad}\,\dot{\bar{D}}.\end{aligned}$$

Using the identity $\dot{\tilde{\mathbf{C}}}_e = \mathbf{U}_v^{-1}\dot{\mathbf{C}}\mathbf{U}_v^{-1} - \left(\tilde{\mathbf{L}}_v^T\tilde{\mathbf{C}}_e + \tilde{\mathbf{C}}_e\tilde{\mathbf{L}}_v\right)$, we are able to reformulate the later part of the second term such that

$$\begin{aligned}\frac{\partial \psi_{neq}}{\partial \tilde{\mathbf{C}}_e} : \dot{\tilde{\mathbf{C}}}_e &= \mathbf{U}_v^{-1}\frac{\partial \psi_{neq}}{\partial \tilde{\mathbf{C}}_e}\mathbf{U}_v^{-1} : \dot{\mathbf{C}} - \frac{\partial \psi_{neq}}{\partial \tilde{\mathbf{C}}_e} : \left(\tilde{\mathbf{L}}_v^T\tilde{\mathbf{C}}_e + \tilde{\mathbf{C}}_e\tilde{\mathbf{L}}_v\right) \\ &= \mathbf{U}_v^{-1}\frac{\partial \psi_{neq}}{\partial \tilde{\mathbf{C}}_e}\mathbf{U}_v^{-1} : \dot{\mathbf{C}} - 2\tilde{\mathbf{C}}_e\frac{\partial \psi_{neq}}{\partial \tilde{\mathbf{C}}_e} : \tilde{\mathbf{D}}_v\end{aligned}$$

Here, we assumed that ψ_{neq} is an isotropic function of its arguments, which enabled us to make use of the symmetric properties of the double contracting product and describe the last term of this equation in terms of the symmetric part of the viscous velocity gradient $\tilde{\mathbf{D}}_v = \operatorname{sym} \tilde{\mathbf{L}}_v$. With this at hand, we can describe the temporal derivative given above as

$$\begin{aligned}
\dot{\psi} = &\left(\frac{\partial f_d}{\partial D} \psi_0 + \frac{\partial \psi_{\bar{d}}}{\partial D} \right) \dot{D} \\
&+ f_d \frac{\Theta}{\Theta_0} \left(\frac{\partial \psi_{eq}}{\partial \mathbf{C}} + \mathbf{U}_v^{-1} \frac{\partial \psi_{neq}}{\partial \tilde{\mathbf{C}}_e} \mathbf{U}_v^{-1} \right) : \dot{\mathbf{C}} \\
&+ 2 f_d \frac{\Theta}{\Theta_0} \tilde{\mathbf{C}}_e \frac{\partial \psi_{neq}}{\partial \tilde{\mathbf{C}}_e} : \tilde{\mathbf{D}}_v \\
&+ \left(\frac{f_d}{\Theta_0} \left(\psi_{eq} + \psi_{neq} \right) + \frac{\partial \psi_\Theta}{\partial \Theta} \right) \dot{\Theta} \\
&+ \frac{\partial \psi_d}{\partial \xi_d} \dot{\xi}_d + \frac{\partial \psi_{\bar{d}}}{\partial \bar{D}} \dot{\bar{D}} + \frac{\partial \psi_{\bar{d}}}{\partial \operatorname{Grad} \bar{D}} \cdot \operatorname{Grad} \dot{\bar{D}}.
\end{aligned}$$

If we include this form into the Clausius-Duhem inequality given by Equation (5.9) and define the co-rotated Mandel stress tensor as $\tilde{\mathbf{M}} = 2 f_d \frac{\Theta}{\Theta_0} \tilde{\mathbf{C}}_e \frac{\partial \psi_{neq}}{\partial \tilde{\mathbf{C}}_e}$, we arrive at

$$\begin{aligned}
\dot{\eta} = &\left[\mathbf{S} - 2 f_d \frac{\Theta}{\Theta_0} \left(\frac{\partial \psi_{eq}}{\partial \mathbf{C}} + \mathbf{U}_v^{-1} \frac{\partial \psi_{neq}}{\partial \tilde{\mathbf{C}}_e} \mathbf{U}_v^{-1} \right) \right] : \dot{\mathbf{C}} \\
&- \underbrace{\left(\frac{\partial f_d}{\partial D} \psi_0 + \frac{\partial \psi_{\tilde{d}}}{\partial D} \right)}_{:= -Y} \dot{D} - \underbrace{\frac{\partial \psi_d}{\partial \xi_d}}_{:= q_d} \dot{\xi}_d \\
&+ \left[\eta - \left(\frac{f_d}{\Theta_0} \left(\psi_{eq} + \psi_{neq} \right) + \frac{\partial \psi_\Theta}{\partial \Theta} \right) \right] \dot{\Theta} + \tilde{\mathbf{M}} : \tilde{\mathbf{D}}_v \\
&+ \left[a_{0_i} - \frac{\partial \psi_{\bar{d}}}{\partial \bar{D}} \right] \dot{\bar{D}} + \left[\mathbf{b}_{0_i} - \frac{\partial \psi_{\bar{d}}}{\partial \nabla \bar{D}} \right] \cdot \operatorname{Grad} \dot{\bar{D}} \\
&- \frac{1}{\Theta} \mathbf{q}_0 \cdot \operatorname{Grad} \Theta \geq 0
\end{aligned}$$

By following the argumentations of Coleman and Noll [1963], the corresponding bracket terms should vanish and yield the definition of the generalized stress measures as well as the entropy. With this, the reduced Clausius-Duhem inequality is given as

$$\tilde{\mathbf{M}} : \tilde{\mathbf{D}}_v - q_d \dot{\xi}_d + Y \dot{D} - \frac{1}{\Theta} \mathbf{q}_0 \cdot \operatorname{Grad} \Theta \geq 0.$$

5.7.3 Derivation of heat sources

To find the thermodynamically consistent heat source terms for the dissipative behaviour of the material, we start with a reformulation of the temporal derivative given in Equation (5.7.2) in terms of the driving forces, i.e.

$$\dot{\psi} = -Y\dot{D} - \eta\dot{\Theta} + q_d\dot{\xi}_d + a_{0_i}\dot{\bar{D}} + \mathbf{b}_{0_i} \cdot \operatorname{Grad}\dot{\bar{D}} + \frac{1}{2}\mathbf{S} : \dot{\mathbf{C}} - \tilde{\mathbf{M}} : \tilde{\mathbf{D}}_v$$

By considering the change of internal energy $\dot{e} = \dot{\psi} + \dot{\eta}\Theta + \eta\dot{\Theta}$ and including the temporal derivative above, we can find the following formulation:

$$\Theta\dot{\eta} = Y\dot{D} - q_d\dot{\xi}_d + \tilde{\mathbf{M}} : \tilde{\mathbf{D}}_v - \operatorname{Div}\mathbf{q}_0 + r_{ext}.$$

With further using the identities $\dot{\eta} = -\frac{\partial\dot{\psi}}{\partial\Theta}$ and $c = -\frac{\partial^2\psi}{\partial\Theta^2}$, we can come up with the balance of energy as given in Equation (5.14), i.e.

$$\begin{aligned} c\dot{\Theta} = &\left(Y - \frac{\partial Y}{\partial\Theta}\Theta\right)\dot{D} - \left(q_d - \frac{\partial q_d}{\partial\Theta}\Theta\right)\dot{\xi}_d + \frac{\partial a_{0_i}}{\partial\Theta}\Theta\dot{\bar{D}} + \frac{\partial\mathbf{b}_{0_i}}{\partial\Theta}\Theta \cdot \operatorname{Grad}\dot{\bar{D}} \\ &+ \left(\tilde{\mathbf{M}} - \frac{\partial\tilde{\mathbf{M}}}{\partial\Theta}\Theta\right) : \tilde{\mathbf{D}}_v + \frac{1}{2}\frac{\partial\mathbf{S}}{\partial\Theta}\Theta : \dot{\mathbf{C}} - \operatorname{Div}\mathbf{q}_0 + r_{ext}. \end{aligned}$$

5.7.4 Influence of damage hardening

The following study shows the influence of damage hardening on the material response. For this, we used the same setup of a constant deformation rate as described in Section 5.5.1.1. To illustrate the effect of damage hardening in a pronounced manner, we used a damage velocity of $\eta_d = 0.5\ \mathrm{s}^{-1}$ for these evaluations. In Figures 5.17, 5.18 and 5.19 we show the influence on the hardening parameters $k,\ r$ and s on both, the damage evolution as well as the stress-strain response. For further and more detailed studies on the effect of damage hardening, we refer the interested reader to Brepols et al. [2017a] and Brepols et al. [2020] and the examples shown therein.

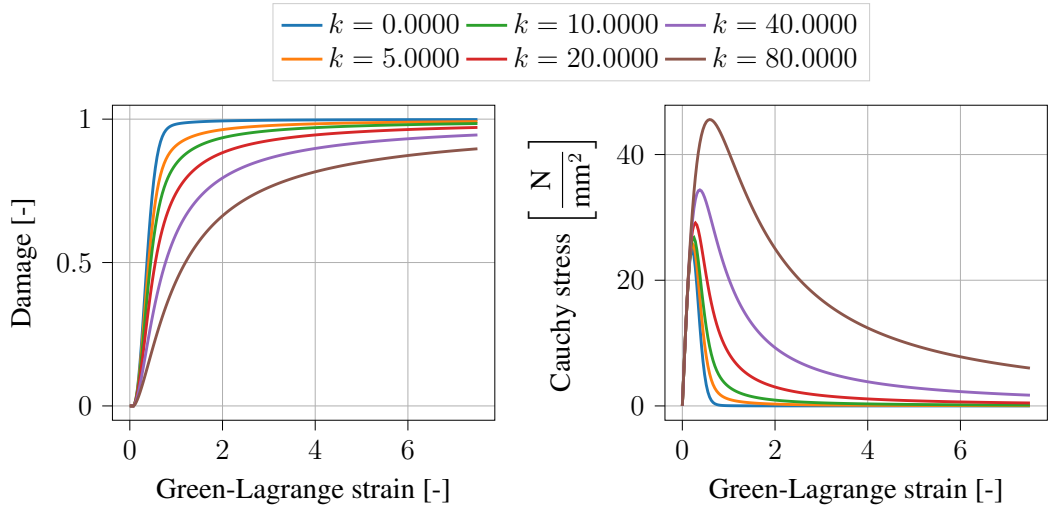

Figure 5.17: Influence of the damage hardening parameter k on the damage evolution and the stress-strain response. Results are given for a viscous relaxation velocity of $\eta_v = 0\ \mathrm{s}^{-1}$.

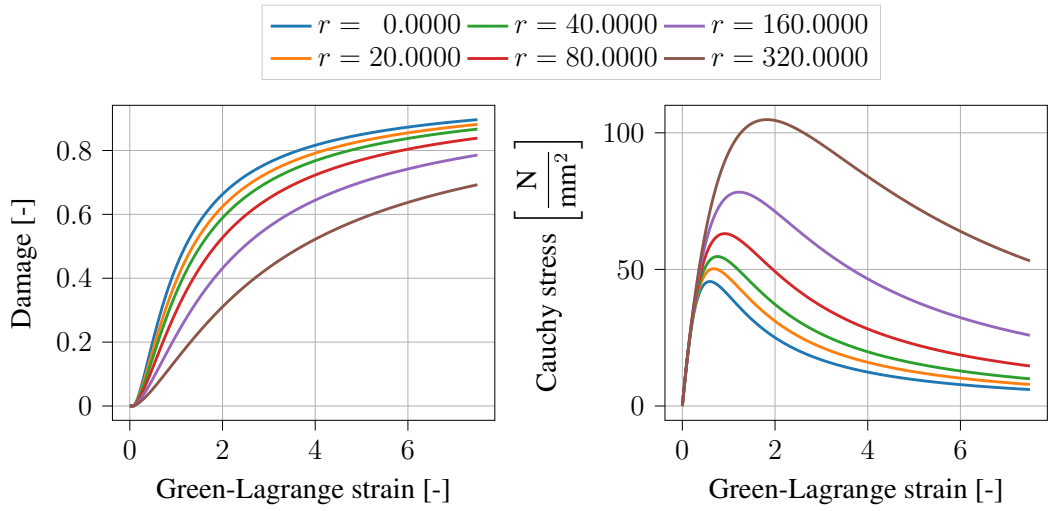

Figure 5.18: Influence of the damage hardening parameter r on the damage evolution and the stress-strain response. Results are given for a viscous relaxation velocity of $\eta_v = 0\ \mathrm{s}^{-1}$.

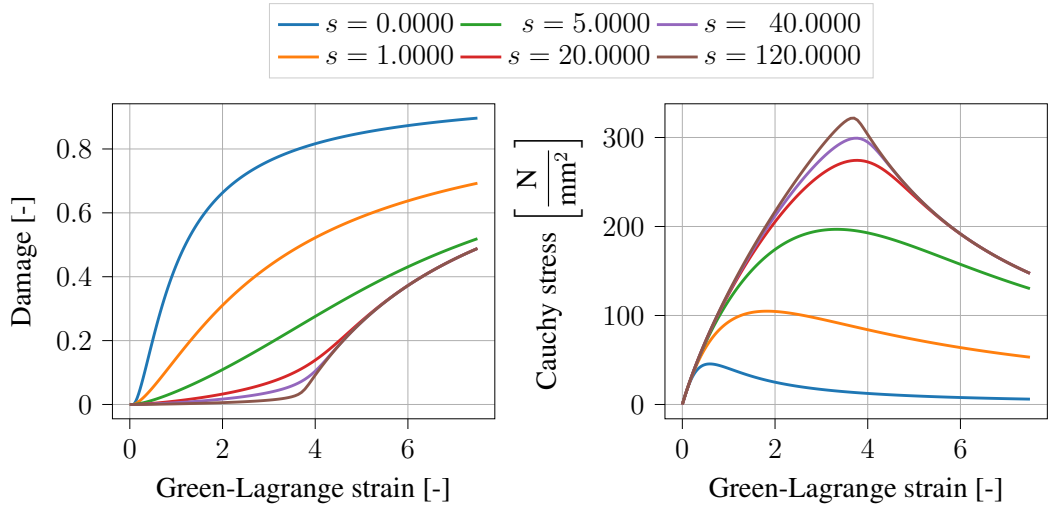

Figure 5.19: Influence of the damage hardening parameter s on the damage evolution and the stress-strain response. Results are given for a viscous relaxation velocity of $\eta_v = 0\ \mathrm{s}^{-1}$.

5.7.5 Force displacement diagrams of cyclic loading scenario

The corresponding force-displacement diagrams for the study conducted in Section 5.5.1.4 are given here in Figure 5.20.

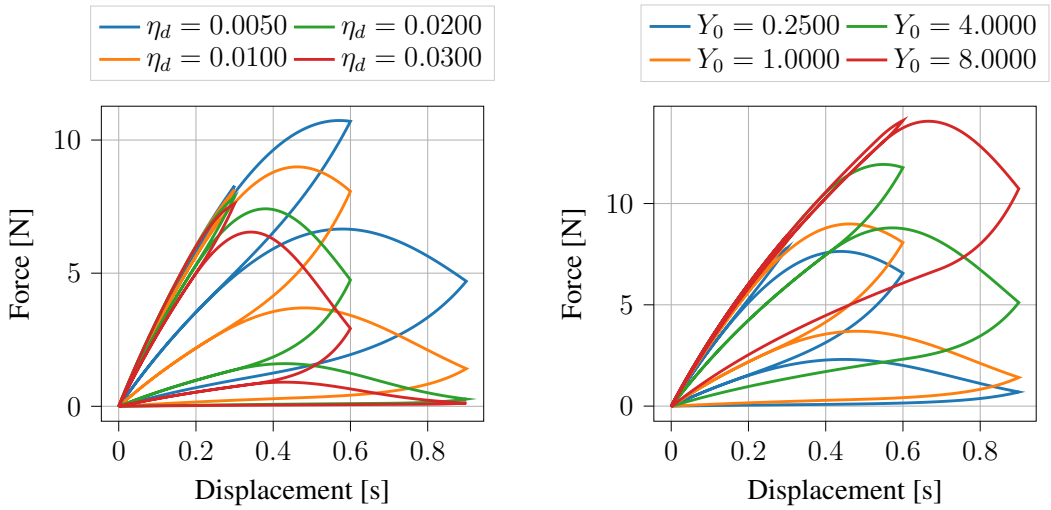

Figure 5.20: Influence of the damage velocity η_d and the damage threshold Y_0 on the internal heat generation for the cyclic loading case given in Section 5.5.1.4. Results are given for a viscous relaxation velocity of $\eta_v = 0\ \mathrm{s}^{-1}$.

6 Conclusions and Outlook

This dissertation was concerned with mathematical modelling approaches for different rate-dependent and inelastic material responses. In this context particular interest was on the description of continuum based modelling approaches for the prediction of biological growth in artificially cultivated tissue as well as rate-dependent damage processes arising in polymeric materials. As is usual in research, not all of the relevant research questions could be fully answered within this work. In the following, a brief summary of the work is given and some open questions are raised, which should be further investigated in subsequent investigations.

The first article presented in Chapter 2 dealt with a novel modelling approach for the prediction of volumetric growth effects arising in artificially grown tissue. Utilizing the assumption of a stress driven homeostatic state, a homeostatic potential was used as the basis for the evolution of the growth related part of the deformation. This novel idea was mainly inspired by the classical methods from the field of finite viscoplasticity and adapted accordingly. The main difference with respect to viscoplastic theory is that the evolution of inelastic strains is triggerd always if the current stress state of the material does not lie on the homeostatic surface. By applying a rate-dependent associative evolution law based on the homeostatic potential, the growth related deformations evolve until homeostasis is reached. Without further modifications, this formulation tends to grow or shrink indefinety if no restricting boundary conditions are applied. The model therefore introduces an additional energy contribution which subsequently counteracts the growth process. This additional energy can be interpreted as some kind of hydrostatic pressure arising from the nearly incompressible growth related part of the deformation. Within the examples presented in this publications, the model was able to predict both, isotropic and anisotropic volumetric growth behaviour using one single material formulation. The destiction between these two types of growth response does not have to be made a-priori anymore but is merely a question of the boundary conditions applied. The growth tensor subsequently takes any form needed to fulfill the assumption of stress driven homeostasis. The advantages of such an approach have been shown in comparison with a classical isotropic growth ansatz. Furthermore, comparisons with experimental data have shown that the model is able to accurately predict the growth induced stress and deformation for

artificially grown tissue. So far, the formulation presented in this article makes use of a simple isotropic elastic ground model and neglects other important aspects of biological tissue. Since the tissue itself is composed of various constituents, such as e.g. collagen, elastin and smooth muscle cells, the assumption of material isotropy is far from ideal. Generally, an initially isotropic material with evolving anisotropy due to collagen disposal in the extracellular matrix should be considered. A first step towards such a model has already been taken in Holthusen et al. [2023] and Sesa et al. [2023]. Furthermore, the influence of various different homeostatic potential formulations should be investigated to find the most suitable for a given biological tissue (see Holthusen et al. [2023]). Furthermore, explicit modelling of cell growth and movement as well as the associated interactions on the production of e.g. elastin and collagen could be investigated. Interesting work that takes similar effects into account can be found, for example, in Manjunatha et al. [2022] or Gierig et al. [2023]. Artificially grown tissue is usually only used in combination with non-biological reinforcement (e.g. polymer fibres) in the context of implant production. Therefore, an extension of the material model should be considered, which also includes these non-biological components. Initial work on this topic can be found for the case of the artificially grown heart valve in Sodhani et al. [2016, 2018].

The second article presented in Chapter 3 considered the rate-dependent modelling of damage within materials subjected to finite strains. It focused on a purely elastic, isotropic continuum damage formulation for which an Perzyna-type ansatz was chosen to describe the evolution of the damage variable. With this simple extension, the publication showed that a rate-dependent damage response can be predicted nicely in a qualitative sense. A quantitative comparison with experimental results has not been conducted in this publication. Furthermore, it is clear that a purely elastic ground model for this material description is far from realistic. This is especially the case when considering highly rate-dependent materials such as polymers.

Article three presented in Chapter 4 therefore showed a thermodynamically consistent extension of the previously published rate-dependent damage model to include also viscoelastic material behaviour at finite strains. For this, the multiplicative decomposition of the deformation gradient into elastic and viscous parts was utilized and the well known approach by Reese and Govindjee [1998] was adopted to describe the evolution of the inelastic deformations. In addition, the model was formulated in terms of a corotated intermediate formulation (Holthusen et al. [2023]) to allow for a more flexible and straightforward implementation into computer code using automatic differentiation. The publication not only showed various parameter studies elaborating on the differences between the two individual rate-dependent formulations used in the model. It also showed first comparisons with experimental data demonstrating that the model formulation is able to accurately predict the creep damage behaviour in polymeric

adhesives under uniaxial tension. This comparison is promising but still far from a full validation of the model. It is therefore of particular interest to perform an extensive validation to the model. Such a process should include experimental data captured under various loading scenarios such as, for example, cyclic or monotonic loading with various loading rates. It is furthermore a well-known fact that any inelastic deformation process leads to a loss of elastic energy during the process itself. This energy is usually assumed to be converted into heat which itself influences the deformation process. This is especially true for polymeric materials, which are known for their strongly termperature and rate-dependent behaviour.

This is the reason why the fourth article presented in Chapter 5 considered the consistent extension of the given rate-dependent damage model to cover also thermomechanical coupling effects. Here, a bilateral coupling was chosen, where the dissipated energy gets converted into heat and the heat influences the material response. This influence is captured by means of an explicit dependency of the material paramters on the current temperature as well as the heat expansion of the material. To achieve this, the publication made use of an additional multiplicative decomposition of the deformatioin gradient into thermal and mechanical parts. Based on the balance of energy, the source terms for heat generation due to inelastic dissipation were derived in a thermodynamically sound manner. Showing extensive parameter studies and structural examples, the model was able to capture the overall dissipative thermomechanical behaviour well.

Following up on the approach taken in the last three articles presented in this dissertation to describe rate-dependent damage in polymers, there are some open questions and investigations that should be addressed in the future. A rigorous validation of the model based on experimental studies is certainly one of them and has already been mentioned in a previous paragraph. Furthermore, polymers are known for their almost incompressible material behaviour, which can lead to some problems when solving the underlying equations using standard finite element formulations. Especially when using simple linear ansatz functions, it is known that incompressible material properties can lead to undesired locking phenomena. In order to avoid this, appropriate technologies should be used in the future that prevent such behaviour. For example, reduced integration methods such as those described in Reese [2005] or Barfusz et al. [2021], among others, could be used for this purpose. Furthermore, filled polymers in particular show pronounced cavity formation under high hydrostatic load. In many cases, this leads to a strong and permanent decrease in stiffness without plastic deformation. Consideration of this effect should therefore be taken into account in subsequent iterations of the material model. The description of the Mullins effect could also be of great importance for a realistic applicability of the material model and should therefore be taken into account in the future.

Finally, it should be mentioned at this point that for some time now there have been major innovations in the field of material modelling in terms of the modelling approaches used. While analytical approaches played a major role until a few years ago, there have been a large number of data-based modelling methods in the field of material modelling since the hype surrounding the topic of machine learning has taken off. The charm of these approaches is usually that the model formulation is determined autonomously and automatically by the machine learning algorithm on the basis of the available experimental data. However, one of the major drawbacks of many formulations in this field is the difficulty in ensuring a priori that generally applicable physical laws, such as thermodynamic consistency, are satisfied by these formulations. It is only recently, for example, that works such as the ones of Linka et al. [2021]; Linka and Kuhl [2023] have made great progress on this issue, possibly opening the door to a new era of material models.

The field of material modelling remains exciting.

List of Figures

List of Tables

Bibliography

Abdel-Tawab, K. and Weitsman, Y. J. [2000], 'A Strain-Based Formulation for the Coupled Viscoelastic/Damage Behavior', *Journal of Applied Mechanics* **68**(2), 304–311.

Aboudi, J. [2011], Micromechanical modeling of viscoelastic behavior of polymer matrix composites undergoing large deformations, *in* 'Creep and Fatigue in Polymer Matrix Composites', Elsevier, pp. 302 – 324.

Ahrens, J., Geveci, B. and Law, C. [2005], Paraview: An end-user tool for large-data visualization, *in* C. D. Hansen and C. R. Johnson, eds, 'Visualization Handbook', Butterworth-Heinemann, Burlington, pp. 717 – 731.

Al-Rub, R. K. A. and Darabi, M. K. [2012], 'A thermodynamic framework for constitutive modeling of time- and rate-dependent materials. Part I: Theory', *International Journal of Plasticity* **34**, 61–92.

Aldakheel, F. and Miehe, C. [2017], 'Coupled thermomechanical response of gradient plasticity', *International Journal of Plasticity* **91**, 1–24.

Ambrosi, D., Ben Amar, M., Cyron, C. J., DeSimone, A., Goriely, A., Humphrey, J. D. and Kuhl, E. [2019], 'Growth and remodelling of living tissues: perspectives, challenges and opportunities', *Journal of The Royal Society Interface* **16**(157), 20190233.

Arruda, E. M. and Boyce, M. C. [1993], 'A three-dimensional constitutive model for the large stretch behavior of rubber elastic materials', *Journal of the Mechanics and Physics of Solids* **41**(2), 389–412.

Ayadi, W., Laiarinandrasana, L. and Saï, K. [2016], 'Anisotropic (continuum damage mechanics)-based multi-mechanism model for semi-crystalline polymer', *International Journal of Damage Mechanics* **27**(3), 357–386.

Bahreman, M., Darijani, H. and Narooei, K. [2022], 'Investigation of multiplicative decompositions in the form of F_eF_v and F_vF_e to extend viscoelasticity laws from small to finite deformations', *Mechanics of Materials* **167**, 104235.

Barenblatt, G. [1962], The mathematical theory of equilibrium cracks in brittle fracture, *in* 'Advances in Applied Mechanics', Elsevier, pp. 55–129.

Barfusz, O., Brepols, T., van der Velden, T., Frischkorn, J. and Reese, S. [2021], 'A single gauss point continuum finite element formulation for gradient-extended damage at large deformations', *Computer Methods in Applied Mechanics and Engineering* **373**, 113440.

Bayat, H. R., Rezaei, S., Brepols, T. and Reese, S. [2020], 'Locking-free interface failure modeling by a cohesive discontinuous galerkin method for matching and nonmatching meshes', *International Journal for Numerical Methods in Engineering* **121**(8), 1762–1790.

Bažant, Z. P. [1976], 'Instability, ductility, and size effect in strain-softening concrete', *Journal of the Engineering Mechanics Division* **102**(2), 331–344.

Bažant, Z. P., Belytschko, T. B. and Chang, T.-P. [1984], 'Continuum theory for strain-softening', *Journal of Engineering Mechanics* **110**(12), 1666–1692.

Bažant, Z. P. and Lin, F.-B. [1988], 'Nonlocal smeared cracking model for concrete fracture', *Journal of Structural Engineering* **114**(11), 2493–2510.

Behnke, R., Kaliske, M. and Klüppel, M. [2016], 'Thermo-mechanical analysis of cyclically loaded particle-reinforced elastomer components: Experiment and finite element simulation', *Rubber Chemistry and Technology* **89**(1), 154–176.

Bergström, J. [1998], 'Constitutive modeling of the large strain time-dependent behavior of elastomers', *Journal of the Mechanics and Physics of Solids* **46**(5), 931–954.

Bertram, A. [1999], 'An alternative approach to finite plasticity based on material isomorphisms', *International Journal of Plasticity* **15**(3), 353–374.

Bonet, J. [2001], 'Large strain viscoelastic constitutive models', *International Journal of Solids and Structures* **38**(17), 2953–2968.

Borino, G., Failla, B. and Parrinello, F. [2003], 'A symmetric nonlocal damage theory', *International Journal of Solids and Structures* **40**(13-14), 3621–3645.

Bourdin, B., Francfort, G. and Marigo, J.-J. [2000], 'Numerical experiments in revisited brittle fracture', *Journal of the Mechanics and Physics of Solids* **48**(4), 797–826.

Braeu, F., Aydin, R. and Cyron, C. [2019], 'Anisotropic stiffness and tensional homeostasis induce a natural anisotropy of volumetric growth and remodeling in soft biological tissues', *Biomechanics and Modeling in Mechanobiology* **18**, 327–345.

Braeu, F., Seitz, A., Aydin, R. and Cyron, C. [2017], 'Homogenized constrained mixture models for anisotropic volumetric growth and remodeling', *Biomechanics and Modeling in Mechanobiology* **16**, 889–906.

Brepols, T., Wulfinghoff, S. and Reese, S. [2017*a*], 'Gradient-extended two-surface damage-plasticity: Micromorphic formulation and numerical aspects', *International Journal of Plasticity* **97**, 64–106.

Brepols, T., Wulfinghoff, S. and Reese, S. [2017*b*], A micromorphic damage-plasticity model to counteract mesh dependence in finite element simulations involving material softening, *in* 'Multiscale Modeling of Heterogeneous Structures', Springer International Publishing, pp. 235–255.

Brepols, T., Wulfinghoff, S. and Reese, S. [2020], 'A gradient-extended two-surface damage-plasticity model for large deformations', *International Journal of Plasticity* **129**, 102635.

Canadija, M. and Mosler, J. [2011], 'On the thermomechanical coupling in finite strain plasticity theory with non-linear kinematic hardening by means of incremental energy minimization', *International Journal of Solids and Structures* **48**(7-8), 1120–1129.

Cervera, M. and Chiumenti, M. [2006], 'Mesh objective tensile cracking via a local continuum damage model and a crack tracking technique', *Computer Methods in Applied Mechanics and Engineering* **196**(1-3), 304–320.

Cervera, M., Oliver, J. and Manzoli, O. [1996], 'A rate-dependent isotropic damage model for the seismic analysis of concrete dams', *Earthquake Engineering & Structural Dynamics* **25**(9), 987–1010.

Chaboche, J. [1978], *Description thermodynamique et phénoménologique de la viscoplasticité cyclique avec endommagement*, Publication - Office national d'études et de recherches aérospatiales, ONÉRA.

Chaboche, J. L., Lesne, P. M. and Maire, J. F. [1995], 'Continuum damage mechanics, anisotropy and damage deactivation for brittle materials like concrete and ceramic composites', *International Journal of Damage Mechanics* **4**(1), 5–22.

Chadwick, P. [1974], 'Thermo-mechanics of rubberlike materials', *Philosophical Transactions of the Royal Society of London. Series A, Mathematical and Physical Sciences* **276**(1260), 371–403.

Chow, C. and Lu, T. [1989], 'On evolution laws of anisotropic damage', *Engineering Fracture Mechanics* **34**(3), 679–701.

Chow, C. and Wang, J. [1987], 'An anisotropic theory of continuum damage mechanics for ductile fracture', *Engineering Fracture Mechanics* **27**(5), 547–558.

Coleman, B. D. and Gurtin, M. E. [1967], 'Thermodynamics with internal state variables', *The Journal of Chemical Physics* **47**(2), 597–613.

Coleman, B. D. and Noll, W. [1963], 'The thermodynamics of elastic materials with heat conduction and viscosity', *Archive for Rational Mechanics and Analysis* **13**(1), 167–178.

Coleman, B. D. and Noll, W. [1974], Foundations of Linear Viscoelasticity, *in* 'The Foundations of Mechanics and Thermodynamics: Selected Papers', Springer Berlin Heidelberg, pp. 113–123.

Cordebois, J. P. and Sidoroff, F. [1982], Damage induced elastic anisotropy, *in* 'Mechanical Behavior of Anisotropic Solids / Comportment Méchanique des Solides Anisotropes', Springer Netherlands, pp. 761–774.

Coulter, F. B., Schaffner, M., Faber, J. A., Rafsanjani, A., Smith, R., Appa, H., Zilla, P., Bezuidenhout, D. and Studart, A. R. [2019], 'Bioinspired heart valve prosthesis made by silicone additive manufacturing', *Matter* **1**(1), 266–279.

Cyron, C. J., Aydin, R. C. and Humphrey, J. D. [2016], 'A homogenized constrained mixture (and mechanical analog) model for growth and remodeling of soft tissue', *Biomechanics and Modeling Mechanobiology* **15**, 1389 – 1403.

Cyron, C. J. and Humphrey, J. D. [2017], 'Growth and remodeling of load-bearing biological softtissues', *Meccanica* **52**, 645 – 664.

Dai, L., Tian, C. and Xiao, R. [2020], 'Modeling the thermo-mechanical behavior and constrained recovery performance of cold-programmed amorphous shape-memory polymers', *International Journal of Plasticity* **127**, 102654.

Davison, L. and Stevens, A. L. [1973], 'Thermomechanical constitution of spalling elastic bodies', *Journal of Applied Physics* **44**(2), 668–674.

de Borst, R., Sluys, L., Muhlhaus, H.-B. and Pamin, J. [1993], 'Fundamental issues in finite element analyses of localization of deformation', *Engineering Computations* **10**(2), 99–121.

de Buyl, F. [2001], 'Silicone sealants and structural adhesives', *International Journal of Adhesion and Adhesives* **21**(5), 411–422.

de Souza Neto, E. A., Perić, D. and Owen, D. R. J. [1998], 'Continuum modelling and numerical simulation of material damage at finite strains', *Archives of Computational Methods in Engineering* **5**(4), 311–384.

de Souza Neto, E. A., Perić, D. and Owen, D. R. J. [2008], *Computational Methods for Plasticity: Theory and Applications*, Wiley & Sons, Ltd.

Dettmer, W. and Reese, S. [2004], 'On the theoretical and numerical modelling of armstrong-frederick kinematic hardening in the finite strain regime', *Computer Methods in Applied Mechanics and Engineering* **193**, 87 – 116.

Dimitrijevic, B. J. and Hackl, K. [2008], 'A method for gradient enhancement of continuum damage models', *Technische Mechanik-European Journal of Engineering Mechanics* **28**(1), 43–52.

Dimitrijevic, B. J. and Hackl, K. [2009], 'A regularization framework for damage-plasticity models via gradient enhancement of the free energy', *International Journal for Numerical Methods in Biomedical Engineering* **27**(8), 1199–1210.

DIN [2012], Kunststoffe – Bestimmung der Zugeigenschaften – Teil 2: Prüfbedingungen für Form- und Extrusionsmassen (ISO 527-2:2012); Deutsche Fassung EN ISO 527-2:2012, Standard, Deutsches Institut für Normung, Berlin, DE.

Dittmann, M., Aldakheel, F., Schulte, J., Schmidt, F., Krüger, M., Wriggers, P. and Hesch, C. [2020], 'Phase-field modeling of porous-ductile fracture in non-linear thermo-elasto-plastic solids', *Computer Methods in Applied Mechanics and Engineering* **361**, 112730.

Dorn, C. and Wulfinghoff, S. [2021], 'A gradient-extended large-strain anisotropic damage model with crack orientation director', *Computer Methods in Applied Mechanics and Engineering* **387**, 114123.

Dugdale, D. [1960], 'Yielding of steel sheets containing slits', *Journal of the Mechanics and Physics of Solids* **8**(2), 100–104.

Eckart, C. [1948], 'The Thermodynamics of Irreversible Processes. IV. The Theory of Elasticity and Anelasticity', *Physical Review* **73**(4), 373–382.

Eichinger, J. F., Paukner, D., Szafrom, J. M., Aydin, R. C., Humphrex, J. D. and Cyron, C. J. [2020], 'Computer-controlled biaxial bioreactor for investigating cell-mediated homeostasis in tissue equivalents', *Journal of Biomechanical Engineering* **142**(7), 071011.

Engelhardt, S., Sauerzapf, S., Preim, B., Karck, M., Wolf, I. and Simone, R. D. [2019], 'Flexible and comprehensive patient-specific mitral valve silicone models with chordae tendineae made from 3d-printable molds', *International Journal of Computer Assisted Radiology and Surgery* **14**(7), 1177–1186.

Escuer, J., Martínez, M. A., McGinty, S. and Peña, E. [2019], 'Mathematical modelling of the restenosis process after stent implantation', *Journal of The Royal Society Interface* **16**(157), 20190313.

Fancello, E., Ponthot, J.-P. and Stainier, L. [2006], 'A variational formulation of constitutive models and updates in non-linear finite viscoelasticity', *International Journal for Numerical Methods in Engineering* **65**(11), 1831–1864.

Fassin, M., Eggersmann, R., Wulfinghoff, S. and Reese, S. [2019], 'Gradient-extended anisotropic brittle damage modeling using a second order damage tensor – theory, implementation and numerical examples', *International Journal of Solids and Structures* **167**, 93–126.

Felder, S., Kopic-Osmanovic, N., Holthusen, H., Brepols, T. and Reese, S. [2022], 'Thermomechanically coupled gradient-extended damage-plasticity modeling of metallic materials at finite strains', *International Journal of Plasticity* **148**, 103142.

Fioretta, E., von Boehmer, L., Motta, S., Lintas, V., Hoerstrup, S. and Emmert, M. [2019], 'Cardiovascular tissue engineering: From basic science to clinical application', *Experimental Gerontology* **117**, 1 – 12.

Firouzi, N. and Rabczuk, T. [2022], 'Growth mechanics of the viscoelastic membranes', *Computer Methods in Applied Mechanics and Engineering* **401**, 115637.

Flory, P. J. [1961], 'Thermodynamic relations for high elastic materials', *Transactions of the Faraday Society* **57**, 829.

Forest, S. [2009], 'Micromorphic approach for gradient elasticity, viscoplasticity, and damage', *Journal of Engineering Mechanics* **135**(3).

Forest, S. [2016], 'Nonlinear regularization operators as derived from the micromorphic approach to gradient elasticity, viscoplasticity and damage', *Proceedings of the Royal Society A: Mathematical, Physical and Engineering Sciences* **472**(2188), 20150755.

Francfort, G. and Marigo, J.-J. [1998], 'Revisiting brittle fracture as an energy minimization problem', *Journal of the Mechanics and Physics of Solids* **46**(8), 1319–1342.

Fung, Y. [1995], 'Stress, strain, growth, and remodeling of living organisms', *Theoretical, Experimental, and Numerical Contributions to the Mechanics of Fluids and Solids* **46**, 469 – 482.

Ganghoffer, J., Sluys, L. and de Borst, R. [1999], 'A reappraisal of nonlocal mechanics', *European Journal of Mechanics - A/Solids* **18**(1), 17–46.

Geers, M. G. D., Brekelmans, W. A. M. and de Borst, R. [1994], Viscous regularization of strain-localisation for damaging materials, *in* G. M. A. Kusters and M. A. N. Hendriks, eds, 'DIANA Computational Mechanics 94', Springer Netherlands, pp. 127–138.

Germain, P., Nguyen, Q. S. and Suquet, P. [1983], 'Continuum thermodynamics', *Journal of Applied Mechanics* **50**(4b), 1010–1020.

Geuzaine, C. and Remacle, J.-F. [2009], 'Gmsh: a three-dimensional finite element mesh generator with built-in pre- and post-processing facilities', *International Journal For Numerical Methods in Engineering* **79**(11), 1309 – 1331.

Ghazanfari, S., Driessen-Mol, A., Strijkers, G., Baaijens, F. and Bouten, C. [2015], 'The evolution of collagen fiber orientation in engineered cardiovascular tissues visualized by diffusion tensor imaging', *PLoS One* **10**, 1 – 15.

Gierig, M., Wriggers, P. and Marino, M. [2023], 'Arterial tissues and their inflammatory response to collagen damage: A continuum in silico model coupling nonlinear mechanics, molecular pathways, and cell behavior', *Computers in Biology and Medicine* **158**, 106811.

Göktepe, S., Abilez, O. and Kuhl, E. [2010], 'A generic approach towards finite growth with examples of athlete's heart, cardiac dilation, and cardiac wall thickening', *Journal of the Mechanics and Physics of Solids* **58**, 1661 – 1680.

Goriely, A. [2018], *The Mathematics and Mechanics of Biological Growth*, Interdisciplinary Applied Mathematics, 1 edn, Springer New York, NY.

Groh, R. M. [2022], 'A morphoelastic stability framework for post-critical pattern formation in growing thin biomaterials', *Computer Methods in Applied Mechanics and Engineering* **394**, 114839.

Guo, Q. and Zaïri, F. [2021], 'A micromechanics-based model for deformation-induced damage and failure in elastomeric media', *International Journal of Plasticity* **140**, 102976.

Guo, Q., Zaïri, F. and Guo, X. [2018], 'A thermo-viscoelastic-damage constitutive model for cyclically loaded rubbers. Part I: Model formulation and numerical examples', *International Journal of Plasticity* **101**, 106–124.

Hagl, A. [2002], 'Synthese aus Glas und Stahl: Die Herz-Jesu-Kirche München', *Stahlbau* **71**(7), 498–506.

Hajikhani, A., Wriggers, P. and Marino, M. [2021], 'Chemo-mechanical modelling of swelling and crosslinking reaction kinetics in alginate hydrogels: A novel theory and its numerical implementation', *Journal of the Mechanics and Physics of Solids* **153**, 104476.

Haupt, P., Lion, A. and Backhaus, E. [2000], 'On the dynamic behaviour of polymers under finite strains: constitutive modelling and identification of parameters', *International Journal of Solids and Structures* **37**(26), 3633–3646.

Himpel, G., Kuhl, E., Menzel, A. and Steinmann, P. [2005], 'Computational modelling of isotropic multiplicative growth', *Computer Modeling in Engineering and Science* **8**, 1–14.

Holthusen, H., Brepols, T., Reese, S. and Simon, J.-W. [2022], 'A two-surface gradient-extended anisotropic damage model using a second order damage tensor coupled to additive plasticity in the logarithmic strain space', *Journal of the Mechanics and Physics of Solids* **163**, 104833.

Holthusen, H., Brepols, T., Simon, J. and Reese, S. [2022], A gradient-extended anisotropic damage-plasticity model in the logarithmic strain space, *in* '8th European Congress on Computational Methods in Applied Sciences and Engineering', CIMNE.

Holthusen, H., Rothkranz, C., Lamm, L., Brepols, T. and Reese, S. [2023], 'Inelastic material formulations based on a co-rotated intermediate configuration—application to bioengineered tissues', *Journal of the Mechanics and Physics of Solids* **172**, 105174.

Holzapfel, G. A. and Simo, J. C. [1996], 'A new viscoelastic constitutive model for continuous media at finite thermomechanical changes', *International Journal of Solids and Structures* **33**(20-22), 3019–3034.

Hottin, A., Naït-Abdelaziz, M., Talha, A. and Charrier, P. [2023], 'An attempt to predict the heat build-up of filled elastomers under multiaxial fatigue', *Polymer Testing* **128**, 108239.

Humphrey, J. D. [2021], 'Constrained mixture models of soft tissue growth and remodeling – twenty years after', *Journal of Elasticity* **145**(1-2), 49–75.

Humphrey, J. D. and Rajagopal, K. R. [2002], 'A constrained mixture model for growth and remodeling of soft tissues', *Mathematical models and methods in applied sciences* **12**(03), 407–430.

Jeridi, M., Laiarinandrasana, L. and Saï, K. [2015], 'Comparative study of continuum damage mechanics and mechanics of porous media based on multi-mechanism model on polyamide 6 semi-crystalline polymer', *International Journal of Solids and Structures* **53**, 12–27.

Jirásek, M. and Grassl, P. [2008], 'Evaluation of directional mesh bias in concrete fracture simulations using continuum damage models', *Engineering Fracture Mechanics* **75**(8), 1921–1943.

Junker, P., Schwarz, S., Jantos, D. R. and Hackl, K. [2019], 'A fast and robust numerical treatment of a gradient-enhanced model for brittle damage', *International Journal for Multiscale Computational Engineering* **17**(2), 151–180.

Kachanov, L. M. [1958], 'Time of the rupture process under creep conditions', *Otdelenie Teckhnicheskikh Nauk* **8**, 26–31.

Kaliske, M. and Rothert, H. [1997], 'Formulation and implementation of three-dimensional viscoelasticity at small and finite strains', *Computational Mechanics* **19**(3), 228–239.

Khaleghi, H., Amiri-Rad, A. and Mashayekhi, M. [2022], 'A thermodynamically consistent continuum damage model for time-dependent failure of thermoplastic polymers', *International Journal of Plasticity* **154**, 103278.

Klosowski, J. and Wolf, A. T. [2016], *Sealants in Construction*, CRC Press.

Korelc, J. [2002], 'Multi-language and multi-environment generation of nonlinear finite element codes', *Engineering with Computers* **18**, 312 – 327.

Korelc, J. [2009], 'Automation of primal and sensitivity analysis of transient coupled problems', *Computational Mechanics* **44**, 631 – 649.

Korelc, J. and Stupkiewicz, S. [2014], 'Closed-form matrix exponential and its application in finite-strain plasticity', *International Journal for Numerical Methods in Engineering* **98**.

Kou, H., He, C., Yang, W., Wu, F., Zhou, Z., Fu, J. and Xiao, L. [2022], 'A fractional nonlinear creep damage model for transversely isotropic rock', *Rock Mechanics and Rock Engineering* **56**, 831–846.

Krajcinovic, D. and Fonseka, G. U. [1981], 'The continuous damage theory of brittle materials, part 1: General theory', *Journal of Applied Mechanics* **48**(4), 809–815.

Kröner, E. [1959], 'Allgemeine Kontinuumstheorie der Versetzungen und Eigenspannungen', *Archive for Rational Mechanics and Analysis* **4**(1), 273–334.

Kuhl, E. and Steinmann, P. [2003], 'Mass- and volume-specific views on thermodynamics for open systems', *Proceedings of the royal society A* **459**, 2547 – 2568.

Kumar, A. and Lopez-Pamies, O. [2016], 'On the two-potential constitutive modeling of rubber viscoelastic materials', *Comptes Rendus Mécanique* **344**(2), 102–112.

Lamm, L., Holthusen, H., Brepols, T., Jockenhövel, S. and Reese, S. [2022], 'A macroscopic approach for stress-driven anisotropic growth in bioengineered soft tissues', *Biomechanics and Modeling in Mechanobiology* **21**(2), 627–645.

Lamm, L., Holthusen, H., Böhm, C., Jockenhövel, S. and Reese, S. [2021], 'Macroscopic modelling of stress driven anisotropic growth in bioengineered tissues', *Proceedings in Applied Mathematics and Mechanics* **21**(1), e202100046.

Lamm, L., Pfeifer, J., Holthusen, H., Schaaf, B., Seewald, R., Schiebahn, A., Brepols, T., Feldmann, M., Reisgen, U. and Reese, S. [2023], 'Gradient-extended damage modelling for polymeric materials at finite strains: Rate-dependent damage evolution combined with viscoelasticity', *European Journal of Mechanics - A/Solids* **103**, 105121.

Lamm, L., Pfeifer, J. M. ., Holthusen, H., Brepols, T. and Reese, S. [2023], 'Modelling and simulation of time-dependent damage and failure within silicone-based, polymeric adhesives', *Proceedings in Applied Mathematics and Mechanics* **22**(1), e202200076.

Laplace, P. [1902], *A Philosophical Essay on Probabilities*, Wiley, London.

Lavoie, S. R., Long, R. and Tang, T. [2016], 'A rate-dependent damage model for elastomers at large strain', *Extreme Mechanics Letters* **8**, 114–124.

Lee, E. H. [1969], 'Elastic-plastic deformation at finite strains', *Journal of Applied Mechanics* **36**(1), 1–6.

Lee, E. H. and Liu, D. T. [1967], 'Finite-strain elastic-plastic theory with application to plane-wave analysis', *Journal of Applied Physics* **38**(1), 19–27.

Lee, T., Holland, M. A., Weickenmeier, J., Gosain, A. K. and Tepole, A. B. [2021], 'The geometry of incompatibility in growing soft tissues: Theory and numerical characterization', *Journal of the Mechanics and Physics of Solids* **146**, 104177.

Lemaitre, J. [1971], Evaluation of dissipation and damage in metals subjected to dynamic loading, *in* 'Proc. ICM 1, Kyoto, Japan'.

Lemaitre, J. [1984], A three-dimensional ductile damage model applied to deep-drawing forming limits, *in* 'Mechanical Behaviour of Materials', Elsevier, pp. 1047–1053.

Lemaitre, J. [1985*a*], 'A continuous damage mechanics model for ductile fracture', *Journal of Engineering Materials and Technology* **107**(1), 83–89.

Lemaitre, J. [1985*b*], 'Coupled elasto-plasticity and damage constitutive equations', *Computer Methods in Applied Mechanics and Engineering* **51**(1-3), 31–49.

Lemaitre, J. and Chaboche, J. [1978], 'Aspect phenomenologique de la rupture par endommagement', *Journal de mécanique appliquée* **2**(3), 317–365.

Levenberg, K. [1944], 'A method for the solution of certain non-linear problems in least squares', *Quarterly of Applied Mathematics* **2**(2), 164–168.

Lian, J., Feng, Y. and Münstermann, S. [2014], 'A modified lemaitre damage model phenomenologically accounting for the lode angle effect on ductile fracture', *Procedia Materials Science* **3**, 1841–1847.

Lin, R. and Schomburg, U. [2003], 'A finite elastic–viscoelastic–elastoplastic material law with damage: theoretical and numerical aspects', *Computer Methods in Applied Mechanics and Engineering* **192**(13-14), 1591–1627.

Linka, K., Hillgärtner, M., Abdolazizi, K. P., Aydin, R. C., Itskov, M. and Cyron, C. J. [2021], 'Constitutive artificial neural networks: A fast and general approach to predictive data-driven constitutive modeling by deep learning', *Journal of Computational Physics* **429**, 110010.

Linka, K. and Kuhl, E. [2023], 'A new family of constitutive artificial neural networks towards automated model discovery', *Computer Methods in Applied Mechanics and Engineering* **403**, 115731.

Lion, A. [1996], 'A constitutive model for carbon black filled rubber: Experimental investigations and mathematical representation', *Continuum Mechanics and Thermodynamics* **8**(3), 153–169.

Lion, A. [1997], 'On the large deformation behaviour of reinforced rubber at different temperatures', *Journal of the Mechanics and Physics of Solids* **45**(11-12), 1805–1834.

Lion, A. [2000*a*], 'Constitutive modelling in finite thermoviscoplasticity: a physical approach based on nonlinear rheological models', *International Journal of Plasticity* **16**(5), 469–494.

Lion, A. [2000*b*], Thermomechanik von Elastomeren: Experimente und Materialtheorie, PhD thesis, University of Kassel.

Lion, A., Mittermeier, C. and Johlitz, M. [2017], 'Heat capacities and volumetric changes in the glass transition range: a constitutive approach based on the standard linear solid', *Continuum Mechanics and Thermodynamics* **29**(5), 1061–1079.

Loew, P. J., Peters, B. and Beex, L. A. [2019], 'Rate-dependent phase-field damage modeling of rubber and its experimental parameter identification', *Journal of the Mechanics and Physics of Solids* **127**, 266–294.

Lu, S. and Pister, K. [1975], 'Decomposition of deformation and representation of the free energy function for isotropic thermoelastic solids', *International Journal of Solids and Structures* **11**(7-8), 927–934.

Lubarda, V. A. [2004], 'Constitutive theories based on the multiplicative decomposition of deformation gradient: Thermoelasticity, elastoplasticity, and biomechanics', *Applied Mechanics Reviews* **57**(2), 95–108.

Lubarda, V. and Hoger, A. [2002], 'On the mechanics of solids with a growing mass', *International Journal of Solids and Structures* **39**, 4627 – 4664.

Lubliner, J. [1985], 'A model of rubber viscoelasticity', *Mechanics Research Communications* **12**(2), 93–99.

Manjunatha, K., Behr, M., Vogt, F. and Reese, S. [2022], 'A multiphysics modeling approach for in-stent restenosis', *Computers in Biology and Medicine* **150**, 106166.

Marquardt, D. W. [1963], 'An algorithm for least-squares estimation of nonlinear parameters', *Journal of the Society for Industrial and Applied Mathematics* **11**(2), 431–441.

Marquis, D. and Lemaitre, J. [1988], 'Constitutive equations for the coupling between elasto-plasticity damage and aging', *Revue de Physique Appliquée* **23**(4), 615–624.

Mehnert, M., Hossain, M. and Steinmann, P. [2017], 'Towards a thermo-magneto-mechanical coupling framework for magneto-rheological elastomers', *International Journal of Solids and Structures* **128**, 117–132.

Mehnert, M., Hossain, M. and Steinmann, P. [2018], 'Numerical modeling of thermo-electro-viscoelasticity with field-dependent material parameters', *International Journal of Non-Linear Mechanics* **106**, 13–24.

Menzel, A. [2005], 'Modelling of anisotropic growth in biological tissues. A new approach and computational aspects', *Biomechanics and Modeling in Mechanobiology* **3**, 147 – 171.

Miehe, C. [2000], 'Superimposed finite elastic–viscoelastic–plastoelastic stress response with damage in filled rubbery polymers. Experiments, modelling and algorithmic implementation', *Journal of the Mechanics and Physics of Solids* **48**(2), 323–365.

Miehe, C., Hofacker, M., Schänzel, L.-M. and Aldakheel, F. [2015], 'Phase field modeling of fracture in multi-physics problems. Part II. Coupled brittle-to-ductile failure criteria and crack propagation in thermo-elastic–plastic solids', *Computer Methods in Applied Mechanics and Engineering* **294**, 486–522.

Miehe, C. and Schänzel, L.-M. [2014], 'Phase field modeling of fracture in rubbery polymers. Part I: Finite elasticity coupled with brittle failure', *Journal of the Mechanics and Physics of Solids* **65**, 93–113.

Moler, C. and van Loan, C. [2003], 'Nineteen dubious ways to compute the exponential of a matrix, twenty-five years later', *SIAM Review* **45**(1), 3–49.

Murakami, S. and Ohno, N. [1981], A continuum theory of creep and creep damage, *in* 'Creep in Structures', Springer Berlin Heidelberg, pp. 422–444.

Nahrmann, M. and Matzenmiller, A. [2021], 'Modelling of nonlocal damage and failure in ductile steel sheets under multiaxial loading', *International Journal of Solids and Structures* **232**, 111166.

Noll, W. [1958], 'A mathematical theory of the mechanical behavior of continuous media', *Archive for Rational Mechanics and Analysis* **2**, 197 – 226.

Ogden, R. W. [1972], 'Large deformation isotropic elasticity: on the correlation of theory and experiment for compressible rubberlike solids', *Proceedings of the Royal Society of London. A. Mathematical and Physical Sciences* **328**(1575), 567–583.

Ovalle Rodas, C., Zaïri, F., Naït-Abdelaziz, M. and Charrier, P. [2016], 'A thermo-visco-hyperelastic model for the heat build-up during low-cycle fatigue of filled rubbers: Formulation, implementation and experimental verification', *International Journal of Plasticity* **79**, 217–236.

Pandey, V., Singh, I. V., Mishra, B., Ahmad, S., Rao, A. and Kumar, V. [2019], 'Creep crack simulations using continuum damage mechanics and extended finite element method', *International Journal of Damage Mechanics* **28**(1), 3–34.

Pereira, L., Weerheijm, J. and Sluys, L. [2017], 'A new effective rate dependent damage model for dynamic tensile failure of concrete', *Engineering Fracture Mechanics* **176**, 281–299.

Perić, D. [1993], 'On a class of constitutive equations in viscoplasticity: Formulation and computational issues', *International Journal for Numerical Methods in Engineering* **36**(8), 1365–1393.

Perzyna, P. [1963], 'The constitutive equations for rate sensitive plastic materials', *Quarterly of Applied Mathematics* **20**, 321–332.

Perzyna, P. [1966], 'Fundamental problems in viscoplasticity', *Advances in Applied Mechanics* **9**, 243–377.

Perzyna, P. [1971], 'Thermodynamic theory of viscoplasticity', *Advances in Applied Mechanics* **11**, 313–354.

Pezeshki, M., Loehnert, S., Wriggers, P., Guidault, P. A. and Baranger, E. [2017], 3d dynamic crack propagation by the extended finite element method and a gradient-enhanced damage model, *in* 'Multiscale Modeling of Heterogeneous Structures', Springer International Publishing, pp. 277–299.

Pijaudier-Cabot, G. and Bažant, Z. P. [1987], 'Nonlocal damage theory', *Journal of Engineering Mechanics* **113**(10), 1512–1533.

Pires, F. A., de Sá, J. C., Sousa, L. C. and Jorge, R. N. [2003], 'Numerical modelling of ductile plastic damage in bulk metal forming', *International Journal of Mechanical Sciences* **45**(2), 273–294.

Pituba, J. J. C. and Fernandes, G. R. [2011], 'Anisotropic damage model for concrete', *Journal of Engineering Mechanics* **137**(9), 610–624.

Rabotnov, Y. N. [1969], *Creep problems in structural members*, North-Holland Pub. Co.

Rahman, M. M., Watton, P. N., Neu, C. P. and Pierce, D. M. [2023], 'A chemo-mechano-biological modeling framework for cartilage evolving in health, disease, injury, and treatment', *Computer Methods and Programs in Biomedicine* **231**, 107419.

Rambausek, M., Mukherjee, D. and Danas, K. [2022], 'A computational framework for magnetically hard and soft viscoelastic magnetorheological elastomers', *Computer Methods in Applied Mechanics and Engineering* **391**, 114500.

Reese, S. [2003], 'A micromechanically motivated material model for the thermo-viscoelastic material behaviour of rubber-like polymers', *International Journal of Plasticity* **19**(7), 909–940.

Reese, S. [2005], 'On a physically stabilized one point finite element formulation for three-dimensional finite elasto-plasticity', *International Journal for Numerical Methods in Engineering* **194**, 4685 – 4715.

Reese, S., Brepols, T., Fassin, M., Poggenpohl, L. and Wulfinghoff, S. [2021], 'Using structural tensors for inelastic material modeling in the finite strain regime - a novel approach to anisotropic damage', *Journal of the Mechanics and Physics of Solids* **146**, 104174.

Reese, S. and Govindjee, S. [1997], 'Theoretical and numerical aspects in the thermo-viscoelastic material behaviour of rubber-like polymers', *Mechanics of Time-Dependent Materials* **1**(4), 357–396.

Reese, S. and Govindjee, S. [1998], 'A theory of finite viscoelasticity and numerical aspects', *International Journal of Solids and Structures* **35**, 3455–3482.

Ren, X. and Li, J. [2013], 'A unified dynamic model for concrete considering viscoplasticity and rate-dependent damage', *International Journal of Damage Mechanics* **22**(4), 530–555.

Rice, J. [1971], 'Inelastic constitutive relations for solids: An internal-variable theory and its application to metal plasticity', *Journal of the Mechanics and Physics of Solids* **19**(6), 433–455.

Rizzi, E. and Loret, B. [1997], 'Qualitative analysis of strain localization. Part I: Transversely isotropic elasticity and isotropic plasticity', *International Journal of Plasticity* **13**(5), 461–499.

Rodriguez, E., Hoger, A. and McCulloch, A. [1994], 'Stress-dependent finite growth in soft elastic tissues', *Journal of Biomechanics* **27**, 455 – 467.

Saanouni, K. [2009], 'Modelling and numerical simulation of ductile damage in bulk metal forming', *Steel Research International* **80**, 645–657.

Sadik, S. and Yavari, A. [2015], 'On the origins of the idea of the multiplicative decomposition of the deformation gradient', *Mathematics and Mechanics of Solids* **22**(4), 771–772.

Satouri, S., Chatzigeorgiou, G., Benaarbia, A. and Meraghni, F. [2022], 'A gradient enhanced constitutive framework for the investigation of ductile damage localization within semicrystalline polymers', *International Journal of Damage Mechanics* **31**(10), 1639–1675.

Schaaf, B., Richter, C., Feldmann, M., Toups, E., Simon, J.-W., Reese, S., Seewald, R., Schiebahn, A. and Reisgen, U. [2020], 'Material parameter determination for the simulation of hyperelastic bonds in civil engineering considering a novel material model', *International Journal of Adhesion and Adhesives* **103**, 102692.

Schwarze, M. and Reese, S. [2011], 'A reduced integration solid-shell finite element based on the eas and the ans concept—large deformation problems', *International Journal for Numerical Methods in Engineering* **85**(3), 289 – 329.

Seewald, R., Schnittcher, M. A., Pauly, F., Rath, S., Schaaf, B., Lamm, L., Schiebahn, A., Brepols, T., Reese, S., Feldmann, M. and Reisgen, U. [2021], 'A mesoscopic analysis of cavities in two components silicone adhesive with cylindrical butt joint specimens', *International Journal of Adhesion and Adhesives* **117**, 103016.

Sempértegui, F. and Avril, S. [2023], 'Re-interpretation of the homogenized constrained mixture theory within the plasticity framework and application to soft tissue growth and remodeling', *Computer Methods in Applied Mechanics and Engineering* **412**, 116059.

Sesa, M., Holthusen, H., Lamm, L., Böhm, C., Brepols, T., Jockenhövel, S. and Reese, S. [2023], 'Mechanical modeling of the maturation process for tissue-engineered implants: Application to biohybrid heart valves', *Computers in Biology and Medicine* **167**, 107623.

Shaw, J. A., Jones, A. S. and Wineman, A. S. [2005], 'Chemorheological response of elastomers at elevated temperatures: Experiments and simulations', *Journal of the Mechanics and Physics of Solids* **53**(12), 2758–2793.

Shlyannikov, V. N. and Tumanov, A. V. [2019], 'Stress- and strain-based models of creep damage accumulation', *Physical Mesomechanics* **22**(6), 514–528.

Sidoroff, F. [1974], 'Un modèle viscoélastique non linéaire avec configuration intermédiaire', *Journal de mécanique* **13**, 679–713.

Simo, J. [1987], 'On a fully three-dimensional finite-strain viscoelastic damage model: Formulation and computational aspects', *Computer Methods in Applied Mechanics and Engineering* **60**(2), 153–173.

Simo, J. [1992], 'Algorithms for static and dynamic multiplicative plasticity that preserve the classical return mapping schemes of the infinitesimal theory', *Computer Methods in Applied Mechanics and Engineering* **99**, 61 – 112.

Simo, J. C. and Ju, J. W. [1987], 'Strain- and stress-based continuum damage models—I. Formulation', *International Journal of Solids and Structures* **23**(7), 821–840.

Simo, J. C. and Miehe, C. [1992], 'Associative coupled thermoplasticity at finite strains: Formulation, numerical analysis and implementation', *Computer Methods in Applied Mechanics and Engineering* **98**(1), 41–104.

Simo, J. C. and Taylor, R. L. [1991], 'Quasi-incompressible finite elasticity in principal stretches. continuum basis and numerical algorithms', *Computer Methods in Applied Mechanics and Engineering* **85**(3), 273–310.

Simo, J. and Hughes, T. [1998], *Computational Inelasticity*, Vol. 7 of *Interdisciplinary Applied Mathematics*, Springer Nature, New York.

Skalak, R. [1981], Growth as a finite displacement field, *in* D. E. Carlson and R. T. Shield, eds, 'Proceedings of the IUTAM Symposium on Finite Elasticity', Springer Netherlands, Dodrecht, pp. 347 – 355.

Skalak, R., Dasgupta, G., Moss, M., Otten, E., Dullemeijer, P. and Vilmann, H. [1982], 'Analytical description of growth', *Journal of Theoretical Biology* **94**(3), 555–577.

Skrzypek, J. J. [1999], *Modeling of Material Damage and Failure of Structures*, Foundations of Engineering Mechanics, Springer, Berlin.

Sodhani, D., Reese, S., Jockenhövel, S., Mela, P. and Stapleton, S. E. [2018], 'Multi-scale modelling and simulation of a highly deformable embedded biomedical textile mesh composite', *Composites Part B: Engineering* **143**, 113–131.

Sodhani, D., Reese, S., Moreira, R., Jockenhoevel, S., Mela, P. and Stapleton, S. E. [2016], 'Multi-scale modelling of textile reinforced artificial tubular aortic heart valves', *Meccanica* **52**(3), 677–693.

Soleimani, M., Muthyala, N., Marino, M. and Wriggers, P. [2020], 'A novel stress-induced anisotropic growth model driven by nutri-cent diffusion: Theory, FEM implementation and applications in bio-mechanical problems', *Journal of the Mechanics and Physics of Solids* **144**, 104097.

Stassi-D'Alia, F. [1967], 'Flow and fracture of materials according to a new limiting condtition of yielding', *Meccanica* **2**, 178 – 195.

Steinmann, P., Hossain, M. and Possart, G. [2012], 'Hyperelastic models for rubber-like materials: Consistent tangent operators and suitability for Treloar's data', *Archive of Applied Mechanics* **82**(9), 1183–1217.

Stojanovic, R., Djuric, S. and Vujosevic, L. [1964], 'On finite thermal deformations', *Archiwum Mechaniki Stosowanej* **1**(16), 103 – 108.

Svendsen, B. [2001], 'On the modelling of anisotropic elastic and inelastic material behaviour at large deformation', *International Journal of Solids and Structures* **38**(52), 9579–9599.

Tange, O. [2011], 'Gnu parallel: The command-line power tool', *;login:* **36**(1), 42 – 47.

Taylor, R. L. and Govindjee, S. [2020], 'Feap - - a finite element analysis program'. [online; accessed 2022-09-15].
URL: `http://projects.ce.berkeley.edu/feap/manual_86.pdf`

Tschoegl, N. [1971], 'Failure surfaces in principal stress space', *Journal of Polymer Science Part C: Polymer Symposia* **32**, 239 – 267.

van der Velden, T., Ritzert, S., Reese, S. and Waimann, J. [2023], 'A novel numerical strategy for modeling the moving boundary value problem of electrochemical machining', *International Journal for Numerical Methods in Engineering* **124**(8), 1856–1882.

van der Velden, T., Rommes, B., Klink, A., Reese, S. and Waimann, J. [2021], 'A novel approach for the efficient modeling of material dissolution in electrochemical machining', *International Journal of Solids and Structures* **229**, 111106.

Vernerey, F. J., Brighenti, R., Long, R. and Shen, T. [2018], 'Statistical damage mechanics of polymer networks', *Macromolecules* **51**(17), 6609–6622.

Virtanen, P., Gommers, R. and Travis Oliphant, e. a. [2020], 'SciPy 1.0: Fundamental algorithms for scientific computing in Python', *Nature Methods* **17**(3), 261–272.

Vladimirov, I. N., Pietryga, M. P. and Reese, S. [2008], 'On the modelling of non-linear kinematic hardening at finite strains with application to springback—comparison of time integration algorithms', *International Journal for Numerical Methods in Engineering* **75**(1), 1–28.

Vladimirov, I. N., Reese, S. and Eggeler, G. [2009], 'Constitutive modelling of the anisotropic creep behaviour of nickel-base single crystal superalloys', *International Journal of Mechanical Sciences* **51**(4), 305–313.

Voce, E. [1948], 'The relationship between stress and strain for homogeneous deformation', *Journal of the Institute of Metals* **74**, 537–562.

Voyiadjis, G. Z., Shojaei, A. and Li, G. [2012], 'A generalized coupled viscoplastic–viscodamage–viscohealing theory for glassy polymers', *International Journal of Plasticity* **28**(1), 21–45.

Vujosevic, L. and Lubarda, V. [2002], 'Finite-strain thermoelasticity based on multiplicative decomposition of deformation gradient', *Theoretical and Applied Mechanics* **28-29**, 379–399.

Wang, J., Peng, L., Deng, Y., Lai, X., Fu, M. and Ni, J. [2019], 'A finite strain thermodynamically-based constitutive modeling and analysis of viscoelastic-viscoplastic deformation behavior of glassy polymers', *International Journal of Plasticity* **122**, 135–163.

Wang, R., Xu, W., Wang, W. and Zhang, J. [2013], 'A nonlinear creep damage model for brittle rocks based on time-dependent damage', *European Journal of Environmental and Civil Engineering* **17**, 111–125.

Wang, S. and Chester, S. A. [2018], 'Experimental characterization and continuum modeling of inelasticity in filled rubber-like materials', *International Journal of Solids and Structures* **136-137**, 125–136.

Weber, G. and Anand, L. [1990], 'Finite deformation constitutive equations and a time integration procedure for isotropic, hyperelastic - viscoplastic solids', *Computer Methods in Applied Mechanics and Engineering* **79**, 173–202.

Wineman, A. [2009], 'On the mechanics of elastomers undergoing scission and cross-linking', *International Journal of Advances in Engineering Sciences and Applied Mathematics* **1**(2-3), 123–131.

Wineman, A. and Shaw, J. [2007], 'Combined deformation- and temperature-induced scission in a rubber cylinder in torsion', *International Journal of Non-Linear Mechanics* **42**(2), 330–335.

Wulfinghoff, S., Fassin, M. and Reese, S. [2017], 'A damage growth criterion for anisotropic damage models motivated from micromechanics', *International Journal of Solids and Structures* **121**, 21–32.

Xia, X., Guo, X. and Weng, G. J. [2022], 'Creep rupture in carbon nanotube-based viscoplastic nanocomposites', *International Journal of Plasticity* **150**, 103189.

Xiang, Y., Zhong, D., Rudykh, S., Zhou, H., Qu, S. and Yang, W. [2020], 'A review of physically based and thermodynamically based constitutive models for soft materials', *Journal of Applied Mechanics* **87**(11).

Xiao, R. and Nguyen, T. D. [2015], 'An effective temperature theory for the nonequilibrium behavior of amorphous polymers', *Journal of the Mechanics and Physics of Solids* **82**, 62–81.

Zahn, A. and Balzani, D. [2017], 'Modeling of anisotropic growth and residual stresses in arterial walls', *Acta Polytechnica* **7**, 85 – 90.

Zeng, G.-W., Yang, X.-H., Bai, F. and Gao, H. [2014], 'Visco-elastoplastic damage constitutive model for compressed asphalt mastic', *Journal of Central South University* **21**, 4007–4013.

Zhu, H. and Sun, L. [2013], 'A viscoelastic–viscoplastic damage constitutive model for asphalt mixtures based on thermodynamics', *International Journal of Plasticity* **40**, 81–100.

Österlöf, R., Wentzel, H. and Kari, L. [2016], 'A finite strain viscoplastic constitutive model for rubber with reinforcing fillers', *International Journal of Plasticity* **87**, 1–14.